Vegard Røine Stenerud

Multiscale-Streamline Inversion for High-Resolution Reservoir Models

Thesis for the degree philosophiae doctor

Trondheim, October 2007

Norwegian University of Science and Technology
Faculty of Information Technology,
Mathematics and Electrical Engineering
Department of Mathematical Sciences

NTNU

NTNU
Norwegian University of Science and Technology

Thesis for the degree philosophiae doctor

Faculty of Natural Sciences and Technology
Department of Mathematical Sciences

ISBN 978-82-471-4641-5 (printed version)
ISBN 978-82-471-4655-2 (electronic version)
ISSN 1503-8181

Doctoral theses at NTNU, 2007:211

Printed by NTNU-trykk

Abstract

The topic of this thesis is streamline-based integration of dynamic data for porous media systems, particularly in petroleum reservoirs. In the petroleum industry the integration of dynamic data is usually referred to as history matching. The thesis starts out by giving an introduction to streamline-based history-matching methods. Implementations and extensions of two existing methods for streamline-based history matching are then presented.

The first method pursued is based on obtaining modifications for streamline-effective properties, which subsequently are propagated to the underlying simulation grid for further iterations. For this method, two improvements are proposed to the original existing method. First, the improved approach involves less approximations, enables matching of porosity, and can account for gravity. Second, a multiscale approach is applied for which the data integration is performed on a hierarchy of coarsened grids. The approach proved robust, and gave a faster and better match to the data.

The second method pursued is the so-called generalized travel-time inversion (GTTI) method, which earlier has proven very robust and efficient for history matching. The key to the efficiency of this method is the quasilinear convergence properties and the use of analytic streamline-based sensitivity coefficients. GTTI is applied together with an efficient multiscale-streamline simulator, where the pressure solver is based on a multiscale mixed finite-element method (MsMFEM). To make the history matching more efficient, a selective work-reduction strategy, based on the sensitivities provided by the inversion method, is proposed for the pressure solver. In addition, a method for improved mass conservation in streamline simulation is applied, which requires much fewer streamlines to obtain accurate production-response curves. For a reservoir model with more than one million grid blocks, 69 producers and 32 injectors, the data integration took less than twenty minutes on a standard desktop computer. Finally, we propose an extension of GTTI to fully unstructured grids, where we in particular address issues regarding regularization and computation of sensitivities on unstructured grids with large differences in cell sizes.

Preface

The following thesis is submitted for the degree of *philosophiae doctor* (PhD) at the Norwegian University of Science and Technology (NTNU), Trondheim, Norway. The thesis is part of the Uncertainty in Reservoir Evaluation (URE) initiative at NTNU, financed by the Research Council of Norway and petroleum companies.

Content
For prediction of future reservoir performance, it is important that all available data, such as geological or geostatistical as well as production data, are properly and consistently incorporated. This thesis focuses on the incorporation/inversion of dynamic production data, such as water cuts, flow rates, and well pressures. In the petroleum industry this process is often referred to as history matching, which usually consists of modifying the grid parameters of the 3D reservoir model. This is a particularly difficult task because of the nonlinearity of the flow model, the general lack of data compared to the number of parameters to be modified, the general high degree of uncertainty involved, and the need for a large number of computationally demanding flow simulations for evaluation of the modifications. Traditionally history matching has been performed by manual or semi-automated approaches with a great deal of subjective trial and error by the reservoir engineers. Moreover, the required flow simulations have traditionally been performed by finite-difference/finite-volume reservoir simulators. All over, history matching has been a very time consuming and challenging task. However, over the last ten years streamline simulation has become a strong rival to traditional simulation methods, in particular for flow cases dominated by reservoir heterogeneity, well rates and placement, mobility ratios, etc. Depending on the flow physics of the reservoir, streamline simulation can be orders of magnitude faster than traditional flow simulators. In addition to generally faster flow simulation by streamlines, the streamline formulation itself can be taken advantage of in history matching. In particular, the access to analytic production-response sensitivities and the explicit determination of flow paths, can speed up and improve history matching considerably.

This thesis consists of an introduction to streamline-based history matching and a collection of four research papers on this topic.

Introduction: *Streamline-Based History Matching: A Review.*
The purpose of the introduction is two-fold. First, to give an introduction and a review of streamline-based history matching methods. Second, to put the research conducted in the research papers into a scientific context.

Paper I: *A Multiscale Streamline Method for Inversion of Production Data.*
We propose two improvements to a recent streamline-based history matching method by Wang and Kovscek [2000]. This method first obtains modifications in streamline-effective permeability, based on fractional-flow curves (water-cut), total well rate, and pressure drops for injector–producer pairs. The modifications are then propagated to the simulation grid for further iterations.

The first improvement concerns the part of the method that relates the breakthrough of individual streamlines/streamline-bundles to increments in the fractional-flow curve at a producer. Instead of using the Dykstra–Parsons' algorithm to represent the relative movement

of displacement fronts in all streamlines connected to an injector–producer pair, we represent the displacement fronts explicitly in real time using the same mathematical model underlying Dykstra–Parsons' algorithm. By this approach, the streamlines can be treated individually, and approximations made in the original Wang-Kovscek method are avoided. Further, we also extend the method to enable history matching of porosity and to account for gravity in the expressions for the modifications in streamline-effective properties.

The second improvement is to incorporate a multiscale approach in the inversion, where the reservoir parameters are matched on a hierarchy of coarsened grids. The improved ability to capture large-scale structures for this approach is demonstrated by two synthetic examples.

In the introduction of the thesis we point out two possible extensions to Paper I. First, the assumption of piston-like displacement in each streamline can be relaxed to assume a Buckley–Leverett profile instead. Second, we outline a fully analytic Bayesian approach for mapping streamline-effective properties back and forth between the simulation grid and the streamlines; i.e. an up- and downscaling approach.

Papers II and III: *Adaptive Multiscale Streamline Simulation and Inversion for High-Resolution Geomodels / Multiscale-Streamline Simulation and Dynamic Data Integration for High-Resolution Subsurface Models.*
Through these two works we propose a very efficient approach for incorporating production data, based on the combination of a multiscale-streamline flow simulator [Aarnes et al., 2005] and the so-called generalized travel-time inversion (GTTI) method [He et al., 2002]. The multiscale-streamline simulator used a pressure/velocity solver based on a multiscale mixed finite-element method (MsMFEM), for which local flow problems are solved to obtain basis functions for the global coarse pressure/velocity solutions. The resulting velocity field is given on the fine scale accounting for the fine-scale heterogeneities. An advantage of the MsMFEM pressure solver is that for small or smooth changes in the parameters of the local flow problems, all basis functions do not necessarily have to be recalculated for every pressure step. This can give drastic reductions in simulation time.

The GTTI method is a promising approach for history matching large reservoir models. Analytic streamline-based sensitivities, requiring a single flow simulation to be evaluated, are used in a constrained minimization of the time deviation of production responses. The method has proved applicable to several field cases and exhibits quasilinear properties resulting in fast convergence even if the prior model is not close to the solution.

To speed up the combination of the multiscale-streamline simulator and the inversion method we propose two approaches. First, in Paper II we propose to use the production-response sensitivities from the inversion method to decide which basis functions to reuse and update during the consecutive flow simulations. Second, in Paper III we propose a method for improved mass balance in streamline simulation, which allows for a drastic reduction in the number of streamlines required in the forward simulations to obtain accurate production-response curves.

The proposed approaches are extensively tested for different flow scenarios involving infill drilling, different mobility ratios, and different permeability structures. Further, the entire approach is applied to a 3D field-scale example with more than one million active grid blocks, 69 production wells, and 32 injection wells. For this case, seven years of production data was incorporated in less than twenty minutes on an ordinary desktop computer.

Paper IV: *Generalized Travel-Time Inversion on Unstructured Grids.*
In this work, the generalized travel-time inversion (GTTI) method [He et al., 2002] is extended to fully unstructured grids. The framework for the inversion method extends directly to fully unstructured grids. However, the smoothing operator involved in the regularization has to be generalized. Moreover, a rescaling of the sensitivities is suggested to avoid grid effects for grids with great heterogeneity in grid-cell sizes. The applicability is verified through three examples involving a comparison of history matching on Cartesian and triangular grid, high degree of heterogeneity in grid-cell sizes, and faults with non-neighboring connections.

Es ist nicht genug, zu wissen, man muß auch anwenden[1]

Johann Wolfgang von Goethe,
Wilhelm Meisters Wanderjahre
oder Die Entsagenden (1821)

Suggested follow-up research: Part of the motivation behind Paper IV is the potential applicability of the promising history-matching approach proposed in Papers II and III to fully unstructured grids, in particular involving faults with non-neighboring connections. Thus, the obvious continuation of this work is to continue towards application to real field cases to really verify the applicability of the history-matching approach. However, the applicability to a real field case may require several extensions to the forward simulator of Papers II and III: handling of different production constraints, three-phase flow, gravity, and compressibility, etc.. Theoretically, the forward simulator can handle most of these extensions directly; some of these extensions have already been addressed elsewhere, but other will require further research. Even tough the simulator does not include all physical effects for the moment, it has the ability of consistently capturing more small-scale heterogeneities in the geologic representation, and can in that sense be considered less approximative. An application of the history-matching methodology to a semi-real field case, involving at least real and complex grid geometry, would be a first step towards real field cases. The ultimate goal would be to properly simulate and history-match directly on the geomodel.

The very efficient forward simulator of Papers II and III has a great potential for application to other history-matching methods that require flow simulation on multiple reservoir-model realizations for assessment of uncertainty, e.g. ensemble Kalman filter, McMC, and the Bayesian version of GTTI.

Contributions: Parts of this work have to be credited to my co-authors. In particular Vegard Kippe, who has implemented the flow simulators used in Papers II–IV and is the main architect of the method for improved mass conservation in Paper III. However, the extensions made to the simulators for linking them with the history-matching methods is joint work. Moreover, I got an implementation of the GTTI method from Akhil Datta-Gupta and his research group at Texas A&M University. However, this code has been improved and extended considerably. It should also be mentioned that the introduction is based on a earlier review of streamline-based history-matching methods [Lie, 2002]. The review is updated and extended to better reflect the current situation and challenges in streamline-based history

[1] Knowing is not enough; we must apply.

matching. The rest of this thesis is my own work, but of course under influence of and in collaboration with my supervisors and co-authors.

Main references

J. E. Aarnes, V. Kippe, and K.-A. Lie. Mixed multiscale finite elements and streamline methods for reservoir simulation of large geomodels. *Adv. Water Resour.*, 28(3):257–271, 2005.

Z. He, S. Yoon, and A. Datta-Gupta. Streamline-based production data integration with gravity and changing field conditions. *SPE J.*, 7(4):423–436, December 2002.

Knut-Andreas Lie. Streamline-based history matching: a literature survey with emphasis on sensitivity computations. SINTEF report SF42 F02027, SINTEF, P.O.Box 124 Blindern, NO-0314 Oslo, Norway, December 2002.

Y. Wang and A.R. Kovscek. A streamline approach to history matching production data. *SPE J.*, 5(4):353–362, December 2000.

Acknowledgments

First I would like to thank my supervisors Prof. Helge Holden and Prof. Knut-Andreas Lie for the support and guidance during the work. In particular I would like to thank Knut-Andreas Lie for his continuous excelent support and sharing of knowledge and ideas. I would also like to thank Prof. Henning Omre for providing the financial support for the work via the URE initiative, and also for guidance and for introducing me to the world of Bayesian statistics. The three last papers of this work are a result of collaboration with Dr. Vegard Kippe. I am very grateful for the many enlightening discussions and for providing me with the excellent flow-simulator code utilized in these papers.

I spent the spring and summer terms 2006 at the Department of Petroleum Engineering, Texas A&M University. I would like to thank Prof. Akhil Datta-Gupta for inviting me, and for providing me with further insight into topics related to my research through a petroleum engineering perspective. I am very thankful for this collaboration, which shaped a great part of this thesis.

I would like to thank all the employees at the Department of Mathematical Sciences at NTNU for a great work environment. Especially, I would like to thank the other graduate students for providing a work environment that has enabled and provided a very good balance between hard work and social activities.

Finally, thanks to my family and friends, in particular my wife Elisabeth, for their interest, care, and support during the work.

Vegard Røine Stenerud
Trondheim, October 1, 2007

Thesis outline

Introduction:
Streamline-Based History Matching: A Review

Paper I:
A Multiscale Streamline Method for Inversion of Production Data.
Vegard Røine Stenerud and Knut-Andreas Lie.
Journal of Petroleum Science and Engineering, Vol. 54, pp. 79–92, 2006.

Paper II:
Adaptive Multiscale Streamline Simulation and Inversion for High-Resolution Geomodels.
Vegard Røine Stenerud, Vegard Kippe, Knut-Andreas Lie, and Akhil Datta-Gupta.
Accepted for publication in *SPE Journal*.

Paper III:
Multiscale-Streamline Simulation and Dynamic Data Integration for High-Resolution Subsurface Models.
Vegard Røine Stenerud, Vegard Kippe, Knut-Andreas Lie, and Akhil Datta-Gupta.
Submitted to *Water Resources Research*.

Paper IV:
Generalized Travel-Time Inversion on Unstructured Grids.
Vegard Røine Stenerud, Knut-Andreas Lie, and Vegard Kippe.
Submitted to *Journal of Petroleum Science and Engineering*.

Introduction

Streamline-Based History Matching: A Review

STREAMLINE-BASED HISTORY MATCHING: A REVIEW

VEGARD RØINE STENERUD AND KNUT–ANDREAS LIE

Abstract. In recent years, several methods for streamline-based history matching have been developed. These methods have proved to be efficient for three reasons: First, streamlines delineate flow patterns and can therefore be used to define reduced inverse models. Second, streamline methods provide fast forward simulation. Third, streamline-based sensitivities can be evaluated directly based on one flow simulation for different reservoir responses. We here give a literature review of streamline-based sensitivities and streamline methods used for history matching.

Man skal ej læse for at sluge,
men for at se, hvad man kan bruge.[1]
Henrik Ibsen, Peer Gynt (1876)

1. Introduction

A reservoir model typically consists of a differential equation of the type

$$F\big(\mathbf{y}, \mathbf{x}, t, \mathbf{p}, \frac{\partial^n \mathbf{y}}{\partial \mathbf{x}^n}, \frac{\partial \mathbf{y}}{\partial t}\big) = 0, \tag{1}$$

equipped with appropriate initial and boundary conditions. Here $\mathbf{y}$ denotes responses of the system, $\mathbf{x}$ the spatial coordinates, t time, and $\mathbf{p}$ the set of rock and fluid parameters. The forward problem consists of solving (1) to compute $\mathbf{y}(\mathbf{x}, t)$ for a given set of parameters $\mathbf{p}$. The inverse problem consists of finding a set of reservoir parameters $\mathbf{m} \subseteq \mathbf{p}(\mathbf{x})$ such that the calculated responses $\mathbf{d}^{\text{cal}} \subseteq \mathbf{y}(\mathbf{x}, t)$ match a set of observations $\mathbf{d}^{\text{obs}}$ from the actual system. For the purpose of the inverse problem we will denote the forward model, based on the actual numerical grid-implementation of (1), by $\mathbf{d} = g(\mathbf{m})$.

The primary parameters in a reservoir model are the rock porosity ϕ and the absolute permeability $\mathbf{K}$, which are defined over a grid model. These parameters describe the void volume fraction of the rock and the ability of the rock to transmit a single fluid and are therefore the parameter that often have the largest influence on the fluid flow in a reservoir. Permeability and porosity have considerable spatial variability (especially permeability) and are typically strongly correlated. Unfortunately, they are difficult to measure: direct measurements are only available at a few spatial locations (e.g., from core samples) and one therefore generally has to rely on geostatistical algorithms for generating plausible realizations that can be adjusted using indirect measurements and inverse estimation methods. There are also a large number of other parameters that are not necessarily directly related to the spatial grid. Examples include fluid parameters (e.g., viscosities and densities), rock-fluid parameters (end-point relative permeabilities, residual saturations), well indices, water aquifer size, fault multipliers, and permeability multipliers ($\mathbf{K}_v/\mathbf{K}_h$). In this paper we will mainly present methods for adjusting permeability (or porosity) based on fluid production data observed in wells.

The data available about a reservoir are often classified as two types depending on their association with fluid movement. Static data or *a priori* (prior) data, come from core analysis, well logs, seismics, outcrops, and so on. Dynamic data or *a posteriori* (posterior) data, primarily come from production history, e.g., rate, fractional flow (water-cut), well pressure, well testing, tracer testing, and so on. Common for all dynamic data is that they originate from dynamic processes in the reservoir. Therefore time-lapse seismics can also indirectly be

[1] One should not read for the sake of reading, but rather, to seek what may be useful.

considered as dynamic data. In this review, the term 'history matching' will be used for the process of integrating data to match dynamic observations of the reservoir in the past.

History matching has traditionally been a manual and time-consuming task for the reservoir engineer, consisting of iteratively modifying the reservoir description and running flow simulations for evaluating the resulting reservoir responses. The most common approaches for automated estimation of reservoir parameters, e.g., permeability and porosity, are based on minimization of an objective function (sometimes called a misfit function), which typically has the following form

$$\mathcal{O} = \sum_{j=1}^{N_d} w_j \big(d_j^{\text{obs}} - d_j^{\text{cal}}\big)^2. \tag{2}$$

Here the scalars w_j have been introduced to weight the influence of the individual observations. Algorithms used for minimizing the objective function can be classified as two types: gradient and nongradient methods. Gradient methods use the gradient of the objective function, where the gradient is defined as $\nabla\mathcal{O} = \partial\mathcal{O}/\partial\mathbf{m}$. This gradient is in turn given by the sensitivity matrix, which is the gradient of the calculated responses $\mathbf{d}^{\text{cal}} = g(\mathbf{m})$ with respect to the parameters $\mathbf{m}$,

$$\mathbf{G} = \frac{\partial \mathbf{d}^{\text{cal}}}{\partial \mathbf{m}}, \qquad G_{ji} = \frac{\partial d_j^{\text{cal}}}{\partial m_i}.$$

The sensitivity coefficients G_{ji} measure how a perturbation in the parameter vector effects the responses of the system. Efficient computation of these quantities is a crucial point when developing an efficient parameter-estimation method. Commonly used gradient algorithms include Gauss–Newton, quasi-Newton, steepest descent, conjugate gradients, and Levenberg–Marquardt, see e.g., [10, 125]. Gradient methods converge relatively fast, but may easily fail if the objective function is nonsmooth, in which case the solution may get stuck in a local minimum. Nongradient methods, as the name says, do not use gradients to minimize the objective function. Common algorithms of this group include simulated annealing, genetic algorithms, neighborhood algorithms, etc. [118, 125]. These methods are fairly simple to implement, are always able to reach a global minimum, but may have relatively slow convergence and thus require a large number of forward simulations, which are usually the most computationally expensive part of a history-matching algorithm.

History-matching is usually an ill-posed problem, for which a unique solution seldom exists. Indeed, the number of data points $\mathbf{d}$ to be matched is typically much lower than the number of parameters $\mathbf{m}$ to be modified. Further, there may be redundancy in the information represented in the data. The inverse problem is therefore usually strongly under-determined, so a lot of possible reservoir parameters $\mathbf{m}$ can potentially match the data $\mathbf{d}$. Moreover, there are strong nonlinearities, model errors, and numerical errors involved in the forward model. In addition, there are uncertainties associated with the measured data. Thus, constraints are required to guide the descent towards the inverse solution and make it more stable. In practice this is often done by adding regularization terms to the objective function, e.g., by constraining to prior geological information. Moreover, the non-uniqueness and all the errors involved make uncertainty assessments important.

History-matching methods can be divided into deterministic and stochastic methods. A deterministic method can be described as a function $\mathbf{m} = f(\mathbf{m}_p, \mathbf{d}, \ldots)$ that takes a single prior reservoir model $\mathbf{m}_p$ to a single updated reservoir model $\mathbf{m}$ that accounts for the production data. In other words, deterministic methods intend to obtain an inverse/backward solution $\mathbf{m} = g^{-1}(\mathbf{d})$ for the deterministic forward model $\mathbf{d} = g(\mathbf{m})$. As discussed above, this is a very hard problem that requires some kind of constraining.

Stochastic methods are often referred to as geostatistical methods, and are sometimes (as we will see) coupled in some sense with deterministic methods. Geostatistical methods describe the reservoir model, more or less formally, by a probability distribution $f(\mathbf{m})$, for which a realization is denoted by $[\mathbf{m}] \sim f(\mathbf{m})$. Rather than having an analytic representation, probability distributions are often represented by an ensemble of realizations said to be sampled from or span the probability distribution. The initial probability distribution is often referred

to as the prior distribution, and should incorporate the static data in a geostatistical manner. The spatial covariance structure of the reservoir properties can be incorporated via a variogram or covariance function. This is referred to as two-point statistics (variogram based), but multi-point statistics are needed to describe complex structures like fractures and channels [25, 129]. Conditioning on the dynamic data can be done by specifying a likelihood model $f(\mathbf{d}|\mathbf{m})$ that relates the reservoir parameters $\mathbf{m}$ of interest to the dynamic data $\mathbf{d}$ through the forward model plus observation error. The prior model and forward model fully specify the posterior model $f(\mathbf{m}|\mathbf{d})$ via Bayes' rule

$$f(\mathbf{m}|\mathbf{d}) = \frac{f(\mathbf{d}|\mathbf{m})f(\mathbf{m})}{f(\mathbf{d})} \propto f(\mathbf{d}|\mathbf{m})f(\mathbf{m}). \tag{3}$$

Although the posterior distribution is generally only known up to a constant, it is possible to sample from the distribution to obtain realizations denoted by $[\mathbf{m}|\mathbf{d}] \sim f(\mathbf{m}|\mathbf{d})$. Methods intended to sample from the posterior distribution, by some kind of simulation-based interference, are referred to as Monte Carlo methods. Commonly used Monte Carlo methods are Markov-chain Monte Carlo (McMC) [44, 119], ensemble Kalman filter (EnKF) [50, 51], particle filter [47], randomized maximum likelihood [87, 107], SIR-algorithm [70], pilot-point (PP) methods [93, 115], and sequential self-calibration (SSC) [28, 62]. The main advantages of geostatistical methods are that small-scale geological variability is incorporated and that uncertainty can be assessed from the realizations. However, history matching of multiple realizations is often very computationally expensive. Therefore, the number of realizations are often kept low or reduced, which may cause poor uncertainty estimates. The selection of a subset of realizations to be pursued for further uncertainty assessments is referred to as ranking, and is usually based on some criteria intended to preserve the information sought to the maximum extent [108]. Comparative studies of geostatistical history-matching methods are reported in the literature [see e.g. 14, 56, 96, 151].

This paper is meant as a review of history-matching methods that are based on a streamline formulation. Streamline simulation has experienced a revival in recent years and has proved to be an effective tools for fast reservoir simulation. Streamline simulators are most efficiently applied to injection-dominated cases and cases where the fluid flow is governed by heterogeneities in the rock properties, well positions and rates, fluid mobilities, etc. Streamlines are well suited for history-matching of reservoir properties to fit dynamic data due to three main reasons: (i) streamline methods are relatively fast compared with traditional finite-difference methods for forward simulation, and (ii) by nature streamline methods give precise information about the geometries of the flow pattern and can be used to define reduced models, for instance injector-producer pairs. (iii) streamline-based sensitivities can be evaluated directly from analytic expressions after a single flow simulation. In this paper we will focus on the latter two points. To this end, we start out by giving a review of streamline-based sensitivities in Section 4, after having introduced the model equations most commonly used in streamline-based history matching in Section 2 and given a quick introduction to streamline simulation in Section 3.

Streamline sensitivities are defined as analytical integrals along streamlines and can be computed very efficiently based on a single flow simulation. First, time-of-flight sensitivities [67, 135, 143] with respect to common reservoir parameters are presented. The time-of-flight sensitivities are the basic building blocks for obtaining streamline-based sensitivities for different dynamic data. Further, we describe streamline-based sensitivities for arrival-time, time-shift, saturation, tracer concentration, fractional flow, and gas-oil ratio. Moreover, we briefly discuss streamline-derived sensitivities for time-lapse amplitudes [136] and sensitivities for pressure interference tests [69, 92]. Finally, we briefly describe sensitivities with respect to the parameters of the gradual deformation method [117].

Section 5 constitutes the main part of this paper and in this section we give a survey of history-matching methods based on streamlines. Rather than discussing methods (or papers) where streamline simulation has been applied merely to provide fast forward simulation, we focus on different uses of streamline methods to modify the geological/reservoir simulation models throughout the history-matching process. However, we will neither go into great

details about different formulations of the history-matching problem as an inverse problem nor will we discuss methods for solving the corresponding inverse problems in great detail. The reference list of this review is quite extensive and will hopefully guide the reader to sources for further reading. In picking references we have tried to cite papers where a complete and/or mature presentation is given, which means that we are not always referring to the first occurrence of an idea. Further, we have prioritized, whenever possible, referring to peer-reviewed papers. Short reviews of streamline-based history matching are also given in [40, 126, 127]. A preliminary version of this paper has also been published as a technical report [95].

The surveyed methods for history matching based upon streamlines can roughly be divided into four different categories:

- *The Assisted History Matching* (AHM) approach was introduced by Emanuel and Milliken [49] and is outlined in Section 5.1. This method defines sub-regions associated with wells in which subsequent targeted changes of grid parameters can be performed manually (or semi-automatic) by a reservoir engineer.
- *Travel-Time Inversion* (TTI) methods were introduced by Vasco, Datta-Gupta and coworkers [135] based upon an analogy with seismic ray inversion. Streamlines are used to estimate sensitivity coefficients analytically, thereby speeding up the optimization on the grid-cell level. The first approach is a two-step approach with a travel-time matching followed by an amplitude matching. Later, so-called *Generalized Travel-Time Inversion* (GTTI) has been introduced to combine travel-time matching and amplitude matching while keeping the desirable convergence properties of travel-time inversion [67]. For the GTTI method time-shifts for the production curves, minimizing the misfit, are jointly propagated to necessary modifications in the reservoir parameters. The methods in this category are described in Section 5.2.
- Methods for matching *streamline effective properties* (SLEP) were first introduced by Wang and Kovscek [141] and have later been extended by others. The key idea of these methods is to relate the mismatch between observed and calculated production data to a mismatch in effective properties along streamlines or streamline bundles, and adjust the effective properties to obtain a satisfactory match. Then the perturbations in effective properties are propagated to individual grid cells (by direct mapping or by a geostatistical algorithm). These methods are described in Section 5.3.
- The final category consists of geostatistical history-matching methods that take advantage of streamline-defined regions or streamline-derived sensitivities. Methods discussed herein include Markov chain Monte Carlo [98], ensemble Kalman filter [9, 45], sequential self-calibration [143], and the gradual deformation method [58, 59]. The methods in this category are described in Section 5.4.

Moreover, in Section 6 we describe some methods for streamline-based ranking of geostatistical realizations of reservoir models [75, 142]. Finally, Section 7 contains a discussion and comparison of some of the methods introduced earlier in the paper.

2. Simplified Flow Models

Almost all the history-matching methods to be surveyed later in the paper are based on simplified flow models. For completeness, we will therefore introduce these models in some detail and specify the accompanying simplifying assumptions.

The fundamental equation describing flow in a porous media is the continuity equation which states that the mass is conserved for phase α

$$\frac{\partial}{\partial t}\left(\phi\rho_\alpha S_\alpha\right) + \nabla\cdot\left(\rho_\alpha \mathbf{u}_\alpha\right) = q_\alpha.$$

Here ϕ denotes porosity, ρ_α is density, S_α is saturation, $\mathbf{u}_\alpha$ is the phase velocity, and q_α models fluid sources and sinks. The saturations are volume fractions and must therefore add up to unity, i.e., $\sum_\alpha S_\alpha = 1$. For the phase velocity, we use the semi-empirical Darcy's law,

which relates the phase velocity to the gradient of the phase pressure p_α,

$$\mathbf{u}_\alpha = -\lambda_\alpha \mathbf{K}\big(\nabla p_\alpha - \rho_\alpha \mathbf{g}\big), \tag{4}$$

where λ is the relative fluid mobility, $\mathbf{K}$ is the tensor of absolute permeability, and $\mathbf{g}$ is the gravity vector (pointing downwards). The relative mobility is defined as $\lambda_\alpha = k_{r\alpha}/\mu_\alpha$, where $k_{r\alpha}$ is the relative permeability, generally a function of the concentrations/saturations of other present phases, and μ_α is the viscosity of phase α.

For two-phase flow of oil and water ($\alpha = o, w$) this gives three equations and a set of constitutive relations, for which it is common to choose a pressure and the water saturation as the primary unknowns. By manipulating continuity equations and Darcy's law, one can derive the so-called fractional formulation consisting of an equation for the pressure and an equation describing fluid transport, which is referred to as the saturation equation. The pressure equation has more or less elliptic characteristics depending on the compressibility of the rock and fluids, and the saturation equation is more or less hyperbolic, depending on capillary pressures. Most of the methods discussed later assume incompressible and immiscible flow. Using these assumptions and introducing the total velocity $\mathbf{u} = \mathbf{u}_o + \mathbf{u}_w$ and a so-called global pressure p (see e.g., [2]) as primary unknowns, the coupled system can be written as,

$$\nabla \cdot \mathbf{u} = q, \qquad \mathbf{u} = -\mathbf{K}\Big[\lambda_t \nabla p - (\lambda_w \rho_w + \lambda_o \rho_o)\mathbf{g}\Big], \tag{5}$$

$$\phi \frac{\partial S_w}{\partial t} + \nabla \cdot \Big[f_w\big(\mathbf{u} + \mathbf{K}\lambda_o \nabla p_{\text{cow}} + \mathbf{K}\lambda_o \mathbf{g}\Delta\rho\big)\Big] = \frac{q_w}{\rho_w}. \tag{6}$$

Here we have introduced the total mobility $\lambda_t = \lambda_w + \lambda_o$, the fractional-flow function of water $f_w = \lambda_w/\lambda_t$, the capillary pressure $p_{\text{cow}} = p_o - p_w$, the density difference $\Delta\rho = \rho_w - \rho_o$, and the total contribution from the wells $q = q_w/\rho_w + q_o/\rho_o$. The two equations are coupled since the mobilities λ_α depend on the water saturation. We will refer to (5) and (6) as the pressure- and the transport equation, respectively.

The majority of the history-matching methods also assume negligible gravity and capillary forces, i.e., that the terms involving $\mathbf{g}$ and p_{cow} vanish, and we can define $p = p_w = p_o$. Further, for incompressible flow $\nabla \cdot \mathbf{u} = 0$ away from the wells, so $\nabla \cdot (f_w \mathbf{u}) = \mathbf{u} \cdot \nabla f_w$. Moreover, when discussing oil-water systems, we drop the subscript 'w'. Hence, the system is considerably simplified

$$\nabla \cdot \mathbf{u} = q, \qquad \mathbf{u} = -\mathbf{K}\lambda_t \nabla p, \tag{7}$$

$$\phi \frac{\partial S}{\partial t} + \mathbf{u} \cdot \nabla f = \tilde{q}. \tag{8}$$

Unless stated otherwise, this will therefore be our flow model in the following sections and the dynamic data observed will typically be the fractional flow (or water cut) in wells.

For streamline methods, the coupled system (7)–(8) is solved using a sequential splitting: First, the current saturation field is used to evaluate the mobilities $\lambda_t(S)$ in (7), and the equation is solved for the pressure and velocity. Then the velocity field $\mathbf{u}$ is held fixed for a given time step while the saturation is advanced forward in time according to (8). How this is done, will be explained in the next section. After the saturation has been advanced forward in time, the new values are used to update the mobilities in (7), an so on.

In the above model, the permeability has been assumed to be a tensor. Within streamline-based history matching, permeability usually is considered as isotropic and can therefore be described by a scalar function. Using anisotropic permeability will make the inversion problem much more under-determined. Moreover, the dynamic well data to be matched are often noisy and spatially convoluted, and therefore contain limited spatial and small-scale information. To adjust the permeabilities in other directions, multipliers or correlations are usually applied, for which the involved parameters may also be history-matched. However, some of the derivations presented later in this paper may in principle apply directly to a diagonal or full permeability tensors as well.

3. Streamline methods

For the sake of completeness we give a very brief introduction to streamline simulation. For a given velocity field $\mathbf{u}$, a streamline is a line that is everywhere tangential to $\mathbf{u}$, that is,

$$\frac{d\mathbf{x}}{dr} = \frac{\mathbf{u}}{|\mathbf{u}|}, \qquad \mathbf{x}(0) = \mathbf{x}_0.$$

Rather than using the arc length r to parameterize streamlines, it is common to introduce the so-called time-of-flight τ, which takes into account the reduced volume available for flow, i.e., the porosity ϕ. Time-of-flight is defined by the following integral

$$\tau(R) = \int_0^R \frac{\phi(\mathbf{x}(r))}{|\mathbf{u}(\mathbf{x}(r))|}\, dr = \int_0^R s(\mathbf{x}(r))\, dr, \tag{9}$$

where τ expresses the time it takes a passive particle to travel a distance R along a streamline (in the interstitial velocity field $\mathbf{v} = \mathbf{u}/\phi$). The function $s(\mathbf{x})$ is often referred to as the slowness function. Alternatively, by the fundamental theorem of calculus and the directional derivative, τ can be expressed by the following differential equation [41]

$$\frac{\phi}{|\mathbf{u}|} = \frac{d\tau}{dr} = \frac{\mathbf{u}}{|\mathbf{u}|}\cdot\nabla\tau \quad \Rightarrow \quad \mathbf{u}\cdot\nabla\tau = \phi, \tag{10}$$

which we, in lack of a better name, will refer to as the time-of-flight equation. We will denote the time-of-flight increment over grid cell i by $\Delta\tau_i$. Hence, the time-of-flight at the well can be written as the sum of the traversal times for all the N_c grid cells intersected by the streamline; $\tau = \sum_{i=1}^{N_c} \Delta\tau_i$. (Regarding subscripts, we will henceforth use indices i, j, k and ℓ to denote grid cells, times, wells and streamlines, respectively. Moreover, we use the expression 'grid cell', rather than 'grid block', when a method in theory can be applicable to more general grid cells than non-degenerated quadrilateral or hexahedral grid blocks.)

Streamlines and time-of-flight can be used to define an alternative curvilinear and flow-based coordinate system in three dimensions. To this end, we introduce the bi-streamfunctions ψ and χ [18], for which $\mathbf{u} = \nabla\psi\times\nabla\chi$. In the streamline coordinates (τ,ψ,χ), the gradient operator is expressed as

$$\nabla_{(\tau,\psi,\chi)} = (\nabla\tau)\frac{\partial}{\partial\tau} + (\nabla\psi)\frac{\partial}{\partial\psi} + (\nabla\chi)\frac{\partial}{\partial\chi}. \tag{11}$$

Moreover, a streamline Ψ is defined by the intersection of a constant value for ψ and a constant value for χ. Because $\mathbf{u}$ is orthogonal to $\nabla\psi$ and $\nabla\chi$, it follows that

$$\mathbf{u}\cdot\nabla_{(\tau,\psi,\chi)} = (\mathbf{u}\cdot\nabla\tau)\frac{\partial}{\partial\tau} = \phi\frac{\partial}{\partial\tau}. \tag{12}$$

Therefore the coordinate transformation $(x,y,z)\to(\tau,\psi,\chi)$ will reduce the three-dimensional transport equation

$$\phi\frac{\partial S}{\partial t} + \mathbf{u}\cdot\nabla f(S) = 0.$$

to a family of one-dimensional transport equations along each streamline [41, 85],

$$\frac{\partial S}{\partial t} + \frac{\partial f(S)}{\partial\tau} = 0. \tag{13}$$

In other words, there is no exchange of the quantity S between streamlines and each streamline can be viewed as an isolated flow system.

For each streamline a constant volumetric flux q_ℓ is associated. Quantities like the total water rate, tracer concentration, fractional flow and gas-oil ratio (GOR) at a well can be obtained by in some sense summing the quantities of the contributing streamlines. For instance the fractional flow and total rate at a producer at time t are given by [17]

$$f(t) = \frac{1}{q}\sum_{\ell=1}^{N_{\mathrm{sl}}} q_\ell f_\ell(t), \qquad q = \sum_{\ell=1}^{N_{\mathrm{sl}}} q_\ell, \tag{14}$$

where N_{sl} is the number of streamlines connected to the well, q_ℓ is the total flux assigned to streamline ℓ, and $f_\ell(t)$ is the fractional flow associated with streamline ℓ at time t.

In modern streamline methods one does not need to represent the path of a streamline explicitly in three-dimensional space to perform the mapping back and forth between physical space and streamlines. Instead, the parameterization, i.e., the integral in (9), can be computed numerically on a cell-by-cell basis. The one-dimensional time-of-flight grid is obtained by tracing a streamline forward and/or backward towards a sink/source (wells) [17]. Most commonly used is a semi-analytical tracing algorithm introduced by Pollock [112], which uses analytical expressions of the streamline paths inside each cell based on the assumption that the velocity field is piecewise linear locally. Although Pollock's method is only valid for regular grids, it is often used also for highly skewed and irregular grids. Other approaches for tracing on unstructured grids and the associated accuracy are discussed in [38, 66, 79, 102, 103, 113].

As mentioned above, (13) is solved numerically forward in time on a sequence of steady-state approximations for the velocity field, just as done for an IMPES formulation in a finite-difference simulator. In general, the streamline trajectories will change for unsteady flow cases, for instance for non-unit mobility ratios (especially favorable) or because of changes in the well configuration (e.g., infill drilling or temporal rates/pressure constraints). For unsteady flow the changes in streamline trajectories are accounted for by regenerating the streamlines periodically through pressure/velocity updates. The saturations/concentrations are then mapped back and forth between the pressure grid and the streamlines for each update (described below). The efficiency of streamline simulation compared to conventional finite-difference simulators is traditionally primarily caused by the ability of taking longer pressure steps within the sequential splitting formulation [86].

The streamline formulation can also be applied to describe flow including more physical effects than those described in the simple two-phase model (7)–(8). A similar decomposition of the 3D transport equation can also be performed for compressible flow [36], in which case the one-dimensional transport equation will have a source term on the right-hand side. Further, the decomposition has been extended to compositional flow with compressibility effects [109]. Moreover, it is possible to include gravity and capillary forces by operator splitting, as discussed in [22, 60, 61, 86]. However, gravity and capillary forces may enforce fluxes traverse to the direction defined by the total velocities, and therefore separate sets of streamlines have to be used for the gravity and capillary steps. Extensions to fractured reservoir flow have also been reported [6, 46, 88], also resulting in source terms in the 1D transport equations.

3.1. **Linear Transport.** For the special case of piston-like displacement, which will be a key assumption in several of the history-matching methods discussed below, the flux function is linear. Similarly, for the neutral advection of a passive tracer, (13) reads

$$\frac{\partial C}{\partial t} + \frac{\partial C}{\partial \tau} = 0. \tag{15}$$

The injector has a concentration history $C_0(t)$, which gives a time-dependent boundary-value problem for (15). The response at the producer reads [41],

$$C(t) = C_0(t-\tau) = C_0\Big(t - \int_\Psi s(\mathbf{x})\, dr\Big), \tag{16}$$

which is easily verified by inserting the expression into (15) and the fact that the solution is unique [73]. For the special case of continuous and constant injection (which is equivalent to piston-like displacement), the solution is particularly simple

$$C(t) = \begin{cases} 0, & t < \tau, \\ C_0, & t > \tau. \end{cases}$$

Dispersion is not accounted for in (15) or (16), but this can also be accounted for [see e.g. 76]. Further, for instance for a partitioning tracer being partially absorbed into the oil phase the travel time along a streamline will be increased in the presence of oil saturation. This can be

accounted for by increasing the slowness $s(\mathbf{x})$ by the partitioning properties of the tracer [76]

$$s(\mathbf{x}) = \frac{\phi(\mathbf{x})}{|\mathbf{u}(\mathbf{x})|}(S_w + P_o S_o). \tag{17}$$

Here, S_o and S_w are the oil and water saturations, respectively, and P_o is the partitioning coefficient of the tracer defined as the ratio of tracer concentration in the oil phase to that in the water phase. Hence, P_0 will take on unity for a neutral tracer.

3.2. **Buckley–Leverett Displacement.** A common assumption in many history-matching methods is to assume a so-called Buckley–Leverett profile along each streamline. That is, one considers the one-dimensional transport equation in (13) and assumes constant initial saturation S_0 along each streamline and a constant injection state S_i. Mathematically, this corresponds to a so-called Riemann problem with initial data

$$S(0,\tau) = \begin{cases} S_i & \text{for } \tau < 0, \\ S_0 & \text{for } \tau \geq 0. \end{cases}$$

Since both the one-dimensional transport equation and the initial data are scale-invariant or self-similar—that is, invariant under the map $\tau \to k\tau$ and $t \to kt$—the solution should also have that property, i.e., $S(t,\tau) = S(\tau/t)$. More specifically, for Riemann initial data the solution of the one-dimensional transport equation is given by the analytic Buckley–Leverett solution (Riemann solution) [73]

$$S(t,\tau) = \begin{cases} S_i & \text{for } \tau \leq t\widetilde{f}'(S_i), \\ (\widetilde{f}')^{-1}(\frac{\tau}{t}) & \text{for } t\widetilde{f}'(S_i) \leq \tau \leq t\widetilde{f}'(S_0), \\ S_0 & \text{for } \tau \geq t\widetilde{f}'(S_0). \end{cases} \tag{18}$$

Here $\widetilde{f}$ denotes the upper concave envelope of f if $S_i > S_0$, and the lower convex envelope of f if $S_i < S_0$. The front saturation $\tilde{S}$ can be determined by solving the equation [73]

$$f'(\tilde{S}) = \frac{f(\tilde{S}) - f(S_0)}{\tilde{S} - S_0},$$

and the injection front will arrive at the well at time $\tau/f'(\tilde{S})$.

3.3. **General Displacement.** For cases where the injection problem is not a simple Riemann problem, the one-dimensional transport equation (13) must generally be solved numerically. The standard approach for solving the scalar problems numerically along streamlines is to use a finite-difference or finite volume method. The simplest such scheme is the first-order upwind scheme,

$$S_i^{j+1} = S_i^j - \frac{\Delta t}{\Delta \tau}\Big[f(S_i^j) - f(S_{i-1}^j)\Big].$$

For explicit schemes a so-called CFL condition has to be fulfilled with respect to time step size to keep the numerical solution stable. The CFL condition usually puts a severe restriction on the time-step size compared to what is required with respect to accuracy. To make the critical time-step size less restrictive, the time-of-flight grid is often mapped to a more regular grid for these schemes. For multi-phase and compositional flow with strong nonlinear couplings in the system of flow equations, the sharpness and the accuracy of the propagation speeds need to be accurately represented, which may require more accurate schemes for solving along streamlines. We here confine ourself with just listing a few recent related works [90, 99, 111, 128, 131].

Alternatively, one may use an implicit scheme of the form

$$S_i^{j+1} = S_i^j - \frac{\Delta t}{\Delta \tau}\Big[f(S_i^{j+1}) - f(S_{i-1}^{j+1})\Big].$$

to escape the stability restrictions. However, numerical diffusion is often associated with these schemes and a system of N_c equations, where N_c is the number of unknowns along the streamline, has to be solved. To reduce the numerical diffusion, it is therefore customary to use implicit time steps that are smaller than the pressure steps. In other words, there are

two different time steps involved in streamline simulation: the pressure step of the sequential splitting, and the local time step used in the transport solve.

For two-phase (and other scalar problems), a much better approach is to use front tracking [73] as discussed in [19–21]. This grid-independent method is based on an entirely different approach than finite-difference schemes and is unconditionally stable and devoid of numerical diffusion. Instead of discretizing the problem spatially, the initial data S_0 and the flux function f are approximated by piecewise constant and piecewise linear functions, respectively. The resulting approximated problem consists of a set of Riemann problems that can be solved exact analytically forward in time given an exact Riemann-solution for the given equation. During the forward solves the different Riemann solutions will interact and create new Riemann problems, and so on. The solution of each Riemann problem is given by the Buckley–Leverett construction discussed in the previous section, which for a linear flux function simplifies to a step-function with discontinuities propagating along space-time rays, see [73] for more details. Extensions to miscible and 3-phase flow for front tracking are addressed in [83, 84].

3.4. **Mapping Between Pressure Grid and Streamlines.** A crucial step in streamline methods is the mapping of saturations from the pressure grid to streamlines, and vice versa. Mapping from pressure grid to streamlines is usually performed by simply picking up the piecewise-constant saturation values from the grid cells that are intersected by the streamline. Alternatively, higher accuracy is obtained if one first makes a piecewise linear reconstruction on the pressure grid before mapping to streamlines, as suggested by Mallison et al. [100]. Contrary, mapping the saturations from streamlines to grid cells is done by

$$S_i = \frac{\sum_\ell S_{\ell,i} V_{\ell,i}}{\sum_\ell V_{\ell,i}}, \tag{19}$$

where $V_{\ell,i} = q_\ell \Delta\tau_{\ell,i}$ is the pore volume associated with streamline ℓ over grid cell i [17]. Unfortunately, this mapping may potentially introduce large errors in the mass balance of the reservoir. Commercial streamline solvers therefore use some kind of correction to counteract the lack of mass balance. One such simple approach is discussed by Stenerud et al. [122], who suggest to adjust the time-of-flight locally to preserve the local pore volume for both the mappings. Doing so reduces significantly the number of streamlines required to obtain accurate production curves, which is more important within history matching than obtaining high local accuracy in space. Mallison et al. [100] suggest another, and entirely different, approach based on a geostatistical kriging mapping in which streamlines are no longer seen as fluid carriers but rather as an unstructured, flow-based grid for computing fluid transport.

Finally, we mention that spatial errors and convergence in streamline simulation have been studied by Jimenez et al. [79]. For further details on streamline simulation, we refer to the upcoming textbook by Datta-Gupta and King [40].

4. Streamline-Based Computation of Sensitivities

One of the benefits of applying streamlines for history-matching is the possibility of fast evaluation of reservoir-response sensitivities. These sensitivities can be evaluated analytically after a single forward simulation. Using streamlines to compute sensitivities is thus an optimal approach. We will here review the current literature on streamline-based sensitivity computations, starting by discussing the computational cost and applicability of streamline-based relative to traditional methods for computing sensitivities.

4.1. **Efficiency and Applicability.** Traditional methods for computing sensitivities of multiphase production data with respect to reservoir parameters can be divided into three categories: perturbation methods, gradient-simulator methods [8, 62], and adjoint or optimal control methods [30, 32, 94, 148, 149]. We will not go into much details about these methods, but we will briefly discuss the computational costs and compare them with the streamline-based approaches.

The perturbation method is the brute force approach for obtaining sensitivities. Each parameter is perturbed followed by a flow simulation to evaluate the resulting perturbations in

the production responses. For N parameters this approach therefore requires $N+1$ simulations and is thus very expensive. Both the gradient-simulator method and the adjoint method require one forward simulation and one or more solutions of a system of linear equations of the same size as the discretized system for the flow equations (different right-hand sides). The gradient-simulator method requires the solution of a linear system to obtain sensitivities for the state variables with respect to a parameter of interest. The linear system is obtained by differentiating a discretized version of the flow equations with respect to the parameter of interest. For instance, consider a pressure system $\mathbf{Ap} = \mathbf{b}$. By differentiating this equation with respect to a parameter m we obtain

$$\frac{\partial \mathbf{A}}{\partial m}\mathbf{p} + \mathbf{A}\frac{\partial \mathbf{p}}{\partial m} = \frac{\partial \mathbf{b}}{\partial m},$$

which can be solved to obtain $\partial\mathbf{p}/\partial m$. Hence, a linear system has to be solved one time for each reservoir parameter of interest for each simulator step. The gradient-simulator method is usually not as expensive as the perturbation method because the sensitivities are not necessarily needed for all steps. For the adjoint method, one needs to solve an adjoint linear system for every gradient needed. Therefore, one solution is needed to obtain the gradient of an objective function, while the number of solutions to obtain the sensitivity matrix is equal to the number of data points to be integrated. The adjoint systems are solved backward in time from the end of the last pressure step, and this requires storage of the intermediate saturation and pressure information for the pressure steps. For a more thorough presentation of the adjoint method see for instance [148], where it is described in the appendix how the adjoint method can be used to obtain time-shift sensitivities, cf. Section 4.4. An alternative to the adjoint method for obtaining the *gradient* of an objective function is the stochastic gradient approach used in the SPSA algorithm [57, 120], which requires two evaluations of the objective function (two flow simulations) to obtain a realization of the gradient. This approach thus has similar computational complexity as the adjoint method, but can easily be implemented on top of any flow simulator because mainly evaluations of the objective function are required. The theoretical foundation for this approach is that at least for a quadratic objective function the expectation value of the stochastic gradient is the true gradient [57]. However, the stochastic nature of the gradient may slow down the convergence of the history matching as demonstrated in [57].

The streamline-based approaches described below are superior with respect to efficiency for obtaining the sensitivity matrix for large systems because they only require one forward simulation and a post-processing step which basically boils down to bookkeeping of analytic arithmetic computations.

Sensitivities describe how calculated reservoir responses will react to a small perturbation in the reservoir description. The sensitivities depend, in principle, on the way the reservoir responses are calculated, e.g., by a flow simulator, by an inverse seismics-to-saturation model, etc., and should account for errors made in the calculation. However, highly accurate sensitivities are seldom needed for applications in inverse modeling of petroleum reservoirs, since sensitivities are mostly used within an iterative inversion algorithm to determine in which direction one should perturb the solution in the next iteration. Moreover, large uncertainties in the reservoir description will in general mask errors made in the calculation of sensitivities. In practice, sensitivities obtained by one reservoir response simulator may perform well for another simulator too. For instance, streamline sensitivities may be obtained by using the velocity fields of a finite-difference simulator, even though streamlines are not used for the actual flow simulation, see e.g., [35]. This extends the applicability of fast streamline-based sensitivity calculations considerably.

4.2. **Time-of-Flight Sensitivities.** The sensitivity of the time-of-flight with respect to reservoir parameters is the basic building block used to obtain streamline-based sensitivities for reservoir responses. We will therefore start out by presenting two different approaches for deriving time-of-flight sensitivities.

The first approach is used in particular by Datta-Gupta and coworkers. By Darcy's law (7) for the total velocity $\mathbf{u}$ and the time-of-flight definition in (9), the time-of-flight is related

to reservoir properties by

$$\tau = \int_\Psi \frac{\phi(\mathbf{x})}{\lambda_t K(\mathbf{x})|\nabla p|}\, dr = \int_\Psi \frac{\phi(\mathbf{x})A(\mathbf{x})}{q}\, dr = \int_\Psi s(\mathbf{x})\, dr. \tag{20}$$

Here ϕ is the porosity, K is the absolute permeability, p is the pressure, λ_t is the total mobility, A is the streamtube cross sectional area, and q is the total volumetric streamline rate.

The sensitivity of τ with respect to a reservoir parameter m can then be defined by [135]

$$\frac{\partial \tau}{\partial m} = \int_\Psi \frac{\partial s(\mathbf{x})}{\partial m(\mathbf{x})}\, dr, \tag{21}$$

where $\partial s(\mathbf{x})/\partial m(\mathbf{x})$ typically is given by, for instance

$$\frac{\partial s}{\partial K} = -\frac{\phi}{\lambda_t K^2 |\nabla p|} = -\frac{s}{K}, \tag{22}$$

$$\frac{\partial s}{\partial \phi} = \frac{1}{\lambda_t K |\nabla p|} = \frac{s}{\phi}, \tag{23}$$

$$\frac{\partial s}{\partial |\nabla p|} = -\frac{\phi}{\lambda_t K |\nabla p|^2} = -\frac{s}{|\nabla p|}, \tag{24}$$

$$\frac{\partial s}{\partial \lambda_t} = -\frac{\phi}{\lambda_t^2 K |\nabla p|} = -\frac{s}{\lambda_t}, \tag{25}$$

$$\frac{\partial s}{\partial q} = -\frac{\phi A}{q^2} = -\frac{s}{q}. \tag{26}$$

Similar expressions for various relative permeability parameters are described in Appendix A. We now assume that each reservoir parameter m_i is constant inside grid cell i. Then a time-of-flight sensitivity can be associated with each grid cell: The sensitivity with respect to permeability, for instance, is given by

$$\frac{\partial \tau}{\partial K_i} = \frac{\partial \Delta\tau_i}{\partial K_i} = \int_{\Psi_i} \frac{\partial s(\mathbf{x})}{\partial K_i}\, dr = \int_{\Psi_i} -\frac{s(\mathbf{x})}{K_i}\, dr = -\frac{\Delta\tau_i}{K_i}. \tag{27}$$

The sensitivities are calculated under the assumption that the streamlines do not shift as a result of a small perturbation in the reservoir properties. Further, it is assumed that the different reservoir properties are independent in the sense that a small perturbation in one property does not perturb any of the other properties. However, especially the pressure will generally depend on the permeability distribution, but this dependence is usually neglected.

Tracer partitioning can be accounted for by defining the slowness function $s(\mathbf{x})$ as in (17) [43, 76]. Illiassov and Datta-Gupta [76] also use this formulation to compute time-of-flight sensitivities with respect to saturations. Further, we remark that it may be possible to account for gravity and capillary pressure in the time-of-flight sensitivities by using the total Darcy velocity (5) accounting for these effects in the slowness function $s(\mathbf{x})$.

Wen et al. [143] present a more general approach to account for the pressure impact on the time-of-flight and the spatial correlation for permeability. These sensitivities were derived for application to the sequential self-calibration (SSC) method, which will be discussed in Section 5.4.3. For the SSC method, the sensitivities are associated with master points rather than grid cells, and therefore the spatial correlations between grid cells and the master points are important. We will here index master points by subscript d. The time-of-flight in each cell i is a function of the transmissibilities $\{T_{i,n}\}$ associated with the cell faces and the pressures $\{p_{i,n}\}$ in the cell and its surrounding neighbors. A straightforward differentiation, applying the chain rule along a streamline intersecting N_c grid cells gives

$$\frac{\partial \tau}{\partial K_d} = \sum_{i=1}^{N_c} \Big[\sum_n \frac{\partial \Delta\tau_i}{\partial T_{i,n}} \frac{\partial T_{i,n}}{\partial K_d} + \sum_n \frac{\partial \Delta\tau_i}{\partial p_{i,n}} \frac{\partial p_{i,n}}{\partial K_d} \Big]. \tag{28}$$

To obtain $\partial \Delta\tau_i/\partial T_{i,n}$ and $\partial \Delta\tau_i/\partial p_{i,n}$ analytically, Wen et al. [143] differentiate the expressions for $\Delta\tau_i$ used in the Pollock's tracing algorithm. Further, the pressure sensitivities $\partial p_{i,n}/\partial K_d$ are obtained by the gradient-simulator method described above [62, 143] and are

not streamline based, and thus more expensive. Finally, using the harmonic average to calculate the transmissibility between two cells gives [62]

$$\partial T_{i,n}/\partial K_d = \frac{T_{i,n}^2}{2}\Big(\frac{\omega_{d,i}}{K_i} + \frac{\omega_{d,n}}{K_n}\Big), \tag{29}$$

where $\omega_{d,i}$ and $\omega_{d,n}$ are the kriging weights associated with master point d, cell i, and face n (adjacent cell). Hence, the spatial correlations of permeability perturbations are accounted for through the kriging weights in (29).

If one assumes that the pressure (the gradient) is independent of a small perturbation in the permeability, like assumed in (27), the sensitivities are reduced to

$$\frac{\partial \tau}{\partial K_d} = \sum_{i=1}^{N_c} \frac{\partial \Delta\tau_i}{\partial K_d} = \sum_{i=1}^{N_c} \frac{\partial \Delta\tau_i}{\partial K_i}\frac{\partial K_i}{\partial K_d} = -\sum_{i=1}^{N_c} \frac{\Delta\tau_i}{K_i}\frac{\partial K_i}{\partial K_d} = -\sum_{i=1}^{N_c} \frac{\Delta\tau_i}{K_i}\omega_{d,i}, \tag{30}$$

where $\omega_{d,i}$ is the kriging weight of master point d and cell i. For given kriging weights, this is a fully analytic approximation to the sensitivity coefficients that should apply directly to the same reservoir parameters as (21) does, given that appropriate covariance structures can be defined for the parameters.

The kriging weights involved in (29) and (30) can be obtained by solving an ordinary kriging system [62]. Further, the kriging weights only depend on the spatial locations of the master points and the locations being interpolated, so the kriging system only need to be solved once for a fixed set of master points, interpolation points, and covariance structure. The same weights may also be used to propagate the updated permeabilities of the master locations in the inverse problem, see Section 5.4.3.

If a master point coincides with a cell j and we assume that a perturbation of the permeability K_j only contribute to a perturbation of $\Delta\tau_j$, i.e.,

$$\omega_{j,i} = \begin{cases} 0, & \text{for } i \neq j, \\ 1, & \text{for } i = j, \end{cases} \tag{31}$$

then (30) reduces to (27).

In choosing between the two approach introduced above, we note that calculating the time-of-flight sensitivities by (21) is the fastest approach because the approach mainly boils down to bookkeeping of time-of-flights over each grid cell. Moreover, we remark that for the purpose of history matching, it often turns out in practice (see [67, 146]) to be sufficient to apply the cell-based approximations (27) and (30), which are the less computationally expensive (but also more approximate).

4.3. **Arrival-Time Sensitivities.** An arrival time measures the time it takes a quantity to propagate from one point in the reservoir to another, e.g., the time it takes from one starts injecting water in at an injector to the water front break through in a producer. In this subsection we will present an approach for computing the sensitivity $\partial t_j/\partial m_i$ of an arrival time t_j with respect to reservoir parameter m_i of grid cell i. This sensitivity is also sometimes referred to as a travel-time sensitivity [67] (analogy to ray-tracing in seismics). Consider a system of two-phase flow given in the time-of-flight coordinate along each streamline by the one-dimensional transport equation (13). If the streamlines are assumed to be invariant under the perturbation in reservoir parameters, the shift in the saturation at the outlet nodes is given by

$$\delta S = \frac{\partial S}{\partial t}\delta t + \frac{\partial S}{\partial \tau}\Big[\frac{\partial \tau}{\partial \mathbf{m}}\Big]^T \delta\mathbf{m}.$$

Let us consider the propagation of a fixed saturation, i.e., $\delta S \equiv 0$, or in other words

$$0 = \frac{\partial S}{\partial t}\delta t + \frac{\partial S}{\partial \tau}\Big[\frac{\partial \tau}{\partial \mathbf{m}}\Big]^T \delta\mathbf{m}.$$

If we now perturb $\mathbf{m}$ only in the ith component and solve for $\delta t/\delta m_i$, we obtain

$$\frac{\partial t}{\partial m_i} = -\frac{\partial S}{\partial \tau}\frac{\partial \tau}{\partial m_i}\cdot\Big(\frac{\partial S}{\partial t}\Big)^{-1} = \frac{1}{f'(S)}\frac{\partial \tau}{\partial m_i}. \tag{32}$$

Here time-of-flight derivative $\partial\tau/\partial m_i$ is computed analytically as described in Section 4.2. In deriving (32) we have tacitly assumed that the fixed saturation propagates with a constant wave-speed $f'(S)$ from its 'release' (at an injector) to its 'arrival' at a well. Whereas this is true for a piston-like displacement or for a neutral tracer flow, for which $f(S) = S$ and we obtain $\partial t/\partial m_i = \partial\tau/\partial m_i$ as expected, it will generally not be true for a general *nonlinear* displacement. For a pure Buckley–Leverett displacement, $f'(S)$ should be replaced by the derivative of the convex envelope of the flux $\widetilde{f}'(S)$, see Section 3.2. (Alternatively, this can be derived directly by direct differentiation of the self-similar Buckley–Leverett solution, for which $\widetilde{f}'(S) = \tau/t$.) In other words, df/dS is evaluated at the saturation of outlet node of the streamline for streamlines with breakthrough (i.e., having outlet saturation larger than the front saturation), and for the front saturation for streamlines without breakthrough. For other flow cases where the initial boundary-value problem along each streamline does not consist of a single Riemann problem, the accuracy of (32) depends on how well $f'(S)$ (or $\widetilde{f}'(S)$) approximates the *true* wave-speed of the fixed saturation during the time interval from release to arrival.

He et al. [67] also extend the arrival-time sensitivity to account for changing saturation distribution along streamlines due to changes in the streamline geometry, pressure updates, and mapping of saturations between streamlines as part of an operator splitting algorithm to account for gravity and/or capillary forces. The change in the saturation in the outlet cell will now also be a function of the initial saturation distribution $\mathbf{S}_0$ along the streamline (i.e., the saturation after the previous pressure update)

$$\delta S = \frac{\partial S}{\partial t}\delta t + \frac{\partial S}{\partial \tau}\Big[\frac{\partial \tau}{\partial \mathbf{m}}\Big]^T \delta\mathbf{m} + \Big[\frac{\partial S}{\partial \mathbf{S}_0}\Big]^T \delta\mathbf{S}_0.$$

If we now assume that the change in the water saturation in the outlet cell is primarily a function of the initial saturation $S_{0,j}$ in the same cell (which is true for a small time due to finite speed of propagation in hyperbolic equations), the last term becomes

$$\Big[\frac{\partial S}{\partial \mathbf{S}_0}\Big]^T \delta\mathbf{S}_0 = \frac{\partial S}{\partial S_{0,j}}\delta S_{0,j} = \frac{\partial S}{\partial S_{0,j}}\Big[\frac{\partial S_{0,j}}{\partial \mathbf{m}}\Big]^T \delta\mathbf{m}.$$

Hence, the overall sensitivity reads [67]

$$\frac{\partial t}{\partial m_i} = -\Big(\frac{\partial S}{\partial \tau}\frac{\partial \tau}{\partial m_i} + \frac{\partial S}{\partial S_{0,j}}\frac{\partial S_{0,j}}{\partial m_i}\Big)\cdot\Big(\frac{\partial S}{\partial t}\Big)^{-1} = \frac{1}{f'(S)}\frac{\partial \tau}{\partial m_i} + \frac{\partial t_j^0}{\partial m_i}.$$

where $\partial t_j^0/\partial m_i$ denotes the travel-time sensitivity at the beginning of the update (i.e., the sensitivity at the end of the previous time step). If operator splitting is applied in the transport solve, e.g., to account for matrix-fracture exchange for fractured systems and/or gravity, $f'(S)$ is evaluated after the corrector steps of the operator splitting [5].

Using the compressible conservation equation for water saturation [36], we can generalize the sensitivity calculations presented above to compressible flow. The sensitivity of arrival time of a water saturation with respect to a reservoir parameter m_i is given by [37]

$$\frac{\partial t}{\partial m_i} = \frac{\dfrac{\partial \tau}{\partial m_i}\dfrac{\partial}{\partial \tau}\Big(\dfrac{S_w}{B_w}\Big)}{\dfrac{\partial}{\partial \tau}\Big(\dfrac{f_w}{B_w}\Big) + \dfrac{f_w}{B_w}\dfrac{c}{\phi}}, \tag{33}$$

where B_w is the volume formation factor of water, and c represents the divergence of flux ($c = \nabla\cdot\vec{u}$) along the streamline, which can be estimated from the velocity field. Again, the time-of-flight derivative $\partial\tau/\partial m_i$ is computed analytically as described above. The rest of the derivatives can be computed by (backward) finite-differences along the streamlines. For incompressible flow, $c \equiv 0$ and B_w is constant, so (33) reduces to (32). Similarly, for gas-oil ratio (GOR), using the compressible conservation equation for gas [36], we can obtain the arrival time sensitivities [37].

As the primary example of an arrival time, we use the arrival of a fixed fractional-flow (fixed saturation) in both the well and along the streamlines. A common arrival-time sensitivity for

each producer is then obtained by a flux-weighted average

$$\frac{\partial t_j}{\partial m_i} = \frac{1}{q}\sum_{\ell=1}^{N_{\mathrm{sl}}} q_\ell \frac{\partial t_{j,\ell}}{\partial m_i}, \qquad q = \sum_{\ell=1}^{N_{\mathrm{sl}}} q_\ell. \tag{34}$$

Here, q_ℓ is the total flux of each streamline, and N_{sl} is the number of streamlines connected to the well.

Finally, we mention that Al-Huthali et al. [7] use (14), (21), (26), and (32) to derive arrival-time sensitivities with respect to injection and production rate. These sensitivities are not used for history matching, but rather for optimal waterflood management by rate control. To compute the arrival-time sensitivities for the producers, the authors only consider a fraction of the streamlines (fastest). Moreover, they also consider sensitivities for a group of producers with a common contributing injector.

4.4. **Time-Shift Sensitivities.** A time-shift is a measure for how much a simulated production response curve should be shifted in time to maximize the cross correlation with an observed production-response curve. The time-shift is described and used with the generalized travel-time inversion method described in Section 5.2.

Consider a small perturbation $\delta\mathbf{m}$ in the reservoir parameters with an accompanying shift δt in the computed production response. In each data point t_j there will be a corresponding shift δt_j, where

$$\delta t = \delta t_j = \left[\frac{\partial t_j}{\partial \mathbf{m}}\right]^T \delta\mathbf{m}, \quad j = 1, \ldots, N_{\mathrm{d}}.$$

Since a perturbation δm_i will lead to the same time-shift in all data points, we sum over all data points and define the sensitivity of the travel time-shift with respect to parameter m_i as the average of the above equations

$$\frac{\partial t}{\partial m_i} = \frac{1}{N_d}\sum_{j=1}^{N_d} \frac{\partial t_j}{\partial m_i}. \tag{35}$$

By convention, one defines $\partial\Delta\widetilde{t}/\partial m_i = -\partial t/\partial m_i$. Now, the arrival-time sensitivities given above can be used to obtain travel-time shift sensitivities, e.g., for fractional flow, gas-oil ratio, or tracer concentration [37].

Practical experience indicates that more robust history matching is achieved by making the sensitivities dimensionless by applying log-sensitivities [67]:

$$\frac{\partial \log(|\Delta\widetilde{t}|)}{\partial \log m_i} = \frac{m_i}{\Delta\widetilde{t}}\frac{\partial \Delta\widetilde{t}}{\partial m_i}.$$

For the generalized travel-time inversion described in Section 5.2, it is therefore common to use logarithmic modifications for the reservoir parameters.

4.5. **Saturation Sensitivities.** By differentiating the expression used for the streamline-to-grid mapping of saturation (see (19)), the sensitivities of saturation with respect to a reservoir parameter m_i at a given time can be calculated by [130]

$$\frac{\partial S_i}{\partial m_i} = \sum_{\ell=1}^{N_{\mathrm{sl},i}} \frac{\partial S_\ell}{\partial m_i}\beta_\ell = \sum_{\ell=1}^{N_{\mathrm{sl},i}} \frac{\partial S_\ell}{\partial \tau_\ell}\cdot\frac{\partial \tau_\ell}{\partial m_i}\beta_\ell, \tag{36}$$

where β_ℓ is the weight assigned to streamline ℓ in the mapping, $\partial\tau_\ell/\partial m_i$ is the time-of-flight sensitivity specified above, and $\partial S/\partial\tau_\ell$ is the derivative of the 1D saturation solution along the streamline. Here we have assumed that β_ℓ is independent of a perturbation in m_i.

For Riemann initial data the solution is self-similar $S(t,\tau) = S(\tau/t)$ and analytically known, as described in Section 3.2. The sensitivity of the saturation in streamline ℓ at a particular (t,τ) with respect to the reservoir parameter m_i in grid cell i is then given analytically by

$$\frac{\partial S_\ell}{\partial m_i} = \frac{\partial S_\ell}{\partial \xi}\frac{\partial \xi}{\partial \tau}\frac{\partial \tau}{\partial m_i} = \frac{1}{t}\frac{\partial S_\ell}{\partial \xi}\frac{\partial \tau}{\partial m_i}, \quad \xi = \frac{\tau}{t}. \tag{37}$$

Hence, if the reservoir parameter m_i is not located upstream, the sensitivity will be zero. Further, this expression may be used as an approximation in (36).

4.6. **Production Data Sensitivities (Amplitude Sensitivities).** Differentiating (14), the sensitivity of fractional flow at a producer with respect to a perturbation in reservoir parameter m_i is obtained by [143, 147]

$$\frac{\partial f(t)}{\partial m_i} = \frac{1}{q} \sum_{\ell=1}^{N_{\rm sl}} q_\ell \frac{\partial f_\ell(t)}{\partial m_i}.$$

This expression also applies to tracer concentration for which $f(C) = C$, and a similar result applies to gas-oil ratios.

We now need to evaluate $\partial f_\ell(t)/\partial m_i$ for the connected streamlines. This can be done by the chain rule, using an expansion involving either time-of-flight sensitivities [135, 143, 147]

$$\frac{\partial f_\ell}{\partial m_i} = \frac{\partial f_\ell}{\partial \tau_\ell} \frac{\partial \tau_\ell}{\partial m_i}, \tag{38}$$

arrival-time sensitivities [45]

$$\frac{\partial f_\ell}{\partial m_i} = \frac{\partial f_\ell}{\partial t} \frac{\partial t}{\partial m_i}, \tag{39}$$

or the saturation sensitivities

$$\frac{\partial f_\ell}{\partial m_i} = \frac{df_\ell}{dS} \frac{\partial S}{\partial m_i}. \tag{40}$$

Expressions for the the time-of-flight, the arrival-time, and the saturation sensitivities for each streamline have been introduced in the previous subsections. The derivatives of the fractional flow ($\partial f_\ell/\partial \tau$, $\partial f_\ell/\partial t$, or df_ℓ/dS) can be obtained either analytically or by using finite-differences.

Another possibility for obtaining fractional-flow sensitivities directly is to apply the chain rule to the production response (at the well), which yields

$$\frac{\partial f}{\partial m_i} = \frac{\partial f}{\partial t_j} \frac{\partial t_j}{\partial m_i}.$$

Here $\partial t_j/\partial m_i$ is given by (34), and $\partial f/\partial t_j$ can be evaluated numerically from the production response curve at the given time. A smoothed approximation to the generally noisy production curve might then be needed.

Below we will present two approaches for determining the fractional-flow derivative along streamlines, starting out by tracer concentration (or piston-like displacement). Following Vasco and Datta-Gupta [132, 133], we start by observing that the transport of tracer concentration along a streamline can be described by (16). Assume an initial distribution of reservoir properties along a streamline Ψ_0. To compute sensitivities, we give the underlying parameters a small perturbation, reflected as a single perturbation in the slowness function

$$s(\mathbf{x}) = s_0(\mathbf{x}) + \delta s(\mathbf{x}) \tag{41}$$

and seek to find the corresponding change in tracer production δC. According to Vasco and Datta-Gupta [134][2], the perturbation in the streamline is of second order in δs. One can therefore assume that the change in the streamlines is so small that the integral over the new streamline Ψ equals that over the old streamline Ψ_0, that is

$$\tau = \int_\Psi s(\mathbf{x})\, dr \approx \int_{\Psi_0} s_0(\mathbf{x})\, dr + \int_{\Psi_0} \delta(\mathbf{x})\, dr = \tau_0 + \delta\tau_0.$$

[2]Vasco and Datta-Gupta [134] refer to King and Datta-Gupta [85]. Unfortunately, we have so far not been able to locate the proof in [85] of the fact that the change in streamlines is second order in δs.

Using the notation from Section 3.1, we may hence write

$$\begin{aligned}\delta C_\ell(\mathbf{x}) &= C_{\ell,0}\big(t-\tau\big) - C_{\ell,0}\big(t-\tau_0\big)\\ &\approx C_{\ell,0}\big(t-\tau_0-\delta\tau_0\big) - C_{\ell,0}\big(t-\tau_0\big) \overset{\text{Taylor}}{\approx} -C'_{\ell,0}\big(t-\tau_0\big)\delta\tau_0\end{aligned}$$

as a first-order approximation. It now remains to determine $\delta\tau_0$, i.e., the integral of δs over Ψ_0. The variation in $s(\mathbf{x})$ due to variation in all properties is given as

$$\delta s(\mathbf{x}) = \frac{\partial s(\mathbf{x})}{\partial K}\delta K + \frac{\partial s(\mathbf{x})}{\partial \phi}\delta\phi + \frac{\partial s(\mathbf{x})}{\partial|\nabla p|}\delta|\nabla p| + \dots, \tag{42}$$

where the expressions for the partial derivatives were given in Section 4.2. For instance, the sensitivity of the concentration due to changes in the reservoir parameter m_i at time t is given by

$$\frac{\partial C_\ell}{\partial m_i} = -C'_{\ell,0}\big(t-\tau_0\big)\int_{\Psi_{0i}}\frac{\partial s(\mathbf{x})}{\partial m_i}\,dr = \underbrace{-C'_{\ell,0}\big(t-\tau_0\big)}_{\approx\frac{\partial C_\ell}{\partial\tau_\ell}}\frac{\partial\tau_\ell}{\partial m_i}.$$

Notice that the same expression could have been obtained directly by differentiating (16) under the assumption of no shift in streamlines due to the perturbation in reservoir parameters.

Wen et al. [143] present another approach to analytic calculation of $\partial C_\ell(t)/\partial m_i$ for tracer flow. We start by assuming a tracer flow with a monotone flow profile, where the analytical solution is given by (see Section 3.1)

$$C_\ell(t) = \begin{cases}1, & \text{if } \tau_\ell \le t,\\ 0, & \text{otherwise.}\end{cases}$$

Here τ_ℓ denotes the time-of-flight of streamline ℓ at the well. To be able to differentiate this discontinuous profile, the authors use an approximation in terms of an error function E_σ for some small parameter σ,

$$C_\ell(t) \approx 1 - E_\sigma\Big(\frac{\tau_\ell}{t}-1\Big), \qquad t \le \tau_\ell,$$

and hence

$$\frac{\partial C_\ell(t)}{\partial m_i} = \frac{\partial C_\ell(t)}{\partial\tau_\ell}\frac{\partial\tau_\ell}{\partial m_i} = -\frac{1}{t}G_\sigma\Big(\frac{\tau_\ell}{t}\Big)\frac{\partial\tau_\ell}{\partial m_i}, \qquad G_\sigma(r) = \frac{1}{\sqrt{2\pi}\sigma}e^{-\frac{(r-1)^2}{2\sigma^2}}.$$

The same approach can be extended to two-phase incompressible flow [135, 147] described by transport equation (13). The analytic Buckley–Leverett solution for Riemann initial data (see Section 3.2), consisting of a shock followed by a rarefaction wave, can be used to calculate analytic fractional-flow sensitivities by

$$\frac{\partial f_\ell}{\partial m_i} = \frac{df_\ell}{dS}\frac{\partial S}{\partial\tau}\frac{\partial\tau}{\partial m_i} = \frac{\tau}{t}\frac{\partial S}{\partial\tau}\frac{\partial\tau}{\partial m_i}$$

since $f'_\ell(S) = \tau/t$ for a self-similar profile.

As mentioned above, $\partial f_\ell/\partial t$ and $\partial f_\ell/\partial\tau$ can be evaluated by finite-differences along the streamlines, which is the most general approach. However, the fully analytic approximations may often be sufficiently accurate.

Finally, we remark that gravity and capillary forces can be accounted for in the fractional flow derivative by defining the fractional flow function from Darcy's law incorporating gravity and capillary forces; i.e., [39]

$$f_w(S) = \frac{\mathbf{q}_w\cdot\mathbf{n}}{\mathbf{q}_t\cdot\mathbf{n}} = \frac{\lambda_w + \frac{\lambda_w\lambda_o}{\mathbf{u}\cdot\mathbf{n}}K(\nabla p_{\text{cow}} + (\rho_w-\rho_o)\mathbf{g})\cdot\mathbf{n}}{\lambda_w+\lambda_o}. \tag{43}$$

Here $\mathbf{n}$ is the unit vector in the flow direction that easily can be estimated from the streamline geometry; i.e. by $\mathbf{n} = \mathbf{u}/|\mathbf{u}|$. Hence, gravity and capillary forces will only be fully accounted for if both (43) is applied and the forward simulator accounts for these effects.

In [150] an argument is given for the spatial additivity of production response sensitivities. We will here outline this argument by a small example. Let $g(\mathbf{m})$ be the production response at a well, and let there be N grid cells $\{1, 2, \ldots, N\}$, with corresponding grid parameters $\{m_1, m_2, \ldots, m_N\}$. The set of production-response sensitivities is then $\{\partial g/\partial m_1, \partial g/\partial m_2, \ldots, \partial g/\partial m_N\}$. By perturbing a subset of the reservoir parameters, e.g., $\{m_4, m_5, m_6, m_7\}$, we obtain the following differential for the resulting perturbation in the production response

$$\delta g = \frac{\partial g}{\partial m_4}\delta m_4 + \frac{\partial g}{\partial m_5}\delta m_5 + \frac{\partial g}{\partial m_6}\delta m_6 + \frac{\partial g}{\partial m_7}\delta m_7.$$

By assuming the same modification or perturbation $\delta m_c = \delta m_4 = \delta m_5 = \delta m_6 = \delta m_7$ in all cells, the differential is

$$\delta g = \underbrace{\left(\frac{\partial g}{\partial m_4} + \frac{\partial g}{\partial m_5} + \frac{\partial g}{\partial m_6} + \frac{\partial g}{\partial m_7}\right)}_{\frac{\partial g}{\partial m_c}} \delta m_c.$$

Hence, it is reasonable to approximate the sensitivities of the production response with respect to a coarse-cell reservoir parameter m_c by the sum of the sub-cell sensitivities. Further, it should be noted that small cells then in general will have smaller sensitivities than large cells.

4.7. **Miscellaneous.** In this last subsection we will briefly comment on a few other uses of streamlines to calculate various sensitivity coefficients that fall in neither of the above categories.

Vasco et al. [136] derive sensitivities for amplitudes from time-lapse seismic with respect to changes in reservoir parameters. We will not go into the details, but the key to obtaining the sensitivities is to relate perturbations in the amplitudes to perturbations in the upstream saturations along streamline trajectories. Further, the perturbations in the upstream saturations can be related to perturbations in the reservoir parameters via the perturbations in time-of-flight by (37).

Kulkarni et al. [92] derive streamline-based sensitivities for the arrival time of a 'pressure front' for use in pressure interference tests, see Section 5.2.3 for details about streamline-based integration of transient pressure data. The arrival time is related to the so-called diffusive time-of-flight by (51) in Section 5.2.3. Similar calculations as used for ordinary time-of-flight and arrival-time sensitivities can then be applied. In [69], sensitivities for the amplitude of the 'pressure front' of a pressure interference test are derived by simply differentiating (49) in Section 5.2.3 in the time domain (inverse Fourier transformed).

In [58, 59] sensitivities of fractional flow and well pressure with respect to the parameters of the gradual deformation method (GDM) are derived by direct differentiation of the discrete equations of a streamline method. Numerical values for the gradients are computed in a two-step procedure (corresponding to the two steps in the fractional step solution method):

(1) Given boundary conditions, the pressure and its gradient are computed on a 3D grid. The pressure gradients with respect to a parameter are obtained by the gradient-simulator method discussed in Section 4.1. This is therefore not a streamline-based approach, but the saturation derivatives involved in the derivation of the linear equation system are streamline based. The pressure gradients are calculated based on information from the previous pressure step.
(2) Then velocities are computed from Darcy's law and streamlines are traced from injectors to producers. The one-dimensional saturation/transport equation is solved along each streamline, and saturation gradients with respect to reservoir properties are computed. Finally, the streamline gradients are mapped back onto the 3D grid to obtain grid-block saturation gradients.

Part of the intermediate derivations are similar or identical to derivations presented above. The entire derivations are too technical to give a condensed presentation here. One should therefore instead read the paper in full [59].

We will just remark that the derivations presented involve a specific streamline simulator implementation involving expressions used in the Pollock's tracing algorithm, the Peaceman well model, and the standard first-order upwind finite-difference scheme. The calculations may therefore need to be adapted for other implementations. Currently, there are two competing streamline technologies: (i) the 3DSL technology of StreamSim, which uses finite differences along each streamline; and (ii) the FrontSim technology by Schlumberger, which also uses front-tracking along each streamline. The results from [59] are based upon the 3DSL-type streamline simulator, and may therefore not be applied directly to FrontSim-type streamline simulators. By using the front-tracking method, one avoids the mapping back and forth between an irregular and a regular discretization along streamlines. This simplifies the calculations of the sensitivities, since the terms arising from equations (22) and (25) in [59] are not needed. On the other hand, an equation for the saturation gradients cannot be obtained by simply differentiating the discretized saturation equation. Instead, one could try to use the approach of Vignes [139], in which saturation gradients are computed 'recursively' as part of the front-tracking algorithm.

As the authors point out in [59], including gravity in the computations should be straightforward. It may also be possible to generalize the computations to obtain sensitivities of other parameters than the gradual deformation parameters. However, for the gradual deformation method, only a few tens of parameters are usually employed [59], which keeps the number of linear solves for the gradient-simulator method down. The streamline-assisted gradual-deformation approach of Gautier et al. [59] is discusses in Section 5.4.4.

Caers [25] and Ravalec-Dupin and Fenwick [116] present analytic sensitivities for the particular gradual deformation approach presented in Section 5.3.4 in the case of Gaussian permeability field. i.e. sensitivities for streamline-effective permeability with respect to the gradual deformation parameters.

5. History-Matching Methods

In this section, which forms the core of the paper, we will review methods for streamline-based history matching. The methods will be sorted into four categories as outlined in the introduction: assisted history matching, (generalized) travel-time inversion, streamline-effective properties, and miscellaneous. The main emphasize will be put on travel-time inversion methods and methods using streamline-effective properties.

5.1. The Assisted History Matching Approach.

Emanuel and Milliken [49] describe what they call an assisted history matching (AHM) approach, where streamline methods are used to assist in the matching of conventional finite-difference reservoir simulation models. The key idea in the AHM approach is to alter "geologic properties along the flow paths connecting a producing well and its flow source" [49]. A 3D streamline method is used to define these flow paths. Once the streamlines are computed, all streamlines are traversed and the grid cells are assigned to the producer at which the particular streamline terminates. This way, the AHM approach identifies bundles of streamlines where the reservoir engineer later must change the reservoir properties, either manually or by some algorithm, in the grid-cells containing the identified streamlines. Rock properties (permeabilities and porosities) are changed on a well-by-well basis through traditional multipliers, or the heterogeneity is changed through a renormalization based upon the Dykstra–Parsons coefficient for controlling the spatial heterogeneity. The manual work typically amounts to targeted adjustments of a few parameter for each well. Emanuel and Milliken [49] illustrate that by using AHM one is often able to reveal nonintuitive connections between grid cells and wells. In [104], the AHM approach is extended to placement of shale bodies between well pairs and the utility of the method is demonstrated for three field cases.

The streamline distribution is generated based on average well conditions over the production period. However, several streamline distributions may be used if there are significant changes in the well configuration [49]. The AHM method changes properties along flow paths derived from the initial geological model and thus relies upon a well-constructed initial model.

The history match is obtained through relatively minor local changes of the initial model under the assumption of invariant streamlines. Thus, the AHM approach is different from automated approaches that come in the form of a computer algorithm for minimizing a mismatch functional. In particular, since the AHM approach uses no gradient-based minimizing technique, the method does not provide any means for sensitivity computations.

The AHM method has been applied with success to a number of real fields [13, 29, 97, 101]. In particular, Cheng et al. [33] present two field cases for which both AHM and the generalized travel-time inversion to be introduced in Section 5.2 are applied.

5.2. **(Generalized) Travel-Time Inversion.** In a series of papers Datta-Gupta, Vasco, and coworkers have developed methods for integrating dynamic data, using a combination of streamline methods and streamline-based sensitivities. The travel-time approach for matching production data is basically motivated by an analogy between seismic ray inversion and streamlines, which will be outlined briefly below. This initial approach consists of travel-time matching at each well of breakthrough time, a distinct peak in tracer concentration, etc., followed by an amplitude matching [135]. An approach built on the same principles is proposed for incorporating transient pressure data [92]. Later a so-called generalized travel-time inversion (GTTI) approach was introduced [67], which can be considered as a combination of travel-time matching and amplitude matching into one step. In contrast to traditional amplitude matching, both the travel-time matching and GTTI have quasilinear properties [34]. Therefore, (generalized) travel-time history matching proceeds rapidly even if the initial model is not close to the global minimum. The original travel time matching and the generalized approach are both deterministic algorithms, but a geostatistical version of GTTI is introduced in [138, 148].

5.2.1. *The Analogy with Seismic Ray Inversion.* For a neutral tracer, the transport is described by the time-of-flight equation, see (10):

$$\mathbf{v} \cdot \nabla\tau(\mathbf{x}) = 1 \quad \Leftrightarrow \quad \mathbf{u} \cdot \nabla\tau(\mathbf{x}) = \phi. \tag{44}$$

Here $\mathbf{v} = \mathbf{u}/\phi$ is the interstitial velocity. A key point in [135] is the observation that the time-of-flight equation has certain properties in common with the Eikonal equation describing (seismic) travel time tomography,

$$\nabla T(\mathbf{x}) \cdot \nabla T(\mathbf{x}) = 1/c(\mathbf{x})^2. \tag{45}$$

Here T is the travel time and c is the propagation speed. (A common form of the Eikonal equation is to write $|\nabla T| = 1/c$). The Eikonal equation allows for wave propagation in both directions along ∇T, whereas the time-of-flight equation only allows for particles traversing in the positive direction of $\nabla\tau$, i.e., toward increasing values of τ along the streamline. Equation (44) can be thought of as the square root of (45) with the positive sign.

5.2.2. *A Two-Step Travel-Time/Amplitude Matching Method.* Motivated by inversion methods for seismic travel times, a two-step inversion method for tracer and fractional-flow data is developed in [135]. In the first step, one chooses a certain characteristic feature of the production curves, e.g., time to breakthrough or a distinct peak. Then the observed and calculated responses are lined up in all wells such that the characteristic features coincide in time. during this stage the dominant features of the permeability field will be matched and the majority of the misfit reduced. In the second step, the 'amplitude' of the production responses are matched.

Cheng et al. [34] give a systematic investigation and comparison of the nonlinearity of travel-time matching, amplitude matching, and generalized travel-time inversion (described below). Their investigations demonstrate quasilinear properties for travel-time matching, while amplitude matching can be order of magnitudes more nonlinear. Travel-time matching generally has fewer local minima and is therefore more robust and has better convergence characteristics. Further, Cheng et al. [34] report that travel-time sensitivities are more uniformly distributed between the wells, in contrast to amplitude sensitivities that tend to be localized near the wells. This contributes to the good robustness and convergence properties of the travel-time matching.

Apart from the two-step methodology, a central ingredient in the method is the use of an efficient method for computing analytic streamline-based sensitivities. The arrival time and fractional-flow sensitivities described in Sections 4.2, 4.3, and 4.6 are used for the travel-time and the amplitude matching, respectively.

The inverse problem is formulated as a minimization of the misfit function defined over a set of N_d observations d_j,

$$\sum_{j=1}^{N_d} \big(d_j - g_j(\mathbf{m})\big)^2,$$

where $\mathbf{m}$ denotes the reservoir parameters (permeability, porosity, etc) and $g_j(\mathbf{m})$ the forward model (streamline simulator). If we now use a Taylor series expansion of $g_j(\mathbf{m})$ about some initial model $\mathbf{m}_p$, we can linearize the residuals as follows

$$d_j - g_j(\mathbf{m}_p) = \delta d_j = \sum_i G_{ji}\,\delta m_i, \qquad G_{ji} = \frac{\partial g_j}{\partial m_i}.$$

Here $\{G_{ji}\}$ are sensitivity coefficients. Since the number of parameters usually is very large compared to the amount of data, the corresponding minimization problem is numerically unstable. The authors therefore add two regularizing terms and seek the modification $\delta\mathbf{m}$ that minimizes the following function [135]

$$\|\delta\mathbf{d} - \mathbf{G}\delta\mathbf{m}\|_2^2 + \beta_1\|\delta\mathbf{m}\|_2^2 + \beta_2\|\mathbf{L}\delta\mathbf{m}\|_2^2. \tag{46}$$

The first regularization term tends to keep the modifications made to the reservoir parameters small, while the second term tends to make the modifications smooth; see the discussion of ill-posedness and regularization in Section 1. The minimum of the regularized function in (46) is obtained as a least-squares solution to the following augmented linear system

$$\begin{pmatrix} \mathbf{G} \\ \beta_1\mathbf{I} \\ \beta_1\mathbf{L} \end{pmatrix} \delta\mathbf{m} = \begin{pmatrix} \delta\mathbf{d} \\ \mathbf{0} \\ \mathbf{0} \end{pmatrix}, \tag{47}$$

and may for instance be computed by an iterative sparse least-squares solver, for instance, LSQR [110].

The travel-time step is faster than the amplitude matching step [34]. In the travel-time inversion a single parameter is matched in each well, giving a total number of N_w parameters to be matched using (47). In the amplitude step, all N_d^k observations per well are matched, giving a total of $N_w \times N_d^k$ parameters to be matched in (47).

Finally, we mention that an overview of the framework under which the two-step approach, and some related approaches, have been developed is given by Vasco and Datta-Gupta [132].

5.2.3. *Inversion of Pressure Interference Tests.* Extensions to compressible flow and integration of dynamic pressure data from pressure interference tests are considered in [42, 92]. A pressure interference test is an important source of dynamic data. The pressure responses from injecting or producing wells are observed in surrounding distant wells. An advantage of pressure interference tests is that the transient pressure responses can be obtained more quickly than tracer and fractional-flow responses, so that the data integration can take place at an earlier stage.

As in the previous papers, the central idea is to draw upon the analogy between propagating waves and propagating fronts and apply the inversion algorithm to a propagating pressure front. The pressure front is obtained by studying high-frequency asymptotic solutions of the diffusivity equation

$$\mu c_t \phi(\mathbf{x}) \frac{\partial p}{\partial t} = \nabla\big(K(\mathbf{x})\nabla p\big). \tag{48}$$

Applying a Fourier transformation to (48) one obtains an equation in the frequency domain

$$(-i\omega)\frac{\phi(\mathbf{x})\mu c_t}{K(\mathbf{x})}\widetilde{p}(\mathbf{x},\omega) = \nabla^2\widetilde{p}(\mathbf{x},\omega) + \frac{\nabla K(\mathbf{x})}{K(\mathbf{x})}\cdot\nabla\widetilde{p}(\mathbf{x},\omega).$$

One can now define a phase function $\tau(\mathbf{x})$ and seek approximations in terms of a series of inverse powers in $\sqrt{-i\omega}$, where the 'pressure front' would correspond to the zeroth order term

$$\widetilde{p}(\mathbf{x},\omega) = A_0(\mathbf{x})e^{-\sqrt{-i\omega}\tau(\mathbf{x})}. \tag{49}$$

By inserting this term and equating the coefficients with highest order in $\sqrt{-i\omega}$, i.e., $(\sqrt{-i\omega})^2$, the following phase function for a propagating pressure front is obtained

$$\sqrt{\alpha(\mathbf{x})}|\nabla\tau(\mathbf{x})| = 1, \qquad \alpha(\mathbf{x}) = \frac{K(\mathbf{x})}{\phi(\mathbf{x})\mu c_t}.$$

Based on the similarity with the time-of-flight equation (see (44)), the authors define what they call the 'diffusive time-of-flight' by

$$\tau(\mathbf{x}) = \int_\Psi \sqrt{\frac{\phi(\mathbf{x})\mu c_t}{K(\mathbf{x})}}\, dr = \int_\Psi \frac{dr}{\sqrt{\alpha(\mathbf{x})}}. \tag{50}$$

The values of $\sqrt{\alpha(\mathbf{x})}$ at the cell faces are used to generate streamlines along which the pressure front will propagate. Hence, these streamlines will not coincide with the velocity-based streamlines, but will be similar. It is also showed that the arrival time of the 'pressure front' in a 3D medium is related to the diffusive time-of-flight by

$$t_{\max} = \frac{\tau^2(\mathbf{x})}{6}. \tag{51}$$

Using this association, the authors derive a travel-time inversion method for the transient pressure data by applying the sensitivities discussed in Section 4.7. Moreover, Kulkarni et al. [92] present a relation between the drainage radius of a well and the diffusive time-of-flight.

The derivation above is performed for a sharp pressure impulse (a propagating peak). In practice, the source function is more like the Heaviside function. Observing that the time derivative of the Heaviside function is an impulse function, the travel-time analysis should instead be carried out with respect to the time derivative of the pressure response at the well [92]. In [23] the relation between a Heaviside source and an impulse source is discussed in more detail, and a conversion factor is derived.

Datta-Gupta et al. [42] compares history matches obtained by travel-time matching of transient pressure, tracer, and fractional-flow data. Further, in [69] both travel-time and amplitude matching of transient pressure responses from pressure interference tests were performed in a similar manner as for the two-step method presented in Section 5.2.2.

5.2.4. *Generalized Travel-Time Inversion.* He et al. [67] introduce an alternative single-step version of the above two-step travel-time inversion method. Assume for simplicity that there are N_d^k observations $y(t_1^k),\dots,y(t_{N_d^k}^k)$ that are to be matched for well k. A traditional amplitude matching would try to minimize a misfit function of the type

$$J = \sum_{j=1}^{N_d^k}\Big(y^{\text{obs}}(t_j^k) - y^{\text{cal}}(t_j^k)\Big)^2,$$

for each well k. The GTTI method, on the other hand, proceeds by selecting an optimal time shift $\Delta\widetilde{t}_k$ in the observed data that minimizes the misfit function

$$J(\Delta\widetilde{t}_k) = \sum_{j=1}^{N_d^k}\Big(y^{\text{obs}}(t_j^k + \Delta\widetilde{t}_k) - y^{\text{cal}}(t_j^k)\Big)^2,$$

or alternatively maximizes the coefficient of determination

$$R^2(\Delta\widetilde{t}_k) = 1 - \frac{\sum_{j=1}^{N_d^k}\left[y^{\text{obs}}(t_j^k + \Delta\widetilde{t}_k) - y^{\text{cal}}(t_j^k)\right]^2}{\sum_{j=1}^{N_d^k}\left[y^{\text{obs}}(t_j^k) - \overline{y^{\text{obs}}(t_j^k)}\right]^2}.$$

In other words, we seek a time-shift $\Delta\widetilde{t}_k$ in each well that maximizes the correlation between the observed and calculated production curves. These time-shifts are then used to match the

reservoir properties for all wells jointly; i.e., by setting $\delta\mathbf{d} = \mathbf{\Delta t} = \{\Delta\widetilde{t}_k\}$ in the minimization system in (47). As for the two-step inversion method, a central part of the algorithm is the calculation of analytic sensitivities as discussed in Section 4.4.

It can be shown that GTTI reduces to the traditional least-square amplitude matching as the match is getting close to the observed data [67]. Thus, GTTI combines travel-time and amplitude matching to some extent, while preserving most of the quasilinear properties of the travel-time matching [34].

Field case studies for GTTI are presented in e.g., [72, 114]. Further, in [33] the performance of GTTI and AHM (described in Section 5.1) is compared.

5.2.5. *Bayesian Generalized Travel-Time Inversion.* In [138, 148] a stochastic version of GTTI is developed, based on Bayesian statistics. Again, let $\mathbf{m}$ and $\mathbf{d}$ denote the reservoir parameters and observed data, respectively. By assuming a Gaussian prior distribution

$$[\mathbf{m}] \sim f(\mathbf{m}) = \mathcal{N}_N(\mathbf{m}_p, \mathbf{\Sigma}_m) = \text{const}_\text{A} \cdot \exp\Big[-\frac{1}{2}(\mathbf{m}-\mathbf{m}_p)^T\mathbf{\Sigma}_m^{-1}(\mathbf{m}-\mathbf{m}_p)\Big],$$

and a Gaussian likelihood model for the observations

$$\begin{aligned}[\mathbf{d}|\mathbf{m}] = \mathbf{g}(\mathbf{m}) + \mathbf{u} \sim f(\mathbf{d}|\mathbf{m}) &= \mathcal{N}_{N_d}(\mathbf{g}(\mathbf{m}), \mathbf{\Sigma}_d) \\ &= \text{const}_\text{B} \cdot \exp\Big[-\frac{1}{2}(\mathbf{d}-\mathbf{g}(\mathbf{m}))^T\mathbf{\Sigma}_d^{-1}(\mathbf{d}-\mathbf{g}(\mathbf{m}))\Big],\end{aligned} \tag{52}$$

the posterior distribution is, by Bayes' rule (3), given by

$$\begin{aligned}[\mathbf{m}|\mathbf{d}] \sim f(\mathbf{m}|\mathbf{d}) = \text{const}_\text{C} \cdot \exp\Big[-\frac{1}{2}\big((\mathbf{d}-\mathbf{g}(\mathbf{m}))^T\mathbf{\Sigma}_d^{-1}(\mathbf{d}-\mathbf{g}(\mathbf{m})) \\ + (\mathbf{m}-\mathbf{m}_p)^T\mathbf{\Sigma}_m^{-1}(\mathbf{m}-\mathbf{m}_p)\big)\Big].\end{aligned} \tag{53}$$

Here $\mathbf{m}_p$ is the prior mean for the reservoir parameters, $g(\mathbf{m})$ is a forward model, $[\mathbf{u}] \sim \mathcal{N}_{N_d}(\mathbf{0}, \mathbf{\Sigma}_d)$ represents the measurement errors, $\mathbf{\Sigma}_d$ is the covariance matrix for the measurement errors, and $\mathbf{\Sigma}_m$ is the (prior) covariance matrix for the reservoir parameters. If the forward model is represented by a linear relation $\mathbf{g}(\mathbf{m}) = \mathbf{A}\cdot\mathbf{m}$, the posterior distribution is Gaussian and can be determined analytically, see Appendix B. However, $\mathbf{g}(\mathbf{m})$ is generally nonlinear, so we only know the posterior distribution up to a constant. Still, it is possible to obtain an estimate for a $\mathbf{m}$ that maximizes the *a posterior* distribution given by

$$\arg\min_{\mathbf{m}} \ \big(\mathbf{d}-\mathbf{g}(\mathbf{m})\big)^T\mathbf{\Sigma}_d^{-1}\big(\mathbf{d}-\mathbf{g}(\mathbf{m})\big) + \big(\mathbf{m}-\mathbf{m}_p\big)^T\mathbf{\Sigma}_m^{-1}\big(\mathbf{m}-\mathbf{m}_p\big). \tag{54}$$

This maximum a posteriori (MAP) estimate gives in general a too smooth reservoir description ('regression toward the mean'). However, the large-scale structures of the reservoir may be discerned from the MAP estimate. The Gauss–Newton algorithm for the minimization of (54) leads to the following iterative scheme

$$\mathbf{m}^{l+1} = \mathbf{m}_p - \mathbf{\Sigma}_m\mathbf{G}_l^T\Big[\mathbf{\Sigma}_d + \mathbf{G}_l\mathbf{\Sigma}_m\mathbf{G}_l^T\Big]^{-1}\Big[\big(\mathbf{g}(\mathbf{m}^l)-\mathbf{d}\big) - \mathbf{G}_l\big(\mathbf{m}^l-\mathbf{m}_p\big)\Big], \tag{55}$$

where $\mathbf{G}$ is the sensitivity matrix for data misfit with respect to a perturbation in the reservoir parameters. Wu and Datta-Gupta [148] apply $\mathbf{g}(\mathbf{m}) - \mathbf{d} = \mathbf{\Delta\widetilde{t}} = \{\Delta\widetilde{t}_k\}$ to obtain a Bayesian version of GTTI, where $\Delta\widetilde{t}_k$ is the time-shift described above. If the data misfits are represented by the time-shifts $\mathbf{\Delta\widetilde{t}}$, then the inverse matrix on the right hand side of (55) has dimension $N_w \times N_w$, where N_w is the number of wells. In conventional methods the inverse matrix is usually of dimension $N_d \times N_d$, where N_d is the total number of observations. Hence, N_d is usually orders of magnitude larger than N_w, so the inversion of the matrix is therefore a minor issue.

Finally, we mention that conditional realizations can be obtained by a similar minimization problem, referred to as randomized maximum likelihood, see e.g., [96]

$$\arg\min_{\mathbf{m}} \ (\mathbf{d}_\text{uc}-\mathbf{g}(\mathbf{m}))^T\mathbf{\Sigma}_d^{-1}(\mathbf{d}_\text{uc}-\mathbf{g}(\mathbf{m})) + (\mathbf{m}-\mathbf{m}_\text{uc})^T\mathbf{\Sigma}_m^{-1}(\mathbf{m}-\mathbf{m}_\text{uc}),$$

in which the prior mean and the observed data have been replaced by unconditioned (uc) realizations $\mathbf{m}_{\text{uc}}$ and $\mathbf{d}_{\text{uc}}$, respectively: that is, random error have been added to the observed data.

Vega et al. [138] investigate the computational scalability of the deterministic and the Bayesian version of GTTI. They demonstrate that the deterministic version scales almost linearly with problem size and that the Bayesian version scales almost quadraticly (as expected). However, by reformulating the Bayesian method Vega et al. [138] were able to obtain an almost linear scaling for the computational cost and results with the same quality as for the deterministic approach, while preserving the statistical foundation of the Bayesian approach. Hence, conditioned realizations can also for this formulation be obtained by the randomized maximum likelihood approach.

To reformulate the Bayesian approach, Vega et al. [138] start by rewriting the minimization problem (54) to obtain an alternative minimization formulation. Further, they approximate the Hessian $\mathbf{H}$ by $\mathbf{J}^T\mathbf{J}$, where $\mathbf{J}$ is the Jacobian. This approximation is the same that is used in the Gauss–Newton algorithm, and is accurate near the solution or for quasilinear problems. The reformulated system reads

$$\begin{bmatrix} \boldsymbol{\Sigma}_d^{-1/2}\mathbf{G} \\ \boldsymbol{\Sigma}_m^{-1/2} \end{bmatrix} \delta\mathbf{m} = \begin{bmatrix} \boldsymbol{\Sigma}_d^{-1/2}[\mathbf{d} - \mathbf{g}(\mathbf{m})] \\ \boldsymbol{\Sigma}_m^{-1/2}[\mathbf{m}_p - \mathbf{m}] \end{bmatrix}. \tag{56}$$

This system is analogous to the deterministic formulation in (47). Here $\boldsymbol{\Sigma}_m^{-1/2}[\mathbf{m}_p - \mathbf{m}]$ plays an equivalent role as the regularization terms in (47), where the covariance matrix $\boldsymbol{\Sigma}_m$ imposes smoothing and the difference $\mathbf{m}_p - \mathbf{m}$ tends to keep the modifications small. Further, by using this formulation, we can thus solve iteratively for a least-square solution by, for instance, the LSQR algorithm. Here, $\boldsymbol{\Sigma}_m$ is generally a matrix of dimension $N \times N$, where N is the number of model parameters. Obtaining $\boldsymbol{\Sigma}_m^{-1/2}$ is therefore very computationally expensive if $\boldsymbol{\Sigma}_m^{1/2}$ is to be computed numerically. Vega et al. [138] therefore rely on a semi-analytical computation of $\boldsymbol{\Sigma}_m^{1/2}$. The key observation to this end is that the inverse of the covariance of the model parameters can be identified with the differential operator (the smoothing operator) in the deterministic approach. They therefore apply a computational stencil based on an approximation of the differential operator associated with $\boldsymbol{\Sigma}_m^{1/2}$, for which they assume an exponential covariance model [138]. The extension to other covariance models is presented in [137].

5.2.6. *Other Extensions.* Barman et al. [15] suggest a procedure for applying two-step inversion approach described above for fractured reservoirs. The idea is to use effective permeability representations for the inversion, obtained based on production based indicators (details not given), while the forward simulations are performed for fractured reservoir representations. Similarly, Al-Harbi et al. [5] also apply the Bayesian version of GTTI fractured reservoir models.

Kulkarni and Datta-Gupta [91] extend the two-step inversion approach to history-matching relative permeability curves. The sensitivities with respect to the parameters used in the relative permeability functions are specified in Appendix A. Further, appropriate regularization terms for (46) are specified in [91].

Illiassov and Datta-Gupta [76] present an extension of the two-step inversion to multiwell, multitracer partitioning interwell tracer tests, applied to a large oil field in Texas. Partitioning tracer sensitivities are described in Section 4 (in particular Section 4.2). They use the two-step inversion approach twice: first for matching permeability and then for matching oil saturation. This procedure is iterated if necessary. A similar work related to ground water transport is found in [43].

Although all the above methods have been based upon streamlines, they all amount more or less to matching the properties in all the grid cells in the reservoir model. To improve the convergence properties of the inversion process, a multiscale approach is proposed by Yoon et al. [150]. The central idea here is to use a hierarchy of coarsened grids to match the dynamic production data. The matching is first performed on the coarser scales, where

the inversion problem is less under-determined, to reduce the ill-posedness of the problem. Moreover, the number of local minima is reduced on the coarser scales and this will speed up the iterative minimizing techniques. The inversion may be aborted before reaching the fine grid to prevent over-parameterization. Finally, the solution is downscaled to fine-grid realizations by sequential simulation, conditioning to well data. The multiscale idea was applied to the two-step inversion method, but the multiscale matching may be applied to other inversion approaches as well, e.g., as done by Stenerud and Lie [121] for matching streamline-effective properties using the Wang–Kovseck formulation to be discussed in the next section.

He et al. [68] propose a manual approach, using the relationship between the diffusive time-of-flight and the drainage radius outlined by Kulkarni et al. [92] to identify reservoir compartmentalizations and flow barriers during primary production. First, the drainage volumes and communications for the different wells are estimated by traditional decline-type-curve analysis of the primary production data. Second, starting from the geologic model, the drainage volumes are recalculated by the diffusive time-of-flight from a streamline-based flow simulation. Finally, reservoir compartmentalization and flow barriers are inferred by matching of the two estimates for the drainage volumes.

An approach for reconciling time-lapse amplitude changes using (47) with the time-lapse amplitude sensitivities discussed in Section 4.7 is proposed in [136].

As noticed in Section 4, any simulator can in theory be used to calculate streamline-based sensitivities, as long as intermediate velocity fields can be outputed during the simulation and streamlines can be traced on the cell geometry, see discussion in Section 4.1. Cheng et al. [35] demonstrate the applicability of a finite-difference simulator to the GTTI method.

In [124] and [122] the deterministic version of GTTI is combined with a very efficient multiscale-streamline simulator. A mixed multiscale finite-element pressure solver [1, 31] is combined with a transport solver based on streamlines and the unconditionally stable front-tracking method [73]. High efficiency of the forward simulator is obtained by selectively reusing the multiscale basis functions based on the spatial sensitivity distribution obtained from GTTI. In addition, a method for improved mass conservation in streamline simulation [122] is applied , which allows for a considerable reduction in the number of streamlines used in the forward simulations. For this combination of forward and backward methodology, a reservoir model with more than one million grid blocks was history-matched in less than twenty minutes on an ordinary desktop PC.

In [123], GTTI is applied to two-dimensional fully unstructured grids. A generalized smoothing operator for $\mathbf{L}$ in (47) is proposed for fully unstructured grids. Further, sensitivities on unstructured grids with varying grid-cell sizes are discussed. Because of spatial additivity (as discussed in Section 4), the sensitivities will scale with cell sizes. Consequently, larger modifications will be induced in large cells and small modifications in small cells, given the same conditions. The regularization involved in (47) can only to a small extent counteract this undesired effect. To remedy grid effects for cases with large variances in grid-cell sizes, Stenerud et al. [123] propose to rescale the sensitivities with the grid-cell volumes. The paper focuses on 2D numerical examples to investigate principal effects of performing GTTI on fully unstructured grids, and contains examples with large cell-size heterogeneities and faults with non-neighboring connections. The framework established in [123] is general and should therefore also apply in 3D, although some care should probably be taken when matching strongly layered structures.

5.3. **Methods Based on Streamline-Effective Properties.** For the methods within this category modifications to effective properties along either streamlines or bundles of streamlines are obtained to match dynamic production data. The modifications in effective properties are then propagated back to the underlying simulation grid by either a deterministic or a geostatistical method. In the following M refers to a grid-cell property and m refers to a streamline-effective property. Similarly we use K and k for a grid and a streamline-effective permeability, respectively.

5.3.1. *Streamline-Effective Properties.* It is not necessary to actually compute the streamline-effective properties for all the methods described below, because it is often only the relative modifications to these properties that are needed. Nevertheless, we will here present and discuss a few approaches for obtaining streamline effective properties; in particular for permeability.

Obtaining effective properties along streamlines or streamline-bundles is simply an upscaling problem. For uni-directional one-phase flow in a medium with constant permeability values perpendicular to the flow direction (serial flow), it can be shown that the correct average is a harmonic average, see Appendix C. This makes sense because for the harmonic average is dominated by the lowest permeability value, which is the bottleneck for the flow. Further, it can also be shown that for uni-directional one-phase flow in a medium with constant permeability values along the flow direction (parallel flow), the correct average is an arithmetic average, see Appendix C. At a first glance, upscaling permeability along streamlines may seem like a 1D upscaling problem, but streamlines are not truly one-dimensional. The different cases of serial and parallel flow indicate that the correct streamline upscaling will depend on the underlying spatial structures in the permeability and thus not be a simple 1D upscaling problem. A one-dimensional streamline represents the flow in a 3D streamtube. Hence, even though streamlines are supposed to be aligned with the flow directions (total velocity), the actual flow may locally escape bottlenecks caused by low-permeable rock (traverse fluxes).

Unweighted arithmetic (A), geometric (G), and harmonic (H) averages are the three classical Pythagorean averages. For $\mathbf{x} = \{x_1, x_2, \ldots, x_n\}$ with all elements positive, the following relation holds

$$\max(\mathbf{x}) \geq A(\mathbf{x}) \geq G(\mathbf{x}) \geq H(\mathbf{x}) \geq \min(\mathbf{x}),$$

with equality if and only if $x_1 = x_2 = \ldots = x_n$. The geometric average is therefore also a reasonable candidate to calculate the effective permeabilities.

Based on this discussion, it seems reasonable to apply a harmonic or a geometric average to obtain effective permeabilities along streamlines (serial flow), and then an arithmetic or a geometric average of the streamline-effective permeabilities to obtain effective sensitivities for streamline bundles (parallel flow).

Wang and Kovscek [141], among others, suggest to represent the effective streamline permeability by the following weighted harmonic average

$$k_\ell^{\text{eff}} = \frac{\sum_{i=1}^{N_c^\ell} \Delta\tau_{\ell,i}}{\sum_{i=1}^{N_c^\ell} \dfrac{\Delta\tau_{\ell,i}}{K_i}}, \tag{57}$$

where N_c^ℓ is the number of grid cells intersected by streamline ℓ, $\Delta\tau_{\ell,i}$ is the time-of-flight increment of streamline ℓ across grid cell i, and K_i is the permeability in grid cell i. Hence, (57) can be considered a variant of (A-3).

Further, Ravalec-Dupin and Fenwick [116] suggest to use the following harmonic average for the effective permeability of a streamline bundle

$$k_\ell^{\text{eff}} = \frac{\sum_{\ell=1}^{N_{\text{sl}}} \sum_{i=1}^{N_c^\ell} q_\ell \Delta\tau_{\ell,i}}{\sum_{\ell=1}^{N_{\text{sl}}} \sum_{i=1}^{N_c^\ell} \dfrac{q_\ell \Delta\tau_{\ell,i}}{K_i}}. \tag{58}$$

Here q_ℓ is the volumetric flux assigned to streamline ℓ.

5.3.2. *The Wang–Kovscek Method.* The idea of using effective properties along streamlines for history matching was first introduced by Wang and Kovscek [141]. Their basic idea was to relate the fractional-flow curve at a producer to the water breakthrough of individual streamlines. Then by adjusting the effective permeability along streamlines, one can determine the breakthrough time of each streamline that reproduces the reference producer fractional-flow curve. This is realized through the following simple algorithm

(1) Start with an initial permeability field

(2) Run a simulation and check match with observed data: fractional-flow, well rate and/or well pressure (drops).
(3) Obtain modifications in effective streamline permeability along each streamline to match the data, as discussed below.
(4) Propagate modifications in streamline permeabilities back to the grid.
(5) Iterate steps 2–4 until a satisfactory match is achieved.

The derivation of the original method assumes two-phase incompressible flow, piston-like displacement along each streamline, no capillary forces, and no gravity. Moreover, we here present the modifications obtained for the data associated with one single producer, but the extension to several producers is straightforward

The ordered streamlines are used to discretize the observed fractional flow in the wells. Since each individual streamline will contribute equal amounts to the total fractional flow for piston-like displacement, the fractional flow increases a fixed amount each time a streamline breaks through. Implicitly, we assume that the fractional-flow curve at the producer is monotone. When a mismatch between observed and calculated fractional flows arises, the streamlines responsible for the mismatch are identified by examining the breakthrough times and the effective permeabilities of the streamlines are adjusted.

The history match along streamlines is obtained as follows. Assuming equal flow rates, the streamlines are ordered with respect to their dimensionless breakthrough times. Let there be N streamlines, each having a length L_ℓ, an average porosity ϕ_ℓ, and an average cross-sectional area A_ℓ. Then the dimensionless breakthrough time of streamline ℓ is defined as

$$\widetilde{T}_\ell = \frac{\sum_{j=1}^{N_{\mathrm{sl}}} (A\phi L)_j \tilde{x}_j^\ell}{\sum_{j=1}^{N_{\mathrm{sl}}} (A\phi L)_j} = \sum_{j=1}^{N_{\mathrm{sl}}} \widetilde{V}_j \tilde{x}_j^\ell, \tag{59}$$

where $\tilde{x}_j^\ell$ is the position in dimensionless units of the displacing phase front in the jth streamline as streamline ℓ breaks through, and $\widetilde{V}_j$ is the ratio of the pore volume of streamline j over the total pore volume. Since the streamlines are considered as independent flow systems with piston-like displacement, the relative positions $\tilde{x}_j^\ell$ can be approximated using Dykstra–Parsons method for non-communicating layers, see e.g., [48, 121]. The expression for the relative position of the front in streamline j as streamline ℓ breaks through, is a function of the effective permeabilities in streamline ℓ and j, that is, $\tilde{x}_j^\ell = f(k_\ell, k_j)$. Now, since the sum in the numerator of (59) runs over all streamlines, the breakthrough time $\widetilde{T}_\ell$ is a function of the permeabilities of all streamlines connected to the producer. In vector notation this can be written $\widetilde{\mathbf{T}} = \mathbf{B}(\mathbf{k})$. Using a Taylor expansion, the mismatch in breakthrough times can be written:

$$\Delta\widetilde{\mathbf{T}} = \widetilde{\mathbf{T}}^{\mathrm{obs}} - \widetilde{\mathbf{T}}^{\mathrm{cal}} = \mathbf{B}(\mathbf{k}^{\mathrm{obs}}) - \mathbf{B}(\mathbf{k}^{\mathrm{cal}}) \approx \mathbf{A}(\mathbf{k}^{\mathrm{obs}} - \mathbf{k}^{\mathrm{cal}}) = \mathbf{A}\,\Delta\mathbf{k}. \tag{60}$$

Here the derivatives $A_{\ell,j} = \partial\widetilde{T}_\ell/\partial k_j$ are obtained by differentiating (59). The system is simplified by defining normalized parameters [141], which makes the system (60) strongly diagonally dominant for unit mobility ratio so that it approximately decouples. By neglecting off-diagonal entries, the relative modifications can then be obtained by

$$r_\ell^t = \frac{\Delta k_\ell^t}{k_\ell^{\mathrm{old}}} \approx \frac{\widetilde{T}_\ell^{\mathrm{cal}} - \widetilde{T}_\ell^{\mathrm{obs}}}{\widetilde{T}_\ell^{\mathrm{obs}}}. \tag{61}$$

This approximation is only valid for unit mobility ratios. For non-unit mobility ratios, the modifications must generally be obtained by solving the full system (60). Moreover, streamlines will generally evolve during a dynamic displacement (as discussed in the introduction), so an accurate inversion would require the use of several different streamline distributions in time to match different segments of the fractional-flow curve. Altogether, this is computationally intensive. Rather than inverting the matrix $\mathbf{A}$, Wang and Kovscek [141] therefore suggest to use (61) for a representative set of streamlines as an approximation also in the non-unit mobility case.

Similarly, a match of pressure drop and total well rate is calculated by

$$r_\ell^{p,q} = \frac{\Delta k_\ell^{p,q}}{k_\ell^{\text{old}}} = \frac{\Delta p^{\text{cal}}\, q^{\text{obs}} - \Delta p^{\text{obs}}\, q^{\text{cal}}}{\Delta p^{\text{obs}}\, q^{\text{cal}}}, \tag{62}$$

which can be derived under the same assumptions as for the Dykstra–Parsons method from Darcy's law for an effective streamline permeability [121, 141]. The superscripts p and q indicate that the corresponding modification is due to mismatch in pressure drop and total well rate, respectively.

The two modifications (61) and (62) are then combined to define a total correction factor α_ℓ for each streamline, so that $k_{\text{new}} = \alpha_\ell k_{\text{old}}$. To this end, one should in general use a weighted geometric average

$$\alpha_\ell = \left[\left(1 + r_\ell^t\right)^{w_1} \cdot \left(1 + r_\ell^{p,q}\right)^{w_2}\right]^{1/(w_1+w_2)}.$$

In practice it turns out that equal weighting is acceptable [141].

Once the relative modifications to effective permeabilities are obtained for each streamline, they must be propagated back to the underlying grid. Then a forward simulation is run and the above process is repeated until the data are satisfactory matched.

To map the modification in effective permeability of a streamline back to grid-cell permeabilities, the simplest procedure would be to modify all grid cells along the streamline with the same amount as the modification in the effective property of the streamline that passes through it; that is, simply multiplying by α_ℓ so that $K_{\text{new}} = \alpha_\ell K_{\text{old}}$. If more than one streamline pass through a grid cell, Wang and Kovscek [141] suggest to use a geometric average of the correction factors. This may be a crude method if the lengths of different streamlines passing through the same cell are not equal. Instead, one can use a sensitivity-weighted approach [26, 140]. The sensitivity of the effective permeability of streamline ℓ with respect to the permeability change in grid cell i is defined by direct differentiation of an expression for the effective permeability

$$g_{\ell,i} = \frac{\partial k_\ell}{\partial K_i}. \tag{63}$$

For instance, if (57) is used for the streamline-effective permeability, the following sensitivity is obtained

$$g_{\ell,i} = \frac{\tau_{\ell i} k_\ell^2}{\tau_\ell K_i^2}, \quad \tau_\ell = \sum_i \Delta\tau_{\ell,i}.$$

This sensitivity is weighted by the incremental time-of-flight for the streamline through the cell to obtain a weighted sensitivity

$$G_{\ell,i} = g_{\ell,i}\, \frac{\Delta\tau_{\ell,i}}{\sum_\ell \Delta\tau_{\ell,i}}.$$

The current approach requires no computation of sensitivity coefficients in the traditional sense.

An advantage of obtaining relative modifications, like in **Eqs. 61** and **62**, is that it results in cancellation of potential proportionality errors. Therefore, the real time or the time-of-flight is commonly used instead of the dimensionless PVI time defined by (59). Moreover, the proposed approach, using modifications (61) and (62), is independent of how the effective streamline permeabilities are defined; except if the sensitivities in (63) are used.

The original method of Wang and Kovscek [141] was later modified by Stenerud and Lie [121] to avoid some of the approximations inherent in the original method and bypass the need for solving a linear system for non-unit mobility ratios. In the modified method, one obtains the following expression for the relative modifications with respect to mismatch in breakthrough time and effective pressure drop

$$r_\ell^{t,p} = \frac{\Delta k_\ell^{t,p}}{k_\ell^{\text{cal}}} = \frac{t_\ell^{\text{cal}} \Delta p^{\text{cal}} - t_\ell^{\text{obs}} \Delta p^{\text{obs}}}{t_\ell^{\text{obs}} \Delta p^{\text{obs}}}. \tag{64}$$

In addition, the method was extended to match porosity or permeability–porosity ratio, and to account for gravity along streamlines. Finally, a multiscale strategy was proposed, inspired by a work of Yoon et al. [150], see Section 5.2.6.

In Appendix D we show that under the same assumptions as used in [121, 141], but by relaxing the assumption of piston-like displacement to Buckley–Leverett profile, the same expressions for the relative modifications can be obtained: that is, (61) and (64). However, relaxing the assumption of piston-like displacement may make it harder to relate the breakthrough of individual streamlines to increments in the fractional-flow curve. The relaxation of the assumption of piston-like displacement is facilitated by the proportionality relation between the time-of-flight and the breakthrough time for the analytic Buckley–Leverett solution, see Section 3.2. This observation has also been made by other authors, see e.g., [3].

5.3.3. *The Agarwal–Blunt Method.* Agarwal and Blunt [3] extend the Wang–Kovseck method to compressible black-oil systems with gravity by using 'full physics' in the forward simulation that determines the match. As in [141], the key idea is to use a piston-like approach to sort streamlines with respect to breakthrough times and match permeability values along individual streamlines. To avoid inverting a matrix system, Agarwal and Blunt [3] use an alternative method to adjust effective permeability values. Assume that the permeability along a streamline is modified by a fixed amount α so that $k_{\text{new}} = \alpha k_{\text{old}}$. By (20) the time-of-flight along a streamline is proportional to an effective permeability–porosity ratio; i.e., $\tau \propto \frac{\phi}{k}$. Therefore, the new time-of-flight is given as $\tau_{\text{new}} = \tau_{\text{old}}/\alpha$. For piston-like displacement (or tracer-like flow), the time-of-flight and the arrival time of a saturation contour will coincide. For non-piston flow, the time-of-flight may be a good enough approximation to the arrival time, because a proportionality factor will anyway cancel out in the correction factor specified above. For instance, for the analytic Buckley–Leverett solution presented in Section 3.2, the arrival time of a saturation contour is proportional to the time-of-flight

$$t \propto \tau \propto \frac{\phi}{k}, \tag{65}$$

where the proportionality factor depends on the saturation value. To match a calculated breakthrough time t_i^{cal} with the observed time t_i^{obs} one may therefore modify the permeability by a factor $\alpha = t_i^{\text{cal}}/t_i^{\text{obs}}$.

In the first case, there is a fixed pressure drops between wells. Now, if the average permeability of the region is incorrect, the well rate at late times may be erroneous. The calculated water rate q_w is therefore first rescaled. We let $t_{\max}$ denote the latest time for which an observed rate is available and introduce an overall modification α_0 of the permeability field (i.e., a modification for all streamlines connected to the producer). To match the end-point we require that

$$\alpha_0 = q_w^{\text{obs}}(t_{\max})/q_w^{\text{cal}}(\alpha_0 t_{\max}) \approx q_w^{\text{obs}}(t_{\max})/q_w^{\text{cal}}(t_{\max}).$$

This gives a rescaling of the calculated water-rate curve. Then the water-rate axis is divided into increments $\alpha_0 q_\ell$. To match water rate $q_w = \alpha_0 \sum_{j=1}^{\ell} q_j$ at time $t_\ell^{\text{cal}}/\alpha_0$, we determine the corresponding time t_ℓ^{obs} from the data $q_w^{\text{obs}}(t_\ell^{\text{obs}})$. To align the two times, we must modify the permeability by a factor $\tilde{\alpha}_\ell = (t_\ell^{\text{cal}}/\alpha_0)/t_\ell^{\text{obs}}$. Thus the overall modification along streamline ℓ becomes

$$\alpha_\ell = \alpha_0\, \tilde{\alpha}_\ell = t_\ell^{\text{cal}}/t_\ell^{\text{obs}}.$$

If the total rate changes, a rescaling of the water rate is done by multiplying the observed and calculated water rates by $q^*/q_{\text{t}}(t)$, where q^* is the water rate when the streamline pattern was taken, and $q_{\text{t}}(t)$ is the time-varying total rate. The method described for fixed rates is then applied to the rescaled water rate. This is similar to matching fractional flow.

A similar modification is proposed for the case where the wells are constrained by total rate. Based on Darcy's law for effective permeability for streamline bundles between two wells, we can define the modification

$$\alpha_0 = \frac{\Delta p^{\text{cal}}}{\Delta p^{\text{obs}}},$$

where Δp^{cal} and Δp^{obs} are the calculated and observed pressure drops between an injector–producer pair when the streamline pattern was computed (e.g., at water breakthrough). For compressible flow, streamlines may originate and terminate away from the wells. Such streamlines are neglected by defining $\alpha_0 = 1$. The total modification along streamline ℓ is then

$$\alpha_\ell = \alpha_0 \cdot \frac{t_\ell^{\text{cal}}}{t_\ell^{\text{obs}}}.$$

To map the modified streamline properties back to the underlying grid, Agarwal and Blunt [3] use the following volume-weighted average in each grid cell

$$K_i^{\text{new}} = \underbrace{\frac{\sum_{\ell=1}^{N_{\text{sl},i}} q_\ell \, \Delta\tau_{\ell,i} \, \alpha_\ell}{\sum_{\ell=1}^{N_{\text{sl},i}} q_\ell \, \Delta\tau_{\ell,i}}}_{\bar{\alpha}} K_i^{\text{old}}. \tag{66}$$

Here $N_{\text{sl},i}$ is the number of streamlines crossing grid cell i, $\Delta\tau_{\ell i}$ is the time-of-flight increment of streamline ℓ across grid cell i, and q_ℓ is the total flux of streamline ℓ.

Jang and Choe [78] apply the method of Agarwal and Blunt [3] as the second step of a two-step approach. The first step is a gradient-based minimization incorporating well pressures and permeability samples, where the necessary sensitivities are calculated by the adjoint method. The motivation of the first step is to get the order in which the streamlines break through more correct prior to the second step, which is intended to make the location of the permeability modifications more accurate. The two steps are iterated if necessary.

In [4] the prior method of Agarwal and Blunt [3] is extended to include modifications to the permeability histogram and the porosity of each well-pair. The first part of the method is as in [3]. Then, water rates at a fractional flow of 10% are matched by adjusting the porosity. Because breakthrough times scale with the effective porosity along the streamlines, the porosities in each producer-region are modified by

$$\phi^{\text{new}} = \phi^{\text{old}} \frac{t^{\text{obs}}}{t^{\text{cal}}}.$$

Finally, the histogram of the permeability is also modified to match the spread in the water rate. To preserve the rank order of the permeability values in a well-region, the following relation is applied

$$K^{\text{new}} = K^{\text{old}} \cdot \left[\frac{K^{\text{old}}}{\bar{K}} \right]^{\xi}, \tag{67}$$

where $\bar{K}$ is a geometric average of the permeability for the well-region. To determine the exponents ξ for capturing heterogeneity, Agarwal and Blunt suggest the following approach: First the time spread Δt between 10% and 90% water rate or fractional flow is determined for both the observed and calculated curves, i.e., Δt^{obs} and Δt^{cal}, respectively. The 'fast' and the 'slow' streamlines are identified. The fast streamlines are the streamlines with breakthrough at 10% or lower fractional flow, and the slow streamlines have breakthrough at 90% or higher fractional flow. Streamline-effective permeabilities $\bar{k}_{\text{f}}$ and $\bar{k}_{\text{s}}$ are calculated by harmonic averaging for the 'fast' and the 'slow' streamlines bundles, respectively. It is then required that

$$\frac{\bar{k}_{\text{f}}^{\text{new}}}{\bar{k}_{\text{s}}^{\text{new}}} = \frac{\bar{k}_{\text{f}}^{\text{old}}}{\bar{k}_{\text{s}}^{\text{old}}} \cdot \frac{\Delta t^{\text{obs}}}{\Delta t^{\text{cal}}}.$$

By assuming that $\bar{K}$ is representative for the 'fast' and the 'slow' streamline bundles and applying (67) one obtains that

$$\left[\frac{\bar{k}_{\text{f}}^{\text{old}}}{\bar{K}} \right]^{\xi} \cdot \left[\frac{\bar{K}}{\bar{k}_{\text{s}}^{\text{old}}} \right]^{\xi} = \frac{\Delta t^{\text{obs}}}{\Delta t^{\text{cal}}} \quad \Leftrightarrow \quad \xi = \frac{\ln\left(\frac{\Delta t^{\text{obs}}}{\Delta t^{\text{cal}}}\right)}{\ln\left(\frac{\bar{k}_{\text{f}}^{\text{old}}}{\bar{k}_{\text{s}}^{\text{old}}}\right)}.$$

When ξ is determined, a new permeability distribution is calculated for each well region. The approach to modify the histogram is only applied at the first iteration of the history-matching procedure. Further, the other modifications for porosity and permeability described above

are performed for the two first iterations. For the subsequent iterations Agarwal and Blunt instead use the Newton iteration

$$\mathbf{m}^{n+2} = \mathbf{m}^{n+1} - J^{n+1}\frac{\mathbf{m}^{n+1} - \mathbf{m}^{n}}{J^{n+1} - J^{n}},$$

where J is an objective function and $\mathbf{m}$ is the reservoir parameters to be modified.

In [3] the method presented above is applied to a portion of the Ekofisk field in the North Sea. Further, in [4] the extended methodology presented above is applied to an Arabian Gulf field.

Kretz et al. [89] matched the time-of-flight from an injector to the fluid front. The location of the fluid front (saturation front) is intended to be localized by 4D seismics, but only synthetic examples are presented in this paper. Motivated by the relation between time-of-flight and effective permeability, the correction factor for the first permeability modification is obtained by

$$\alpha_\ell^1 = \frac{\tau_{\text{4D}}^1}{\tau_{\text{cal}}^1}.$$

By this correction factor the permeability is modified between the injector and the fluid front. For the consecutive iterations the following modification factor is applied between the previous front and the current front

$$\alpha_\ell^n = \frac{\tau_{\text{4D}}^n - \tau_{\text{4D}}^{n-1}}{\tau_{\text{cal}}^n - \tau_{\text{cal}}^{n-1}}.$$

To propagate the modifications to the underlying grid (66) is applied, i.e., the same approach as suggested by Agarwal and Blunt [3].

5.3.4. *Adding Geostatistics.* Caers et al. [26] present an extended version of the method in [141] in two spatial dimensions consisting of a two-step mapping of the effective streamline permeabilities back to grid-cell permeabilities. The first step consists of obtaining modifications of effective streamline permeabilities, and to propagate the modifications to the underlying grid by the same deterministic approach as described above [26, 141]. In the second step, the updated grid permeability is used as an initial seed for a Gauss–Markov iteration (McMC). This two-step mapping is iterated until the history match is converged. The overall method thus consists of an outer iteration and an inner geostatistical iteration. Flow simulations are only needed in the iterations of the outer loop. Through the use of this geostatistical framework, the authors are able to match streamline-effective permeabilities to the production data and at the same time honor prior geological information.

In [25] a similar method is presented, where gradual deformation [74] (see Section 5.4.4) is used instead of the Gauss–Markov random function method. Because the gradual-deformation method can be used with any sequential simulation algorithm [25], the assumption of a Gaussian random permeability field can be relaxed and the approach can be extended to include multi-point geostatistics to match more complex geological structures like fractures and channels. A straightforward application of gradual deformation would seek to minimize the misfit in the production data. A key point in Caers' method is to instead apply gradual deformation to minimize an objective function measuring the misfit with respect to the effective streamline permeabilities derived by the original Wang–Kovscek method described above:

$$E(K^{\text{new}}) = \sum_{\ell=1}^{N_{\text{sl}}} \big(k_\ell^{\text{old}} - k_\ell(K^{\text{new}})\big)^2. \tag{68}$$

According to Caers [25], the required number of forward simulations is dramatically reduced (convergence typically requires only 5-10 flow simulations). However, a number of sequential simulations from a multivariate probability distribution have to be conducted in the inner loop that minimizes (68), but for large reservoir models the forward simulation will dominate the computational cost [25]. To apply this gradual-deformation approach for multi-well patterns, streamline-defined regions and a method for global optimization are required [25]. If a gradient-based method is used for the optimization, sensitivities for the objective function

in (68) with respect to the gradual-deformation parameters are required. Caers [25] presents analytic sensitivities for this approach, in the case of Gaussian permeability field, by assuming that the streamline-effective permeability is given by the harmonic average in (57).

The overall methods in [25, 26] allow for drastic changes in the geological model as opposed to for instance the AHM method of Emanuel and Milliken [49] and the travel-time methods of He et al. [67], Vasco et al. [135], which seek minor changes to the model. Moreover, it should be mentioned that only synthetic two-dimensional cases are presented in [25, 26].

Ravalec-Dupin and Fenwick [116] present an alternative two-step method based upon the same ideas as Caers [25]. In the first step, the method of Agarwal and Blunt [3] is used to estimate corrections along bundles of streamlines (as opposed to individual streamlines in [3]). The effective permeability along a streamline bundle ℓ is here defined by (58); see the discussion in Section 5.3.1. The streamline bundles are identified by first sorting the streamlines according to breakthrough time and then segmenting the fractional flow curves so that all streamlines responsible for each given fractional flow increment are identified in a corresponding bundle. In the second step, the desired streamline-effective permeabilities are propagated back onto the underlying grid. To this end, the gradual-deformation method is used to minimize the misfit between the desired effective streamline permeabilities and those calculated for the given permeability field as above.

In [27, 53] Caers, Fenwick and coworkers present another extended version of the Wang–Kovscek method. Again, by the approximation in (65) a correction factor is defined by

$$\alpha = \frac{(\frac{\phi}{k})_{\mathrm{sl}}^{\mathrm{new}}}{(\frac{\phi}{k})_{\mathrm{sl}}^{\mathrm{old}}} = \frac{\tau^{\mathrm{new}}}{\tau^{\mathrm{old}}},$$

where $(\phi/k)_{\mathrm{sl}}$ represents an effective permeability–porosity ratio for each streamline-bundle. The correction factor above can be used to modify the porosity, the permeability, or the permeability–porosity ratio in the effective region (along streamline, streamline-bundle, or producer zone)

Inspired by [141], the piston-like breakthrough in each streamline is related to the fractional-flow curve. The relative modification for a time-average producer zone is of amplitude type and defined by [27]

$$\alpha = 1 - \frac{1}{N_{\mathrm{d}}} \sum_{j=1}^{N_{\mathrm{d}}} \left(\frac{q_w^{\mathrm{cal}}(t_j)}{q_t^{\mathrm{cal}}(t_j)} - \frac{q_w^{\mathrm{obs}}(t_j)}{q_t^{\mathrm{obs}}(t_j)} \right) = 1 + \frac{1}{N_{\mathrm{d}}} \sum_{j=1}^{N_{\mathrm{d}}} \big(f_w^{\mathrm{obs}}(t_j) - f_w^{\mathrm{cal}}(t_j) \big). \tag{69}$$

Here, $q_w(t_j)$ and $q_t(t_j)$ are the water and total production rate at time t_j. This modification is equivalent to considering the whole flow zone as a single effective streamline bundle. To propagate the permeability modifications back to the underlying grid, direct sequential simulation (DSSIM) [81] with locally varying mean is applied. In contrast to common methods for sequential simulation, like sequential Gaussian simulation, that require transformation into a standard Gaussian space, DSSIM can be performed directly in data space. Journel [82] showed that the sequential simulation algorithm, without any prior transformation, succeeded in reproducing a covariance model, provided that the simulated values are drawn from local conditional distributions identifying the simple kriging mean and variance derived from that covariance model. This fundamental result is known as DSSIM; for more details on DSSIM see e.g., [24]. However, DSSIM does not honor the prior histogram, which is not necessarily a disadvantage if the histogram is not known with sufficient accuracy. Further, the fact that the histogram is allowed to change, while at the same time honoring the covariance structure, gives flexibility to for instance perturb the local mean [27]. Application of the approach to a real field case is presented in [65].

In [53] the method of locally varying mean (LVM) presented in [27, 65] is extended, and combined with the probability perturbation method (PPM) of Hoffman and Caers [71]. While LVM perturbs large scale structures, PPM perturbs the small-scale variations, and in this manner the combination of the methodologies is considered a multiscale approach. The combination of LVM and PPM was first proposed in [27], but without any implementation. The two methodologies are applied sequentially. However, for the examples presented, PPM

did not give any substantial contribution to the history matching. We will therefore not give any further description of PPM.

Under the assumption of piston-like displacement along each streamline, the correction factor for a bundle of streamlines with water breakthrough in the time interval from t_{j-1} to t_j is given by [53]

$$\alpha = 1 - \frac{\int_{t_{j-1}}^{t_j} q_w^{\mathrm{cal}} dt}{\int_{t_{j-1}}^{t_j} q_t^{\mathrm{cal}} dt} + \frac{\int_{t_{j-1}}^{t_j} q_w^{\mathrm{obs}} dt}{\int_{t_{j-1}}^{t_j} q_t^{\mathrm{obs}} dt} = 1 + \int_{t_{j-1}}^{t_j} f_w^{\mathrm{obs}} - f_w^{\mathrm{cal}} dt. \tag{70}$$

This equation is derived by assuming fixed streamlines for the time interval from t_{j-1} to t_j, and can be considered as an extension of (69). To account for non-piston-like displacement in the streamlines and that streamlines going through a single grid cell can be connected to multiple producers, the following weighting is applied

$$\bar{\alpha}_{\Delta t} = \frac{\sum_{k=1}^{N_{w,p}^{\Delta t}} \left(\alpha_k q_w^k + q_t^k - q_w^k\right)}{\sum_{k=1}^{N_{w,p}^{\Delta t}} q_t^k}. \tag{71}$$

Here $N_{w,p}^{\Delta t}$ is the number of production wells connected to the streamlines in a grid cell. The correction factor is calculated for each grid cell exclusively using rate information from the streamlines intersecting the cell. For piston-like displacement, $q_w^k = q_t^k$, so that the correction factor simply reduces to simple weighting by the total flow rate. If in addition a streamline formulation with equal total rate for each streamline is used the correction factor reduces to an arithmetic average. To average the correction factor over $N_{\Delta t}$ sets of streamlines, a time-weighted average is used

$$\bar{\alpha} = \frac{\sum_{j=1}^{N_{\Delta t}} \Delta t_j \bar{\alpha}_{\Delta t}}{t_{N_{\Delta t}} - t_1}, \quad \Delta t_j = t_j - t_{j-1}. \tag{72}$$

Gross [63, 64] presents another version of the LVM method. First, modifications in streamline-effective permeability are obtained and propagated to the pressure grid by a version of the methods presented above. Second, the permeability modifications are propagated to other reservoir properties accounting for prior cross-property correlations. Like in [27, 65] the modifications to streamline-effective permeability give locally varying means that are propagated to the underlying grid by direct sequential simulation (DSSIM). The permeability modifications are then propagated to the other properties by a kind of Monte Carlo sampling. The prior probability distribution for the reservoir properties is arranged into discrete classes. The properties can for instance be permeability (horizontal,vertical), porosity, facies, net-to-gross, etc. For continuous properties, the ranges of the properties have to be carefully subdivided into 'bins' (classes). The prior model can be computed in two manners: by direct user specification after pore-network studies, or by scanning a set of training models to establish frequencies for the different classes in local control volumes [64]. The latter approach is applied here. The probability distribution needed in the cross-property propagation is simply

$$P(c^{\mathrm{new}}) = P(c^{\mathrm{prior}} | K^{\mathrm{new}}),$$

where c is a class configuration. This posterior distribution is simple to obtain from a prior distribution by extracting the configurations with the correct permeability bin. A renormalization is then necessary by summing over the extracted classes. Further, it is also possible to keep other properties fixed, which will shrink the total number of classes to be extracted.

To obtain the correction factor α_i^t with respect to the fractional-flow data, an approach similar to the original Wang–Kovscek approach is used [63, 64]. Relative modifications $\Delta k_{i,R}^t$ are obtained by a time-streamline-average of relative modifications of type given in (61) for all streamlines contributing to a producer and intersecting a grid cell i. Correction factors for fractional flow are then obtained by

$$\alpha_i^t = 10^{\Delta k_{i,R}^t}.$$

To account for mismatch in the total production rate q_k at producer k and the pressure drop $\Delta p_{k,l}$ between an injector l and producer k, the following correction factor is used

$$\alpha_i^{p,q} = \frac{1}{|\Omega_i|} \sum_{(k,l)\in\Omega_j} \left[\frac{q_k}{\Delta p_{k,l}}\right]^{\text{obs}} \cdot \left[\frac{\Delta p_{k,l}}{q_k}\right]^{\text{cal}}.$$

Here Ω_i is the set of injector-producer pairs for the streamlines intersecting grid cell i.

Jang [77] adds geostatistics to the method of Agarwal and Blunt [3] described above, by a simple approach. A two-step approach is proposed, where the first step consists of the method of Agarwal and Blunt [3]. The second step consists of generating Gaussian realizations conditioned to randomly selected grid-cell permeabilities of the resulting permeability field of the first step. If a flow simulation reveals a sufficient decrease in the objective function, a realization is accepted. The two steps are iterated if necessary.

Finally, we outline an idea for a fully analytic Bayesian approach for propagating/downscaling the modifications in streamline effective properties to the simulation grid. This approach relies on two assumptions. The first assumption is that the streamline effective properties can be obtained by weighted arithmetic averages of the reservoir properties (possibly transformed, e.g., by the logarithm). Hence, the weighted geometric average for a set of parameters is equivalent to a weighted arithmetic average for the logarithm of the parameters. The second assumption is that the (possibly transformed) reservoir properties can be considered Gaussian. Then, there is a linear relation between the streamline-effective properties and the (possibly transformed) reservoir properties, which enables analytic determination of the posterior Gaussian distribution of the reservoir properties, conditioned on the history-matched streamline-effective properties. Details are given in Appendix E.

5.4. **Miscellaneous Methods.** In this section we describe how streamline-defined regions or streamline-derived sensitivities have been used to boost the performance of existing geostatistical methods that were originally introduced without any connection to streamlines. The methods we here pursue are within the realm of: Markov chain Monte Carlo (McMC), ensemble Kalman filter (EnKF), sequential self-calibration (SSC), and the gradual deformation method (GDM).

5.4.1. *Markov chain Monte Carlo.* In [98] a two-stage Markov chain Monte Carlo (McMC) approach is proposed. McMC is a sampling approach for sampling rigorously from the posterior distribution. The sampling consists of iterations over a two-step algorithm. In the first proposal step modifications to the reservoir parameters are drawn from a proposal distribution. In the second acceptance/rejection step one determines if the proposal should be kept based on the resulting simulated reservoir responses. The algorithm is shown to converge in probability distribution in the limit of infinitely many iterations. Thus, an extensive number of iterations may be required to get close to convergence to the posterior distribution. Moreover, rigorous sampling also requires a full flow simulation to be performed for each proposal step. Consequently, the accurate sampling has a high computational demand.

The two-stage approach proposed by Ma et al. [98] is intended to speed-up the McMC approach considerably without reducing the accuracy. The first stage consists of obtaining approximate production responses analytically for the proposed modified reservoir configuration by applying streamline-derived sensitivities. The approximate production responses are obtained by a linear approximation in the vicinity of the current production response:

$$\mathbf{g}^*(\mathbf{m}) = \mathbf{g}(\mathbf{m}_p) + \mathbf{G}\delta\mathbf{m}.$$

Here $\mathbf{g}(\cdot)$ denote a forward model (i.e., the reservoir simulator), $\mathbf{G}$ is the sensitivity matrix, and $\delta\mathbf{m} = \mathbf{m} - \mathbf{m}_p$ is the proposed modifications to the reservoir parameters. Only if the approximate production responses achieve acceptance for the proposed reservoir parameter field, a full reservoir simulation is performed to really check for actual acceptance/rejection.

5.4.2. *Ensemble Kalman Filter.* Among the geostatistical methods discussed in this section, the ensemble Kalman filter (EnKF) [51] has gained the most interest lately. EnKF is very flexible with respect to the type of data incorporated, can do sequential data integration and state updates during the production period, assessment of uncertainty is available from the ensemble representing the posterior, and it has recently been applied to several field cases, see e.g., [52, 105].

The ensemble Kalman filter is a Monte Carlo approach for sequentially integrating data into a reservoir model represented by an ensemble of realizations. The method utilizes cross-covariances between measurements and model parameters estimated from the ensemble to update the ensemble members. It is advantageous to keep the ensemble size low for high computational efficiency. However, this will increase the error in the estimated cross-covariances and the updated model parameters. To speed up the estimation of covariances, Arroyo-Negrete et al. [9] used streamlines and Devegowda et al. [45] used streamline-based sensitivities. Both the streamline trajectories and the production-response sensitivities include information about spatial correlations between production responses and model parameters. Therefore, in [9, 45] it is suggested to rescale the estimated cross-covariances by streamline-based influence weights using two slightly different approaches. The first approach is a streamline-trajectory assisted approach where the authors investigate the simple choice of a binary weighting based on streamline-defined regions [9]. For measurements of fractional-flow type it is possible to further condition based on information of water-front movement, which is easy to keep track of for streamlines. The second approach is sensitivity assisted [45], where the weights consist of rescaled production-response sensitivities, for which the smallest sensitivity values are neglected. For both approaches the 'regions of influence' from all the ensemble members are stacked to obtain a 'common region of influence' for each well.

5.4.3. *Sequential Self-Calibration.* In a series of papers [130, 143, 144, 146, 147], Wen and coworkers extended the so-called sequential self-calibration (SSC) method [62, 145] by applying and deriving streamline-based sensitivities. Streamlines are used for two purposes: (i) fast forward flow solution and (ii) fast calculation of sensitivity coefficients.

The SSC method is used for inversion of dynamic data and is an iterative geostatistically-based method coupled with an optimization procedure. Key points in the SSC method are: (i) the concept of master points to reduce the degrees of freedom in the optimization problem; (ii) propagation of perturbations at master points to the permeability field by kriging to account for spatial correlations; and (iii) computation of sensitivities by a combined streamline-based and gradient-simulator approach as described in Sections 4.2 and 4.6. The SSC algorithm starts with a set of initial realizations generated by a geostatistical algorithm and then performs the following steps:

(1) Solve flow equations and calculate sensitivities
(2) Evaluate the objective function and exit if satisfactory match is obtained.
(3) Select master points
(4) Optimization: find optimal perturbation at master points
(5) Propagate the perturbations back to the entire field by kriging.
(6) Iterate Steps 1–5 until a satisfactory match is achieved.

Let us assume that the observations to be used in the history match are the pressures and fractional flow in production wells. Then the history match is obtained by minimizing the following objective function

$$\mathcal{O} = \sum_{k=1}^{N_w^p}\sum_{j=1}^{N_d^p} W_{k,j}^p \left(p_{k,j}^{\text{obs}} - p_{k,j}^{\text{cal}}\right)^2 + \sum_{k=1}^{N_w^f}\sum_{j=1}^{N_d^f} W_{k,j}^f \left(f_{k,j}^{\text{obs}} - f_{k,j}^{\text{cal}}\right)^2. \tag{73}$$

Here $p_{k,j}$ and $f_{k,j}$ denote pressure and fractional flow, respectively, at well k at time t, and $W_{k,j}$ are weights. A gradient based-method is used to minimize the objective function $\mathcal{O}$. This requires the sensitivity coefficients of well pressure and fractional flow.

In [130], the SSC method is extended to include inversion of spatially distributed saturation data, e.g., from 4D-seismics. To include the saturation data, the following term is added to

the objective function:

$$\sum_{\mathbf{x}} \sum_{j=1}^{N_d^S} W_j^S(\mathbf{x}) \Big(S_j^{\text{obs}}(\mathbf{x}) - S_j^{\text{cal}}(\mathbf{x}) \Big)^2.$$

Here S is the saturation field, W_j are weights, and $\mathbf{x}$ are the observation points in the reservoir domain. The calculation of analytic streamline-based saturation sensitivities is described in Section 4.5. A synthetic 3D example is presented where saturation data is incorporated, but where most weight is given to the fractional-flow data based on an assumption of less uncertainty.

In [130, 144] a two-stage multiscale approach is used. The first stage consists of using the method outlined above on an upscaled initial geostatistical realization. Then the coarse-scale history-matched model is geostatistically downscaled to obtain fine-scale realizations. Simulated annealing and sequential Gaussian simulation is used for the downscaling in [144] and [130], respectively. This approach is less CPU-intensive than simulated annealing, and should remedy features of the SA approach like the tendency of fuzziness (high nugget effect) [130]. Part of the motivation for the upscaling in Tran et al. [130] is that the saturation data, e.g., from 4D-seismics, often have lower resolution.

5.4.4. *Gradual Deformation Methods.* Gradual deformation [74, 117] is a parameterization method that reduces the number of unknown parameters considerably by seeking new realizations as linear combinations of independent or dependent [106] realizations drawn from a geostatistical probability distribution. The method is motivated by the fact that linear combinations of multi-Gaussian random functions remain multi-Gaussian random functions. The gradual deformation method (GDM) does not necessarily rely on a Gaussian probability distribution, but a sequential simulation algorithm is required [74]. Further, the gradual deformation can also be performed with respect to structural parameters like mean, variance, and correlation range [74].

Gautier et al. [58, 59] develop a GDM-based history-matching method for two-phase incompressible flows, where they use a Gauss–Newton method equipped with partly streamline-based sensitivity coefficients to minimize the objective function (or misfit functional). Further, the use of gradual deformation incorporates geostatistics and reduces the number of parameters. The sensitivity calculations are discussed in Section 4.7. Gautier et al. [59] present the method and preliminary results on synthetic examples. The objective function obtained by this approach is highly irregular with many local minima, which makes the optimization problem harder. In [58] the optimization problem is discussed in more detail and some methods for smoothing the objective function are presented.

Barthelemy et al. [16] investigate a methodology for local gradual deformation with regions defined by streamlines. Rather than solving a global minimization problem, the authors investigate the applicability of gradual deformation for the local independent streamline-defined regions in parallel. Further, the authors propose a definition of an objective function, inspired by the travel-time matching described in Section 5.2, based on temporal moments of the production data. The proposed objective function was consistent with the conventional amplitude based objective function, but did not remove the irregularity considerably.

Finally, we remark that two gradual-deformation approaches for history-matching effective permeabilities along streamlines and streamline-bundles [25, 116] were presented in Section 5.3.4.

6. Streamline-based ranking of geostatistical realizations

Ranking is the process of reducing the number of realizations of a reservoir model, while spanning the probability space to a maximum extent. To rank the realizations a criterion correlated to production/economical outcome is typically used. Ranking is closely related to history-matching because it can be performed both before, during, and/or after the history matching itself. It is therefore natural to briefly describe two streamline-based methods for ranking.

Wang and Kovscek [142] present a method for ranking geostatistical models with respect to production data. First, a single model is history-matched with respect to production data. Then, multiple realizations are ranked with regard to streamline properties like time-of-flight, flow rate etc., by comparing with the history-matched model. According to the authors, this gives a fast method for generating multiple models that incorporate production data.

Idrobo et al. [75] investigate and discuss the use of an approximation for the swept volume based on the streamline coordinates (τ, ψ, χ) introduced in Section 3. Calculations of the swept volume are facilitated by the fact that the Jacobian with respect to the spatial coordinates (x, y, z) takes a simple form [41, 85]

$$\left\| \frac{\partial(\tau, \psi, \chi)}{\partial(x, y, z)} \right\| = \nabla\tau \cdot (\nabla\psi \times \nabla\chi) = \nabla\tau \cdot \mathbf{u} = \phi.$$

Here the time-of-flight equation (10) and the property $\mathbf{u} = \nabla\psi \times \nabla\chi$ are applied. Thus, the time-of-flight coordinates preserve the pore volume by $\phi\, dx\, dy\, dz = d\tau\, d\psi\, d\chi$. Further, the volume swept at a time t can be approximated by [41, 85]

$$V_{\text{swept}}(t) = \int\int\int \theta\big(t - \tau(x, y, z)\big)\, \phi\, dx\, dy\, dz = \int\int\int \theta\big(t - \tau(\psi, \chi)\big)\, d\tau\, d\psi\, d\chi, \tag{74}$$

where θ is the Heaviside function. Notice in particular, that this derivation is exact for piston-like displacement. Now the integral in (74) can be approximated by [75]

$$V_{\text{swept}} = \sum_{\ell} \int_{\Psi_\ell} \theta(t - \tau) q_\ell d\tau,$$

where q_ℓ is the volumetric flux assigned to streamline Ψ_ℓ. Considering a 3D grid, an indicator variable can be defined at each cell based on the time-of-flight. A cell is marked 'unswept' if the time-of-flight at the cell is greater than the time of interest, and 'swept' if the time-of-flight is less than or equal to the time of interest. Summing the pore volumes of the 'swept' cells, an approximation for the total swept volume at the time of interest can be obtained, and thereby also the sweep efficiency by dividing by the total pore volume. To account for changing well conditions, the time-of-flight distribution is calculated for the different well-configurations.

An indicator for recovery can be used for ranking stochastic reservoir models, because realizations in the range from pessimistic to optimistic can be chosen for closer studies and determination of uncertainty. In [75] it is demonstrated that the proposed swept volume indicator is strongly correlated with waterflood recovery, and is thus proposed as a ranking criteria. However, it is not specified for which mobility ratios the numerical experiments are conducted. In [11] the above swept-volume indicator for ranking and uncertainty is used for analysis of a Middle Eastern carbonate reservoir.

7. Discussion

In the last section, we discuss and compare the different methods for streamline-based history-matching and point out similarities and differences, and discuss some potential problems, restrictions, advantages, etc. The history-matching methods presented in this review are the assisted history matching (AHM), (generalized) travel-time inversion ((G)TTI) methods, and methods for matching streamline effective properties (SLEP). In addition, we have discussed streamline-based sensitivity calculations and reviewed various geostatistical history-matching methods where streamlines have been used to boost the performance. The discussion in this section is mainly focused on the three streamline-based approaches: AHM, (G)TTI, and SLEP.

Simplicity. The AHM approach [49, 104] is in many aspects the least sophisticated in the sense that it merely provides useful functionality to reservoir engineers that perform manual or semi-automated history matches. AHM appears to be fairly simple to implement on top of any existing streamline simulator, as this would not imply changing the flow solver itself, and would very likely offer useful functionality to reservoir engineers, see the histories of success in e.g., [29, 97]. However, the approach is manual, and as such not particularly suited to form the basis for an automated history-matching approach. An advantage of AHM, compared

with traditional manual history-matching methods, is that the modifications made to the reservoir parameters seem to be more targeted, and thus results in a better preservation of prior geologic information.

Modifications to Reservoir Parameters. An obvious similarity for the three methods is that they more or less explicitly impose targeted modifications to the reservoir parameters along streamline paths. This is a general feature of all streamline methods, which both can be considered a strength and a weakness. The strength is that making targeted modifications along the streamlines is what is sought when the principal physical effects are aligned with the streamlines, which is the conditions for which streamline simulation is particularly well suited. In reality, however, traverse physical effects may be important in the forward simulation, but these effects are strongly convoluted in the production data, and may thus be hard to account for by any history-matching method.

The GTTI and SLEP methods are similar in the sense that the mismatches $\Delta\widetilde{t}$ and α_ℓ, respectively, are propagated to modifications in the reservoir parameters. However, the approaches for propagating the mismatch in data for the SLEP and the GTT methods are quite different. Even for methods within the SLEP class, there are large variations in how the modifications are propagated. Still, the two methods can theoretically be defined in terms of the propagation approach of the other method, see Appendix F.

The GTTI method tends, like the AHM method, to keep the modifications small, smooth, and targeted to preserve the prior geology description and the geologic realism. As discussed above, this is motivated by the general low spatial resolution of the production data and the need for stabilizing the under-determined inversion process. Some of the SLEP methods are constrained to geostatistical information. On the other hand, the approaches presented in [25, 26], for instance, are claimed to allow for quite drastic alterations to the reservoir model. The key to enable small targeted modifications for GTTI is the application of production-response sensitivities, which are not applied for AHM and SLEP.

Complexity of Flow Model. The streamline-based sensitivities for the travel-time inversion methods are derived assuming the analytical Buckley–Leverett profile described in Section 3.2 along each streamline. However, the minimization problem of the travel-time inversion methods is general without any assumptions on the flow profile. The methods for adjusting effective streamline properties (SLEP) are mainly derived by assuming piston-like displacement. However, in Appendix D we show that similar (or sometimes identical) expressions can be derived by replacing the piston-like displacement front by an analytic Buckley–Leverett profile. Generally, the application of the analytic Buckley–Leverett solution is only an approximation, because pressure updates, varying saturation along streamlines, and transverse flow effects are not explicitly accounted for. However, this approximation often turns out to be sufficiently accurate in practice to perturb the iteration in the correct direction. (If necessary, some of the inversion methods can be accompanied by more accurate forward simulations using 'full physics' to evaluate the quality of the match derived in each iteration).

To a certain extent, both GTTI and the SLEP methods account for changing pressure/velocity distribution during the forward simulation, and thereby changing streamline distribution. For GTTI, pressure updates are implicitly accounted for because an optimal time-shift for the whole production curve is obtained, and because the sensitivities are calculated for the different pressure steps by the respective streamline distributions. For the early SLEP methods one or a few representative streamline distributions are used. However, for the association of the breakthrough of individual streamlines to increments in fractional-flow curves, it is implicitly assumed that the streamline trajectories are fixed in time. Exactly how information from more than one streamline distribution should be used seems to be a subjective implementation issue in the earlier approaches of SLEP. On the other hand, the more recent SLEP approach of Fenwick et al. [53] uses different streamline distributions to match different parts of the production curve (see (72)), which is similar to how sensitivities are obtained in GTTI. Moreover, multiple streamline distribution can be used in the AHM approach to guide the manual modifications.

Assessment of uncertainties in history-matching is particularly important for the purpose of predictions. This often requires a vast number of realizations and forward simulations. Properly implemented streamline simulators can be much faster than conventional finite-difference simulators, see e.g., [122], and is therefore well suited for this purpose. However, streamline simulators are under some conditions considered approximate simulators, even though the physics to be accounted for and the robustness of streamline simulators have improved considerably recently [40]. An alternative may then be to run a vast number of forward runs with a fast "approximate" simulator (i.e., streamline simulator), and a small number with the slower trusted simulator for calibration [108].

Convergence Properties. Both the original and the generalized travel-time inversion have shown quasilinear properties, while traditional amplitude matching exhibits orders of magnitude more non-linear behavior [34]. Most of the SLEP approaches are of travel-time type since the mismatch in arrival time of saturation fronts (breakthrough) are matched. However, multiple data points are usually incorporated for SLEP. On the other hand, the modifications in (69) and (70) are of amplitude type. Whether the different SLEP approaches share similar convergence properties or not, has not yet been addressed systematically. However, fast convergence is at least observed for the very simple test examples in the early travel-time-like SLEP approaches [121, 141].

Types of Data to be Matched. What kind of data can be incorporate and what kind of reservoir parameters can be modified by the different methods? For SLEP methods, water-cut, total well rate, pressure drops, and saturation-front (from seismics) have been incorporated. The parameters matched, are so far restricted to permeability, porosity, or permeability-porosity ratio, mainly because the approximation $t \propto \tau \propto \phi/k$ is heavily exploited in the SLEP methods. However, other quantities involved in the expressions relating streamline-effective properties with the data, like the end-point mobility ratio or residual saturations (see e.g., Eq. 13 in [121]), may be matched for each producer region.

For GTTI, on the other hand, tracer concentration, fractional-flow, and gas-oil ratio data have been incorporated. For these quantities, arrival-time sensitivities of some contributing quantity can be computed and related to the time-of-flight. Thus, it is the time-of-flight sensitivities that determine which reservoir parameters that can be modified: permeability, porosity, and relative permeability curves (mobility ratios), see Section 4.2. The matrix system in (47) is quite general, so as long as sensitivities relating mismatch in data and perturbations in reservoir parameters can be computed, any data type can potentially be incorporated. The Bayesian system in (56) is also general, but requires in addition a specification of a covariance structure for the reservoir parameters. A weakness of the current GTTI formulation is that well pressure has not yet been incorporated. It may be especially important to constrain jointly on pressure observations and other dynamic data when free gas is present. Streamline-based sensitivities can be obtain analytically for several reservoir responses, based on a single forward simulation, but streamline-based well/grid-pressure sensitivities have not been derived. However, sensitivities for the response of the propagation of a sharp 'pressure front' is derived, see Section 4.7. In Appendix G we outline two potential approaches for obtaining well-pressure sensitivities, which will allow for incorporating well pressures in GTTI.

Finally, the literature contains three papers that discuss how time-lapse seismics can be incorporated. The method in [130] is within the sequential self-calibration scope, the method described in [89] is inspired by the SLEP methods, while the method described in [136] is derived within the TTI scope.

Finally, we will just refer to a few papers [12, 54, 55] presenting streamline-based history-matching work flows applied to real field cases.

References

[1] J. E. Aarnes, V. Kippe, and K.-A. Lie. Mixed multiscale finite elements and streamline methods for reservoir simulation of large geomodels. *Adv. Water Resour.*, 28(3):257–271, 2005.

[2] J. E. Aarnes, T. Gimse, and K.-A. Lie. *Geometrical Modeling, Numerical Simulation, and Optimization: Industrial Mathematics at SINTEF*, chapter An introduction to the numerics of flow in porous media using Matlab, pages 265–306. Springer Verlag, 2007.

[3] B. Agarwal and M. J. Blunt. Streamline-based method with full-physics forward simulation for history-matching performance data of a North Sea field. *SPE J.*, 8(2):171–180, June 2003.

[4] B. Agarwal and M. J. Blunt. A streamline-based method for assisted history matching applied to an Arabian Gulf field. *SPE J.*, 9(4):437–449, December 2004.

[5] M. Al-Harbi, H. Cheng, Z. He, and A. Datta-Gupta. Streamline-based productoin data integration in naturally fractured reservoirs. *SPE J.*, 10(4):426–439, December 2005.

[6] A. Al-Huthali and A. Datta-Gupta. Streamline simulation of counter-current imbibition in naturally fractured reservoirs. *J. Petrol. Sci. Eng.*, 43:271–300, 2004.

[7] A.H. Al-Huthali, D. Oyerinde, and A. Datta-Gupta. Optimal waterflood management using rate control. In *SPE Annual Technical Conference and Exhibition*, San Antonio, Texas, USA, 24–27 September 2006. SPE 102478.

[8] F. Anterion, R. Eymard, and B. Karcher. Use of parameter gradients for reservoir history matching. In *SPE Symposium on Reservoir Simulation*, Houston, Texas, USA, 6–8 February 1989. SPE 18433.

[9] E. Arroyo-Negrete, D. Devegowda, A. Datta-Gupta, and J. Choe. Streamline assisted ensemble Kalman filter for rapid and continuous reservoir model updating. In *International Oil & Gas Conference and Exhibition in China*, Beijing, China, 5–7 December 2006. SPE 104255.

[10] R. Aster, B. Borchers, and C. Thurber. *Parameter Estimation and Inverse Problems (International Geophysics)*. Academic Press, 2004.

[11] H. Ates, A. Bahar, S. El-Abd, M. Charfeddine, M. Kelkar, and A. Datta-Gupta. Ranking and upscaling of geostatistical reservoir models by use of streamline simulation: A field case study. *SPE REE.*, 8(1):22–32, February 2005.

[12] R.O. Baker. Streamline technology: reservoir history matching and forecasting = its success, limitations, and future. *J. of Canadian Petroleum Technology, Distinguished Author Series*, 40(4):23–27, April 2001.

[13] R.O Baker, F. Kuppe, S. Chugh, R. Bora, S. Stojanovic, and R. Batycky. Full-field modeling using streamline based simulation: Four case studies. *SPE REE.*, 5(2):126–134, April 2002.

[14] J.W. Barker, M. Cuypers, and L. Holden. Quantifying uncertainty in production forecasts: Another look at the PUNQ-S3 problem. *SPE J.*, 6(4):433–441, December 2001.

[15] I. Barman, A. Ouenes, and M. Wang. Fractured reservoir characterization using streamline-based inverse modeling and artificial intelligence tools. In *SPE Annual Technical Conference and Exhibition*, Dallas, Texas, USA, 1–4 October 2000. SPE 63067.

[16] M. Barthelemy, D.H. Fenwick, Y. Gautier, and M.J. Blunt. A fremawork for history matching using local optimization in streamline defined regions. In *SPE Annual Technical Conference and Exhibition*, Houston, Texas, USA, 26–29 September 2004. SPE 90137.

[17] R.P. Batycky. *A Three-Dimensional Two-Phase Field-Scale Streamline Simulator*. PhD thesis, Stanford University, Dept. of Petroleum Engineering, 1997.

[18] J. Bear. *Dynamics of Fluids in Porous Media*. American Elsevier, New York, 1972.

[19] F. Bratvedt, K. Bratvedt, C.F. Buchholz, T. Gimse, H. Holden, L. Holden, and N.H. Risebro. A new front-tracking method for reservoir simulation. *SPE Reservoir Eng.*, pages 107–116, February 1992.

[20] F. Bratvedt, K. Bratvedt, C.F. Buchholz, T. Gimse, H. Holden, L. Holden, and N.H. Risebro. Frontline and Frontsim: two full-scale, two-phase, black oil reservoir simulators

based on front tracking. *Surv. Math. Ind.*, 3:185–215, 1993.

[21] F. Bratvedt, K. Bratvedt, C.F. Buchholz, T. Gimse, H. Holden, L. Holden, R. Olufsen, and N.H. Risebro. Three-dimensional reservoir simulation based on front tracking. In Norwegian Institute of Technology, editor, *North Sea Oil and Gas Reservoirs – III*, pages 247–257. Kluwer Academic Publishers, 1994.

[22] F. Bratvedt, T. Gimse, and C. Tegnander. Streamline computations for porous media flow including gravity. *Transp. Porous Media*, 25:63–78, 1996.

[23] R. Brauchler, R. Liedl, and P. Dietrich. A travel time based hydraulic tomographic approach. *Water Resour. Res.*, 39(12):1370, 2003. doi: 10.1029/2003WR002262.

[24] J. Caers. Adding local accuracy to direct sequential simulation. *Math. Geol.*, 32(7): 815–850, 2000.

[25] J. Caers. Efficient gradual deformation using a streamline-based proxy method. *J. Petrol. Sci. Eng.*, 39(1–2):57–83, 2003.

[26] J. Caers, S. Krishnan, Y. Wang, and A.R. Kovscek. A geostatistical approach to streamline-based history matching. *SPE J.*, 7(3):250–266, September 2002.

[27] J. Caers, H. Gross, and A.R. Kovscek. A direct sequential simulation approach to streamline-based history matching. In *Proceedings of the 2004 International Geostatistics Congress*, Banff, Canada, 26 September – 1 October 2004.

[28] J.E. Capilla, J.J. Gómez-Hernánez, and A. Sahuquillo. Stochastic simulation of transmissivity fields conditional to both transmissivity and piezometric data 2. Demonstration on a synthetic aquifer. *J. Hydrol.*, 203:175–188, 1997.

[29] A. Chakravarty, D.B. Liu, and W. Scott Meddaugh. Application of 3D streamline methodology in the saladin reservoir and other studies. In *SPE Annual Technical Conference and Exhibition*, Dallas, Texas, USA, 1–4 October 2000. SPE 63154.

[30] G. Chavent, M. Dupuy, and P. Lemonnier. History matching by use of optimal theory. *SPE J.*, 15(1):74–86, February 1975.

[31] A. Chen and T. Hou. A mixed multiscale finite element method for elliptic problems with oscillating coefficients. *Math. Comp.*, 72(242):541–576, 2002.

[32] W.H. Chen, G.R. Gavalas, J.H. Seinfeld, and M.L. Wasserman. A new algorithm for automatic history matching. *SPE J.*, 14(6):593–608, December 1974.

[33] H. Cheng, X.-H. Wen, W.J. Milliken, and A. Datta-Gupta. Field experiences with assisted and automatic history matching using streamline models. In *SPE Annual Technical Conference and Exhibition*, Houston, Texas, USA, 26–29 September 2004. SPE 89857.

[34] H. Cheng, A. Datta-Gupta, and Z. He. A comparison of travel-time and amplitude matching for field-scale production-data integration: Sensitivity, nonlinearity, and practical implications. *SPE J.*, 10(1):75–90, March 2005.

[35] H. Cheng, A. Kharghoria, Z. He, and A. Datta-Gupta. Fast history matching of finite-difference models using streamline-derived sensitivities. *SPE Reserv. Eval. Eng.*, 8(5): 426–436, October 2005.

[36] H. Cheng, I. Osako, and A. Datta-Gupta. A rigorous compressible streamline formulation for two- and three-phase black-oil simulation. *SPE J.*, 11(4):407–417, December 2006.

[37] H. Cheng, D. Oyerinde, A. Datta-Gupta, and W. Milliken. Compressible streamlines and three-phase history matching. In *SPE/DOE Symposium on Improved Oil Recovery*, Tulsa, Oklahoma, USA, 22–26 April 2006. SPE 99465.

[38] C. Cordes and W. Kinzelbach. Continous groundwater velocity fields and path lines in linear, bilinear, and trilinear finite elements. *Water Resour. Res.*, 28(11):2903–2911, 1992.

[39] L.P. Dake. *Fundamentals of Reservoir Engineering*. Elsevier, 1978.

[40] A. Datta-Gupta and M. J. King. *Streamline Simulation: Theory and Practice*. SPE Textbook Series. to appear.

[41] A. Datta-Gupta and M.J. King. A semianalytic approach to tracer flow modeling in heterogeneous permeable media. *Adv. Water Resour.*, 18:9–24, 1995.

[42] A. Datta-Gupta, K.N. Kulkarni, S. Yoon, and D.W. Vasco. Streamlines, ray tracing and production tomography: Generalization to compressible flow. *Petrol. Geosci.*, 7: 75–86, 2001.

[43] A. Datta-Gupta, S. Yoon, D.W. Vasco, and G.A. Pope. Inverse modeling of partitioning interwell tracer tests: A streamline approach. *Water Resour. Res.*, 38(6), 2002. doi:10.1029/2001WR000597.

[44] P. Dellaportas and G. O. Roberts. An introduction to MCMC. In J. Møller, editor, *Spatial Statistics and Computational Methods*, number 173 in Lecture Notes in Statistics, pages 1–41. Springer, Berlin, 2003.

[45] D. Devegowda, E. Arroyo-Negrete, A. Datta-Gupta, and S.G. Douma. Efficient and robust reservoir model updating using ensemble Kalman filter with sensitivity-based covariance localization. In *SPE Reservoir Simulation Symposium*, Houston, Texas, USA, 26–28 February 2007. SPE 106144.

[46] G. Di Donato, W. Huang, and M. Blunt. Streamline-based dual porosity simulation of fractured reservoirs. In *SPE Annual Technical Conference and Exhibition*, Denver, Colorado, USA, 5–8 October 2003. SPE 84036.

[47] A. Doucet, N. de Freitas, and N. Gordon. *Sequential Monte Carlo Methods in Practice*. Springer, 2001.

[48] H. Dykstra and R.L. Parsons. The prediction of oil recovery by waterflood, secondary recovery of oil in the United States, principles and practice, second ed. Technical report, American Petroleum Institute, Dallas, Texas, 1950.

[49] A.S. Emanuel and W.J. Milliken. History matching finite difference models with 3D streamlines. In *SPE Annual Technical Conference and Exhibition*, New Orleans, Louisiana, USA, 27–30 September 1998. SPE 49000.

[50] G. Evensen. Sequential data assimilation with a nonlinear quasi-geostrophic model using Monte Carlo methods to forecast error statistics. *J. Geophys. Res.*, 99(C5):10143–10162, 1994.

[51] G. Evensen. *Data Assimilation: The Ensemble Kalman Filter*. Springer, 2007.

[52] G. Evensen, J. Hove, H.C. Meisingset, E. Reiso, K.S. Seim, and O. Espelid. Using the EnKF for assisted history matching of a North Sea reservoir model. In *SPE Reservoir Simulation Symposium*, Houston, Texas, USA, 26–28 February 2007. SPE 106184.

[53] D. Fenwick, M. Thiele, M. Agil, A. Hussain, F. Humam, and J. Caers. Reconciling prior geologic information with production data using streamlines: Application to a giant Middle-Eastern oil field. In *SPE Annual Technical Conference and Exhibition*, Dallas, Texas, USA, 9–12 October 2005. SPE 95940.

[54] M. Galacho, P. Vázquez, V. Pací, G. Fernández, and C. Canosa. Streamline-based global history matching for geological modeling calibration, application to a giant fluvio-lacustrine sandstones reservoir field. In *SPE Latin American and Caribbean Petroleum Engineering Conference*, Rio de Janeiro, Brazil, 20–23 June 2005. SPE 94815.

[55] M. Galacho, P. Vázquez, G. Laiz, A. Krittian, F. Gutiérrez, and V. Pací. Streamline-based integral modeling for waterflooding design optimization, surveillance and monitoring. In *Latin American & Caribbean Petroleum Engineering Conference*, Buenos Aires, Argentina, 15–18 April 2007. SPE 107831.

[56] G. Gao, M. Zafari, and A.C. Reynolds. Quantifying uncertainty for the PUNQ-S3 problem in a Bayesian setting with RML and EnKF. *SPE J.*, 11(4):506–515, December 2006.

[57] G. Gao, G. Li, and A.C. Reynolds. A stochastic optimization algorithm for automatic history matching. *SPE J.*, 12(2):196–208, June 2007.

[58] Y. Gautier, F. Roggero, and B. Nœtinger. Computation of gradients based on a streamline method. application to history matching. In *8th ECMOR*, Freiberg, Germany, 3–6 September 2002.

[59] Y. Gautier, B. Nœtinger, and F. Roggero. History matching using a streamline-based approach and gradual deformation. *SPE J.*, 9(1):88–101, March 2004.

[60] Robert H. J. Gmelig Meyling. A characteristic finite element method for solving nonlinear convection-diffusion equations on locally refined grids. In D. Guerillot and O. Guillon, editors, *2nd European Conference on the Mathematics of Oil Recovery*, pages 255–262, Arles, France, Sept 11-14 1990. Editions Technip.

[61] Robert H. J. Gmelig Meyling. Numerical methods for solving the nonlinear hyperbolic equations of porous media flow. In *Third International Conference on Hyperbolic Problems, Vol. I, II (Uppsala, 1990)*, pages 503–517. Studentlitteratur, Lund, 1991.

[62] J.J. Gómez-Hernánez, A. Sahuquillo, and J.E. Capilla. Stochastic simulation of transmissivity fields conditional to both transmissivity and piezometric data - I. Theory. *J. Hydrol.*, 203(1–4):162–174, 1997.

[63] H. Gross. *History matching production data using streamlines and geostatistics*. PhD thesis, Stanford University, Dept. of Petroleum Engineering, 2006.

[64] H. Gross. History-matching multiple attributes with streamlines and statistics. In *SPE Annual Technical Conference and Exhibition*, San Antonio, Texas, USA, 24–27 September 2006. SPE 106520-STU.

[65] H. Gross, M.R. Thiele, M.J. Alexa, J.K. Caers, and A.R. Kovscek. Streamline-based history matching using geostatistical constraints: Application to a giant, mature carbonate reservoir. In *SPE Annual Technical Conference and Exhibition*, Houston, Texas, USA, 26–29 September 2004. SPE 90069.

[66] H. Hægland, H. K. Dahle, G. T. Eigestad, K.-A. Lie, and I. Aavatsmark. Improved streamlines and time-of-flight for streamline simulation on irregular grids. *Adv. Water Resour.*, 30(4):1027–1045, 2007.

[67] Z. He, S. Yoon, and A. Datta-Gupta. Streamline-based production data integration with gravity and changing field conditions. *SPE J.*, 7(4):423–436, December 2002.

[68] Z. He, H. Parikh, A. Datta-Gupta, J. Perez, and T. Pham. Identifying reservoir compartmentalization and flow barriers from primary production using streamline diffusive time of flight. *SPE J.*, 7(3):238–247, June 2004.

[69] Z. He, A. Datta-Gupta, and D.W. Vasco. Rapid inverse modeling of pressure interference tests using trajectory-based traveltime and amplitude sensitivities method. *Water Resour. Res.*, 42(W03419), 2006. doi:10.1029/2004WR003783.

[70] B.K. Hegstad and H. Omre. Uncertainty in production forecasts based on well observations, seismic data, and production history. *SPE J.*, 6(4):409–424, December 2001.

[71] B.T. Hoffman and J. Caers. Regional probability perturbations for history matching. *J. Petrol. Sci. Eng.*, 46:53–71, 2005.

[72] D. Hohl, E.A. Jimenez, and A. Datta-Gupta. Field experiences with history matching an offshore turbiditic reservoir using inverse modeling. In *SPE Annual Technical Conference and Exhibition*, San Antonio, Texas, USA, 24–27 September 2006. SPE 101983.

[73] H. Holden and N.H. Risebro. *Front Tracking for Hyperbolic Conservation Laws*, volume 152 of *Applied Mathematical Sciences*. Springer, New York, 2002.

[74] L.Y. Hu, G. Blanc, and B. Nœtinger. Gradual deformation and iterative calibration of sequential stochastic simulations. *Math. Geol.*, 33:375–489, 2001.

[75] E.A. Idrobo, M.K. Choudhary, and A. Datta-Gupta. Swept volume calculations and ranking of geostatistical reservoir models using streamline simulation. In *SPE/AAPG Western Regional Meeting*, Long Beach, California, USA, 19–23 June 2000. SPE 62557.

[76] P.A. Illiassov and A. Datta-Gupta. Field-scale characterization of permeability and saturation distribution using partitioning tracer tests: The Ranger field, Texas. *SPE J.*, 7(4):409–422, December 2002.

[77] M. Jang. 3D aquifer characterization using stochastic streamline calibration. *Adv. Water Resour.*, 30(3):420–429, 2007.

[78] M. Jang and J. Choe. An inverse system for incorporation of conditioning to pressure and streamline-based calibration. *J. Contam. Hydrol.*, 69(1–2):139–156, 2004.

[79] E. Jimenez, K. Sabir, A. Datta-Gupta, and M.J. King. Spatial error and convergence in streamline simulation. *SPE J.*, 10(3):221–232, June 2007.

[80] R.A. Johnson and D.W. Wichern. *Applied Multivariate Statistical Analysis, 6th edition*. Prentice Hall, 2007.
[81] A.G. Journel. Geostatistics: Roadblocks and challenges. In Soares, editor, *Geostatistics Troia '92*, volume 1. Kluwer Publ., 1993.
[82] A.G. Journel. Modelling uncertainty: Some conceptual thoughts. In Dimitrakopoulos, editor, *Geostatistics for the next century*. Kluwer Publ., 1993.
[83] R. Juanes and K.-A. Lie. Numerical modeling of multiphase first-contact miscible flows. Part 1. analytical Riemann solver. *Transp. Porous Media*, 67(3):375–393, April 2007.
[84] R. Juanes and K.-A. Lie. Numerical modeling of multiphase first-contact miscible flows. Part 2. analytical Riemann solver. *Transp. Porous Media*, to appear. doi: 10.1007/s11242-007-9139-y.
[85] M.J. King and A. Datta-Gupta. Streamline simulation: A current perspective. *In Situ*, 22(1):91–140, 1998.
[86] M.J. King, I. Osako, and A. Datta-Gupta. A predictor–corrector formulation for rigourous streamline simulation. *Int. J. Numer. Meth. Fluids*, 47:739–758, 2005.
[87] P.K. Kitanidis. Quasi-linear geostatistical theory for inversing. *Water Resour. Res.*, 31 (10):2411–2419, October 1995.
[88] A. Kozlova, F. Bratvedt, K. Bratvedt, and A. Myasnikov. A three-phase compressible dual-porosity model for streamline simulation. In *SPE Annual Technical Conference and Exhibition*, San Antonio, Texas, USA, 24–27 September 2006. SPE 102549.
[89] V. Kretz, B. Valles, and L Sonneland. Fluid front history matching using 4D seismic and streamline simulation. In *SPE Annual Technical Conference and Exhibition*, Houston, Texas, USA, 26–29 September 2004. SPE 90136.
[90] S. Krishnamurthy and M. Gerritsen. A variable relaxation scheme for multiphase, multicomponent flow. *Transp. Porous Media*, to appear. doi: 10.1007/s11242-007-9130-7.
[91] K.N. Kulkarni and A. Datta-Gupta. Estimating relative permeability from production data: A streamline approach. *SPE J.*, 5(4):402–411, December 2000.
[92] K.N. Kulkarni, A. Datta-Gupta, and D.W. Vasco. A streamline approach for integrating transient pressure data into high-resolution reservoir models. *SPE J.*, 6(3):273–282, September 2001.
[93] A.M. LaVenue and B.S. RamaRao. Pilot point methodology for automated calibration of an ensemble of conditionally simulated transmissivity fields 2. Application. *Water Resour. Res.*, 31(3):495–516, March 1995.
[94] R. Li, A.C. Reynolds, and D.S. Oliver. History matching of three-phase flow production data. *SPE J.*, 8(4):328–340, December 2003.
[95] K.-A. Lie. Streamline-based history matching: a literature survey. SINTEF Report STF42 F02027, SINTEF Applied Mathematics, 2002.
[96] N. Liu and D.S. Oliver. Evaluation of Monte Carlo methods for assessing uncertainty. *SPE J.*, 8(2):188–195, June 2003.
[97] T. Lolomari, K. Bratvedt, M. Crane, William J, Milliken, and J.J. Tyrie. The use of streamline simulation in reservoir management: Methodology and case studies. In *SPE Annual Technical Conference and Exhibition*, Dallas, Texas, USA, 1–4 October 2000. SPE 63157.
[98] X. Ma, M. Al-Harbi, A. Datte-Gupta, and Y. Efendiev. A multistage sampling method for rapid quantification of uncertainty in history matching geological models. In *SPE Annual Technical Conference and Exhibition*, San Antonio, Texas, USA, 24–27 September 2006. SPE 102476.
[99] B.T. Mallison, M.G. Gerritsen, K. Jessen, and F.M. Orr Jr. High order upwind schemes for two-phase, multicomponent flow. *SPE J.*, 10(3):297–311, September 2005.
[100] B.T. Mallison, M.G. Gerritsen, and S.F. Matringe. Improved mappings for streamline-based simulation. *SPE J.*, 11(3):294–302, September 2006.
[101] C. Maschio and D.J. Schiozer. Assisted history matching using streamline simulation. *Petrol. Sci. Tech.*, 23(7–8):761–774, 2005.

[102] S.F. Matringe and M.G. Gerritsen. On accurate tracing of streamlines. In *SPE Annual Technical Conference and Exhibition*, Houston, Texas, USA, 26-29 September 2004. SPE 89920.

[103] S.F. Matringe, R. Juanes, and H.A. Tchelepi. Streamline tracing on general triangular or quadrilateral grids. *SPE J.*, 12(2):217–233, June 2007.

[104] W.J. Milliken, A.S. Emanuel, and A. Chakravarty. Application of 3-D streamline simulation to assist history matching. In *SPE Annual Technical Conference and Exhibition*, Dallas, Texas, USA, 1–4 October 2000. SPE 63155.

[105] G. Nævdal, L.M. Johnsen, S.I. Aanonsen, and E.H. Vefring. Reservoir monitoring and continuous model updating using ensemble Kalman filter. *SPE J.*, 10(1):66–74, March 2005.

[106] Combination of Dependent Realizations Within the Gradual Deformation Method. L.y. hu. *Math. Geol.*, 34(8):953–963, 2002.

[107] D.S. Oliver and N. He. Conditioning permeability fields to pressure data. In *Proceedings of the 5th European Conference on the Mathematics of Oil Recovery (ECMOR)*, Leoben, Austria, 3–6 September 1996.

[108] H. Omre and O.P. Lødøen. Improved production forecasts and history matching using approximate fluid-flow simulators. *SPE J.*, 9(3):339–351, September 2004.

[109] I. Osako and A. Datta-Gupta. A compositional streamline formulation with compressibility effects. In *SPE Reservoir Simulation Symposium*, Houston, Texas, USA, 26-28 February 2007. SPE 106148.

[110] C.C. Paige and M.A. Saunders. Lsqr: An algorithm for sparse linear equations and sparse least squares. *ACM Transactions on Mathematical Software*, 8(1):43, March 1982.

[111] S. Peddibhotla, A. Datta-Gupta, and G. Xue. Multiphase streamline modeling in three dimensions: Further generalizations and a field application. In *SPE Reservoir Simulation Symposium*, Dallas, Texas, USA, 8–11 June 1997. SPE 38003.

[112] D.W. Pollock. Semianalytical computation of path lines for finite-difference models. *Ground Water*, 26(6):743–750, 1988.

[113] M. Prevost, M.G. Edwards, and M.J. Blunt. Streamline tracing on curvilinear structured and unstructured grids. *SPE J.*, 7(2):139–148, June 2002.

[114] H. Qassab, M. Khalifa, R. Pavlas, N. Afaleg, H. Ali, A. Kharghoria, Z. He, S.H. Lee, and A. Datta-Gupta. Streamline-based production data integration under realistic field conditions: Experience in a giant Middle-Eastern reservoir. In *SPE Annual Technical Conference and Exhibition*, Denver, Colorado, USA, 5-8 October 2003. SPE 84079.

[115] B.S. RamaRao and A.M. LaVenue. Pilot point methodology for automated calibration of an ensemble of conditionally simulated transmissivity fields 1. Theory and computational experiments. *Water Resour. Res.*, 31(3):475–493, March 1995.

[116] M. Le Ravalec-Dupin and D.H. Fenwick. A combined geostatistical and streamline-based history matching procedure. In *SPE Annual Technical Conference and Exhibition*, San Antonio, Texas, USA, 29 September–2 October 2002. SPE 77378.

[117] F. Roggero and L.Y. Hu. Gradual deformation of continuous geostatistical models for history matching. In *SPE Annual Technical Conference and Exhibition*, New Orleans, Louisiana, USA, 27-30 September 1998. SPE 49004.

[118] M. Sambridge. Geophysical inversion with a neighbourhood algorithm –I. Searching a parameter space. *Geophys. J. Int.*, 138:479–494, 1999.

[119] A. F. M. Smith and G. O. Roberts. Bayesian computation via the Gibbs sampler and related Markov chain Monte Carlo methods (with discussion). *JRSSB*, 55:3–23, 1993.

[120] J.C. Spall. Multivariate stochastic approximation using a simultaneous perturbation gradient approximation. *IEEE Transactions on Automatic Control*, 37:332–341, 1992.

[121] V.R. Stenerud and K.-A. Lie. A multiscale streamline method for inversion of production data. *J. Petrol. Sci. Eng.*, 54:72–92, 2006. doi:10.1016/j.petrol.2006.08.003.

[122] V.R. Stenerud, V. Kippe, K.-A. Lie, and A. Datta-Gupta. Multiscale-streamline simulation and dynamic data integration for high-resolution subsurface models. *Water Resour. Res.*, submitted.

[123] V.R. Stenerud, K.-A. Lie, and V. Kippe. Generalized travel-time inversion on unstructured grids. *J. Petrol. Sci. Eng.*, submitted.

[124] V.R. Stenerud, V. Kippe, K.-A. Lie, and A. Datta-Gupta. Adaptive multiscale streamline simulation and inversion for high-resolution geomodels. *SPE J.*, to appear.

[125] A. Tarantola. *Inverse Problem Theory and Methods for Model Parameter Estimation*. SIAM, 2005. ISBN 0-89871-572-5.

[126] M.R. Thiele. Streamline simulation. In *6th International Forum on Reservoir Simulation*, Schloss Fuschl, Austria, 3–7 September 2001.

[127] M.R. Thiele. Streamline simulation. In *8th International Forum on Reservoir Simulation*, Stresa / Lago Maggiore, Italy, 20–24 June 2005.

[128] M.R. Thiele, R.P. Batycky, and M.J. Blunt. A streamline-based 3d field-scale compositional reservoir simulator. In *SPE Annual Technical Conference and Exhibition*, San Antonio, Texas, USA, 5–8 October 1997. SPE 38889.

[129] H. Tjelmeland and J. Besag. Markov random fields with higher-order interactions. *Scand. J. Statist.*, 25(3):415–433, 1998.

[130] T.T. Tran, X.-H. Wen, and R.A. Behrens. Efficient conditioning of 3D fine-scale reservoir model to multiphase production data using streamline-based coarse-scale inversion and geostatistical downscaling. *SPE J.*, 6(4):364–374, December 2001.

[131] G. Valenti, K. Jessen, B.T. Mallison, and M.G. Gerritsen. High-order upwind schemes for three-phase multicomponent flows, a preliminary investigation. In *SPE Annual Technical Conference and Exhibition*, Houston, Texas, USA, 26–29 September 2004. SPE 90594.

[132] D.W. Vasco and A. Datta-Gupta. Asymptotics, streamlines and reservoir modeling: A pathway to production tomography. *The Leading Edge, Special Issue on Reservoir Modeling*, pages 91–140, October 2001.

[133] D.W. Vasco and A. Datta-Gupta. Asymptotics, saturation fronts, and high resolution reservoir characterization. *Transp. Porous Media*, 42:315–350, 2001.

[134] D.W. Vasco and A. Datta-Gupta. Asymptotic solutions for solute transport: A formalism for tracer tomography. *Water Resour. Res.*, 35(1):1–16, 1999.

[135] D.W. Vasco, S. Yoon, and A. Datta-Gupta. Integrating dynamic data into high-resolution models using streamline-based analytic sensitivity coefficients. *SPE J.*, 4 (4):389–399, December 1999.

[136] D.W. Vasco, A. Datta-Gupta, R. Behrens, P. Condon, and J. Rickett. Seismic imaging of reservoir flow properties: Time-lapse amplitude changes. *Geophysics*, 69(6):1425–1442, November–December 2004.

[137] L. Vega. *An Efficient Bayesian Formulation for Production Data Integration*. PhD thesis, Texas A&M University, College Station, Texas, USA, 2003.

[138] L. Vega, D. Rojas, and A. Datta-Gupta. Scalability of the deterministic and Bayesian approaches to production data integration. *SPE J.*, 9(3):330–338, September 2004.

[139] O. Vignes. *Application of optimization methods in oil recovery problems*. PhD thesis, Norwegian Institute of Technology, 1993. Dr.Ing. thesis.

[140] Y. Wang. *Streamline approaches for integrating production history with geologic information in reservoir models*. PhD thesis, Stanford University, Dept. of Petroleum Engineering, 2002.

[141] Y. Wang and A.R. Kovscek. A streamline approach to history matching production data. *SPE J.*, 5(4):353–362, December 2000.

[142] Y. Wang and A.R. Kovscek. Integrating production history into reservoir models using streamline-based time-of-flight ranking. *Petrol. Geosci.*, 9(2):163–174, 2003.

[143] X.-H. Wen, C.V. Deutsch, and A.S. Cullick. Integrating pressure and fractional flow data in reservoir modeling with fast streamline-based inverse method. In *SPE Annual Technical Conference and Exhibition*, New Orleans, Louisiana, USA, 27-30 September 1998. SPE 48971.

[144] X.-H. Wen, C.V. Deutsch, and A.S. Cullick. High-resolution reservoir models integrating multiple-well production data. *SPE J.*, 3(4):344–355, December 1998.

[145] X.-H. Wen, J.E. Capilla, C.V. Deutsch, J.J. Gómez-Herández, and A. S. Cullick. A program to create permeability fields that honor single-phase flow rate and pressure data. *Computers & Geosciences*, 25:217–230, 1999.
[146] X.-H. Wen, C.V. Deutsch, and A.S. Cullick. Construction of geostatistical aquifer models integrating dynamic flow and tracer data using inverse technique. *J. Hydrol.*, 255(1–4):151–168, 2002.
[147] X.-H. Wen, C.V. Deutsch, and A.S. Cullick. Inversion of dynamic production data for permeability: Fast streamline-based computation of sensitivity coefficients of fractional flow rate. *J. Hydrol.*, 281:296–312, 2003.
[148] Z. Wu and A. Datta-Gupta. Rapid history matching using a generalized travel-time inversion method. *SPE J.*, 7(2):113–122, June 2002.
[149] Z. Wu, A.C. Reynolds, and D.S. Oliver. Conditioning geostatistical models to two-phase production data. *SPE J.*, 4(2):142–155, June 1999.
[150] S. Yoon, A.H. Malallah, A. Datta-Gupta, D.W. Vasco, and R.A. Behrens. A multiscale approach to production-data integration using streamline models. *SPE J.*, 6(2):182–192, June 2001.
[151] D.A. Zimmerman, G. de Marsily, C.A. Gotway, M.G. Marietta, C.L. Axness, and et al. A comparison of seven geostatistically based inverse approaches to estimate transmissivities for modeling advective transport by groundwater flow. *Water Resour. Res.*, 34 (6):1373–1413, June 1998.

Appendix A. Sensitivities for Relative Permeability

In Section 4.2 we presented time-of-flight sensitivities for various reservoir parameters. Kulkarni and Datta-Gupta [91] derived similar sensitivities for parameters involved in describing relative permeability curves. They present sensitivities for two different representations of the relative permeability curves.

In the first case, the oil and water relative permeability are represented by power functions (Corey curves)

$$k_{ro} = k^o_{ro} S^{\alpha_o}_{no}, \qquad k_{rw} = k^o_{rw} S^{\alpha_w}_{nw}.$$

Here $S_{n\alpha}$ is the normalized saturation and $k^o_{r\alpha}$ is the end-point relative permeability.

Alternatively, one may use a B-spline expansion for each curve. This gives more flexibility to the function representation because the assumption of a particular shape of the function is relaxed. For oil, the B-spline expansion is given by

$$k_{ro} = \sum_{j=1}^{N} c_{o,j} B^m_{o,j}(S_{no}),$$

where $c_{o,j}$ is the jth B-spline coefficient and $B^m_{w_j}(S_{no})$ is the jth B-spline of polynomial order m. A similar B-spline representation is used for the relative permeability functions of water.

Considering the relative permeability functions for oil we obtain the following sensitivities for slowness $s(\mathbf{x})$, given by (20), with respect to k^o_{ro}, α_o and $c_{o,j}$

$$\begin{aligned}
\frac{\partial s}{\partial k^o_{ro}} &= \frac{\partial s}{\partial \lambda_t}\frac{\partial \lambda_t}{\partial k^o_{ro}} = -\frac{s}{\lambda_t}\frac{S^{\alpha_o}_{no}}{\mu_o}, \\
\frac{\partial s}{\partial \alpha_o} &= \frac{\partial s}{\partial \lambda_t}\frac{\partial \lambda_t}{\partial \alpha_o} = -\frac{s}{\lambda_t}\frac{k^o_{ro} S^{\alpha_o}_{no} \ln S_{no}}{\mu_o}, \\
\frac{\partial s}{\partial c_{o,j}} &= \frac{\partial s}{\partial \lambda_t}\frac{\partial \lambda_t}{\partial c_{o,j}} = -\frac{s}{\lambda_t}\frac{B^m_{o,j}}{\mu_o},
\end{aligned}$$

where μ_o is the oil viscosity. Similarly, sensitivities are obtained with respect to the parameters for the water relative permeability. Time-of-flight sensitivities can now be obtained by (21).

Appendix B. Gaussian Linearity and Analytic Conditional Distribution

In this section we will show how a conditional Gaussian distribution can be determined analytically for a linear model. To this end, we start by considering a stochastic variable $\mathbf{m} \in \mathbb{R}^p$ from a multivariate Gaussian distribution

$$[\mathbf{m}] \sim \mathcal{N}_p(\mu_m, \mathbf{\Sigma}_{mm}). \tag{A-1}$$

Further, we assume a linear relation $\mathbf{d} = \mathbf{A}\mathbf{m} + \mathbf{u}$ between $\mathbf{m}$ and another stochastic variable $\mathbf{d} \in \mathbb{R}^k$, where $[\mathbf{u}] \sim \mathcal{N}_k(\mathbf{0}, \mathbf{\Sigma}_u)$ is an error term that is assumed to be independent of $\mathbf{m}$. Standard Gaussian theory then gives [80]

$$[\mathbf{d}] \sim \mathcal{N}_k(\mu_d, \mathbf{\Sigma}_{dd}), \tag{A-2}$$

where the expectation and covariance are

$$\mu_d = \mathbf{A}\mu_m, \qquad \mathbf{\Sigma}_{dd} = \mathbf{A}\mathbf{\Sigma}_{mm}\mathbf{A}^T + \mathbf{\Sigma}_u.$$

Further, a combination of (A-1) and (A-2) gives the joint probability distribution

$$\begin{bmatrix} \mathbf{m} \\ \mathbf{d} \end{bmatrix} \sim \mathcal{N}_{p+k}\left(\begin{bmatrix} \mu_m \\ \mu_d \end{bmatrix}, \begin{bmatrix} \mathbf{\Sigma}_{mm} & \mathbf{\Sigma}_{md} \\ \mathbf{\Sigma}_{dm} & \mathbf{\Sigma}_{dd} \end{bmatrix} \right),$$

where $\mathbf{\Sigma}_{dm}$ describes the covariance between $\mathbf{d}$ and $\mathbf{m}$,

$$\mathbf{\Sigma}_{dm} = \mathrm{Cov}\{\mathbf{d}, \mathbf{m}\} = \mathbf{A}\mathbf{\Sigma}_{mm},$$

and $\mathbf{\Sigma}_{md}$ is the transpose of $\mathbf{\Sigma}_{dm}$. Finally, from the joint distribution, the posterior distribution for $\mathbf{m}$ given $\mathbf{d}$ can be derived:

$$[\mathbf{m}|\mathbf{d}] \sim \mathcal{N}_p(\mu_{m|d}, \mathbf{\Sigma}_{m|d}),$$

where the conditional expectation and covariance are

$$\begin{aligned} \mu_{m|d} &= \mu_m + (\mathbf{A}\mathbf{\Sigma}_{mm})^T[\mathbf{A}\mathbf{\Sigma}_{mm}\mathbf{A}^T + \mathbf{\Sigma}_u]^{-1}(\mathbf{d} - \mathbf{A}\mu_m), \\ \mathbf{\Sigma}_{m|d} &= \mathbf{\Sigma}_{mm} - (\mathbf{A}\mathbf{\Sigma}_{mm})^T[\mathbf{A}\mathbf{\Sigma}_{mm}\mathbf{A}^T + \mathbf{\Sigma}_u]^{-1}\mathbf{A}\mathbf{\Sigma}_{mm}. \end{aligned}$$

Computing the inverse of the $(k \times k)$ matrix can be very costly for large k.

Appendix C. One-dimensional upscaling

Assume one-phase flow in a uni-directional system partitioned by $N+1$ nodes into N (sub) cells, with a total length of Δx and a pressure drop of Δp. Further, assume no gravity. For each node there is associated a pressure p_i. The distance between node i and node $i+1$ is denoted Δx_i. The pressure drop over the reservoir is equal to the sum of the pressure drops between two consecutive nodes, i.e., $\Delta p = \Delta p_1 + \Delta p_2 + \ldots + \Delta p_N$, and the total length is $\Delta x = \Delta x_1 + \Delta x_2 + \ldots + \Delta x_N$. An average/effective Darcy velocity over the one-dimensional system is then given by Darcy's law:

$$\bar{u} = -\frac{K}{\mu}\frac{\Delta p}{\Delta x}.$$

Summing the contributions of the subintervals gives

$$-\frac{\bar{u}\Delta x}{K} = \frac{1}{\mu}\Delta p = \frac{1}{\mu}\Big(\Delta p_1 + \Delta p_2 + \ldots + \Delta p_N\Big) = -\left(\frac{u_1\Delta x_1}{K_1} + \frac{u_2\Delta x_2}{K_2} + \ldots + \frac{u_N\Delta x_N}{K_N}\right).$$

Hence the upscaled/effective permeability is given by the following weighted harmonic average

$$K = \frac{\bar{u}\Delta x}{\frac{u_1\Delta x_1}{K_1} + \frac{u_2\Delta x_2}{K_2} + \ldots + \frac{u_N\Delta x_N}{K_N}}.$$

For uni-directional without internal sinks/sources the flow equations state that the velocity is constant ($\nabla \cdot \mathbf{u} = du/dx = 0$), i.e., $\bar{u} = u_1 = u_2 = \ldots = u_N$, which gives

$$K = \frac{\Delta x}{\frac{\Delta x_1}{K_1} + \frac{\Delta x_2}{K_2} + \ldots + \frac{\Delta x_N}{K_N}}. \tag{A-3}$$

Assume instead a set of parallel one-dimensional uni-directional flow systems with a single permeability each (like homogeneous layers or streamlines). The parallel layers are numbered by $i \in \{1, 2, \ldots, N\}$ and have a common pressure drop Δp and length Δx. Similarly as above, Darcy's law over all layers then reads

$$-\frac{KA}{\mu}\frac{\Delta p}{\Delta x} = \bar{q} = q_1 + q_2 + \ldots + q_N = -\frac{1}{\mu}\frac{\Delta p}{\Delta x}\big(K_1A_1 + K_2A_2 + \ldots + K_NA_N\big).$$

The upscaled/effective permeability is therefor given by the weighted arithmetic average

$$K = \frac{1}{A}\big(K_1A_1 + K_2A_2 + \ldots + K_NA_N\big).$$

Appendix D. Modifications for 1D Buckley–Leverett Displacement

In this section we will derive the effective permeability modifications for a 1D Buckley–Leverett displacement. Assuming Riemann initial data, the arrival time t_ℓ of a saturation front S_{wf} is discussed in Section 3.2, that is,

$$t_\ell = \frac{\tau_\ell}{\widetilde{f'}(S_{wf})}.$$

Inserting (20) for the time-of-flight and assuming a streamline effective permeability k_ℓ gives

$$t_\ell = \frac{1}{\widetilde{f'}}\int_\Psi \frac{\phi(\mathbf{x})}{\lambda_t k_\ell |\nabla p|}dr \quad \Leftrightarrow \quad k_\ell = \frac{1}{t_\ell \widetilde{f'}}\int_\Psi \frac{\phi(\mathbf{x})}{\lambda_t|\nabla p|}dr. \tag{A-4}$$

By assuming that the streamline paths of the prior permeability field and the quantities involved in the integral are exact (also assumed in [141]), the relative modifications are then given by

$$r_\ell^t = \frac{\Delta k_\ell^t}{k_\ell^{\text{cal}}} = \frac{k_\ell^{\text{obs}} - k_\ell^{\text{cal}}}{k_\ell^{\text{cal}}} = \frac{t_\ell^{\text{cal}} - t_\ell^{\text{obs}}}{t_\ell^{\text{obs}}}.$$

Hence, (61) is recovered. If also the effective pressure drop Δp for an injector–producer pair is to be matched, we can use an effective pressure gradient of $\Delta p/L_\ell \approx |\nabla p|$, where L_ℓ is the length of streamline ℓ. The relative modification of (64) is then obtained by the same approach.

Appendix E. Analytic Gaussian Upscaling/Downscaling

Assume there are N grid parameters $\mathbf{M} = \{M_i\}$ (possibly transformed) contributing to s effective/upscaled parameters $\mathbf{m} = \{m_\ell\}$. Further, assume that the effective parameter m_ℓ can be calculated by the weighted arithmetic average

$$m_\ell = \frac{1}{\sum_i w_{\ell i}}\Big[w_{\ell 1}M_1 + w_{\ell 2}M_2 + \ldots + w_{\ell N}M_N\Big] + u_\ell, \tag{A-5}$$

where u_ℓ is a random error term that will be described below. Hence, the weights are zero if a grid parameter does not contribute to the effective parameter. All the s effective parameters can then be calculated by

$$\mathbf{m} = \mathbf{A}\mathbf{M} + \mathbf{u}, \tag{A-6}$$

where

$$\mathbf{A} = \left\{A_{\ell i} = \frac{w_{\ell i}}{\sum_i w_{\ell i}}\right\} \quad \text{and} \quad \mathbf{u} = \{u_\ell\}.$$

Assuming multivariate Gaussian reservoir parameters $[\mathbf{M}] \sim \mathcal{N}_N(\mu_M, \mathbf{\Sigma}_M)$ and Gaussian noise error $[\mathbf{u}] \sim \mathcal{N}_s(\mathbf{0}, \mathbf{\Sigma}_u)$, it follows from Gaussian linearity that also the effective parameters $\mathbf{m}$ are Gaussian, see Appendix B. Following the derivation given in Appendix B the

conditional distribution for $\mathbf{M}|\mathbf{m}$ is Gaussian and given analytically by

$$[\mathbf{M}|\mathbf{m}] \sim \mathcal{N}_N(\mu_{M|m}, \mathbf{\Sigma}_{M|m}), \tag{A-7}$$

$$\mu_{M|m} = \mu_M + (\mathbf{A}\mathbf{\Sigma}_{MM})^T[\mathbf{A}\mathbf{\Sigma}_{MM}\mathbf{A}^T + \mathbf{\Sigma}_u]^{-1}(\mathbf{m} - \mathbf{A}\mu_M), \tag{A-8}$$

$$\mathbf{\Sigma}_{M|m} = \mathbf{\Sigma}_{MM} - (\mathbf{A}\mathbf{\Sigma}_{MM})^T[\mathbf{A}\mathbf{\Sigma}_{MM}\mathbf{A}^T + \mathbf{\Sigma}_u]^{-1}\mathbf{A}\mathbf{\Sigma}_{MM}. \tag{A-9}$$

The computation of the inverse $(s \times s)$ matrix may be computer intensive. However, some kind of sequential local downscaling (e.g., for streamline-based regions) may be applied to reduce the dimension s.

For permeability it is sometimes assumed a log-Gaussian model, which entails that $M_i = \log K_i$ is Gaussian. The approach outlined above can then be applied if the effective permeability for streamline/coarse cell ℓ can be represented by the weighted geometric average (see discussion in Section 5.3.1)

$$k_\ell = u_\ell \cdot \left(\Pi_i K_i^{w_{\ell i}}\right)^{1/\sum_i w_{\ell i}},$$

where u_ℓ is a log-Gaussian approximation error. Because taking the logarithm on each side of the geometric average gives

$$\begin{aligned}\log k_\ell &= \frac{1}{\sum_i w_{\ell i}} \log(\Pi_i K_i^{w_{\ell i}}) + \log u_\ell \\ &= \frac{1}{\sum_i w_{\ell i}} \Big[w_{\ell 1} \log K_1 + w_{\ell 2} \log K_2 + \ldots + w_{\ell N} \log K_N\Big] + \log u_\ell,\end{aligned}$$

which is on a linear form equivalent to (A-5). Further, applying the logarithm of the permeability ensures a positive permeability. For porosity it is sometimes assumed a Gaussian distribution directly, i.e., $M_i = \phi_i$, but a porosity within the interval $[0, 1]$ is then not guaranteed. However, the variability in porosity is usually much smaller than for permeability. In addition, it is possible to use some transformation that ensures a porosity within range, e.g., a logit transformation.

Appendix F. Equivalence Between SLEP and GTTI

First, we consider GTTI propagation of the SLEP modifications. For SLEP modifications $\delta\mathbf{k}$ are obtained (as described above). Further, sensitivities with respect to grid permeability $\mathbf{G} = \partial\mathbf{k}/\partial\mathbf{K}$ are given by for instance (63). Hence, the streamline-effective permeabilities can be propagated to obtain grid-permeability modifications $\delta\mathbf{K}$ by the minimization system in (47) or (56) that were originally used for the deterministic and the Bayesian version of the GTTI, respectively. We may also normalize the modifications and the sensitivities to obtain relative modifications instead. Further, it should be noted that the size of the inverse system generally is larger than for GTTI, unless only one streamline-bundle is used for each production well.

Second, we consider SLEP propagation of the GTTI modifications. The time-shift $\Delta\widetilde{t}$ propagated in GTTI can be propagated by the same methodology as used in SLEP by specifying the modifications along a streamline-bundle ℓ by $\alpha_\ell = f(\Delta\widetilde{t}, \ldots)$. Here f is some function of the time-shift and possibly other variables. Inspired by (61), an example of a modification factor would be $\alpha_\ell = f(\Delta\widetilde{t}, \bar{t}^{\text{obs}}) = 1 + \Delta\widetilde{t}/\bar{t}^{\text{obs}}$. To obtain a time-shift for each streamline-bundle it is possible to partition the fractional-flow curve into several segments vertically, like done in SLEP, to obtain one time-shift for each segment (streamline-bundle).

Appendix G. Potential Strategies for Incorporating Well Pressures in GTTI

For streamline-effective properties, the effective pressure drop can be explicitly related to the permeability/porosity as shown in Appendix D above. Therefore, sensitivities are not really needed in this case, but can of course be obtained by differentiation of the explicit

expressions; i.e. to obtain $\partial \Delta p / \partial k_\ell$. By the chain rule we obtain

$$\frac{\partial \Delta p}{\partial K_i} = \sum_{\ell=1}^{N_{\text{sl}}^i} \frac{\partial \Delta p}{\partial k_\ell} \cdot \frac{\partial k_\ell}{\partial K_i},$$

which makes it possible to define GTTI also to match effective pressure drops. Here $\partial k_\ell / \partial K_i$ is given by for instance (63). Ideally, however, compressibility should also have been incorporated in the expressions for the relation between the permeability and the pressure drop, but it may be better with an approximate pressure constraint than no constraint at all.

Another potential approach for incorporating well pressure (or well rate) in GTTI is to use

$$\frac{\partial p}{\partial m_i} = \frac{\partial p}{\partial q} \cdot \frac{\partial q}{\partial t} \cdot \frac{\partial t}{\partial m_i} = \frac{\partial p}{\partial q} \cdot \frac{\partial q}{\partial m_i}.$$

Here $\partial p / \partial q$ can potentially be obtained by differentiating a well model (e.g., the Peacemann well model like in [59]). The term $(\partial q / \partial t)^{-1}$ is discussed in [7] and Section 4.3 and the arrival-time sensitivity $\partial t / \partial m_i$ is discussed in Section 4.3. Again, it may be better with an approximate pressure constraint than no constraint at all.

Appendix H. Nomenclature

Symbols:

- reservoir property: m
- absolute grid permeability: K
- streamline effective permeability: k
- porosity: ϕ
- pressure: p
- flow rate: q
- total mobility: λ_t
- viscosity: μ
- density: ρ
- time-of-flight: τ
- bi-streamfunctions: ψ, χ
- streamline: Ψ
- fractional flow function: f
- sensitivity matrix: $\mathbf{G}$
- number of grid cells: N
- number of streamlines: N_{sl}
- number of data: N_d
- number of wells: N_w
- constant: const

Indices:

- streamline: ℓ
- grid cell: i
- time step: j
- well: k
- master point: d
- total: t
- phase: α

Sub/super scripts:

- water: w
- oil: o
- gas: g
- calculated: cal
- observed: obs

Paper I

A Multiscale Streamline Method for Inversion of Production Data

Vegard Røine Stenerud and Knut-Andreas Lie.

Journal of Petroleum Science and Engineering, Vol. 54, pp. 79–92, 2006.

Available online at www.sciencedirect.com
ScienceDirect
Journal of Petroleum Science and Engineering 54 (2006) 79–92
JOURNAL OF PETROLEUM SCIENCE & ENGINEERING
www.elsevier.com/locate/petrol

A multiscale streamline method for inversion of production data

Vegard R. Stenerud [a,*], Knut-Andreas Lie [b]

[a] Department of Mathematical Sciences, NTNU, NO-7491 Trondheim, Norway
[b] Department of Applied Mathematics, SINTEF, P.O. Box 124 Blindern, NO-0314, Oslo, Norway

Received 19 January 2006; received in revised form 28 July 2006; accepted 2 August 2006

Abstract

We propose two improvements to a recent streamline method by Wang and Kovscek for inversion of production data. The key idea of the Wang–Kovseck method is to associate increments in fractional flow curves (water-cut) with breakthrough of individual streamlines and match breakthrough times of each streamline by adjusting the effective streamline permeabilities. The perturbations in effective streamline permeabilities are given by a linear system, which can be solved in a decoupled fashion under additional simplifying assumptions. Finally, the permeability perturbations defined along streamlines are mapped onto the underlying simulation grid, typically using a geostatistical algorithm to constrain the corresponding corrections to the geological model to prior geological data.

Our first improvement is to model the flow in each streamline independently using real time, instead of using Dykstra–Parsons' algorithm for all streamlines connected to a producer–injector pair. This way, there is no coupling between individual streamlines, and permeability modifications can be obtained directly. Our approach uses less approximations, enables extension of the formulation to include gravity, and enables history matching of porosity. Three synthetic test cases show that this approach gives a better match and faster convergence.

Our second point is to use a multiscale inversion process, where the reservoir parameters are matched on a hierarchy of recursively coarsened grids. Two synthetic test cases demonstrate that this approach captures the large-scale trends of the reservoir parameters more accurately. The proposed approach has proven robust in the sense that it is able to capture structures of the permeability field on the basis of limited information.

Keywords: History matching; Streamlines; Permeability; Multiscale

1. Introduction

Obtaining a reliable history match is an ill-posed and time-consuming exercise for reservoir engineers. In this paper we consider one component of history matching, namely how to modify permeabilities (and/or porosities) to match observed production data. The process for history matching permeabilities typically consists of two basic steps: (1) modification of grid-block permeabilities, and (2) forward simulation of fluid responses to validate the accuracy/correctness of a given permeability distribution. History matching real-life reservoirs typically requires numerous flow simulations, which often makes forward simulation the most time-consuming part of a history match.

* Corresponding author. Fax: +47 73593524.
E-mail addresses: vegarste@math.ntnu.no (V.R. Stenerud), Knut-Andreas.Lie@sintef.no (K.-A. Lie).
URL's: http://www.math.ntnu.no/vegarste (V.R. Stenerud), http://www.folk.uio.no/kalie (K.-A. Lie).

0920-4105/$ - see front matter © 2006 Elsevier B.V. All rights reserved.
doi:10.1016/j.petrol.2006.08.003

Streamline simulation (Datta-Gupta and King, 1995; Thiele, 2005) is a complementary technology for flow simulation in petroleum reservoirs. Compared to traditional finite-difference simulators, streamline simulation offers unparallelled computational efficiency for simulating reservoir responses for large and complex geomodels and for flow scenarios dominated by wells, fluid mobilities, and heterogeneity in the rock properties. Replacing a conventional finite-difference solver by a much faster streamline solver may therefore drastically reduce the computational time, thereby allowing more frequent model updates and possibly also models with a larger number of gridblocks.

However, the most promising use of streamlines in history matching has come from their ability to locate regions in the reservoir that may contain potential sources for mismatch in production data. Several authors have exploited streamlines to develop efficient inversion methods using a sensitivity approach, in which one needs to compute gradients of production characteristics with respect to the geological parameters; see e.g., Gautier et al. (2001, 2004), Vasco and Datta-Gupta (1999), Vasco et al. (1999), Wen et al. (2003).

As an alternative, novel inversion methods can be developed using two types of data that are not offered in conventional simulators: flow paths (the streamlines) and time-of-flight. The streamlines give a natural way to delineate the reservoir volume to be matched. Emanuel and Milliken (1998) and Milliken et al. (2000) use streamlines to define subregions, in which subsequent changes in grid properties can be performed manually (or semi-automatically) by the reservoir engineer to match production data.

Wang and Kovscek (2000) use streamlines as a natural parameterisation of the reservoir and modify effective properties along streamlines to increase/decrease breakthrough times (computed from the time-of-flights), thereby reducing the mismatch between observed and calculated fractional flows, pressure drops, and total flow rates. The modified effective properties is then mapped back to individual grid cells in the underlying geological grid model and a flow simulation performed to check the match for the new permeability estimate. This procedure is repeated until the history match is converged. Although this approach is quite robust in the sense that a reasonable history match can be obtained from a small data set, modifying grid properties directly along flow paths may introduce artifacts and violate geological constraints. To improve the predictive powers and impose geological consistency in every step of the inversion, Caers and coworkers apply the modified effective streamline properties to constrain geostatistical algorithms; see Caers (2003), Caers et al. (2002, 2004), Gross et al. (2004). Moreover, as an alternative to perturbing effective properties associated with a single streamline, streamlines and time-of-flight can be used to perform corrections on all streamlines associated with a single well, an injector–producer pair, or on all wells in a reservoir.

In this paper, we go back to the original method of Wang and Kovscek (2000) and present two possible improvements. Our first point is that one can simplify the calculation of modified streamline permeabilities. Rather than using Dykstra–Parsons' algorithm to model all streamlines connected to a well as the relative motion of saturation fronts in a set of non-communicating layers, resulting in a linear system for the perturbations in effective permeabilities, we model each streamline independently using real time and obtain directly a set of (simple) algebraic relations between the effective parameters of the streamline and the mismatch in production data. This approach generally gives a better match and faster convergence and uses less approximations and assumptions on the mobility ratios than Wang and Kovscek in their inversion method. Moreover, our new formulation is more flexible and can easily be extended to include gravity (and possibly also more complex flow physics). Finally, since the new formulation only changes the way the modified streamline permeabilities are calculated, the method can immediately be applied within the geostatistical framework developed by Caers (2003), Caers et al. (2002, 2004), Gross et al. (2004).

Our second point is that the use of a multiscale inversion process may speed up the convergence and improve the quality of the history match. We use a family of hierarchically refined grids that are formed by coarsening an underlying fine geogrid for the desired permeability. Starting with the coarsest grid, we match production data using effective permeabilities and map the perturbed streamline permeabilities back onto the coarse grid. Next, an interpolation of the coarse-grid permeabilities is used as initial value for a new match on the next hierarchically refined grid, and so on until the finest grid is reached or a sufficiently good match is obtained. There are several advantages to this approach. First, the refinement level of the inverted permeability field will correspond to the resolution of the production data, and one reduces spurious effects due to over-parameterisation. Second, decomposing the inverse problem by scale will generally improve the identification of large-scale heterogeneity structures. Finally, since only a few parameters are matched on the coarser grids, the inversion process will be much faster than using a direct fine-scale streamline inversion. A similar approach has previously been introduced by Yoon et al. (1999) to

regularise and accelerate an inversion method based on analytical streamline sensitivities.

The outline of the paper is as follows: Section 2 presents a simplified model for flow along streamlines underlying the original method of Wang and Kovscek (2000), which is presented in Section 3, and our alternative method, which is presented in Section 4. The two methods are compared in Section 5 using three synthetic examples. Finally, in Section 6 we present the multiscale inversion method and make a few comparisons.

2. Basic flow model

The original method of Wang and Kovscek (2000) and the alternative inversion method we present in Section 4 are both derived from the same simplified flow model for incompressible flow of two fluids (oil and water) in a single horizontal rock layer. For simplicity we assume piston-like displacement with no capillary forces, where the injected water displaces the in-situ oil instantaneously at the water front. The front position is located at x and the total length of the streamline is L. The pressure drops behind and ahead of the front are denoted Δp_w and Δp_o, respectively. Finally, we assume (for the moment) that gravity can be neglected.

The average Darcy velocities for oil and water are given by

$$u_o = -k\lambda_o \frac{\Delta p_o}{L-x}, \quad u_w = -k\lambda_w \frac{\Delta p_w}{x}, \tag{1}$$

where k represents the effective permeability and λ_o and λ_w the oil- and water end-point mobilities. The total pressure drop over the flow region is given by

$$\Delta p = \Delta p_w + \Delta p_o. \tag{2}$$

For an incompressible system, the two velocities are equal, i.e.,

$$u = u_o = u_w.$$

The actual front velocity v, derived by mass conservation over the front, is given by

$$v = \frac{dx}{dt} = \frac{u}{\Delta S \cdot \phi}, \tag{3}$$

where $\Delta S = 1 - S_{or} - S_{wir}$ is the difference in end-point saturation and ϕ is the effective porosity.

Combining the above equations, we wind up with the following ordinary differential equation for the front position

$$\frac{dx}{dt} = -\frac{\Delta p}{\phi \Delta S} \frac{k}{\frac{x}{\lambda_w} + \frac{L-x}{\lambda_o}} = -\frac{\lambda_w \Delta p}{\phi \Delta S} \frac{k}{ML + (1-M)x}, \tag{4}$$

where $M = \lambda_w / \lambda_o$ is the end-point mobility ratio.

The effective streamline permeabilities are calculated based on the permeabilities of the underlying simulation grid. More precisely, the effective permeability of a streamline is given by the harmonic average, weighted by the time-of-flight through grid blocks,

$$k = \frac{\sum_j \tau_j}{\sum_j \frac{\tau_j}{K_j}}, \quad j \in N_b.$$

Here N_b is the set of indices of the grid blocks the streamline intersects, K_j is the permeability of grid block j, and τ_j is the associated increment in time-of-flight.

Because we regard an incompressible system, each streamline can only originate from an injection well and terminate at a production well. In other words, each streamline will connect an injector to a producer. If q_i denotes the flow rate of streamline i, the total flow rate of a well with N streamlines connected is given by

$$q = \sum_{i=1}^{N} q_i.$$

In the next section we will derive the Wang–Kovscek inversion method, assuming that all streamlines connecting an injector and a producer can be modelled as a set of non-communicating (horizontal) layers, where the flow in each layer is described as outlined above.

3. The Wang–Kovscek method

Wang and Kovscek (2000) introduced an iterative method for modifying permeabilities defined on a grid to match calculated with observed production data. The method is based upon two ideas: (i) the flow in an injector–producer pair can be represented by a set of N streamlines, where each streamline contributes a given amount (rate, pressure drop) to the production data; and (ii) each increment in the fractional-flow curve of the producer can be associated with the breakthrough of the injected fluid in a single streamline. By aligning the streamlines according to breakthrough times, one can identify the streamline causing a certain increment in the production data. Assuming that the streamlines in the estimated model are approximately the same as in the true model, the effective properties (here permeability) of the streamline can then be adjusted to match the corresponding increment in the observed fractional flow.

Each iteration of the Wang–Kovscek method requires one flow simulation and consists of two steps: First, modifications of the effective streamline permeabilities are identified in accordance with the mismatch in fractional-flow, well pressures, and well rates. Second, the perturbed

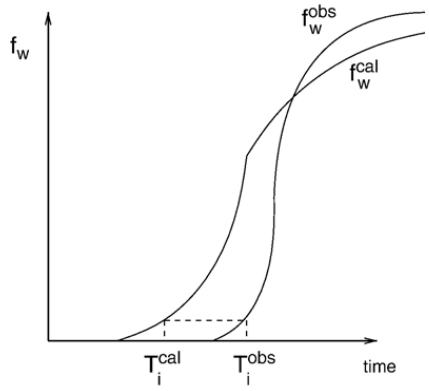

Fig. 1. Observed and calculated fractional-flow curves are used to obtain breakthrough times.

effective permeabilities are propagated to the underlying grid in physical space and a flow simulation is performed to check the match. Although we here only present the method for a single injector–producer pair, the extension to multiple wells is straightforward.

Next we will outline how to obtain the permeability modifications for fractional flow and for pressure drop and flow rate.

3.1. Match of fractional-flow

The fractional-flow at a producer is not matched directly, but is used to align observed and calculated breakthrough times for the streamlines terminating at the producer. By assuming that the order of breakthroughs is approximately the same for the estimated and the true permeability fields, the mismatches in breakthrough times for the streamlines can then be applied to modify the streamline permeability.

If we assume piston-like displacement and apply a streamline formulation with equal total flow-rate for all streamlines, each streamline will contribute equally to the total fractional-flow curve at the producer. Observed and calculated breakthrough times can therefore easily be obtained from the corresponding fractional-flow curves, see Fig. 1. The assumption of equal flow rate for the streamlines is a simplifying assumption and is not crucial for the derivation of the method. However, if the streamlines have different flow rates, each streamline will contribute differently to the fractional-flow curve when breaking through, and the order in which the streamlines break through may be more important.

To derive an expression for the breakthrough times in each of the N individual streamlines connecting an injector to a producer, Wang and Kovscek model the flow along N streamlines as the flow in N non-communicating (horizontal) layers. This means changing perspective from streamlines to streamtubes, such that each "streamline" is assigned a certain flow volume. Suppose now that each layer has length L_i, average cross-sectional area A_i, average porosity ϕ_i and permeability k_i, and end-point saturation difference $\Delta S_i = 1 - S_{\mathrm{wir}} - S_{\mathrm{or}}$. Expressed in terms of *pore-volumes injected* (PVI) for the injector–producer pair, the breakthrough time $\tilde{T}_i$ of streamline i can now be written

$$\tilde{T}_i = \frac{\sum_{j=1}^{N} (A\phi L)_j \tilde{x}_j^i}{\sum_{j=1}^{N} (A\phi L)_j}. \tag{5}$$

Here $\tilde{x}_j^i$ represents the relative front position along streamline j when streamline i breaks through, and is provided by Dykstra–Parsons' method (Dykstra and Parsons, 1950). The relative front position can be derived from the differential Eq. (4) for the front position in a single layer. Dividing the expressions for layers j and i, we obtain

$$\frac{\mathrm{d}\tilde{x}_j}{\mathrm{d}\tilde{x}_i} = F_j^i \frac{M_i + (1-M_i)\tilde{x}_i}{M_j + (1-M_j)\tilde{x}_j}, \quad F_j^i = \frac{k_j \phi_i \Delta S_i \lambda_{wj} L_i^2}{k_i \phi_j \Delta S_j \lambda_{wi} L_j^2}, \quad \tilde{x} = \frac{x}{L}.$$

Integrating this differential equation over the streamlines and evaluating $\tilde{x}_j$ at breakthrough for streamline i ($\tilde{x}_i = 1$) gives $\tilde{x}_j^i$.

The next step is to use this simplified flow model to relate the discrepancies in breakthrough times to discrepancies in effective streamline permeabilities k_i. Because the sum in the numerator of Eq. (5) runs over all streamlines, the breakthrough time $\tilde{T}_i$ is a function of the permeabilities of all streamlines. Linear approximation therefore gives

$$\Delta \tilde{T}_i = \frac{\partial \tilde{T}_i}{\partial k_1}\Delta k_1 + \frac{\partial \tilde{T}_i}{\partial k_2}\Delta k_2 + \frac{\partial \tilde{T}_i}{\partial k_3}\Delta k_3 + \ldots + \frac{\partial \tilde{T}_i}{\partial k_n}\Delta k_n, \tag{6}$$

where

$$\Delta k_i = k_i^{\mathrm{obs}} - k_i^{\mathrm{cal}} \text{ and } \Delta \tilde{T}_i = \tilde{T}_i^{\mathrm{obs}} - \tilde{T}_i^{\mathrm{cal}}.$$

This equation gives a relation between the mismatch in breakthrough times for streamline i and the permeability modifications for all streamlines. The derivatives $a_{ij} = \partial \tilde{T}_i / \partial k_j$ are obtained by differentiating Eq. (5). Applying the same linear approximation for all streamlines results in the following system

$$\begin{bmatrix} a_{11} & a_{12} & \ldots & a_{1N} \\ a_{21} & a_{22} & \ldots & a_{2N} \\ \vdots & \vdots & \ddots & \vdots \\ a_{N1} & a_{N2} & \ldots & a_{NN} \end{bmatrix} \begin{bmatrix} \Delta k_1 \\ \Delta k_2 \\ \vdots \\ \Delta k_N \end{bmatrix} = \begin{bmatrix} \Delta \tilde{T}_1 \\ \Delta \tilde{T}_2 \\ \vdots \\ \Delta \tilde{T}_N \end{bmatrix}. \tag{7}$$

The system is simplified by defining relative or normal parameters (Wang and Kovscek, 2000). For unit mobility ratios, the system is strongly diagonally dominant and approximately decouples so that

$$\frac{\Delta k_i^t}{k_i^{\mathrm{cal}}} \approx \frac{\tilde{T}_i^{\mathrm{cal}} - \tilde{T}_i^{\mathrm{obs}}}{\tilde{T}_i^{\mathrm{obs}}}. \tag{8}$$

The superscript t indicates that the modification is due to mismatch in break through time. As explained by Wang and Kovscek (2000), the approximation Eq. (8) becomes better the more streamlines are involved, because off-diagonal elements scale like $1/N$. The approximation Eq. (8) is used for practical applications (even for nonunit mobility ratios) to obtain the modifications; see Wang and Kovscek (2000), Caers et al. (2002), Caers (2003).

3.2. Match of pressure drop and rate

The description in Wang and Kovscek (2000) is a bit ambiguous as to how the modifications due to pressure drop and rate are calculated. In this section we describe how we understood the derivation of pressure and rate modifications. Further, these derivations create a foundation for parts of the derivation of our improved method.

If we assume that all streamlines have the same flow rate, the error in flow rate of an injector–producer pair is distributed equally among all streamlines. If a streamline formulation with varying streamline rate is used, the error in flow rate may instead be distributed by weighting. The error in pressure drop is common to all streamlines of an injector–producer pair.

To modify the permeability due to mismatch in pressure drop and rate, an expression relating these three quantities is used. To derive this expression we start out by Eq. (4), reading

$$v_i = \frac{\lambda_w \Delta p}{\phi_i \Delta S} \frac{k_i}{ML_i + (1-M)x_i}.$$

We regard Δp as the effective pressure drop for the streamline, possibly obtained by temporal averaging over the depletion period. Averaging the velocity over the streamline then gives

$$\bar{v}_i = -\frac{\ln M}{M-1} \frac{k_i \lambda_w \Delta p}{L_i \phi_i \Delta S}. \tag{9}$$

The average actual front velocity can be estimated by

$$\bar{v}_i = \frac{q_i}{\phi_i \Delta S A_i}. \tag{10}$$

Here A_i is the average cross-sectional area of a streamline/streamtube and q_i is the effective streamline rate derived by distributing the well rate among all streamlines connected to a well. Having an explicit expression for A_i is not important, since it will cancel out later in the derivation. Finally, rearranging Eq. (9) gives the permeability by

$$k_i = -\frac{M-1}{\ln M} \frac{\bar{v}_i L_i \phi_i \Delta S}{\lambda_w \Delta p}. \tag{11}$$

In the limit of unit mobility ratio, the last expression can be obtained directly from the averaged Darcy's law (Eq. (1)).

Evaluating Eq. (11) for calculated and observed data, with $\bar{v}_i$ estimated by Eq. (10), we obtain

$$\frac{\Delta k_i^{p,q}}{k_i^{\mathrm{cal}}} = \frac{\Delta p^{\mathrm{cal}} q_i^{\mathrm{obs}} - \Delta p^{\mathrm{obs}} q_i^{\mathrm{cal}}}{\Delta p^{\mathrm{obs}} q_i^{\mathrm{cal}}}. \tag{12}$$

The superscripts p and q indicate that the corresponding modification is due to mismatch in pressure drop and rate. If there are no observations of the pressure drop or the rate, it would be natural to assume that the calculated response for the quantity is correct, i.e., calculated and observed responses coincide. This will make the quantity cancel out from the expression for the modification.

3.3. Updating grid permeability

To obtain a total correction factor r_i for streamline i, geometric averaging is used to combine the relative modifications, Eqs. (8) and (12):

$$r_i = \left[(1 + \Delta k_i^t / k_i^{\mathrm{cal}}) \cdot (1 + \Delta k_i^{p,q} / k_i^{\mathrm{cal}}) \right]^{1/2}.$$

If the streamline distribution is updated during the forward simulation, one or several of the temporary streamline distributions are used for the inversion; see the discussion in Section 4.4.

For simplicity, and to focus on the improved quality of the streamline permeability corrections, we will in the following only use a simple deterministic method to propagate the modifications for the streamline permeabilities onto the underlying geological grid; see Wang and Kovscek (2000). More sophisticated geostatistical mapping methods incorporating e.g., prior information on the permeability distribution have been developed by Caers et al. (2002), Caers (2003), Caers et al. (2004). In Caers et al. (2002) the grid permeabilities are described by

a Gauss–Markov random function. The grid permeabilities are modified by sampling from the random function conditioning on the updated streamline effective permeabilities k_i^{new}. This approach honors the variogram and the histogram and may therefore result in permeability fields that better preserve geologic realism. In Caers (2003) the mapping is performed using gradual deformation, which preserves the geological continuity. Further, the use of multiple-point geostatistics may enable history matching of complex heterogeneous geological structures, like fractures and channels, which is beyond the scope of variogram-based methods. Finally, in Caers et al. (2004) the effective permeability modifications are obtained for the flow zone associated with each producer. The mapping to the grid is performed with Direct Sequential Simulation (DSSIM) to honor the variogram while allowing the histogram to change.

4. Improved inversion of effective streamline permeabilities

In this section we present an alternative inversion method that is not based upon the Dykstra–Parson algorithm. Instead, our method solves the differential Eq. (4) for the front position in each streamline and uses these solutions to relate the discrepancies in observed and calculated breakthrough times to perturbations of the effective streamline permeabilities. There are several advantages to this approach: (i) we avoid solving the linear system (7) or making further approximations by decoupling to Eq. (8); (ii) our new formulation is easier to generalise; and (iii) we generally obtain faster convergence and a better history match.

In the Dykstra–Parsons method, Eq. (4) is used to relate positions of saturation fronts in different streamlines. This eliminates real time and pressure, and couples the streamlines. We propose to avoid this coupling by using Eq. (4) directly to model absolute front positions in real time for each streamline. Integrating Eq. (4) over streamline i

$$\int_0^{L_i}[ML_i+(1-M)x_i]\mathrm{d}x_i=-\int_0^{T_i}\frac{k_i\lambda_w\Delta p(t)}{\phi_i\Delta S}\mathrm{d}t,$$
$$\frac{1}{2}(M+1)L_i^2=-\frac{k_i\lambda_w}{\phi_i\Delta S}\int_0^{T_i}\Delta p(t)\mathrm{d}t,$$

and solving for the effective permeability k_i gives

$$k_i=-\frac{M+1}{2}\frac{L_i^2\phi_i\Delta S}{\lambda_w\int_0^{T_i}\Delta p(t)\mathrm{d}t}=-\frac{M+1}{2}\frac{L_i^2\phi_i\Delta S}{\lambda_w}\frac{1}{\overline{\Delta p}\,T_i}. \tag{13}$$

Here $\overline{\Delta p}$ is the temporal average of the pressure drop over $[0, T_i]$.

Evaluating the permeability for observed and calculated data gives the relative modification

$$\frac{\Delta k_i^{t,p}}{k_i}=\frac{k_i^{\text{obs}}-k_i^{\text{cal}}}{k_i^{\text{cal}}}=\frac{\overline{\Delta p}^{\text{cal}}\,T_i^{\text{cal}}-\overline{\Delta p}^{\text{obs}}\,T_i^{\text{obs}}}{\overline{\Delta p}^{\text{obs}}\,T_i^{\text{obs}}}, \tag{14}$$

for streamline i. If $\bar{v}_i$ is estimated by

$$\bar{v}_i=L_i/T_i, \tag{15}$$

the permeability modifications Eqs. (13) and (11) only differ by the mobility factors $(M-1)/\ln M$ and $(M+1)/2$. However, for unit mobility ratio the two expressions coincide.

Notice that no *mathematical* approximations were made in the derivation of Eq. (14) from Eq. (4). Under the same *physical* assumptions, the modifications Eq. (14) should therefore be more accurate than those obtained by Eqs. (7) and (8). Further, notice that we also could have solved for ϕ_i, or for (k_i/ϕ_i), instead of k_i in Eq. (13), and thereby obtained expressions for relative modifications in effective porosity or permeability–porosity ratios.

4.1. Accounting for gravity along streamlines

Using the new inversion method introduced above, it is straightforward to account for gravity in the flow direction. To this end, consider the Darcy velocities for oil and water in the presence of gravity

$$u_{\text{oi}}=-k_i\lambda_{\text{o}}\left(\frac{\Delta p_{\text{o}}}{L_i-x_i}+\rho_{\text{o}}\,g\,\sin\,\alpha_i\right),$$
$$u_{\text{wi}}=-k_i\lambda_{\text{w}}\left(\frac{\Delta p_w}{x_i}+\rho_w\,g\,\sin\,\alpha_i\right). \tag{16}$$

Here α_i is the streamline effective dip angle, $g=|\vec{g}|$ the acceleration of gravity, and ρ_α the density of phase α. The effective dip angle of a streamline Ψ_i is given by the time-of-flight weighted average of the local dip angle $\alpha(\tau)$,

$$\alpha_i=\frac{\int_{\Psi_i}\alpha(\tau)\mathrm{d}\tau}{\int_{\Psi_i}\mathrm{d}\tau}.$$

Combining Eqs. (2) and (3) with Eq. (16), we can now extend the differential Eq. (4) for the front position to account for gravity

$$\frac{\mathrm{d}x_i}{\mathrm{d}t}=-\frac{k_i\lambda_w}{\phi_i\Delta S}\cdot\frac{[\Delta p+\rho_{\text{o}}\,g\,L_i\sin\alpha_i+x_i(\rho_{\text{w}}-\rho_{\text{o}})g\sin\alpha_i]}{ML_i+(1-M)x_i}. \tag{17}$$

For constant pressure drop, the same procedure as above gives

$$\frac{\Delta k_i}{k_i} = \frac{T_i^{\mathrm{cal}} I^{\mathrm{obs}} - T_i^{\mathrm{obs}} I^{\mathrm{cal}}}{T_i^{\mathrm{obs}} I^{\mathrm{cal}}}, \tag{18}$$

where

$$I^{\xi} = \int_0^{L_i} \frac{ML_i + (1-M)x_i}{\Delta p^{\xi} + \rho_{\mathrm{o}}\, g\, L_i \sin\alpha_i + (\rho_{\mathrm{w}} - \rho_{\mathrm{o}}) g\, x_i \sin\alpha_i} \mathrm{d}x_i,$$
$$\xi = \mathrm{cal}, \mathrm{obs}. \tag{19}$$

The integral has the following analytic solution

$$I^{\xi} = c^{-2}(ac - bd) \cdot \ln(|d + c\, L_i|/|d|) + bc^{-1} L_i,$$

where $a = L_i\, M$, $b = 1 - M$, $c = (\rho_{\mathrm{w}} - \rho_{\mathrm{o}})\, g\, \sin\, \alpha_i$, and $d = \Delta p^{\xi} + \rho_{\mathrm{o}}\, g\, L_i\, \sin\, \alpha_i$. For unit mobility ratios the integral simplifies considerably. Letting the effective dip angle turn to zero in Eq. (19), Eq. (18) simplifies to Eq. (14).

4.1.1. Time-dependent pressure drops

Allowing for a time-dependent pressure drop in Eq. (17) and rearranging terms we obtain the following first-order differential equation

$$e(a + bx_i)\, \dot{x}_i + k_i c x_i = -k_i d(t), \tag{20}$$

where $e = (\phi_i \cdot \Delta S / \lambda_{\mathrm{w}})$, while a, b, c and d are as given above, except that the pressure drop in d is now time-dependent. This equation generally has a nonlinearity in the first term. However, for unit mobility ratios it is linear and can be solved for the special case of $\rho_{\mathrm{o}} = \rho_{\mathrm{w}}$

$$k_i = -\frac{L_i^2 \phi_i \Delta S}{\lambda} \frac{1}{(\overline{\Delta p} + \rho\, g\, L_i \sin\alpha_i) T_i}. \tag{21}$$

In the limit $\alpha_i \to 0$, Eq. (21) simplifies to Eq. (13).

In the general case we will proceed as in Section 3.2 and rely on spatial averaging rather than trying to solve Eq. (20) explicitly for k_i. The front velocity $v_i = \mathrm{d}x_i/\mathrm{d}t$ is given by Eq. (17), where we regard Δp as effective pressure drop for the streamline, possibly obtained by temporal averaging over the depletion period. Spatial averaging of the front velocity over the streamline gives

$$\overline{v}_i = -\frac{k_i \lambda_w}{L_i \phi_i \Delta S} \frac{1}{(M-1)^2} \cdot (a(M)\Delta p - (b(M)\rho_o - c(M)\rho_{\mathrm{w}}) g\, L_i \sin\alpha_i),$$

where $a(M) = (M-1)\, \ln\, M$, $b(M) = \ln\, M - M + 1$, and $c(M) = M\, \ln\, M - M + 1$. For unit mobility ratios the average front velocity is

$$\overline{v}_i = -\frac{k_i \lambda_w}{L_i \phi_i \Delta S} \left(\Delta p + \frac{1}{2}(\rho_{\mathrm{o}} + \rho_{\mathrm{w}}) g\, L_i \sin\alpha_i \right).$$

Similarly to Eq. (11), we wind up with

$$k_i = -\frac{\overline{v}_i L_i \phi_i \Delta S (M-1)^2}{\lambda_w [a(M)\Delta p - (b(M)\rho_{\mathrm{o}} - c(M)\rho_{\mathrm{w}}) g\, L_i \sin\alpha_i]} \tag{22}$$

for nonunit mobility ratio, while for unit mobility ratio we get

$$k_i = -\frac{\overline{v}_i L_i \phi_i \Delta S}{\lambda_w \left(\Delta p + \frac{1}{2}(\rho_{\mathrm{o}} + \rho_{\mathrm{w}}) g\, L_i \sin\alpha_i \right)}. \tag{23}$$

These two expressions, with $\overline{v}_i$ estimated by Eq. (10) or Eq. (15), can be used to obtain streamline modifications. An advantage of these expressions is that the streamline rate can be included. As expected, letting α_i tend to zero in Eqs. (22) and (23) results in Eq. (11). For the case with constant pressure drop, equal densities $\rho_{\mathrm{o}} = \rho_{\mathrm{w}}$, and $\overline{v}_i$ estimated by Eq. (15), one can show that the modification Eq. (23) coincides with the exact modification Eq. (21).

4.2. Match of rate

For several injectors and/or producers, it may be necessary to match the error in the total flow rate of the wells considered. The rate can be matched similarly to how it is done for the Wang–Kovscek method. Combining the permeability expressions Eqs. (11), (22) or (23) with Eq. (10), relates the permeability and the streamline rate. By using these permeability expressions, relative modifications $\Delta k_i^{p,q}/k_i^{\mathrm{cal}}$ for rate and pressure can be obtained (see Eq. (12)).

4.3. Total modifications

If breakthrough times and pressure drops are matched, the correction factor becomes

$$r_i^{t,p} = 1 + \Delta k_i^{t,p}/k_i^{\mathrm{cal}}.$$

This modification factor can be combined with the modification due to rate and pressure drop $\Delta k_i^{p,q}/k_i^{\mathrm{cal}}$ to

give a total correction factor by the geometric average (possibly weighted)

$$r_i = \left[(1 + \Delta k_i^{t,p}/k_i^{\mathrm{cal}}) \cdot (1 + \Delta k_i^{p,q}/k_i^{\mathrm{cal}})\right]^{1/2}.$$

Since the mismatch in pressure drop contributes to both the relative modifications, the mismatch in pressure drop may be distributed between the two expressions. The modification factors can be propagated to the underlying simulation grid by any of the geostatistical approaches described in Section 3.3. However, we will for our implementations use the simple deterministic approach proposed in Wang and Kovscek (2000). The breakthrough times are obtained by the approach described in Section 3.1.

4.4. Evolving streamlines

A general problem for streamline-based history matching is the fact that the streamlines only exist during a single pressure time step. If streamlines are evolving, one should ideally compose effective streamlines by adding one segment for each time step. This requires that one is able to keep track of each streamline from one time step to the next. This means that the number of streamlines for each injector–producer pair must be constant, which is a hard constraint to fulfil for a general streamline implementation. To deal with the problem of streamlines existing for a single pressure step, Wang and Kovscek (2000) suggest to pick one of the temporary streamline distributions as a representative streamline distribution. The geometry and time-of-flight information is therefore not correct for the whole streamline, so the calculations of effective properties may be inaccurate. However, this is not critical, because effective properties are only used to *perturb* the history match in a given direction and the quality of this perturbation is estimated in the consecutive forward flow simulation.

5. Numerical examples

In this section we assess the new inversion methods introduced in the previous section. To make the comparison with the original Wang–Kovseck method as clean as possible, we focus on simple and idealised test cases with a small number of parameters. Applications of the Wang–Kovseck method to more realistic test cases and real reservoirs can be found in Gross et al. (2004), Caers et al. (2004).

We consider three synthetic reservoirs with dimensions $200 \times 200 \times 10$ m^3, where pure water ($\rho_w = 1000$ kg/m^3, $\mu_w = 1$ cp) is injected at a rate of 300 STB/day into a reservoir initially filled with pure oil ($\rho_o = 700$ kg/m^3, $\mu_o = 1$ cp). Further, we assume a zero residual oil saturation after depletion.

5.1. Case 1: quarter five-spot

We first consider a quarter five-spot example with no flow over the outer boundaries and one injector in the lower-left corner and a producer in the upper-right corner. Because the total flow rate at the wells is preserved, only data from fractional flow and pressure drop are matched for this example. For the flow model we assume linear relative permeabilities, $\lambda_w(s) = s$ and $\lambda_o(s) = 1 - s$.

The true permeability is represented on a $20 \times 20 \times 1$ uniform grid and consists of a low-permeable background with an ellipsoidal high-permeability region imposed along the diagonal; see Fig. 2. Matching the main permeability trends should be rather easy for any

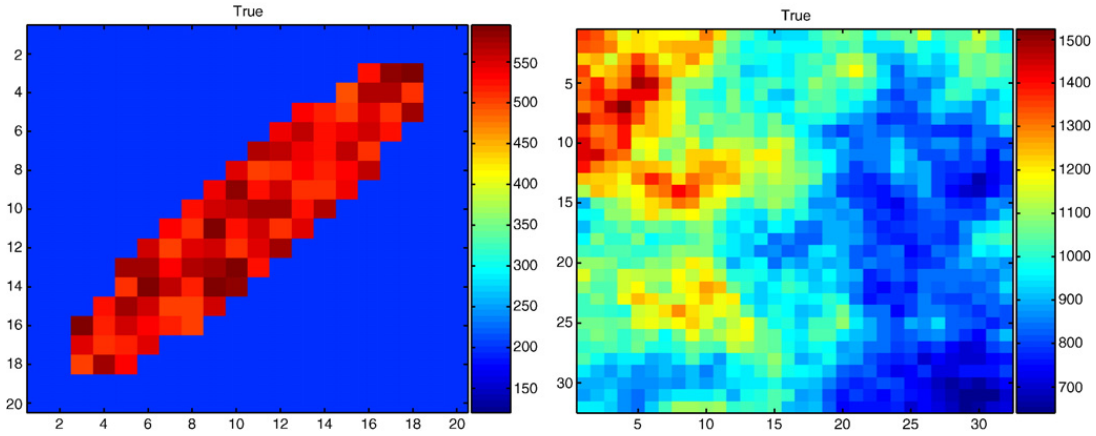

Fig. 2. The true permeability field in mD for Cases 1 and 2 (left) and Case 3 (right).

streamline-based method, since the high permeable region is aligned with the major flow direction (from injector to producer). For both methods we start the iterations from a homogeneous permeability field of 150 mD (no prior information).

Fig. 3 shows inferred permeability fields, matched fractional flow curves, and relative errors obtained using nine iterations with the original Wang–Kovscek inversion method, (8) and (12), and with our improved method, Eq. (14). Both methods match the fractional flow and pressure drop, but whereas the Wang–Kovscek method has not converged fully after nine iterations, our method has converged after five. The inferred permeability fields for the two methods are qualitatively similar; both methods capture the high-permeable region, but the estimated permeability is too low in both the ellipsoidal region and in the low-permeable background. On the other hand, the permeabilities close

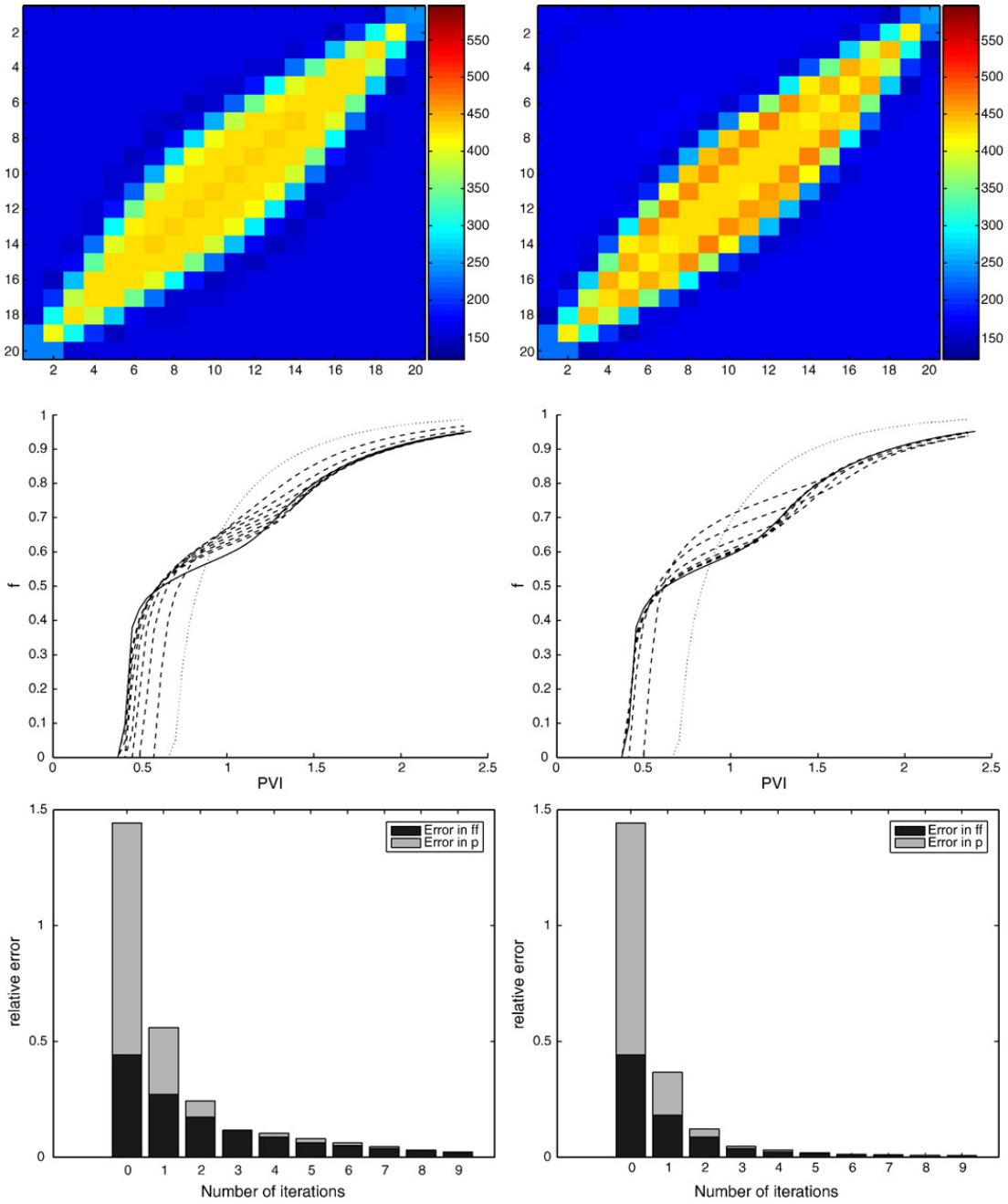

Fig. 3. Case 1. Comparison of inferred permeability fields, matched fractional-flow curves, and relative errors for the original Wang–Kovseck method (left) and our new method (right). In the middle plot, the observed fractional flow is given by a solid line, the calculated curve by a dotted line, and matched curves by dashed lines.

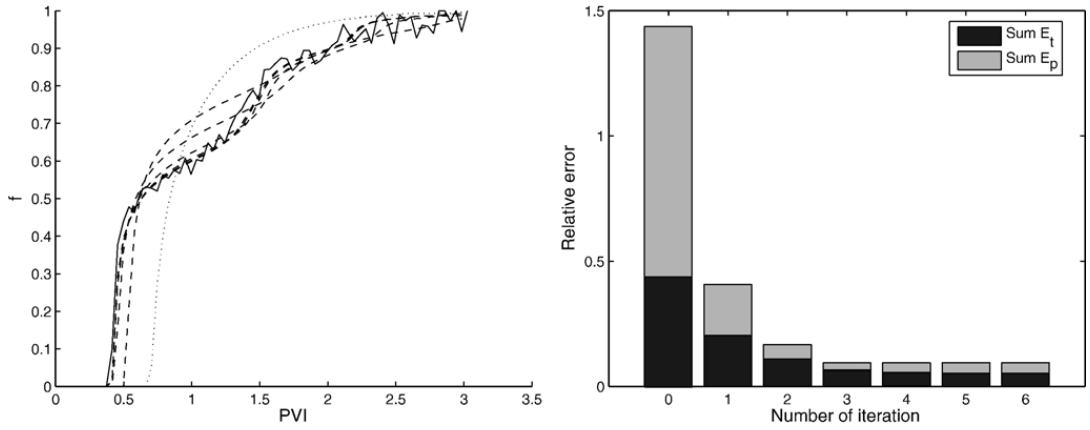

Fig. 4. Case 1. Matched fractional-flow curves (dashed lines) with 5% white noise added to the observed fractional-flow curve (solid line).

to the wells are too high, which makes the effective streamline permeabilities consistent with the effective permeabilities of the true permeability field.

If 5% white noise is added to the observed fractional-flow curve, our method is still able to match the fractional flow (see Fig. 4) if we avoid using the streamlines contributing to approximately the upper 5% of the fractional-flow curve. Due to the flatness in this part of the curve, the calculated breakthrough times are more sensitive to noise.

5.2. Case 2: tilted quarter five-spot

We now tilt the reservoir from Case 1, such that the edges of the reservoir are aligned with the vectors [0.9539, 0, 0.3] and [−0.0943, 0.9493, 0.3]. We compare the inversion obtained using two different formulas from Section 4: Eq. (18) accounts for gravity along streamlines, and Eq. (14) does not.

Fig. 5 shows inferred permeability fields and matched fractional flow curves for six iterations. By accounting

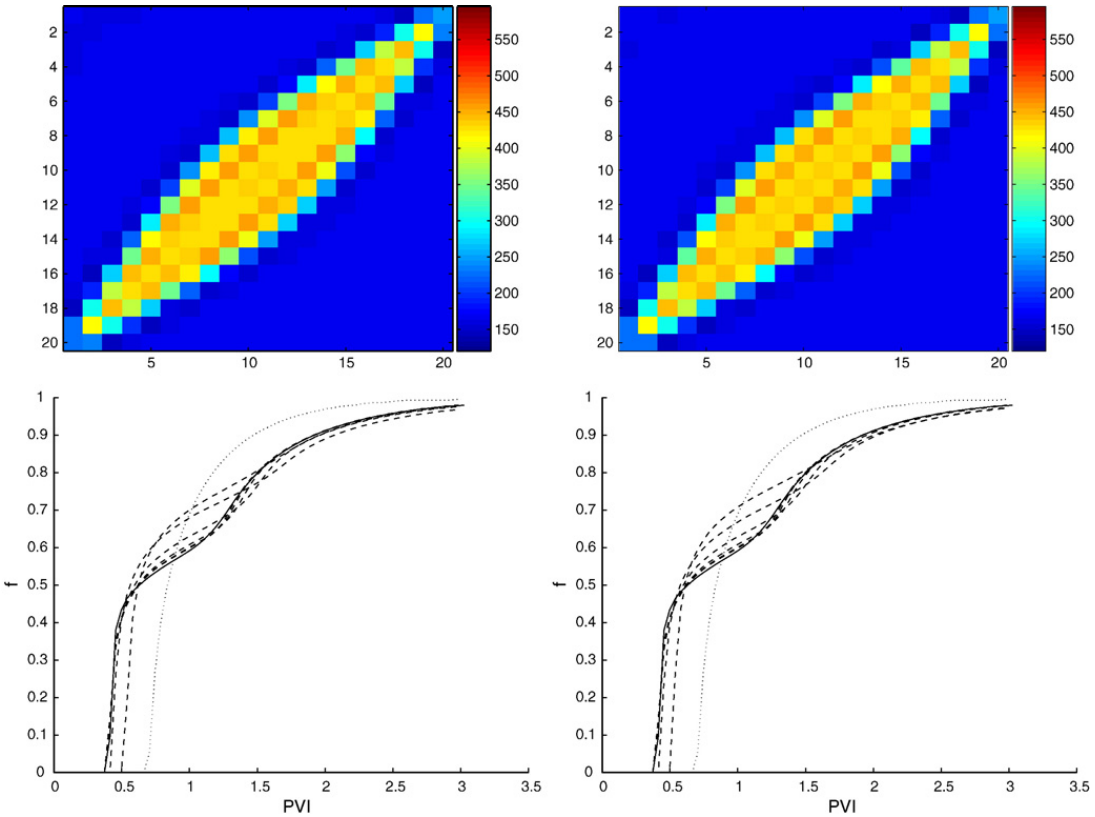

Fig. 5. Case 2. Comparison of inferred permeability fields and matched fractional-flow curves with and without accounting for gravity (left and right, respectively).

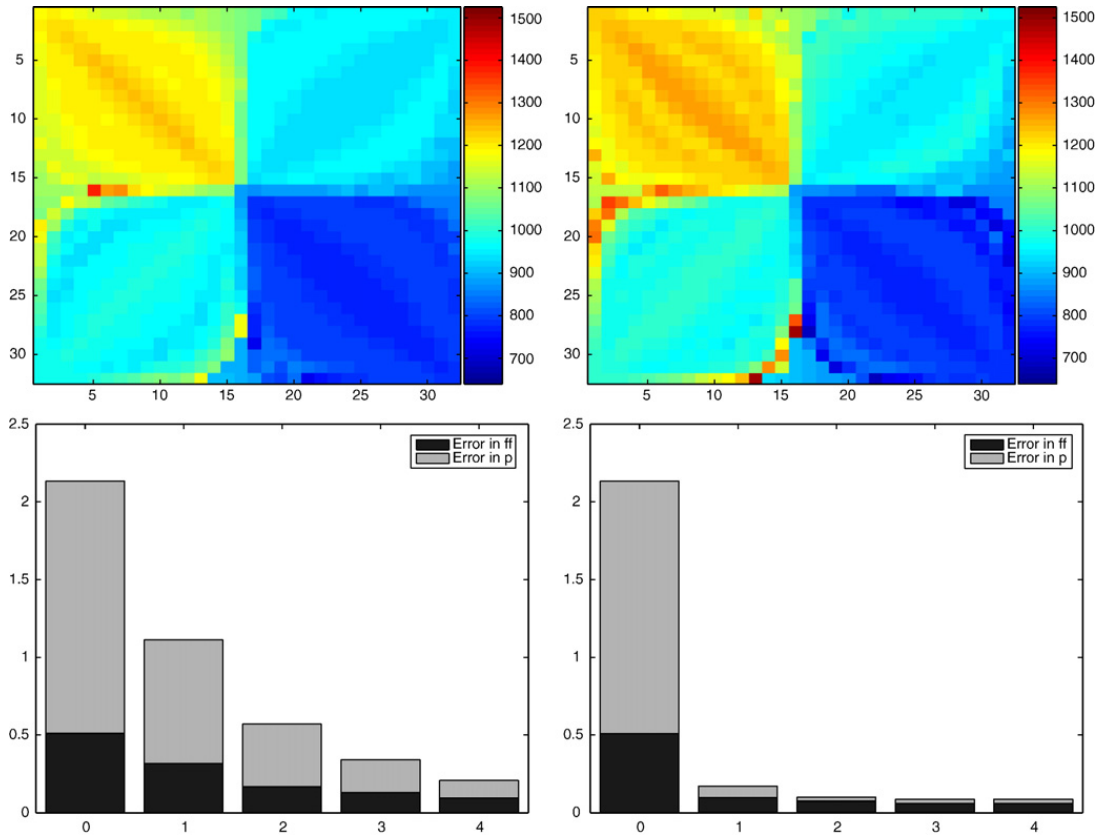

Fig. 6. Case 3. Comparison of inferred permeability fields and relative errors for the original Wang–Kovseck method (left) and our new method (right).

for gravity we observe a bit faster match for the pressure drops, but apart from this, there is little difference in the matching process. We obtain essentially the same result as for Case 1, both with and without accounting for gravity in the inversion. The reason is that we calculate relative modifications, for which proportionality errors cancel out. Although gravity does not give a pure proportionality error, it has the same impact on calculating both I^{cal} and I^{obs} for each streamline; see Eqs. (18) and (19). This example demonstrates the robustness of using relative modifications.

5.3. Case 3: five-spot with nonunit mobility ratio

Finally, we consider a five-spot pattern in a square domain, but now with an injector in the centre and one producer in each of the four corners. The reference permeability is given on a 32×32 grid as shown in Fig. 2. We assume quadratic relative permeabilities, $\lambda_{\mathrm{w}}(s)=s^2/\mu_{\mathrm{w}}$ and $\lambda_{\mathrm{o}}(s)=(1-s)^2/\mu_{\mathrm{o}}$ and $\mu_{\mathrm{o}}=0.4$ cp, which gives a nonunit end-point mobility ratio of $M=0.4$. As in the previous example, we match fractional flows and pressure drops using the original Wang–Kovscek method and our improved method from Section 4. We start the iterations by a homogeneous initial permeability field of 700 mD (no prior information), and 5% white noise is added to the observed fractional-flow curve.

Fig. 6 shows the inferred permeability fields and relative errors for the two methods. The error bars show the sum of the relative errors for fractional flow and pressure drop for all producers. As above, our method

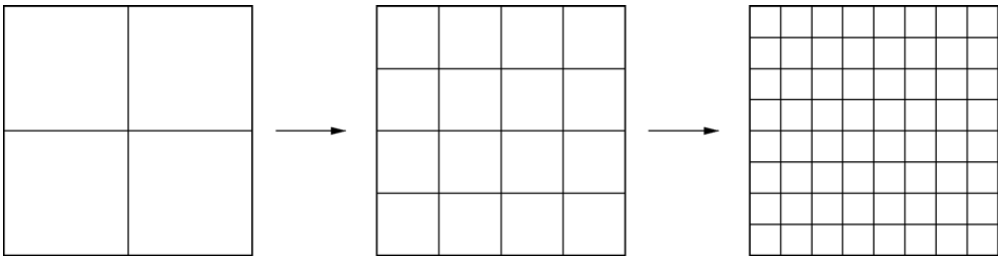

Fig. 7. Illustration of the hierarchically coarsened grids used in the multiscale inversion process.

converges faster, especially for the pressure drop. We observe that both methods capture the mean permeability correctly in the four injector–producer sectors, but fail to capture permeability structures within each sector properly. In particular we notice the artifacts along streamline paths, caused by the direct mapping of effective properties and the lack of a prior (geostatistical) model. In the next section we propose a multiscale approach that will improve the resolution of large-scale permeability structures that affect several injector–producer pairs.

6. A multiscale method

Many inversion methods are based upon minimisation of an objective functional using a gradient descent method. Inverse problems are generally underdetermined in the sense that one has a few observations and a large number of unknown parameters. Moreover, since the inversion process is highly nonlinear, the objective functionals tend to have a large number of local minima that must be avoided. Multiscale inversion has been suggested by several authors as a means to stabilise the

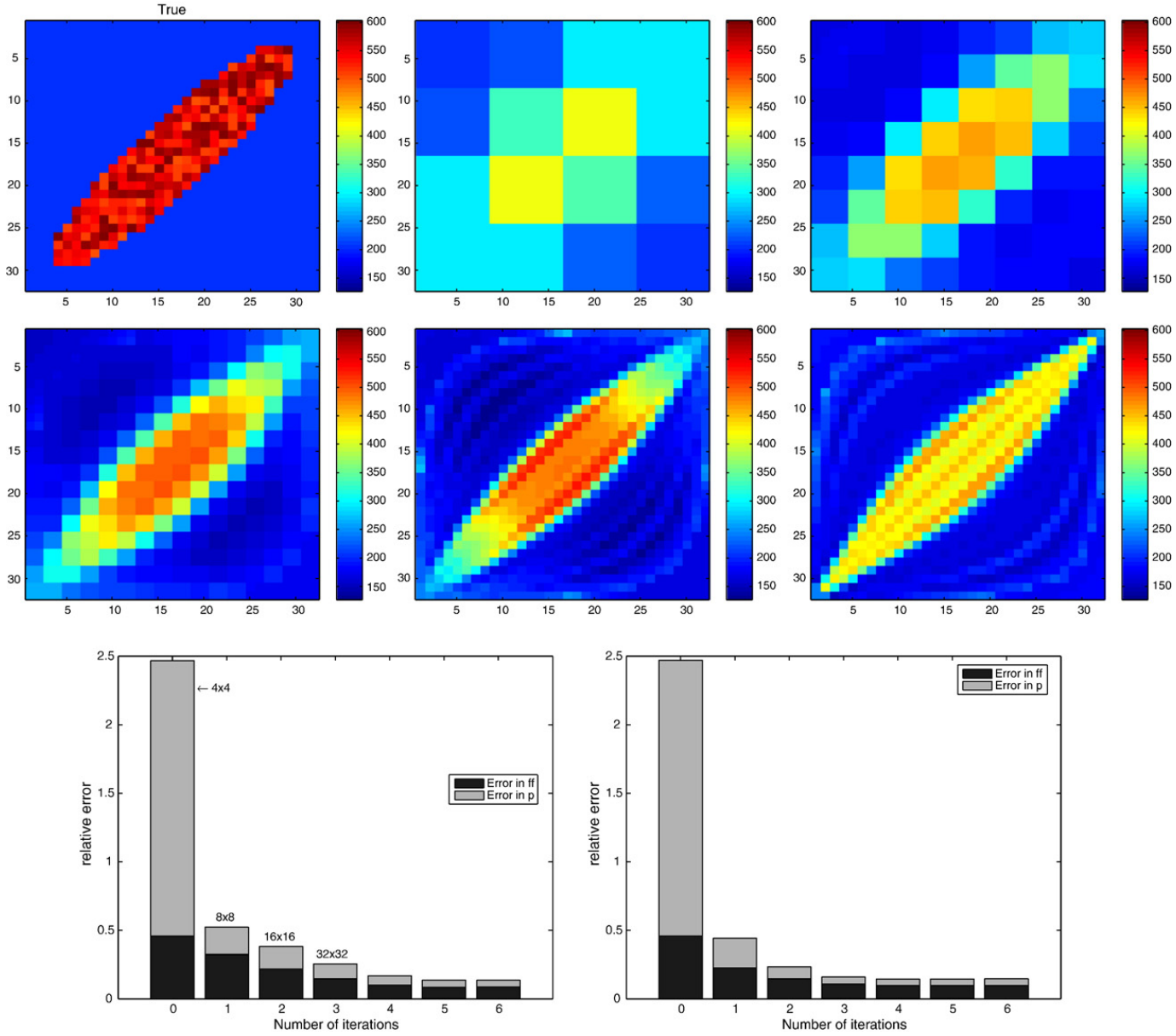

Fig. 8. Case 4. Comparison of inferred permeability fields and relative errors with and without the multiscale approach. The true permeability field in mD (upper left). The four next plots (from left to right) show the inferred permeability fields on the 4×4, 8×8, 16×16, and 32×32 grids. The last plot in the second row shows the inferred permeability field obtained by a direct inversion on the 32×32 grid. The two plots in the last row show the relative error with (left) and without (right) the multiscale approach.

inversion and avoid local minima; see e.g., Yoon et al. (1999) for a multiscale inversion method based on analytical streamline sensitivities.

Although our streamline approach is not based upon minimisation of an error functional, we here suggest to use a similar approach to speed up and stabilise the inversion. To this end we introduce a family of hierarchically coarsened grids, as illustrated in Fig. 7, where the finest grid coincides with the geogrid on which we seek to match permeabilities. Given the family of grids, the idea is quite simple: Starting with a small set of streamlines, we modify the effective streamline permeabilities to match observed production data as described in Section 4 and map the perturbed streamline permeabilities back onto the coarsest grid. Depending on the complexity of the reservoir, one or more iterations can be performed. The resulting permeabilities on the coarsest grid are then interpolated (linearly) onto the next grid in the family and used as initial values for the match on the next scale. The process is continued until the finest grid is reached, or can be terminated when a sufficiently good match is obtained or if no improvement in the misfit is observed from one level to the next. By allowing for early termination, the resolution of the resulting permeability field will correspond to the information content in the production data, and spurious effects from over-parameterisation are reduced. On the coarser grid levels, the ratio between the number of grid permeabilities to be history-matched and the number of streamlines/data-points can be more favourable, and therefore the inversion problem may be less underdetermined. Even though we modify the permeability on different coarse grids, the streamlines can be traced and fluid simulation can be performed on a much finer grid (e.g., the underlying geogrid) to avoid problems with loss of accuracy and representation of wells.

We will present two simple synthetic cases to illustrate the multiscale approach. For simplicity, we assume that the reservoir is square, start with a uniform 4×4 grid as the coarsest grid, and recursively refine by subdividing each grid block into four square grid blocks; see Fig. 7. The dimensions of the grids thus become 4×4, 8×8, 16×16, 32×32, etc. In the inversion, we perform only one iteration on all grids, except for the finest grid, where we iterate until convergence. More iterations could have been performed on each refinement level, but we only want to capture the trends of the large-scale permeability structures on each level. The reservoir and fluid parameters (except permeability and the mobility ratio) used in these examples are as described in Section 5. For the two examples we assume quadratic relative permeabilities like for Case 3 and add 5% white noise to the fractional-flow observations.

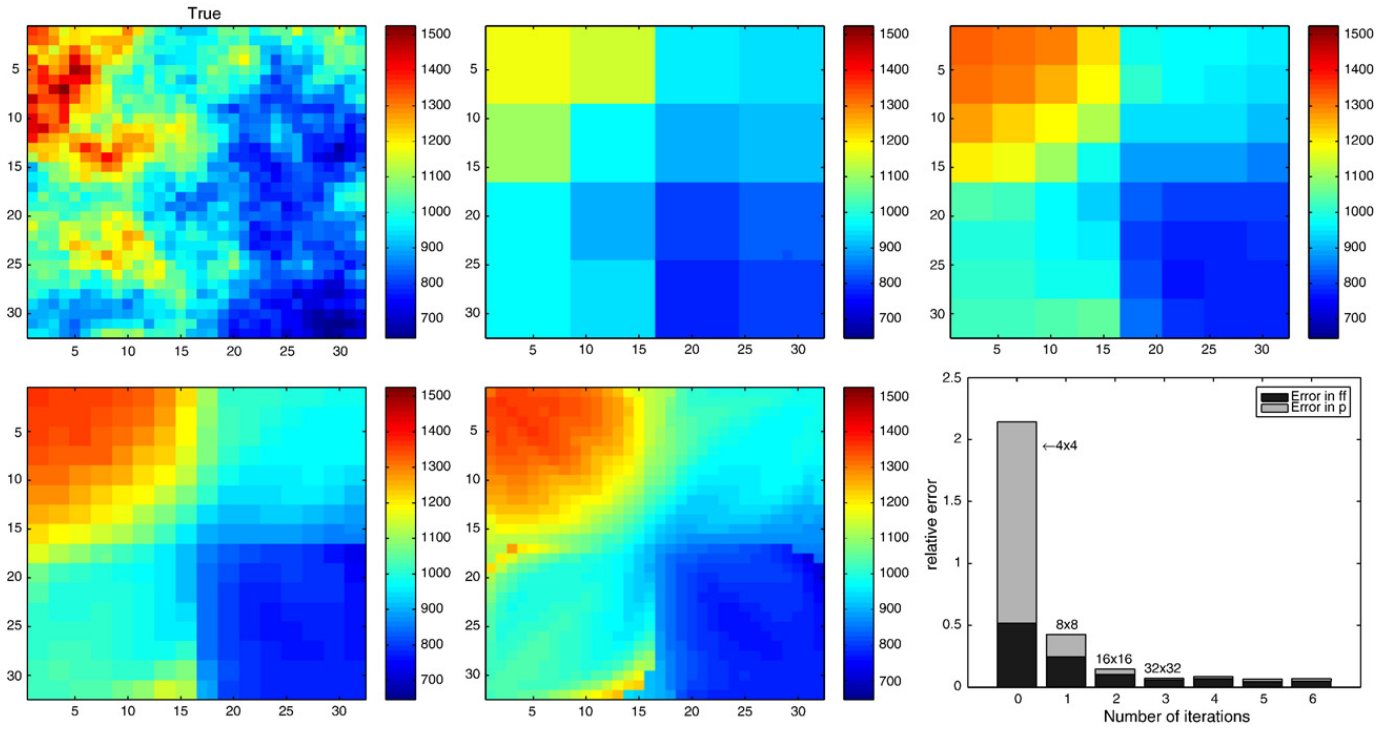

Fig. 9. Case 5. Comparison of inferred permeability fields and relative errors with and without the multiscale approach. The true permeability field in mD (upper left). The four next plots (from left to right) show the inferred permeability field on the 4×4, 8×8, 16×16, and 32×32 grids. The last plot in the second row shows the relative errors for the multiscale approach.

6.1. Case 4: quarter five-spot

This example is similar to Case 1 from Section 5, except that the true permeability field is represented on a 32×32 grid (see Fig. 8). Besides, for this example the oil viscosity is 2.5 cp, which gives an end-point mobility ratio of $M = 2.5$.

Fig. 8 shows the inferred permeability field on each refinement level compared with the permeability field inferred after seven iterations of the inversion algorithm directly on the 32×32 grid. The high permeable region is located already on the 4×4 grid. Even though the inferred permeability field of the multiscale approach seems smoother, the location of the high-permeable region is more accurately positioned and is less smeared out between the wells. On the plot for the final match on the fine grid, the streamline pattern is clearly visible. This effect appears during the last few iterations and seems to be a consequence of an over-parameterisation that could have been avoided if we had terminated the iteration earlier.

Fig. 8 also shows the error reduction with and without the multiscale approach. Although the error reduction is slightly slower for the multiscale approach, the same number of iterations are necessary for convergence for both approaches, and therefore the computational effort for the multiscale method is smaller since fewer iterations are performed on the finest scale.

6.2. Case 5: five-spot

In the next example we revisit Case 3. Fig. 9 shows the inferred permeability field on each refinement level and the inferred field after five iterations directly on the finest grid. Already on the 4×4 grid some of the large-scale structures of the permeability field are located. Compared with the inversion in Case 3, the multiscale approach captures more of the large-scale structures in the reference permeability field and avoids the artificial streamline-induced zonation structure observed in Fig. 6. Moreover, the multiscale approach is faster, because fewer iterations are necessary on the fine scale.

7. Concluding remarks

We have suggested two improvements to the streamline inversion method introduced by Wang and Kovscek (2000). The resulting inversion method is able to match production data and capture large-scale permeability structures, but fails to incorporate the (a priori) variability of the permeability field. Combining the inversion method with existing geostatistical inversion methods, the method can be extended to yield inferred permeability fields that also satisfy geological constraints.

Acknowledgement

Funded by the Uncertainty in Reservoir Evaluation (URE) program at the Norwegian University of Science and Technology and by the Research Council of Norway through grant no. 152732/S30.

References

Caers, J., 2003. Efficient gradual deformation using a streamline-based proxy method. J. Pet. Sci. Eng. 39, 57–83.

Caers, J., Krishnan, S., Wang, Y., Kovscek, A.R., 2002. A geostatistical approach to streamline-based history matching. SPE J. 6, 250–266.

Caers, J., Gross, H., Kovscek, A.R., 2004. A direct sequential simulation approach to streamline based history matching. In: Leuangthong, O., Deutsch, C.V. (Eds.), Geostatistics Banff 2004: Proceedings to the Seventh International Geostatistics Congress. Springer.

Datta-Gupta, A., King, M.J., 1995. A semianalytic approach to tracer flow modeling in heterogeneous permeable media. Adv. Water Resour. 18, 9–24.

Dykstra, H., Parsons, R., 1950. The prediction of oil recovery by waterflood, secondary recovery of oil in the United States, principles and practice, Tech. Rep., second ed. American Petroleum Institute, Dallas, Texas.

Emanuel, A.S., Milliken, W.J., 1998. History Matching Finite Difference Models with 3D Streamlines. SPE Paper, vol. 49000.

Gautier, Y., Noetinger, B., Roggero, F., 2001. History Matching Using a Streamline-Based Approach and Exact Sensitivity Coefficients. SPE Paper, vol. 71626.

Gautier, Y., Noetinger, B., Roggero, F., 2004. History matching using a streamline-based approach and gradual deformation. SPE J. 9 (1), 88–101 (March).

Gross, H., Thiele, M.R., Alexa, M.J., Caers, J.K., Kovscek, A.R., 2004. Streamline-Based History Matching Using Geostatistical Constraints: Application to a Giant, Mature Carbonate Reservoir. SPE Paper, vol. 90069.

Milliken, W.J., Emanuel, A.S., Chakravarty, A., 2000. Applications of 3D Streamline Simulation to Assist History Matching. SPE Paper, vol. 63155.

Thiele, M.R., 2005. Streamline simulation. Eight International Forum on Reservoir Simulation. Stresa/Lago Maggiore, Italy.

Vasco, D.W., Datta-Gupta, A., 1999. Asymptotic solutions for solute transport: a formalism for tracer tomography. Water Resour. Res. 35 (1), 1–16 (January).

Vasco, D.W., Yoon, S., Datta-Gupta, A., 1999. Integrating dynamic data into high-resolution reservoir models using streamline-based analytic sensitivity coefficient. SPE J. 4 (4), 389–399 (December).

Wang, Y., Kovscek, A.R., 2000. A streamline approach for history matching production data. SPE J. 5, 353–362.

Wen, X.-H., Deutsch, C.V., Cullick, A.S., 2003. Inversion of dynamic production data for permeability: fast streamline-based computation of sensitivity coefficients of fractional flow rate. J. Hydrol. 281 (4), 296–312.

Yoon, S., Malallah, A.H., Datta-Gupta, A., Vasco, D.W., Behrens, R.A., 1999. A Multiscale Approach to Production Data Integration Using Streamline Models. SPE Paper, vol. 56653.

Paper II

Adaptive Multiscale Streamline Simulation and Inversion for High-Resolution Geomodels

Vegard Røine Stenerud, Vegard Kippe, Knut-Andreas Lie,
and Akhil Datta-Gupta.

Accepted for publication in *SPE Journal*.

SPE 106228

Adaptive Multiscale Streamline Simulation and Inversion for High-Resolution Geomodels

V. R. Stenerud, SPE, Norwegian U. of Science and Technology; V. Kippe, SINTEF ICT; K.-A. Lie, SINTEF ICT; and A. Datta-Gupta, SPE, Texas A&M U.

This paper was prepared for presentation at the 2007 SPE Reservoir Simulation Symposium held in Houston, Texas, U.S.A., 26–28 February 2007.

Abstract

A particularly efficient reservoir simulator can be obtained by combining a recent multiscale mixed finite-element flow solver with a streamline method for computing fluid transport. This multiscale-streamline method has shown to be a promising approach for fast flow simulations on high-resolution geologic models with multimillion grid cells. The multiscale method solves the pressure equation on a coarse grid while preserving important fine-scale details in the velocity field. Fine-scale heterogeneity is accounted for through a set of generalized, heterogeneous basis functions that are computed numerically by solving local flow problems. When included in the coarse-grid equations, the basis functions ensure that the global equations are consistent with the local properties of the underlying differential operators. The multiscale method offers a substantial gain in computation speed, without significant loss of accuracy, when basis functions are updated infrequently throughout a dynamic simulation.

In this paper we propose to combine the multiscale-streamline method with a recent 'generalized travel-time inversion' method to derive a fast and robust method for history matching high-resolution geo-cellular models. A key point in the new method is the use of sensitivities that are calculated analytically along streamlines with little computational overhead. The sensitivities are used in the travel-time inversion formulation to give a robust quasilinear method that typically converges in a few iterations and generally avoids much of the time-consuming trial-and-errors seen in manual history matching. Moreover, the sensitivities are used to enforce basis functions to be adaptively updated only in areas with relatively large sensitivity to the production response. The sensitivity-based adaptive approach allows us to selectively update only a fraction of the total number of basis functions, which gives substantial savings in computation time for the forward flow simulations.

We demonstrate the power and utility of our approach using a simple 2D model and a highly detailed 3D geomodel. The 3D simulation model consists of more than one million cells with 69 producing wells. Using our proposed approach, history matching over a period of seven years is accomplished in less than twenty minutes on an ordinary workstation PC.

Introduction

It is well known that geomodels derived from static data only – such as geological, seismic, well-log and core data – often fail to reproduce the production history. Reconciling geomodels to the dynamic response of the reservoir is critical for building reliable reservoir models. In the past few years, there have been significant developments in the area of dynamic data integration through the use of inverse modeling. Streamline methods have shown great promise in this regard (Vasco et al. 1999; Wang and Kovscek 2000; Milliken et al. 2001; He et al. 2002; Al-Harbi et al. 2005; Cheng et al. 2006). Streamline-based methods have the advantages that they are highly efficient "forward" simulators and allow production-response sensitivities to be computed analytically using a single flow simulation (Vasco et al. 1999; He et al. 2002; Al-Harbi et al. 2005; Cheng et al. 2006). Sensitivities describe the change in production responses due to small perturbations in reservoir properties such as porosity and permeability and are a vital part of many methods for integrating dynamic data.

Even though streamline simulators provide fast forward simulation compared with a full finite-difference simulation in 3D, the forward simulation is still the most time-consuming part of the history-matching process. A streamline simulation consists of two steps that are repeated: (i) solution of a 3D pressure equation to compute flow velocities; and (ii) solution of 1D transport equations for evolving fluid compositions along representative sets of streamlines, followed by a mapping back to the underlying pressure grid. The first step is referred to as the pressure step and is often the most time-consuming. Consequently, history matching and flow simulation are usually performed on upscaled simulation models, which imposes the need for a subsequent downscaling if the dynamic data are to be integrated in the geomodel. Upscaling and downscaling may result in loss of important fine-scale information.

Recently, so-called multiscale methods have proven to be a promising alternative to standard upscaling, both with respect to accuracy and efficiency (Gautier et al. 1999; Arbogast and Bryant 2002; Jenny et al. 2004; Aarnes et al. 2005). These methods are specially designed to perform well when the underlying parameters exhibit a multiscale structure; that is, when the parameter values span several orders of magnitude or the correlation lengths of the heterogeneity structures vary over several orders. Like standard upscaling methods, the multiscale methods compute pressure and/or velocities by solving the global flow problem on a coarsened grid. However, whereas upscaling methods use local decoupled flow problems to derive upscaled permeabilities or transmissibilities, and thus only preserve the local flow in an averaged sense, multiscale methods use the solutions of these localized flow problems as building blocks to form a global flow solution that is correct in an averaged sense on the coarse grid and at the same time contains representative subscale variations on the original fine grid.

Multiscale methods are primarily targeted at dynamic flows where the pressure needs to be computed repeatedly. Since temporal changes in the coefficients of the pressure equation are typically moderate compared to the spatial variability, it is seldom necessary to recompute the local flow problems each time the pressure is updated. Instead, local flow problems are computed initially as part of a preprocessing step (that is embarrassingly simple to parallelize) and typically only updated if the local domain is swept by a strong front in the fluid compositions or the global flow pattern changes significantly due to shut-in of wells, infill drilling, well conversion, etc. Hence, a pressure update typically consists of recomputing a few local flow problems and then solving a global flow problem on the coarse grid. This means that one can obtain an approximate solution on the original grid at the cost of solving the same problem on a much coarser grid.

In this paper, we combine multiscale-streamline simulation and streamline-based history matching in one efficient approach. As a flow solver we apply the multiscale mixed finite-element method (MsMFEM) (Chen and Hou 2002; Aarnes 2004). MsMFEM produces mass-conservative solutions both on the coarse grid and on the underlying fine grid, is flexible with respect to grid representation (geometry/topology), and has a rigorous mathematical framework.

For the history matching we use the generalized travel-time inversion method (Vasco et al. 1999; He et al. 2002), which has previously been successfully applied to many field cases. There are several advantages associated with travel-time inversion of production data. First, it is robust and computationally efficient. Unlike conventional 'amplitude' matching, which can be highly nonlinear, it has been shown that the travel-time inversion has quasilinear properties (Vasco et al. 1999; Wu and Datta-Gupta 2002). As a result; the minimization proceeds rapidly even if the initial model is not close to the solution. Second, travel-time sensitivities are typically distributed more uniform between wells compared to 'amplitude' sensitivities that tend to be localized near the wells. This prevents over-correction in the near-well regions (Wu and Datta-Gupta 2002). Finally, in practical field applications, production data are often characterized by multiple peaks. Under such conditions, the travel-time inversion can prevent the solution from converging to secondary peaks in the production response (Vasco et al. 1999).

Central in the inversion method is the computation of analytic streamline sensitivities in terms of simple 1-D integrals along streamlines. The sensitivities can be computed using a single streamline simulation. The second novel idea in this paper is a strategy based on sensitivity thresholding for reducing the workload for the forward simulation and for the inversion process. Altogether, the analytic sensitivities are used for three purposes: (i) in the inversion method, (ii) to reduce the computational complexity of the forward simulations by reducing the number of local flow solves, and (iii) to reduce computational complexity of the inversion process.

The outline of our paper is as follows. First, we discuss the basic steps in our proposed approach and illustrate the history-matching procedure using a simple synthetic example. Second, we describe the multiscale-streamline flow simulation and the history-matching procedure. Third, we discuss and demonstrate the impact of selective sensitivity-based workload reduction. Finally, we present a high-resolution history-matching example to demonstrate the efficiency and the practical applicability of our method.

Background and Illustration of the Procedure

Streamline-based history matching utilizes streamline-derived sensitivities to calibrate geomodels to dynamic data. The major steps involved in the proposed process are: (i) Multiscale-streamline flow simulation to compute production responses at the wells. (ii) Quantification of the mismatch between observed and computed production responses via a generalized travel time. An optimal 'travel-time shift' is computed by systematically shifting the computed production responses towards the observed data until the cross-correlation between the two is maximized (He et al. 2002). (iii) Computation of streamline-based analytic sensitivities of the production responses (water-cuts) to reservoir parameters, specifically permeability. (iv) Updating of reservoir properties to match the production history via inverse modeling. We propose a sensitivity-based thresholding strategy to reduce the computational work for this step.

This four-step process is repeated until a satisfactory match in production data is obtained. To reduce the computational workload for the forward simulation, we propose to reuse basis functions in regions with low sensitivity to the production responses.

In the next sections we will discuss the details of the mathematical formulation behind the multiscale mixed finite-element formulation and the inversion method, and propose a sensitivity-based strategy for selective work reduction. However, for clarity of exposition, we first illustrate the history-matching procedure using a synthetic 2-D example.

A Synthetic Example. This synthetic case (Case 1) involves reconstruction of a reference permeability distribution on a uniform 21×21 grid, based on the observed water-cut production history from a 9-spot pattern. For the forward simulation we apply the multiscale-streamline

simulator (to be described below), with the 21×21 grid as the underlying fine grid. We construct a uniform coarse grid of dimension 7×7 so that each block in the coarse grid consists of 3×3 subcells. **Figure 1** illustrates the two-grid approach for a slightly more general case with nonmatching blocks in the coarse grid. The multiscale simulator basically works as follows: For each pair of adjacent blocks in the coarse grid, a local flow problem is solved to obtain a local (multiscale) basis function associated with the corresponding internal face in the coarse grid (see **Fig. 2**). The local basis functions are then incorporated into a global system of equations defined on the coarse grid, which is solved to obtain a flux for each face in the coarse grid. Fine-scale flow velocities are then obtained by multiplying the coarse-grid fluxes with the corresponding multiscale basis function and summing over all faces in the coarse grid.

The flow is described using quadratic relative permeability curves with zero residual oil and water saturations and end-point mobility ratio $M_{end} = \mu_o/\mu_w$. We consider three flow cases: two with favorable mobility ratios (M_{end}=0.2 and M_{end}=0.5) and one with unfavorable mobility ratio (M_{end}=10). Synthetic dynamic data were generated by adding 5% white noise to the water-cut responses obtained from the reference permeability field using the streamline method with a standard two-point pressure solver. We treat these as the observed data. Next, starting from a homogenous initial permeability field, we match the water-cut data via the generalized travel-time inversion. To demonstrate the robustness of this method, we match the observed data for M_{end}=0.2, 0.5, 10 starting from a homogeneous initial permeability field. Here the permeability in each cell is treated as an adjustable parameter, giving a total of 441 unknown parameters to be estimated.

Plots of the time-shift and amplitude residuals in **Fig. 3** show that the iteration converges very fast (after 3-4 iterations). **Figure 4** shows a comparison of the initial and final match of the water-cut curves for M_{end}=0.5 for the three wells with lowest initial, highest initial, and highest final mismatch after six iterations. Overall, the match to the production data is quite satisfactory for all three mobility ratios. The corresponding permeability fields after six iterations are shown in **Fig. 5**. The three permeability models clearly capture the large-scale trends of the reference permeability field; a unique solution is not obtained since the data integration is ill-posed.

Mathematical Formulation

Multiscale Flow Simulation. An important aspect of the proposed history-matching algorithm is the use of a multiscale mixed finite-element method (MsMFEM) for the pressure equation. This method belongs to a family of multiscale finite-element methods, first introduced by Hou and Wu (1997). The basic idea of the methods is to construct special finite-element basis functions that are adaptive to the local properties of the elliptic differential operator. To ensure local mass conservation on the coarse and fine grid, Chen and Hou (2002) introduced a multiscale method based on a mixed finite-element discretization. The method was later modified by Aarnes (2004) to ensure local mass conservation also for

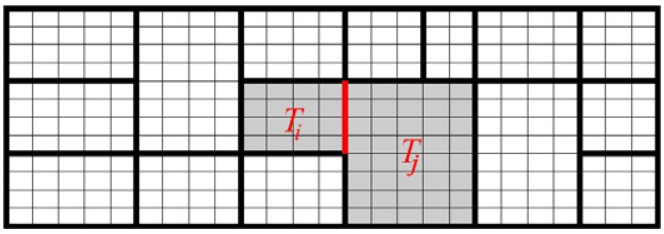

Fig. 1 - A general coarse grid overlying a uniform fine grid with the gray area giving support of basis function Ψ_{ij}, which is associated with the edge/face indicated by the red line.

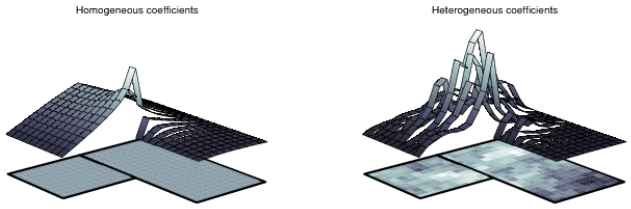

Fig. 2 – The x-component of the velocity basis function associated with an edge/face between two blocks of different size for a homogeneous and a heterogeneous permeability field, respectively.

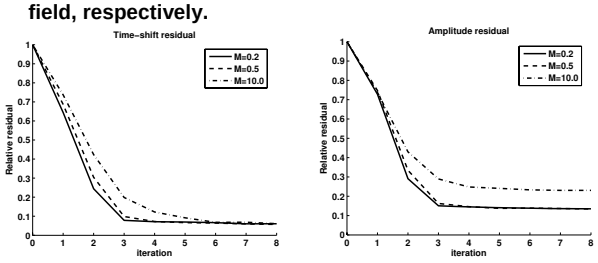

Fig. 3 - Case 1: Reduction of residuals for all producers for mobility ratios M_{end}=0.2, 0.5, and 10.

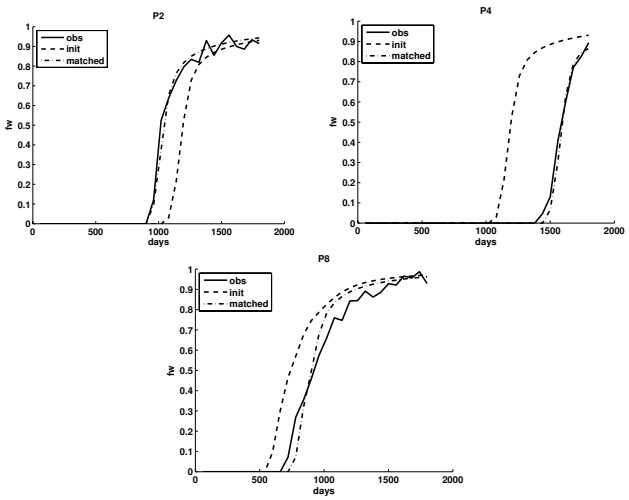

Fig. 4 - Case 1: Water-cut curves for water for producers P2 (north-west), P4 (south-east), and P8 (east). These wells had lowest initial, highest initial, and highest final mismatch, respectively.

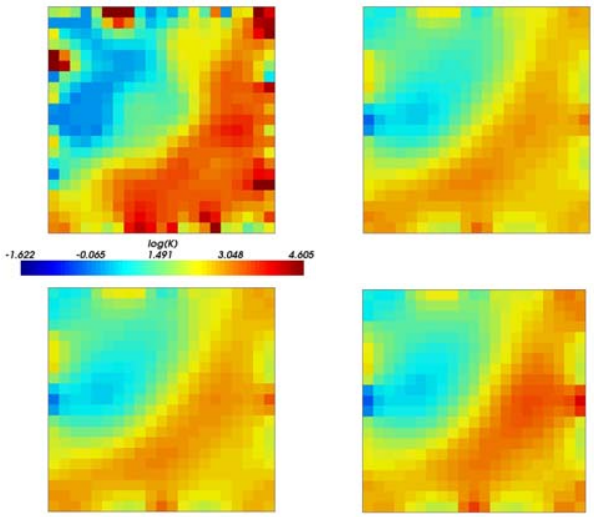

Fig. 5 – Case 1: The plots show, from upper left to lower right, reference permeability field and matches obtained after six iterations for mobility ratios M_{end}=0.2, 0.5 and 10.

blocks containing source terms. In the current paper, we use a slightly different formulation due to Aarnes and Lie (2004).

Governing Equations. We consider incompressible two-phase flow of oil and water in a non-deformable permeable medium. For simplicity, we neglect the effects of gravity, compressibility and capillary forces. For simplicity, we also assume no-flow boundary conditions. The flow equations can be formulated as an elliptic equation for the pressure p and the total velocity u,

$$u = -\lambda_t k \nabla p, \quad \nabla \cdot u = q. \qquad (1)$$

Here q is a source term representing injection and production wells, k is the absolute permeability, and $\lambda_t = \lambda_t(S_w)$ is the total mobility. We will solve Eq. 1 for the fine-scale velocity field u using MsMFEM, for which the details will be described in the next subsections.

The velocity field is used to obtain a streamline distribution. Along each streamline the 3D transport equation reduces to a 1D transport equation with the time-of-flight τ as the spatial coordinate

$$\frac{\partial S_w}{\partial t} + \frac{\partial f_w(S_w)}{\partial \tau} = 0. \qquad (2)$$

The time-of-flight is defined as

$$\tau(r) = \int_0^r \frac{\phi(\xi)}{|u(\xi)|} d\xi, \qquad (3)$$

and expresses the time it takes a passive particle to travel a distance r along the streamline. Equation 2 is solved forward in time along each streamline using front tracking (Holden and Risebro 2002). This method is unconditionally stable and therefore avoids the usual CFL-constraint that would otherwise have put a severe limitation on the size of the time step.

Mixed Finite Elements. The mixed finite-element formulation of the flow equation (Eq. 1) in a domain Ω seeks a pair (u,p) in $U \times V$, such that

$$\int_\Omega u \cdot (\lambda k)^{-1} v \, dx - \int_\Omega p \nabla \cdot v \, dx = 0, \qquad \forall v \in U, \qquad (4)$$

$$\int_\Omega l \nabla \cdot u \, dx = \int_\Omega q l \, dx, \quad \forall l \in V. \qquad (5)$$

Here U and V are (finite-dimensional) function spaces for pressure and velocity, respectively. Now, letting $\{\Psi_i\}$ and $\{\Phi_k\}$ be bases for U and V, respectively, we obtain approximations $u = \Sigma u_i \Psi_i$ and $p = \Sigma p_k \Phi_k$, where the coefficients $\mathbf{u} = \{u_i\}$ and $\mathbf{p} = \{p_k\}$ solve a linear system of the form

$$\begin{bmatrix} \mathbf{B} & \mathbf{C} \\ \mathbf{C}^T & \mathbf{0} \end{bmatrix} \begin{bmatrix} \mathbf{u} \\ -\mathbf{p} \end{bmatrix} = \begin{bmatrix} \mathbf{0} \\ \mathbf{q} \end{bmatrix}, \qquad (6)$$

where $\boldsymbol{B} = \{b_{ij}\}$, $\boldsymbol{C} = \{c_{ik}\}$ and $\boldsymbol{q} = \{q_k\}$ are defined by

$$b_{ij} = \int_\Omega \Psi_i \cdot (\lambda k)^{-1} \Psi_j \, dx, \qquad (7)$$

$$c_{ik} = \int_\Omega \Phi_k \nabla \cdot \Psi_i \, dx, \qquad (8)$$

$$q_k = \int_\Omega \Phi_k q \, dx. \qquad (9)$$

Multiscale Basis Functions. In a standard discretization, the spaces U and V typically consist of low-order piecewise polynomials. In multiscale methods, U and V are given by the solution of local flow problems. For incompressible flows, the actual pressure solution is immaterial for the flow simulation, and so only the velocity field is needed. We will therefore only construct an accurate multiscale approximation space U^{ms} for the velocity and use a standard approximation space V for pressure consisting of piecewise constant functions.

Let $\{K_m\}$ be a partitioning of Ω into mutually disjoint (fine) grid cells. Furthermore, let $\{T_i\}$ be a coarse partitioning of Ω, in such a way that whenever $K_m \cap T_i \neq 0$, then $K_m \subset T_i$ (see Fig. 1). Let Γ_{ij} denote the non-degenerate interfaces $\Gamma_{ij} = \partial T_i \cap \partial T_j$. For each Γ_{ij}, we assign a basis function Ψ_{ij} in U^{ms}, and for each T_i we assign a basis function Φ_i in V. The basis function Ψ_{ij} is obtained by forcing a unit flow from block T_i to T_j; that is, by solving a local flow problem in $\Omega_{ij} = T_i \cup T_j$

$$\Psi_{ij} = -\lambda_t k \nabla \Phi_{ij}, \quad \nabla \cdot \Psi_{ij} = \begin{cases} w_i(x), & x \in T_i, \\ -w_j(x), & x \in T_j, \end{cases} \qquad (10)$$

with $\Psi \cdot n = 0$ on the boundary of Ω_{ij}. Here the total mobility $\lambda_t = \lambda_t(S_w)$ is given on the underlying fine grid K_m. To give a unit flow from T_i to T_j, the source terms $w_i(x)$ are normalized

$$w_i(x) = W_i(x) \cdot \left(\int_{T_i} W_i(\xi) d\xi \right)^{-1}. \qquad (11)$$

To ensure a conservative approximation of v on the fine grid, we choose $W_i = q$ for coarse blocks containing a well (Aarnes 2004). For coarse blocks where $q = 0$, we scale W_i according to the trace of the permeability tensor (Arnes et al. 2006); i.e., we use

$$W_i(x) = \begin{cases} \text{trace}(k(x)), & \text{if } q(x)\big|_{T_i} = 0, \\ q(x), & \text{otherwise.} \end{cases} \quad \text{(12)}$$

The local flow problems in Eq. 10 can be solved numerically by any consistent and conservative method; here we use the standard two-point flux-approximation (TPFA) scheme. The corresponding basis functions can be seen as generalizations of the lowest-order Raviart-Thomas basis functions in a standard mixed method (Raviart and Thomas 1975). Figure 2 illustrates the *x*-velocity basis functions in two different cases.

Implementation of MsMFEM. We will briefly describe some implementation aspects related to the efficiency and generality of MsMFEM. The mixed formulation leads to an indefinite global system (Eq. 6), which may be more difficult to solve efficiently than the symmetric positive-definite (SPD) systems that typically arise from standard discretization methods. However, it is possible to obtain an SPD system also for MsMFEM by reformulating Eq. 4 and Eq. 5 to an equivalent (so-called) hybrid system. Like the indefinite system in Eq. 6, the hybrid system will be sparse because the basis functions have local support, and the solution can be obtained using one of the efficient linear solvers specialized for sparse SPD systems. The hybrid formulation is described in more detail by Aarnes et al. (to appear). We note that in our current implementation, we solve the global system in Eq. 6 using a direct sparse solver, since we only deal with moderately sized coarse systems.

Most of the computational work in MsMFEM is associated with solving the local flow problems defined by Eqs. 10 to 12, and the choice of solution strategy for these equations is crucial to the overall performance of the method. The local problems are usually small to moderately sized, and the resulting systems can be solved using iterative or direct sparse linear solvers. The optimal choice of linear solver typically depends on the problem size, and we recommend having available a range of solvers tuned to different system sizes. Alternatively, if one has access to a highly efficient solver for large sparse systems, it may be beneficial to lump together several local problems to form a larger system. Solving larger systems may be advantageous because the most efficient linear solvers typically require an initial setup phase. Regardless of the choice of solution strategy, efficient parallelization is easy, since the local flow problems are completely decoupled.

In the examples presented in this paper, we only use Cartesian grids. However, MsMFEM is flexible with respect to the choice of both fine and coarse grids. Given a fine-grid solver, basis functions can be defined for almost any collection of connected fine-grid cells (Aarnes et al. 2006). Recently, the method has been implemented for (matching) corner-point and tetrahedral grids in 3D (Aarnes et al., to appear), and based on this experience we are confident that the methodology presented in the current paper is easily extended to corner-point grid models.

Integration of Production Data. In our approach, integration of production data is carried out using a 'generalized travel-time inversion' as described by He et al. (2002). First, the production-data mismatch is determined by computing a 'generalized travel-time misfit' for the water-cut at each producing well. This is accomplished by shifting the computed water-cuts towards the observed data until the correlation between the two is maximized. The inversion algorithm simultaneously minimizes the travel-time misfit for all the wells using an iterative least-square minimization algorithm (LSQR) (Vasco et al. 1999; He et al. 2002). The basic underlying principles behind the history-matching algorithm are briefly as follows:

- Match the field-production history within a specified tolerance. This is accomplished by minimizing the travel-time misfit for water-cut.
- Preserve geological realism by keeping changes to the prior geological model minimal, if possible. The prior model already incorporates static data (well and seismic data) and available geological information.
- Only allow for smooth and large-scale changes; the production data has low resolution and cannot be used to infer small-scale variations in reservoir properties.

Formulation of Inverse Problem. Mathematically, this algorithm leads to the minimization of a penalized misfit function consisting of the following three terms (Vasco et al. 1999; He et al. 2002):

$$\left\|\Delta\tilde{\mathbf{t}} - \mathbf{G}\delta\mathbf{m}\right\| + \beta_1\left\|\delta\mathbf{m}\right\| + \beta_2\left\|\mathbf{L}\delta\mathbf{m}\right\| \quad \text{(13)}$$

Here $\Delta\tilde{\mathbf{t}}$ is the vector of generalized travel-time shifts at the wells, $\mathbf{G}$ is the sensitivity matrix containing the sensitivities of the generalized travel time with respect to changes $\delta\mathbf{m}$ in the reservoir properties, and $\mathbf{L}$ is a second-order spatial difference operator. The first term ensures that the difference between the observed and calculated production response is minimized. The two remaining terms are standard regularization terms. The second term is a norm constraint that penalizes deviations from the initial (prior) geological model and as such helps to preserve the geological realism in the history match. The third term, which is a 'roughness' constraint that measures the regularity of the changes, is introduced to stabilize the inversion. Physically, it only allows for large-scale changes that are consistent with the low resolution of the production data. The weights β_1 and β_2 determine the relative strengths of the prior model and the roughness term.

The minimum in Eq. 13 can be obtained by an iterative least-squares solution to the augmented linear system

$$\begin{pmatrix} \mathbf{G} \\ \beta_1\mathbf{I} \\ \beta_2\mathbf{L} \end{pmatrix}\delta\mathbf{m} = \begin{pmatrix} \Delta\tilde{\mathbf{t}} \\ \mathbf{0} \\ \mathbf{0} \end{pmatrix}. \quad \text{(14)}$$

This system is solved with the iterative least-square minimization algorithm, LSQR (Paige and Saunders 1982), for which the computational cost scales linearly with respect to the number of degrees-of-freedom (Vega et al. 2004). Fine-grid sensitivities close to zero are eliminated, which makes the system more sparse and reduces the number of arithmetic operations for the LSQR-iterations. In the next section we will discuss an approach to further reduce the number of nonzero sensitivities based on thresholding of coarse-grid sensitivities.

In our implementations we focus on inverting water-cut data. However, the generalized travel-time inversion method has earlier been extended to compressible three-phase flow, so

that water-cut and gas-oil ratios are incorporated jointly (Cheng et al. 2006).

Water-Cut Sensitivities. A unique feature of streamline methods is that the parameter sensitivities can be computed using a single flow simulation, leading to very fast history-matching or inverse-modeling algorithms. Moreover, because the sensitivities are simple integrals along streamlines, the runtime scales very favorable with respect to the number of grid cells, thus making streamlines the preferred approach for history matching highly-detailed geological models.

To derive the desired streamline-based sensitivities, we consider the velocity of propagation for a given saturation contour S_w along a streamline,

$$\left.\frac{\partial \tau}{\partial t}\right|_{Sw} = \frac{df_w}{dS_w}, \quad \text{.....(15)}$$

from which it follows that the arrival time t_a of the saturation contour will be,

$$t_a = \tau \Big/ \frac{df_w}{dS_w} \quad \text{..... (16)}$$

We use the above relationship to compute the sensitivity of the arrival time of the saturation contour based on the sensitivity of the time-of-flight (Vasco et al. 1999; He et al. 2002). Specifically, the sensitivity of the arrival time of the saturation front with respect to reservoir parameter m is computed as,

$$\frac{\partial t_a}{\partial m} = \frac{\dfrac{\partial \tau}{\partial m}}{\dfrac{df_w}{dS_w}}. \quad \text{.....(17)}$$

Here the sensitivity of the time-of-flight is computed analytically from a single streamline simulation under the assumption that the streamlines do not shift because of small perturbations in reservoir properties. For example, the time-of-flight sensitivity with respect to permeability in grid cell i, under the assumption of the same permeability for the whole grid cell, will be given by (Vasco et al. 1999)

$$\frac{\partial \tau}{\partial k_i} = \frac{\partial \Delta \tau_i}{\partial k_i} = \int_{\Sigma_i} \frac{\partial s(\xi)}{\partial k_i} d\xi = -\int_{\Sigma_i} \frac{s(\xi)}{k_i} d\xi = -\frac{\Delta \tau_i}{k_i}, \quad \text{.....(18)}$$

where the integral is along the streamline trajectory Σ and $s(x)$ is the 'slowness' defined as the reciprocal of the total interstitial velocity

$$s(x) = \frac{\phi(x)}{|u(x)|} = \frac{\phi(x)}{\lambda_t k(x) |\nabla p|}. \quad \text{.....(19)}$$

Similarly, the time-of-flight sensitivities can be calculated with respect to mobility or to the product of mobility and permeability.

Finally, the sensitivity of the shift $\Delta \tilde{t}$ in the generalized travel time with respect to reservoir parameters is given by

$$\frac{\partial \Delta \tilde{\tau}}{\partial m} = -\frac{1}{N_d} \sum_{a=1}^{N_d} \frac{\partial t_a}{\partial m}, \quad \text{.....(20)}$$

where N_d represents the number of observed data for a well. Worth mentioning here is an important practical aspect. Our experience indicates that the selective work reduction and the data integration are more robust if the sensitivities are made dimensionless by calculating the sensitivities of the logarithm of the time shifts as described by He et al. (2002).

Finally, we remark that the streamline-based sensitivity computation has also been addressed for cases including gravity, changing field conditions, and fractured reservoirs (He et al. 2002; Al-Harbi et al. 2005).

Sensitivity-Based Selective Work Reduction

In this section, we discuss how the sensitivities introduced above can be used to reduce the computational complexity of the history matching with negligible loss in quality of the derived match. To this end, we compute a sensitivity coefficient for each coarse block by summing the corresponding fine-grid sensitivities (Yoon et al. 2001). Based on these sensitivity coefficients, we decide when to update and when to not update the corresponding basis functions. Similarly, we will reduce the inverse system by only including fine-scale sensitivities from coarse blocks having a sufficiently high sensitivity coefficient as described in more detail below.

Selective Updating of Basis Functions. We propose to reduce the computational work for MsMFEM by only updating basis functions in areas with large production-response sensitivities. To determine which basis functions to update, one can either: (i) use a predefined threshold for the sensitivity values, or (ii) update a predefined fraction of the basis functions. The first approach is fully adaptive in the sense that the number of updated basis functions may change from iteration to iteration. However, this approach requires (general) guidelines for setting the threshold. The second approach requires us to sort the sensitivities. This is a minor concern since the number of operations for sorting N numbers scales like $N \cdot \log N$ and the number of basis functions scales with the number of coarse blocks. For our implementations we therefore stick to the second approach.

By inspecting Eq. 10, we notice that there are three factors that may require the basis functions to be updated before a new pressure solve. First of all, we notice that if the absolute permeability $k(x)$ changes, the basis functions will change, too. In history matching, the absolute permeability will typically change in certain regions from one forward simulation to the next. Secondly, if the well rate q changes, the source terms $w_i(x)$ will change and hence basis functions with support in well-blocks will change. Finally, if the total mobility λ_t changes, due to changes in saturation (or viscosities), the basis functions will change.

In the first flow simulation of the history-matching procedure, we update all basis functions in every pressure step, because no sensitivities are yet available. (In a more sophisticated implementation, one would typically have used another kind of indicator to ensure that basis functions are only updated near the saturation front (Aarnes 2004; Jenny et al. 2004)). After the first simulation, the permeability field is updated by the inversion method. Since the permeability field has changed, we should, at least in principle, recalculate all basis functions for the first pressure step of the next flow simulation. For the subsequent pressure steps of the simulation, we apply the proposed selective updating strategy.

For the subsequent simulations we repeat the strategy of the second simulation. The approach described in this paragraph, when x% of the basis functions are updated dynamically each time step, is referred to as x% DU (dynamical update). Finally, we remark that for 0% DU, sensitivities are not really needed. Therefore, if we for this strategy choose to not update basis functions during the first flow simulation, we will denote the strategy 0% DU*. This special case deviates from what we specified above.

An extended approach would be to reuse basis functions from the previous forward simulation in the coarse blocks where the absolute permeability has undergone small or no changes in the last inversion step, or generally in coarse blocks that have little effect on the overall production characteristics. We will refer to this strategy, where x% of the basis functions are updated initially and the remaining *(100-x)*% are kept from the previous flow simulation, as x% IU (initial update).

Selective Reduction of the Inversion System. Since the water-cut data contain limited information about fine-scale variations, it can be advantageous to avoid involving areas of low sensitivity in the inversion, and instead focus on resolving large-scale structures in areas with higher sensitivities. We therefore propose to eliminate fine-scale sensitivities from the LSQR-system (Eq. 14) in areas of low sensitivity to reduce the computational work in the inversion process. To determine the areas of low and high sensitivity, we use the sensitivity coefficients of the coarse grid-blocks. That is, we introduce a threshold and only include fine-scale sensitivities associated with cells inside coarse blocks having a summed sensitivity above the given threshold. The coarse blocks that are eliminated in this process will usually mainly contain cells with zero or low sensitivity.

The constraints involved in Eq. 13 are important for the elimination of coarse blocks to work. As for the thresholding of basis functions, we can either use a predefined threshold for the sensitivity values or a predefined fraction of coarse blocks; here we use the second approach. Henceforth, keeping y% of the coarse blocks is referred to as y% CB. It should be noted that eliminating fine cells for a fraction of the coarse blocks having low sensitivity will not necessarily decrease the number of fine-grid sensitivities in the inverse system by the same fraction. The reason is cells with zero or small sensitivity are already eliminated, and such fine-grid sensitivities are more likely represented in coarse blocks with low sensitivity.

Impact of Selective Work Reduction To investigate the accuracy of the proposed selective work reduction, we apply it to the synthetic 9-spot case presented earlier in this paper (Case 1). We will still refer to this case as Case 1 even though we will vary some parameters and strategies for selective work reduction. To further assess the quality of the data integration, we will in the following also report the average discrepancy between the reference and matched permeability field measured by

$$\overline{\Delta \log k} = \frac{1}{N} \sum_{i=1}^{N} | \log(k_i^{\text{reference}}) - \log(k_i^{\text{derived}}) | \quad \text{.....(21)}$$

Further, we also report time-shift and amplitude residuals measured by $\left\| \Delta \tilde{\mathbf{t}} \right\|_2$ and

$$\left(\sum_k \sum_j \left[f_w^{\text{obs}}\left(t_j^k\right) - f_w^{\text{cal}}\left(t_j^k\right) \right]^2 \right)^{\frac{1}{2}} \quad \text{.....(22)}$$

respectively. Here f^{obs} and f^{cal} are the observed and calculated water-cut data, respectively, in well k at time j.

To test our work reduction strategy we use a 5×5 test matrix with x% dynamical update and y% initial update for x,y=0,25,…,100. **Figure 6** shows the reduction of time-shift and amplitude residuals after six iterations, as well as the discrepancy between matched and reference permeability fields, compared with similar results obtained by using the full method with a TPFA pressure solver. Judging from the amplitude residual and the permeability discrepancy, the data are well matched for all parameters x and y, and the quality of the history match does not seem to decline dramatically compared with the TPFA solver. For the time-shift residual, the use of the multiscale pressure solver gives better match than for the TPFA solver. On the other hand, this measure is also more sensitive to the choice of parameters for the selective work reduction. The quality of the match generally decays with decreasing percentage of cells being dynamically updated, except for the time-residual for M_{end}=0.5, which somewhat surprisingly shows the opposite trend.

The derived permeability fields for the unfavorable mobility ratio do not seem to change much when reducing the number of dynamically updated basis functions. Following Aarnes (2004), one can argue that it is in general quite safe to reduce the number of dynamically updated basis functions for unfavorable flow cases, since these are characterized by weak shocks and mostly smooth variations in the total mobility. For the favorable mobility ratio (M_{end}=0.2), the derived permeability fields seem to change more by reducing the fraction of basis functions updated; see **Fig. 7**. In this case, the flow will generally have strong saturation fronts, which induce major changes in the basis functions as the leading water fronts move through the corresponding grid blocks.

Finally, we investigate the effect of the proposed strategy for selective reduction of the inverse system. To this end, we keep the fine-grid sensitivities corresponding to 100%, 75%, and 50% of the coarse blocks, selected by thresholding the summed sensitivities in the coarse grid. This strategy was tested in combination with x% dynamical update for x=0,25,…,100. Reducing the number of parameters in the inversion had little influence on the convergence of the inversion and small effect on the quality of the final match (see **Fig. 8** and Table 1). Some derived permeability fields for M_{end}=0.5 are shown in **Fig. 9**. On the other hand, the inverse system could not be reduced much further than 50%. For lower values, we typically observed lack of convergence and/or (highly) non-realistic final matches. We also note that for some cases, the selective reduction of the inverse system resulted in a slightly slower convergence for the inversion. The method converged to the same residual level as without selective work reduction, but the inversion required one or two additional iterations, thus resulting in increased total computation time. Even though the selective reduction of the inversion system can result in a slightly slower convergence, our experiments demonstrate robustness for the generalized travel-time inversion.

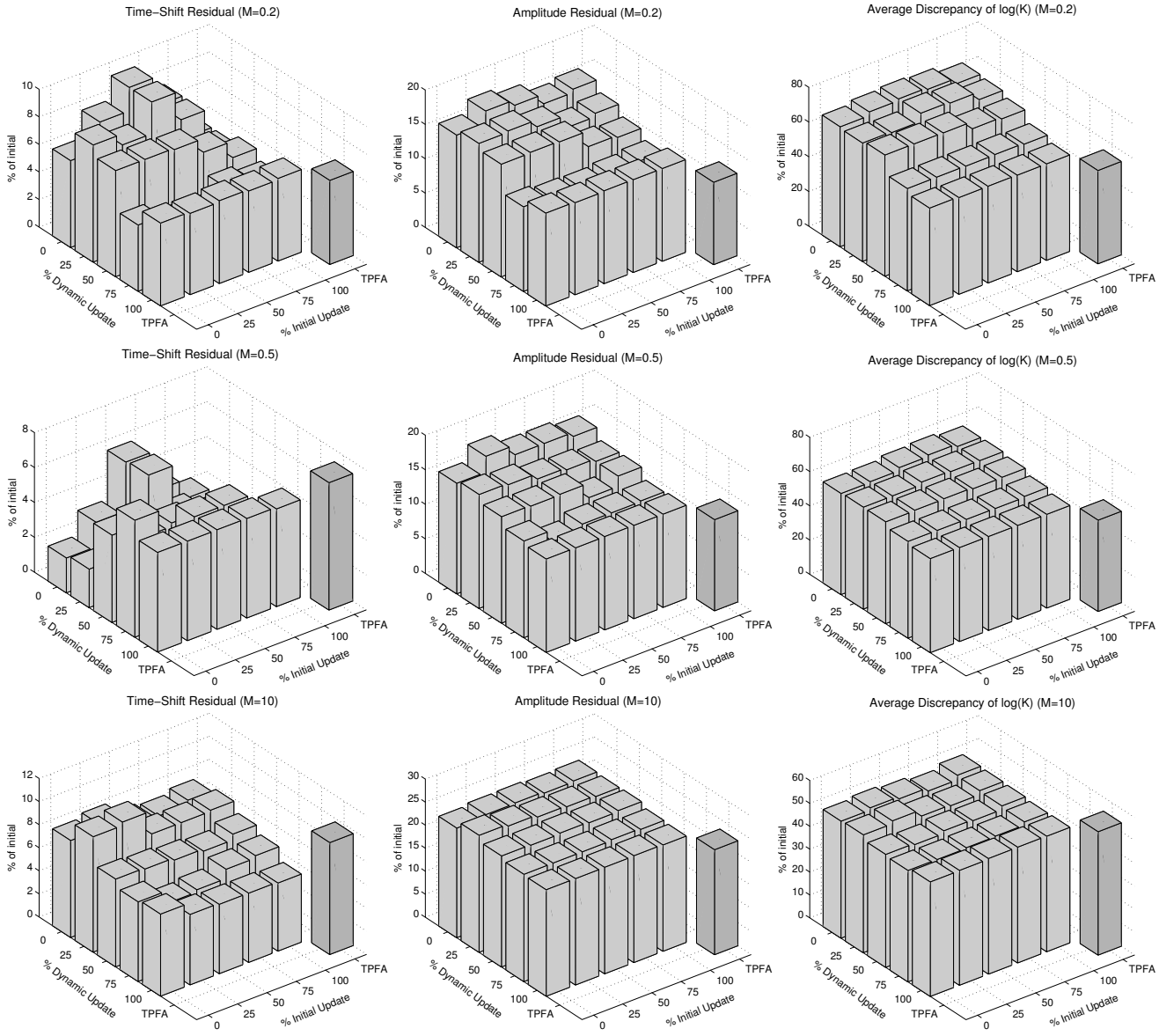

Fig. 6 – Case 1: Robustness of selective work reduction for basis function updates.

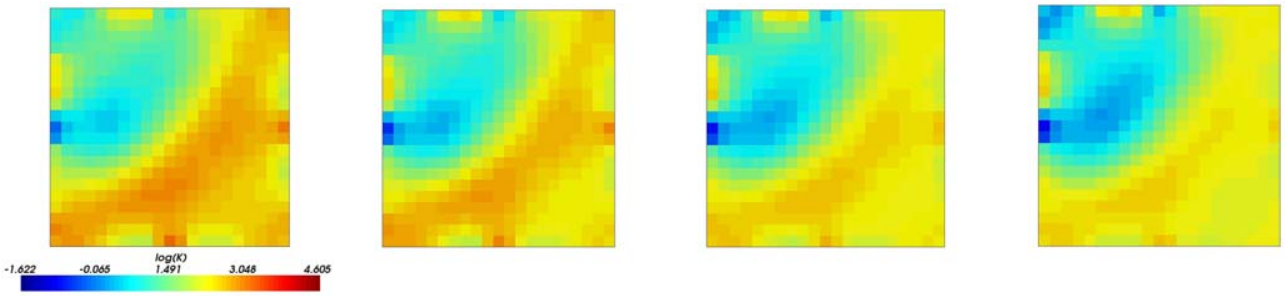

Fig. 7 – Case 1: Derived permeability field updating (from upper left to lower right) 100%, 75%, 50%, and 25% of the basis functions dynamically for mobility ratio M_{end}=0.2. The reference permeability field is shown in Fig. 5.

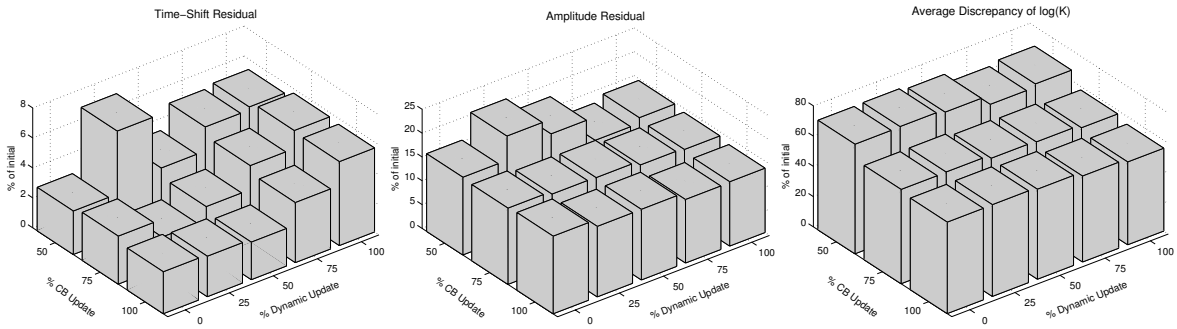

Fig. 8 – Case 1: Robustness of selective work reduction of inverse system for mobility ratio M_{end}=0.5.

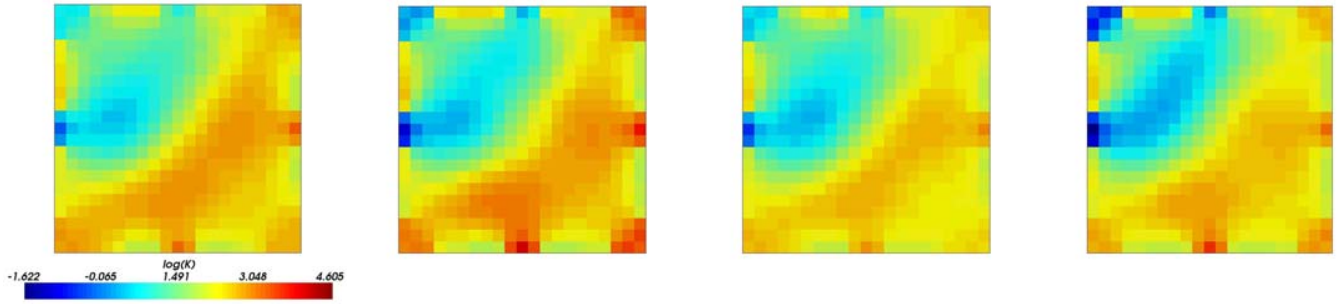

a) 100% DU + 75% CB **b) 100% DU + 50% CB** **c) 50% DU + 75% CB** **d) 50% DU + 50% CB**

Fig 9 – Case 1: Derived permeability field using selective work reduction also for the inversion system. Mobility ratio M_{end}=0.5. The reference permeability field is shown in Fig. 5.

TABLE 1 – Case 1: REDUCTION OF MISFIT FOR SELECTIVE WORK REDUCTION OF INVERSE SYSTEM

Method			M_{end}=0.2			M_{end}=0.5			M_{end}=10		
DU	IU	CB	T (res. %)	A (res. %)	Δlog(*k*)	T (res. %)	A (res. %)	Δlog(*k*)	T (res. %)	A (res. %)	Δlog(*k*)
Initial			100.0	100.0	1.045	100.0	100.0	1.045	100.0	100.0	1.045
100%	100%	100%	6.0	13.5	0.581	5.6	13.5	0.572	5.9	23.1	0.527
100%	100%	75%	5.8	13.6	0.602	5.7	14.1	0.602	7.4	23.1	0.564
100%	100%	50%	8.1	17.3	0.623	5.3	14.6	0.698	7.0	27.5	0.695
50%	100%	75%	4.8	16.3	0.672	2.9	15.3	0.629	6.8	23.3	0.572
50%	100%	50%	3.8	13.7	0.670	3.5	18.3	0.741	19.1	29.4	0.638

History Matching a Full 3D Geomodel

In this section we demonstrate the feasibility of the approach for field studies by application to a high-resolution 3-D example (Case 2). As mentioned before, streamlines and the time-of-flight are used to compute the sensitivity of the production data with respect to reservoir parameters as described above. In this synthetic field-scale example, water-cuts were matched to update the reservoir permeability distribution using the multiscale-streamline simulator for the forward simulation.

Model Description. The geomodel consists of a fine grid with 256×128×32 cells, which gives a total of 1,048,576 grid cells, each of size 10×10×2 m. The fine-grid cells are collected into a uniform 32×16×8 coarse grid, so that each coarse block consists of 8×8×4 cells in the fine grid. All the cells are treated as active.

The permeability is log-normally distributed in the range 0.017 mD to 79.5 mD with mean 2.2 mD (see **Fig. 10b**). The correlation length is about 270 meters in the horizontal direction and about 90 meters in the vertical direction. For our purposes, this permeability field was used as a true model, from which we generated our synthetic production data using the standard TPFA method directly on the fine grid.

A total number of 32 injectors and 69 producers were included in the simulation model (see **Fig. 11**). All the wells are vertical and intersect all layers. The production history consists of 2475 days of water-cut data from the 69 producers (**Fig. 12**). The water injectors were injecting at constant total reservoir volume rate of 1609 bbl/day, and each producer was producing with constant reservoir volume rate fulfilling the total voidage rate. For each simulation, we used 15 pressure steps of length 165 days, quadratic relative permeability curves, and end-point mobility ratio of M_{end}=5.

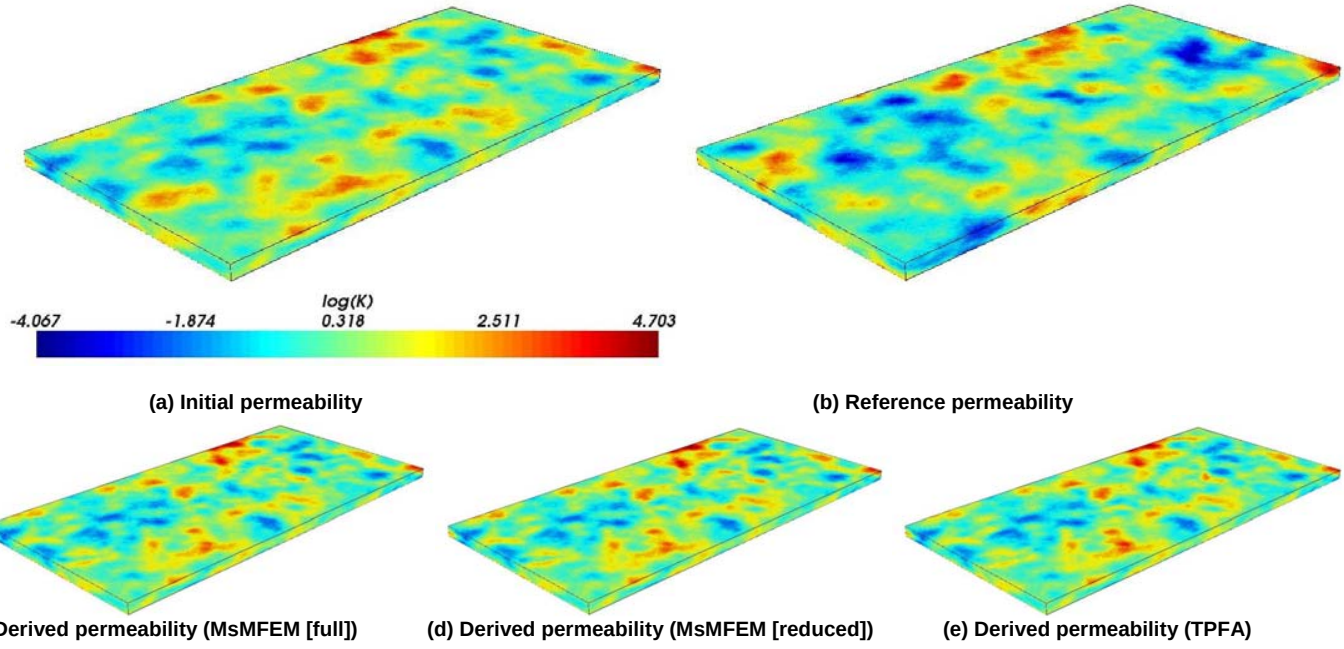

(a) Initial permeability

(b) Reference permeability

(c) Derived permeability (MsMFEM [full])

(d) Derived permeability (MsMFEM [reduced])

(e) Derived permeability (TPFA)

Fig. 10 – Case 2: Initial, reference and derived permeability fields.

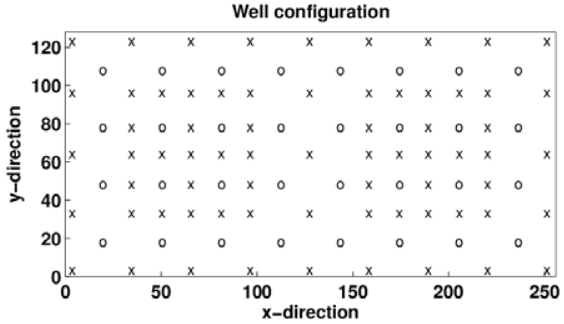

Fig. 11 – Case 2: Well configuration for the geologic model example. The symbol x represents a producer while the symbol o represents an injector.

Integration of Production Data. To generate an initial permeability model, we treat the permeability values in the well-blocks of the reference model as known data. By conditioning on the well blocks, sequential Gaussian simulation was used to generate multiple realizations of the permeability model (Deutsch and Journel 1998).

In the following we will mainly consider three approaches: MsMFEM [full], MsMFEM [reduced], and TPFA. The two first approaches are multiscale approaches, while the last one simulates directly on the fine grid. Further, for the first and the last approach no selective work reduction occurs. For MsMFEM [reduced], the extended approach for reducing the computations of basis functions is applied. For each new forward simulation, the basis functions are sorted according to summed sensitivities and the basis functions having the lowest 50% sensitivites are kept from the previous flow simulation. The remaining 50% of the basis functions are updated once before the first pressure solve. Moreover, selective reduction of the inverse system is used to keep fine-grid sensitivities only for 50% of the coarse blocks. In other words:

- MsMFEM [full] = 100% DU + 100% IU + 100% CB,
- MsMFEM [reduced] = 0% DU* + 50% IU + 50% CB.

Figure 13 and Table 2 show the convergence of the inversion algorithm (residuals given by Eq. 22). In six iterations, all misfits in time-shift and amplitude for the water-cut dropped appreciably for all three approaches. Reference, initial, and matched water-cut curves are shown in Fig. 12 for a few selected producers. Some of the wells had a quite good match initially, and at the end of the history matching all wells had a quite satisfactory match.

Figure 10 compares the initial and reference permeability models with the updated (derived) models. The scale is logarithmic and the minimum permeability is 0.017 mD and the maximum is 110.3 mD. The three approaches gave almost identical derived permeability fields. Therefore, just one of the derived permeability fields (for MsMFEM [full]) is picked for closer inspections. From a casual look, it is hard to discern the changes made to the initial model. This is because the inversion algorithm is designed to preserve the geologic continuity and the initial geologic features to the maximum possible extent. However, a careful comparison reveals many differences between the initial and the updated geologic models.

Next, we examine if the changes made to the initial model are consistent with the 'reference' permeability model. **Figure 14** shows the differences between the updated and initial permeability model. These differences represent 'changes made'. This is to be compared with the 'changes needed', which is the difference between the reference and the initial permeability model. We see that there is clearly close agreement, particularly in regions where the permeability needs to be reduced (negative changes). As might be expected, there are also some discrepancies. Many of the wells had a good match initially even though the permeability fields differ. Because the water-cut data curves are a result of the total flow pattern between a producer and one or more injectors, this data source may have limited spatial information. Some of the changes occur in correct horizontal position, but incorrect vertical position. This can occur because the water-cut data has no vertical spatial resolution. Finally, it is worth pointing out that this inversion problem is highly ill-posed, and therefore a variety of possible solutions exist. Table 2 shows average discrepancies between the reference and the derived permeability fields (see Eq. 21) for TPFA, MsMFEM [full], MsMFEM [reduced]. The average discrepancies indicate that the history-matching procedure is stable with respect to the selective work-reduction strategies. We have also investigated some other selective work-reduction strategies, and the results with respect to both misfit and average discrepancies turned out to be as stable as for Case 1.

To sum up, the changes made to the permeability field preserved the geologic realism, were mostly in accordance with the 'changes needed' (see Fig. 14), and resulted in satisfactory match of the water-cut data. Further, the different strategies for selective work-reduction turned out to give stable results with respect to 'changes made' and misfit (see Table 2).

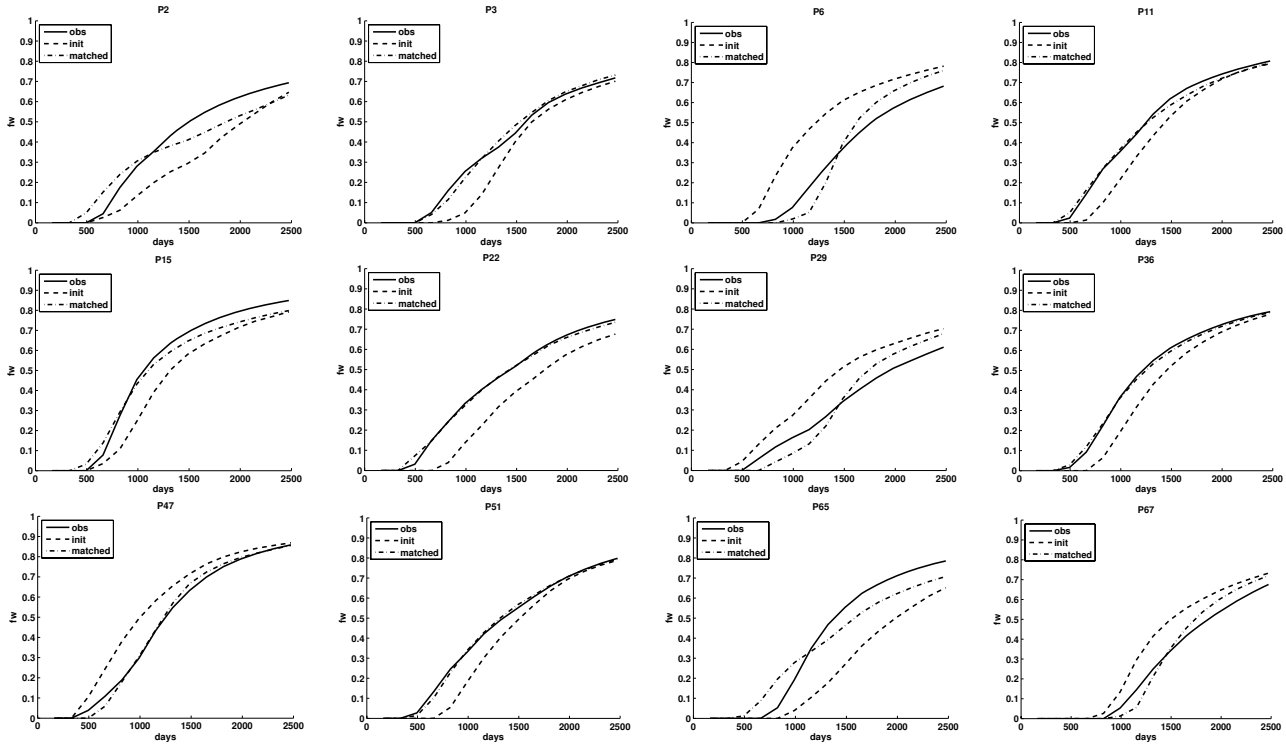

Fig. 12 – Case 2: Water-cut match for 12 of the 69 production wells included in the history match of the geologic model (MsMFEM [full]). For each plot the solid line, the dashed and the dash-dotted line represents the reference, the initial and the updated water-cut curve, respectively.

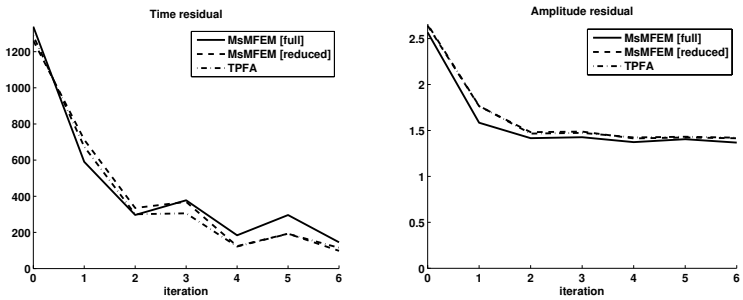

(a) Shift-time residuals (days). **(b) Amplitude residuals.**

Fig. 13 – Case 2: Reduction of residuals for all producers. Forward simulation: MsMFEM [full] (solid curve), MsMFEM [reduced] (dashed curve) and TPFA (dash-dotted curve).

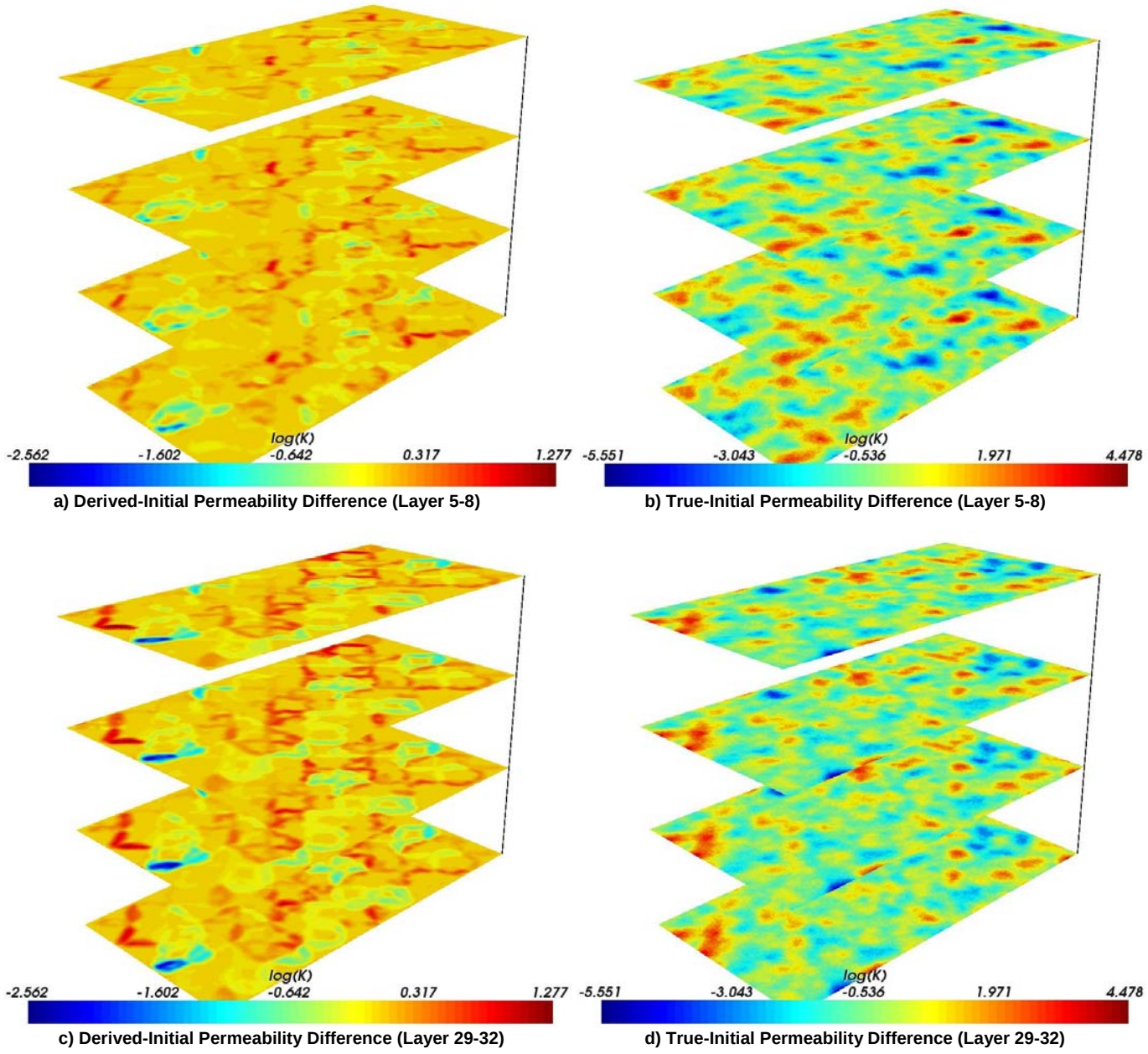

a) Derived-Initial Permeability Difference (Layer 5-8)

b) True-Initial Permeability Difference (Layer 5-8)

c) Derived-Initial Permeability Difference (Layer 29-32)

d) True-Initial Permeability Difference (Layer 29-32)

Fig. 14 – Case 2: Comparison of the "derived-initial" permeability difference and the "true-initial" permeability (MsMFEM [full]).

TABLE 2 – Case 2: REDUCTION OF MISFIT AND EFFICIENCY FOR HISTORY-MATCHING PROCEDURE

	T (res. %)	A (res. %)	Δlog(*k*)	Total simulation time (Wall clock)		Total CPU-time:			
						Pressure		Transport	
				PC1	PC2	PC1	PC2	PC1	PC2
Initial	100.0	100.0	0.821	-	-	-	-	-	-
TPFA	8.9	53.5	0.806	2h 12min	1h 04min	1h 02min	33min	54min	28min
MsMFEM [full]	10.3	53.1	0.796	2h 42min	2h 29min	1h 17min	1h 54min	1h 06min	32min
MsMFEM [reduced]	7.8	53.7	0.823	1h 34min	43min	9min	7min	1h 07min	32min
MsMFEM [reduced - SL]	7.6	48.7	0.808	36min	17min	9min	7min	12min	6min

Computational Efficiency. Finally, we will assess the efficiency of our multiscale method compared to a standard streamline method using a TPFA pressure solver. To this end, we consider two different computers running Linux: PC 1 is a laptop PC with a 1.7 GHz Intel Dothan Pentium M processor, 2Mb cache and 1.5 Gb memory. PC 2 is a workstation with a 2.4 GHz Intel Core 2 Duo, 4Mb cache, and 3 Gb memory.

Table 2 reports simulation times observed on the two computers. Here the total simulation time includes time for inversion, IO, and seven forward simulations, each with fifteen pressure steps. Similarly, we report the total time for the pressure solves and the transport solves (including mappings and tracing of streamlines).

When all basis functions are updated in all steps, the multiscale solver is, as expected, about 25% slower than TPFA with an optimal algebraic multigrid (AMG) solver on the laptop (PC1). On the other hand, the memory requirements for MsMFEM are quite low and this solver could easily have been run on larger models, as opposed to the TPFA solver, for which AMG almost exceeded the available memory. Moreover, on highly skewed, non-Cartesian grids (e.g., corner-point grids), MsMFEM uses a much better spatial discretization (Aarnes et al., to appear) and will therefore give more accurate predictions of flow.

The comparison of TPFA and MsMFEM [full] is not very interesting on the workstation (PC2). Due to an immature compiler for the particular hardware, we were not able to optimize the direct solver used to compute basis functions, while AMG could be (almost) fully optimized by using a vendor-specific compiler. The runtimes for the pressure solves (and the total runtime) on PC2 are therefore somewhat higher than expected, and will probably improve significantly when a more mature compiler becomes available in a few months.

By MsMFEM [reduced], we were able to reduce time for pressure solves by about 80% on both computers. In MsMFEM [reduced] the basis functions to be reused were read from file. Slow disc access on the laptop therefore prevented a further reduction in runtime. The workstation, on the other hand, had a faster disc, but further reductions in runtime were prevented by the unoptimized linear solver (as discussed above).

Reduction of the inverse system was expected to have a very small effect on the runtime, since a fully optimized compilation on a GHz processor gives a floating-point performance that would make the reduced number of arithmetic operations insignificant compared to other kinds of operations, which indeed is consistent with what we observe in Table 2. However, the results from the reduction of the inverse system indicate robustness for the generalized travel-time inversion method.

Finally, to speed the method further up, and to make our simulations comparable to state-of-the-art commercial streamline solvers, we apply a method for improved mass conservation for streamline simulation proposed by Kippe et al. (2007). Using this method, the total number of streamlines could be reduced from 500 000 to 50 000, thereby reducing the time for the transport solves by 80%. Altogether, this meant that the full history match could be performed in an impressive runtime of 17 minutes on the workstation (PC2) and 36 minutes on the laptop (PC1)!

For the workstation there is an obvious potential for further improvements by using a better compiler. Moreover, on the Core 2 Duo processor one should also exploit the natural parallelism in updating basis functions and in the streamline computations.

Summary and Conclusions

A novel approach to history matching using multiscale-streamline simulation and analytic sensitivities is presented. The power and utility of our proposed approach is demonstrated using both a synthetic and a field-scale example. The synthetic case includes matching of water-cut from a 9-spot pattern and is used to validate the method. The field-scale example consists of more than a million grid cells. Starting with a prior geomodel, production data were integrated using a generalized travel time inversion. The entire history matching process took less than 40 minutes using a laptop PC and about 17 minutes using an ordinary workstation PC. The permeability changes were found to be reasonable and geologically realistic.

Some specific conclusions from this paper can be summarized as follows.

1. A multiscale-streamline flow simulator was used for history matching by generalized travel-time inversion.
2. By utilizing the production-response sensitivities provided by the generalized travel-time inversion, we were able to reduce the total workload for the multiscale simulator considerably and still preserve the accuracy of the flow simulation.
3. By utilizing the production-response sensitivities, we were able to selectively reduce the number of non-zero sensitivities in the inverse system considerably without reducing the accuracy of the production data integration. This demonstrates robustness for the generalized travel-time inversion.
4. The approach proved applicable and efficient for a high-resolution reservoir model.

Acknowledgements

The research of Stenerud was funded by the *Uncertainty in Reservoir Evaluation (URE)* program at the Norwegian University of Science and Technology. The research of Kippe and Lie was funded by the Research Council of Norway under grant number 152731/S30.

Nomenclature

u = total Darcy velocity
p = pressure
l,v = test functions
V,U = function spaces
K = fine grid cells/elements
T = coarse grid blocks/elements
Ω = domain
Γ = coarse block interface
n = unit normal vector
Ψ = basis function velocity

Φ = basis function pressure
q = total rate (source/sink)
f_w= fractional flow function (water)
S_w = saturation of water
k = absolute permeability
λ_t = total mobility
M_{end} = end-point mobility ratio
m = reservoir parameter
N_d= number of data points
N = number of grid cells
t_a = arrival time
τ = time-of-flight

Subscripts
ms = multiscale

References

1. Aarnes, J.E. 2004. On the Use of a Mixed Multiscale Finite Element Method for Greater Flexibility and Increased Speed or Improved Accuracy in Reservoir Simulation. *Multiscale Modeling and Simulation* **2(**3): 421-439.
2. Aarnes, J.E., and Lie, K.-A. 2004. Toward Reservoir Simulation on Geological Grid Models. *Proc.*, 9th European Conference on the Mathematics of Oil Recovery, Cannes, France, 30 August - 2 September (2004), B21.
3. Aarnes, J.E., Kippe, V., and Lie, K.-A. 2005. Mixed Multiscale Finite Elements and Streamline Methods for Reservoir Simulation of Large Geomodels. *Advances in Water Resources* **28(**3): 257-271.
4. Aarnes, J.E., Krogstad, S., and Lie, K.-A. 2006. A Hierarchical Multiscale Method for Two-Phase Flow Based upon Mixed Finite Elements and Nonuniform Coarse Grids. *Multiscale Modeling and Simulation* **5(**2): 337-363.
5. Aarnes, J.E., Krogstad, S., and Lie, K.-A. to appear. Multiscale Mixed/Mimetic Methods on Corner-Point Grids. *Computational Geosciences* (to appear).
6. Al-Harbi, M., Cheng, H., He, Zhong, and Datta-Gupta, A. 2005. Streamline-based Production Data Integration in Naturally Fractured Reservoirs. *SPEJ* **10**(4): 426-439. SPE-89914-PA.
7. Arbogast, T., and Bryant, S. L. 2002. A Two-Scale Numerical Subgrid Technique for Waterflood Simulations. *SPEJ* **7**(4): 446-457. SPE-81909-PA.
8. Chen, A., and Hou, T.H. 2002. A Mixed Multiscale Finite Element Method for Elliptic Problems with Oscillating Coefficients. *Mathematics of Computation* **72(**242): 541-576.
9. Cheng, H., Oyerinde, D., Datta-Gupta, A., and Milliken, W. 2006. Compressible Streamlines and Three-Phase History Matching. Paper SPE 99465 presented at the 2006 SPE/DOE Symposium on Improved Oil Recovery, Tulsa, Oklahoma, 22–26 April.
10. Deutsch, C.V., and Journel, A.G. 1998. *GSLIB Geostatistical Software Library and User's Guide*, Oxford University.
11. Gautier, Y., Blunt, M.J., and Christie, M.A. 1999. Nested Gridding and Streamline-Based Simulation for Fast Reservoir Performance Prediction. *Computational Geosciences* **3(**3-4): 295-320.
12. He, Z., Datta-Gupta, A., and Yoon, S. 2002. Streamline-Based Production Data Integration with Gravity and Changing Field Conditions. *SPEJ* **7**(4): 423-436. SPE-81208-PA.
13. Holden, H., and Risebro, N.H. 2002. *Front Tracking for Hyperbolic Conservation Laws*, Springer-Verlag New York Inc., ISBN 3-540-43289-2.
14. Hou, T.Y. and Wu, X.-H. 1997. A Multiscale Finite Element Method for Elliptic Problems in Composite Materials and Porous Media. *Journal of Computational Physics* **134(**1): 169-189.
15. Jenny, P., Lee, S.H., and Tchelepi, H.A. 2004. Adaptive Multiscale Finite-Volume Method for Multiphase Flow and Transport in Porous Media. *Multiscale Modeling and Simulation* **3(**1): 50-64.
16. Kippe, V., Hægland, H., and Lie, K.-A. 2007. A Method to Improve the Mass Balance in Streamline Methods. Paper SPE 106250 presented at the SPE Annual Reservoir Simulation Symposium 2007, Houston, Texas, 26-28 February.
17. Milliken, W. J., Emanuel, A. S., and Chakravarty, A. 2001. Application of 3D Streamline Simulation to Assist History Matching. SPEJ **4**(6): 502-508. SPE-74712-PA
18. Paige, C.C., and Saunders, M.A. 1982. LSQR: An Algorithm for Sparse Linear Equations and Sparse Least Squares. *ACM Transactions on Mathematical Software* (March 1982) 8, No. 1, 43.
19. Raviart, P.-A., and Thomas, J.M. 1975. A Mixed Finite Element Method for 2nd Order Elliptic Problems. *Mathematical Aspects of Finite Element Methods (Proc. Conf., Consiglio Naz. Delle Ricerche (C.N.R), Rome, 1975)*, Lecture Notes in Mathematics, Springer, Berlin (1977) **606**: 292-315.
20. Vasco, D.W., Yoon, S., and Datta-Gupta, A. 1999. Integrating Dynamic Data Into High-Resolution Models Using Streamline-Based Analytic Sensitivity Coefficients. *SPEJ* **4**(4): 389-399. SPE-59253-PA.
21. Vega, L., Rojas, D., and Datta-Gupta, A. 2004. Scalability of the Deterministic and Bayesian Approaches to Production-Data Integration into Reservoir Models. *SPEJ* **9**(3): 330-338. SPE-88961-PA.
22. Wang, Y., and Kovscek, A. R. 2000. A Streamline Approach to History Matching Production Data. *SPEJ* **5**(4): 353-362. SPE-58350-PA.
23. Wu, Z., and Datta-Gupta, A. 2002. Rapid History Matching Using a Generalized Travel Time Inversion Method. *SPEJ* **7**(2) : 113-122. SPE-78359-PA.
24. Yoon, S., Malallah, A.H., Datta-Gupta, A., Vasco, D.W., and Behrens, R.A. 2001. A Multiscale Approach to Production-Data Integration Using Streamline Models, *SPEJ* **6**(2): 182-192. SPE- 71313-PA.

Paper III

Multiscale-Streamline Simulation and Dynamic Data Integration for High-Resolution Subsurface Models

Vegard Røine Stenerud, Vegard Kippe, Knut-Andreas Lie,
and Akhil Datta-Gupta.

Submitted to *Water Resources Research*.

Multiscale-Streamline Simulation and Dynamic Data Integration for High-Resolution Subsurface Models

V.R. Stenerud, V. Kippe, K.–A. Lie, and A. Datta–Gupta

Abstract. We discuss an efficient method for integrating dynamic data in high-resolution subsurface models. The method consists of two key technologies: (i) a very fast multiscale-streamline flow simulator, and (ii) a fast and robust 'generalized travel-time inversion' method. The travel-time inversion is based on sensitivities computed analytically along streamlines using only one forward simulation. The sensitivities are also used to selectively reduce the updating of basis functions in the multiscale mixed finite-element pressure solver. Moreover, we propose a new streamline formulation that improves the accuracy of production curves and allows a drastic reduction in the number of streamlines required to calculate accurate dynamic data responses.

The accuracy and robustness of our method is discussed using two 2-D test cases. Furthermore, we demonstrate the efficiency and utility of our approach using a highly detailed 3-D subsurface model consisting of more than one million cells and 69 producing wells, for which seven years of dynamic data are integrated in less than twenty minutes on a standard workstation PC.

1. Introduction

Subsurface models are usually built based on static date that are either confined in space or have low spatial resolution. Dynamic data must therefore be integrated into the subsurface model in order to give reliable predictions of future dynamic flow responses. In recent years it has become common to formulate the integration of dynamic data as an inverse problem and inversion methods based on a streamline formulation have shown to be particularly promising in this regard. In a recent paper (*Stenerud et al.*, to appear), we introduced a particularly efficient inversion strategy designed especially for integrating dynamic data into high-resolution subsurface models with millions of cells. The strategy consists of two technologies: a generalized travel-time inversion method (*Vasco et al.*, 1999; *He et al.*, 2002) based on sensitivities computed analytically along streamlines and a highly efficient multiscale-streamline flow solver (*Aarnes et al.*, 2005).

The generalized travel-time inversion method (*Vasco et al.*, 1999; *He et al.*, 2002) has previously been successfully applied to many field cases from the petroleum industry (see e.g., *Qassab et al.*, 2003; *Hohl et al.*, 2006). The method was chosen primarily because it is robust, computationally efficient, and tends to conserve geological realism in the inverted model. Unlike conventional amplitude inversion, which can be highly nonlinear, the travel-time inversion has been shown to have quasilinear properties (*Vasco et al.*, 1999; *Cheng et al.*, 2005). The minimization therefore proceeds rapidly even if the initial model is not close to the

global minimum, avoids over-corrections near fluid sources and sinks, and does not converge to secondary peaks that are typically seen in dynamic data from real-field cases, e.g., tracer data.

Each iteration in the inversion method must be accompanied by a forward simulation, which typically will be the most time-consuming part of the inversion process. Streamline methods are particularly suitable for simulating flow in large and geologically complex models, where the fluid flow is dictated primarily by heterogeneity in rock properties, positions of fluid sinks/sources, and phase mobilities. In general, streamline simulators have low memory requirements, high computational efficiency, and scale (almost) linearly with model size. Therefore, streamline simulation offers the opportunity to solve outstanding engineering queries that might otherwise be difficult or impossible to address using other approaches. Within the petroleum industry, streamline simulators are progressively being used more by operating companies as an alternative to traditional reservoir simulators in several reservoir engineering workflows, including: screening of enhanced recovery projects, rapid sensitivity studies, history matching, uncertainty assessment, upscaling, flood optimization, or simulation studies of sector or full-field models.

Even though streamline simulation provides fast forward simulation compared with a full finite-difference simulation in 3-D, computing pressure and fluid velocities still remains an expensive part of the inversion algorithm. As a result, the inversion process is therefore usually performed on upscaled subsurface models, although this may result in loss of important fine-scale information. In (*Stenerud et al.*, to appear), we proposed to replace the conventional pressure solver used in current streamline simulators by a much faster multiscale pressure solver (*Aarnes et al.*, 2005). The multiscale solver can be seen as a method that upscales and downscales the flow equations in a single step. In an upscaling method, the fine grid of the subsurface model is coarsened to form a simulation grid, on which the global flow equation is solved. To this end, one typically solves local flow problems inside each (pair of) grid block(s) and computes the effective permeability (or transmissibility) value that preserves this flow in an averaged sense. Similarly, the multiscale mixed finite-element method (MsMFEM) used herein solves a local flow problem for each pair of neighboring grid blocks in the coarse grid and uses the local flow solution as a basic building block (basis function) on the coarse grid. As other multiscale methods, MsMFEM is primarily targeted at dynamic flow simulations, where the pressure needs to be computed repeatedly. High efficiency is achieved since most basis functions can be reused from the previous pressure solve and updating reduces to solving a global equation on the coarse grid. In (*Stenerud et al.*, to appear) we proposed to use sensitivity coefficients to locate basis functions that need to be updated from one pressure solve to the next. The resulting pressure solver is robust and produces mass-conservative flow velocities both on the coarse grid and on the underlying fine grid.

The purpose of the current paper is two-fold: First, we present a modified streamline formulation that allows us to drastically reduce the number of streamlines needed to compute accurate production curves from the flow simulation. Second, we present a more in-depth analysis of the efficiency and robustness of the multiscale-streamline data-integration method, and in particular for the associated strategy for work reduction based on sensitivity coefficients.

To achieve high efficiency in the streamline simulation, it is clearly desirable to use as few streamlines as possible. On the other hand, the set of streamlines should be representative and sufficiently dense to ensure accurate prediction of flow patterns and production responses, and to limit errors in the mass balance. Lack of mass conservation is a problem of particular concern to reservoir engineers, and in this paper we will try to analyze the lack of mass

conservation and suggest methodological improvements that will strongly improve the quality of measured production curves (dynamical responses). This will in turn allow a significant reduction in the number of streamlines required to ensure highly accurate production curves.

The outline of the paper is as follows. Section 2 presents the multiscale-streamline solver. In Section 3 we discuss mass-balance errors and present a strategy to obtain accurate production curves using a small number of streamlines. Section 4 presents our approach for data integration and discusses its practical applicability using several numerical examples. Finally, our results are summarized in Section 5.

2. Multiscale-Streamline Simulation

We consider incompressible two-phase flow of oil and water in a non-deformable permeable medium and neglect the effects of gravity, compressibility and capillary forces. Further, we also assume for simplicity no-flow boundary conditions for the reservoir. Our flow model then consists of an elliptic pressure equation

$$\vec{u} = -\lambda_t(S)k\nabla p, \quad \nabla \cdot \vec{u} = q_t \tag{1}$$

and a quasilinear hyperbolic transport equation

$$\phi\frac{\partial S}{\partial t} + \nabla \cdot (f_w(S)\vec{u}) = q_w. \tag{2}$$

The primary unknowns in the coupled system **Eqs. 1** and **2** are the pressure p, the total (Darcy) velocity $\vec{u}$, and the water saturation S. The underlying porous rock formation is modeled in terms of the absolute permeability k and the porosity ϕ, which henceforth are assumed to depend on the spatial variable only. Further, q_t and q_w represent volumetric fluid sources and sinks (e.g., injection and production wells). Finally, $\lambda_t = \lambda_w + \lambda_o$ denotes the total mobility, where the mobility of each phase λ_j is given as the relative permeability k_{rj} of phase j divided by the phase viscosity μ_j $(j = o, w)$ and $f_w = \lambda_w/\lambda_t$ is the fractional-flow function of water.

Streamline solvers are based on a sequential time-stepping procedure. First the known initial saturation distribution is used to compute the mobilities $\lambda_t(S)$ in **Eq. 1**, after which the pressure equation can be solved to give total velocity $\vec{u}$ and pressure distribution p. Next, the total velocity $\vec{u}$ is kept fixed in **Eq. 2**, while the saturation is advanced a given time step. The new saturation values are used to update the mobilities in **Eq. 1**, the pressure equation is solved again, and so on.

2.1. Multiscale Pressure Solver. Our multiscale method is based on a mixed finite-element formulation of the flow equation **Eq. 1** in which one computes an approximation to the pressure and velocity simultaneously. That is, one seeks a pair $(\vec{u}, p)$ in $\mathcal{U} \times \mathcal{V}$, such that

$$\int_\Omega \vec{u} \cdot (\lambda_t k)^{-1}\vec{w}\, dx - \int_\Omega p\nabla \cdot \vec{w}\, dx = 0, \quad \forall \vec{w} \in \mathcal{U}, \tag{3}$$

$$\int_\Omega l\nabla \cdot \vec{u}\, dx = \int_\Omega ql\, dx, \quad \forall l \in \mathcal{V}. \tag{4}$$

In a standard discretization, the finite-dimensional function spaces $\mathcal{U}$ and $\mathcal{V}$ for velocity and pressure, respectively consist of low-order piecewise polynomials. In the multiscale mixed finite-element method (MsMFEM) (*Chen and Hou*, 2002; *Aarnes*, 2004), the approximation space $\mathcal{U}_{\text{ms}}$ for velocity has a multiscale structure, whereas $\mathcal{V}$ is chosen simply as the space of of piecewise constant functions, since the pressure is immaterial for the incompressible flows

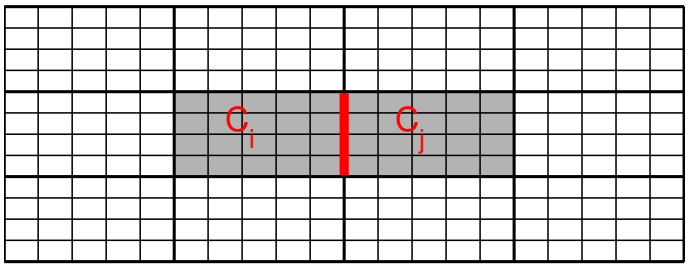

FIGURE 1. A coarse grid overlying a fine grid with the gray area giving support of basis function $\vec{\Psi}_{ij}$, which is associated with the edge/face indicated by the thick.

considered herein. If the pressure solution is needed, a more accurate pressure distribution can be constructed either by adaptively gridding around fluid sources and sinks, or by locally extracting a subgrid pressure distribution from the multiscale approximation space.

Basis Functions. Although MsMFEM can be defined for general unstructured grids (*Aarnes et al.*, 2006, to appear), we only consider Cartesian grids herein. Let $\{K_m\}$ be a (uniform) partitioning of Ω into mutually disjoint grid cells. Furthermore, let $\{C_i\}$ be a coarse partitioning of Ω, defined in such a way that each fine cell K_m overlaps with a single coarse block C_i, see **Fig. 1**. The multiscale approximation space $\mathcal{U}_{\text{ms}}$ is defined by assigning a $\vec{\Psi}_{ij}$ to each non-degenerate interface between two coarse blocks, $\Gamma_{ij} = \partial C_i \cap \partial C_j$. The basis functions $\vec{\Psi}_{ij}$ are computed numerically by forcing unit flow from block C_i to C_j; that is, by solving a local flow problem in each pair of blocks $\Omega_{ij} = C_i \cup C_j$

$$\vec{\Psi}_{ij} = -\lambda_t k \nabla \Phi_{ij}, \quad \nabla \cdot \vec{\Psi}_{ij} = \begin{cases} w_i(x), & x \in C_i, \\ -w_j(x), & x \in C_j, \end{cases} \tag{5}$$

with $\vec{\Psi} \cdot \vec{n} = 0$ on the boundary of Ω_{ij}. To solve **Eq. 5** we can use any consistent and mass-conservative method; here we use the standard two-point flux-approximation (TPFA) scheme. By choosing $w_i \propto q$ for coarse blocks containing sources or sinks, we ensure a conservative approximation to $\vec{u}$ on the fine grid. In all other blocks, we set $w_i \propto \text{trace}(k(x))$. Moreover, to give a unit flow from C_i to C_j, the source terms $w_i(x)$ are normalized such that $\int_{C_i} w_i(x)\,dx = 1$; this is discussed in more detail by *Aarnes* (2004) and *Aarnes et al.* (2006). The corresponding basis functions can be seen as generalizations of the lowest-order Raviart–Thomas basis functions in a standard mixed method. **Figure 2** illustrates the x-component of the basis function for a homogeneous and a heterogeneous medium.

Selective Updating of Basis Functions. Solving local flow problems is typically the most expensive step in a multiscale method, and the overall computational cost of generating basis functions. Computing basis functions and solving the coarse-grid system is comparable to solving the pressure equation directly on the fine grid using a highly efficient linear solver, like e.g., algebraic multigrid (*Stüben*, 2000); a more detailed discussion is given by *Kippe et al.* (to appear). Huge computational savings can be obtained if basis functions can be computed only initially or recomputed infrequently throughout the simulation. From **Eq. 5**, we see that $\vec{\Psi}_{ij}$ depends on three quantities that may change from one pressure solve to the next: the total mobility λ_t, the absolute permeability k, and the forcing terms $w(x)$, which again are determined by k and q.

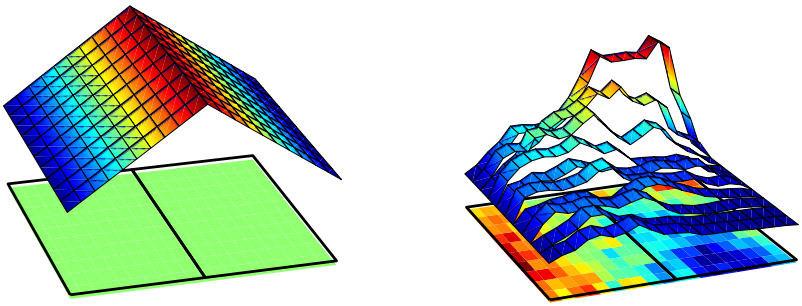

FIGURE 2. The x-component of the velocity basis function associated with an edge/face between two coarse blocks for a homogeneous and a heterogeneous permeability field, respectively.

Changes in fluid sources q may have a strong impact both on the local and global flow patterns, in particular if the changes are due to large changes in well rates, shut-in of wells, infill drilling, etc. Basis functions containing a well within their support should therefore be recomputed whenever the well configuration changes significantly.

The absolute permeability k may in principle change from one forward simulation to the next. Changes in k are accounted for on the coarse scale (**Eq. 3**), but not in the local basis functions (**Eq. 5**) unless these are updated. However, using a 'wrong' basis function may not have a significant impact on the calculated dynamic data. As a simple means for detecting changes in the permeability that significantly affect calculated dynamic data, we suggest to use the production-response sensitivities to be introduced in Section 4. A single sensitivity coefficient can be assigned to each coarse block by summing the sensitivities over the underlying fine grid; see *Yoon et al.* (2001). Due to the low resolution of dynamic data and the use of spatial regularization terms in the inversion process, changes in absolute permeability k from one inversion step to the next will mainly appear in regions of high sensitivity. Basis functions should therefore be recomputed initially in regions with high sensitivity; in the rest of the reservoir, reasonable accuracy is obtained by reusing basis functions from the previous forward simulation.

Changes in total relative mobility $\lambda_t(S)$ are relatively smooth, unless a strong saturation front passes through the block, and can be accounted for on the coarse scale (**Eq. 3**) with reasonable accuracy. Moreover, changes in total mobility in high-sensitivity regions will have a stronger influence on the dynamic reservoir responses, indicating that basis functions in these regions should be updated dynamically throughout the simulation. The errors induced by not updating basis functions in low-sensitivity regions will have a limited effect on the dynamical reservoir responses, and one may therefore avoid updates there.

Our selective updating strategy is summarized as follows (*Stenerud et al.*, to appear): In the first forward simulation of the inversion procedure, we typically update all basis functions in every pressure step, because no sensitivities are yet available. After the first forward simulation, we sort the sensitivity coefficients of the coarse blocks in ascending order and mark a predefined fraction to be updated. We will refer to the strategy where $x\%$ of the basis functions are updated initially and the remaining $(100-x)\%$ are kept from the previous flow simulation, as $x\%$ initial update. Similarly, the coarse-grid sensitivities are used to pick blocks in which we may avoid dynamic updates of basis functions from one pressure step to the next. We refer to this as $x\%$ dynamical update when $x\%$ of the basis functions are

updated dynamically each time step. We will assess the efficiency and robustness of this strategy in Section 4.

2.2. Streamline Solver. Instead of discretizing and solving the transport directly on the given grid, a streamline method decouples the 3-D equation, **Eq. 2**, into multiple 1-D equations along streamlines. To parameterize the streamlines, we introduce the time-of-flight variable τ defined by,

$$\tau(r) = \int_0^r \frac{\phi(\zeta)}{|\vec{u}(\zeta)|}\, d\zeta = \int_0^r s(\zeta)\, d\zeta, \tag{6}$$

which expresses the time it takes a passive particle to travel a distance r along a streamline. In differential form **Eq. 6** reads $\vec{u}\cdot\nabla\tau = \phi$. Using the bi-streamfunctions ψ and χ (*Bear*, 1972), for which $\vec{u} = \nabla\psi\times\nabla\chi$, we can define an alternative 3-D curvilinear coordinate system $(\tau,\ \psi,\ \chi)$, where the velocity $\vec{u}$ and hence the streamlines are orthogonal to the ψ and χ axes. In the streamline coordinates $(\tau,\ \psi,\ \chi)$, the gradient operator is expressed as

$$\nabla_{(\tau,\psi,\chi)} = (\nabla\tau)\frac{\partial}{\partial\tau} + (\nabla\psi)\frac{\partial}{\partial\psi} + (\nabla\chi)\frac{\partial}{\partial\chi}. \tag{7}$$

Because $\vec{u}$ is orthogonal to $\nabla\psi$ and $\nabla\chi$, it follows that $\vec{u}\cdot\nabla = \phi\frac{\partial}{\partial\tau}$, which together with the incompressibility condition $\nabla\cdot\vec{u} = 0$ can be used to rewrite **Eq. 2** as a family of one-dimensional transport equations along streamlines

$$\frac{\partial S}{\partial t} + \frac{\partial f_w}{\partial\tau} = 0. \tag{8}$$

The solution of **Eq. 2** is obtained by tracing numerous streamlines, mapping the initial saturations from the 3-D pressure grid to 1-D streamlines, and then solving **Eq. 8** along each streamline. Afterwards, the new streamline saturations are mapped (or averaged) back to the underlying 3-D grid to update mobilities before the pressure equation is solved to recompute the velocity field.

To trace streamlines, most streamline solvers use a simple semi-analytical procedure due to *Pollock* (1988), by which each streamline is traced numerically cell-by-cell, either from injector to producer, or vice versa, or from an arbitrary point in the reservoir and forward to fluid sinks and backward to fluid sources. After the tracing, each streamline ℓ is given as the indices of the cells the streamline traverses, the entry and exit points, and the incremental time-of-flights $\{\Delta\tau_{\ell,i}\}$ for each cell i. These increments form the cells in the streamline grid, on which **Eq. 8** will be solved. Initial values for **Eq. 8** are obtained by picking up the piecewise constant values from the underlying (pressure) grid,

$$S_{\mathrm{sl},i} = S_i. \tag{9}$$

To solve **Eq. 8**, we will herein use a front-tracking method (*Holden and Risebro*, 2002) that is unconditionally stable and can directly utilize the time-of-flight grid resulting from the streamline trace. This makes the method very efficient and devoid of numerical diffusion. In contrast, solvers based on a finite-volume formulation typically need to map the initial data to a more regular grid.

To map values from the streamlines back to the underlying 3-D grid, we use volumetric averaging. Volumes are associated with streamlines by considering each streamline as a representation of the cross-section of a streamtube with an associated constant volumetric

flux $q_\ell = |\vec{u}(\zeta)|A(\zeta)$. This gives the volume of the streamline as

$$\begin{aligned} V_\ell &= \int_0^s \phi(\zeta)A(\zeta)\, d\zeta \\ &= q_\ell \int_0^s \frac{\phi(\zeta)}{|\vec{u}(\zeta)|}\, d\zeta = q_\ell\, \tau_\ell. \end{aligned} \tag{10}$$

The volume of a streamline in grid cell i is then $V_{\ell,i} = q_\ell \Delta\tau_{\ell,i}$, and the precise definition of the streamline-to-grid volumetric averaging is,

$$S_i = \frac{\sum_\ell S_{\ell,i} V_{\ell,i}}{\sum_\ell V_{\ell,i}}. \tag{11}$$

We note that considering streamlines as fluid carriers also makes it natural to define production characteristics simply by summing the outflow fluxes during time step Δt from all streamlines connected to each well

$$\mathrm{PRD}_{\Delta t} = \sum_\ell q_\ell \int_{\Delta t} f_{w,\ell}(t)\, dt. \tag{12}$$

To associate fluxes to each streamline, we generate equally spaced starting points on the faces of grid cells containing injection wells. The number of starting points on each face is proportional to the volumetric flux across the face; i.e., streamlines carry approximately equal amounts of fluids, $q_\ell \approx C$. An advantage of this approach is that the sums in **Eqs. 11** and **12** can be computed incrementally as streamlines are traced (*Batycky*, 1997) without knowing the associated volumetric flux, thus allowing completely independent processing of streamlines.

For the volumetric mapping **Eq. 11** to make sense, each grid cell should in principle be traversed by at least one streamline. In general, there will be a number of grid cells that are not traversed by any of the streamlines traced from the faces of injector-cells. One can therefore perform an additional tracing process, where one picks a point inside one of the untraced cells and traces a streamline from this point and backward/forward to a fluid source/sink or to a cell that has been traversed by another streamline (*Batycky*, 1997). This is repeated until there are no untraced cells. Alternatively, one may simply ignore the untraced cells, as these often are in regions that contribute little to the production characteristics. To keep the amount of streamline tracing at a minimum, we here employ the latter approach.

3. Improving Local and Global Mass Balance

Lack of mass conservation is a well-known problem for streamline simulators and may lead to both incorrect saturation distributions and incorrect production curves. To illustrate typical errors observed as the number of streamlines is reduced, we consider a large 3-D reservoir model of a Brent sequence consisting of $60 \times 220 \times 85$ grid cells, see (*Christie and Blunt*, 2001) for more details. The reservoir is produced using a five-spot pattern of vertical wells; the central injector has a constant rate of 5 000 bbl/day (reservoir conditions), and the four producers operate at 4 000 psi bottom-hole pressure. We assume quadratic relative permeability curves with $S_{wc} = S_{or} = 0.2$. The initial saturation is $S_0 \equiv S_{wc}$, and the viscosities are $\mu_o = 3.0$ cP and $\mu_w = 0.3$ cP, respectively. We neglect gravity and compressibility, since these have smaller impact on the production curves than the numerical diffusion inherent in any numerical scheme. Moreover, for the pressure equation we use a

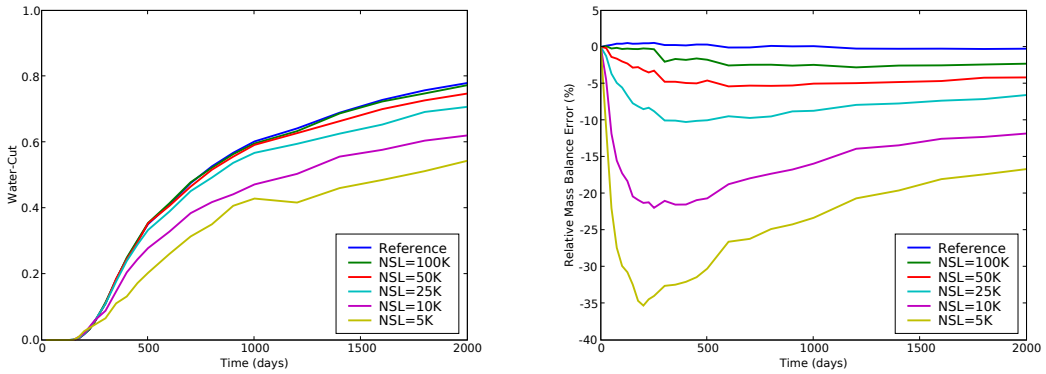

FIGURE 3. Fractional flow (left) and relative mass-balance errors (right) for Producer 1 from Model 2, SPE 10 for various number of streamlines (1K = 1 000).

standard two-point discretization with an AMG linear solver (*Stüben*, 2000). The time-steps are those reported for the commercial streamline simulator used in the study.

Figure 3 shows fractional-flow curves in Producer 1 for simulations with various number of streamlines. The water production is clearly underestimated when the number of streamlines is too small. Since the correct total amount of injected water is distributed among streamlines at the injecting end of each streamline, there must effectively be a loss of mass in the method. We can quantify this loss by the relative *global mass-balance error* for water in each time-step,

$$\epsilon_{\Delta t} = \frac{\mathrm{INJ}_{\Delta t} - \mathrm{PRD}_{\Delta t} + \mathrm{FIP}_t - \mathrm{FIP}_{t+\Delta t}}{\mathrm{INJ}_{\Delta t}}, \tag{13}$$

which is equivalent to an error in the volume balance, since we have assumed incompressibility. **Figure 3** also shows that the errors increase rapidly in the beginning of the simulation and decay slowly as the fractional-flow curves increase. Notice that since production curves are calculated directly from the individual streamlines using **Eq. 12**, inaccurate production curves do not necessarily imply inaccurate saturation distributions, and vice versa.

3.1. Global Mass-Balance Errors. Viewing streamlines as fluid carriers introduces a fundamental problem in that the pore volume represented by a finite number of streamlines does not necessarily match the pore volume of the original grid (in physical space); in other words, the two grids are not automatically compatible. This will generally lead to mass-balance errors when mapping saturation between the streamlines and the pressure grid. From **Eq. 10** we have that the streamline pore volume is given by,

$$\mathrm{V}_{\mathrm{sl}} = \sum_{\ell} q_\ell \, \tau_\ell. \tag{14}$$

Thus, the flux q_ℓ and the total time-of-flight τ_ℓ associated with streamline ℓ are two parameters we can play with to improve the mass-balance properties of our streamline discretization. Both parameters are generally subject to approximation errors.

Using the semi-analytical streamline tracing method introduces errors in τ_ℓ, even for Cartesian grids with given analytical fluxes on the faces, see (*Matringe and Gerritsen*, 2004).

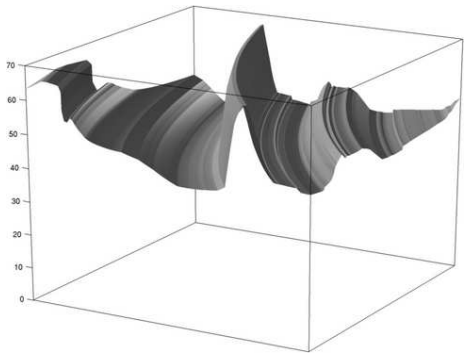

FIGURE 4. Time-of-flight in grid cell $(200, 36)$ of Layer 76 in Model 2 of SPE 10 sampled in 2000×2000 evenly distributed points inside each cell. Here the variation of τ is of the same order as the values of τ.

However, for the Cartesian geometries considered herein, careful numerical studies revealed that Pollock's method was sufficiently accurate.

Errors in the fluxes q_ℓ correspond to errors in the *transversal* discretization in (ψ, χ), which is determined implicitly by the distribution of streamlines and association of fluxes. The fluxes q_ℓ represent velocity integrals over the cross-section of the associated streamtubes. Assigning equal fluxes $q_\ell = C$ to all streamlines at the injector may be inaccurate and will in particular mean that the total flux of all streamlines passing through a particular cell face elsewhere in the reservoir will not necessarily match the corresponding flux in the pressure grid. However, only minor improvements in the mass conservation were observed when using more accurate assignment of fluxes, e.g., by scaling q_ℓ according to the interpolated velocity at the starting point and the cross-section area of the associated streamtube as discussed by *Ponting* (1998) and *Pallister and Ponting* (2000). Lifting the restriction of equal streamline fluxes also makes it possible to apply other streamline distribution schemes. For instance, in situations where there is a large variation in total fluid rates between different fluid sinks (producers), it may be beneficial to start streamlines also on the faces of cells containing sinks to ensure that sufficient accuracy is achieved for sinks with small rates. Similarly, streamline fluxes may be assigned at the faces of producers or as a weighted averages of the flux at the injector and the producer. None of these ideas had a significant effect for the applications considered herein, see (*Kippe et al.*, 2007) for more details.

In our experience, the *global* mass-balance errors we observe as the number of streamlines is reduced are primarily caused by the fact that τ_ℓ may not be a good approximation to the average time-of-flight over cross-sections of the associated streamtube. This is illustrated in **Fig. 4**, which shows the time-of-flight sampled at 2000×2000 evenly distributed points within a single cell of Layer 76 in the SPE 10 data set. Here the variation of τ is of the same order as the values of τ itself. Increasing the number of streamlines decreases the streamtube cross-sections and hence reduces this error. However, considering the very large variation in τ shown in **Fig. 4**, it is evident that a large number of streamlines is necessary to obtain accurate streamline volumes and thereby low error in the global mass balance. On the other hand, if we insist on keeping the number of streamlines low, we can use the fact that mass should be conserved, and correct the computed values of τ_ℓ to enforce the mass-balance constraint.

3.2. Improved Accuracy of Production Curves. Exact global conservation of mass is guaranteed if the streamline volume matches the true pore volume, i.e., $\sum_\ell V_{\ell,i} = V_i$, in every grid-block touched by streamlines. In this case, the mappings back-and-forth between streamlines and the pressure grid preserve mass. Indeed, for the mapping from grid to streamlines, **Eq. 9**, we have,

$$\begin{aligned} V^w_{\text{grid}} = \sum_i V_i S_i \quad &= \sum_i \Big(\sum_\ell V_{\ell,i} \Big) S_i \\ &= \sum_\ell \sum_i V_{\ell,i} S_{\ell,i} = V^w_{\text{sl}}, \end{aligned} \tag{15}$$

and similarly for the mapping from streamlines to grid, **Eq. 11**,

$$\begin{aligned} V^w_{\text{sl}} = \sum_\ell \sum_i V_{\ell,i} S_{\ell,i} \quad &= \sum_i \sum_\ell \frac{V_i}{\sum_\ell V_{\ell,i}} V_{\ell,i} S_{\ell,i} \\ &= \sum_i V_i S_i = V^w_{\text{grid}}. \end{aligned} \tag{16}$$

Here V^w_{grid} and V^w_{sl} are the total volumes of water on the pressure and streamline grids, respectively. Since the streamline flux is constant along each streamline, our only option for ensuring $\sum_\ell V_{\ell,i} = V_i$ is to modify the local time-of-flight increments, $\Delta\tau_{\ell,i}$. Specifically, prior to solving the one-dimensional saturation equation **Eq. 8** along streamlines, we propose to scale the time-of-flight values $\tau_{i,\ell}$ in block i by a factor $\alpha_i = V_i / \sum_\ell V_{\ell,i}$. This means that streamlines can no longer be processed independently, and we need to store streamlines in memory, or alternatively perform the complete tracing procedure twice; once to compute the values of α_i, and then a second time for the solution of the one-dimensional problems. The memory required to store streamlines is usually (significantly) less than the memory required to solve the pressure equation **Eq. 1**. Hence, we prefer storing rather than retracing, since tracing is an expensive process.

Scaling the time-of-flight amounts to locally stretching or shrinking the grid on which **Eq. 8** is solved. By enforcing mass conservation we thus introduce local errors in the saturation distribution, but as we demonstrate below, the global properties of the resulting solutions are better. However, special care must be taken to not ruin important (local) characteristics like the breakthrough-time for producers, which e.g., will be important in the inversion procedure discussed below. To make sure breakthrough is estimated correctly, we only apply the scaling along streamlines after breakthrough has occurred.

In **Fig. 5** we have recomputed the simulation reported in **Fig. 3**, but now correcting for incorrect streamline volumes. The mass-balance errors are still large initially since the time-of-flight scaling is only applied after breakthrough, but the errors decrease rapidly. The improvement of the fractional-flow curves is significant, to say the least, with as few as 5 000 streamlines giving acceptable results. **Table 1** reports the errors in the fractional-flow curves $w(t)$ for all four producers, as measured by

$$\delta(w) = \|w - w^{\text{ref}}\|_2 / \|w^{\text{ref}}\|_2. \tag{17}$$

For completeness, **Table 1** also shows the corresponding results for the standard streamline approach, where we have started streamlines in both injectors and producers and used weights given by the area of the perpendicular bisection of the cell faces to assign fluxes to streamlines (since this gives slightly better results for the original method). Moreover, the table reports

TABLE 1. Errors in fractional flow $\delta(w)$ for producers P1 to P4 and average saturation error $\delta(S)$ for the original (O) and modified (M) streamline methods on Model 2, SPE 10 for various number of streamlines (NSL). Columns T_{sl} and T_{tot} report the total computational time for the streamline solves and the overall simulation, respectively, measured on a workstation PC with a 2.4 GHz Intel Core 2 Duo processor with 4 Mb cache and 3 Gb memory.

NSL	O/M	P1	P2	P3	P4	$\delta(S)$	T_{sl} (s)	T_{tot} (s)
100 000	O	8.91e-03	6.24e-03	2.44e-03	2.99e-03	2.75e-02	508.92	974.94
	M	9.86e-03	4.61e-03	1.97e-03	3.67e-03	2.83e-02	508.20	979.03
50 000	O	2.53e-02	1.72e-02	6.42e-03	9.38e-03	4.00e-02	266.48	728.42
	M	1.66e-02	7.88e-03	3.72e-03	7.03e-03	3.81e-02	265.87	727.79
25 000	O	6.49e-02	4.85e-02	1.74e-02	2.28e-02	5.89e-02	147.36	608.46
	M	1.43e-02	1.47e-02	8.12e-03	7.12e-03	5.27e-02	146.23	613.00
10 000	O	1.78e-01	1.29e-01	5.53e-02	7.30e-02	9.54e-02	75.65	541.17
	M	3.26e-02	1.94e-02	1.56e-02	1.38e-02	8.06e-02	75.33	545.09
5 000	O	3.20e-01	2.30e-01	1.02e-01	1.30e-01	1.29e-01	50.91	512.75
	M	4.25e-02	2.19e-02	1.86e-02	2.37e-02	1.12e-01	51.74	516.63

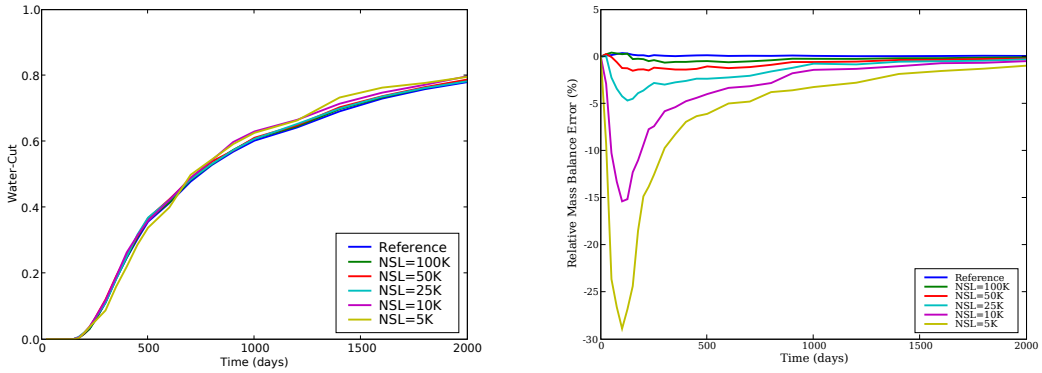

FIGURE 5. Fractional flow (left) and relative mass-balance errors (right) for Producer 1 from Model 2, SPE 10 for various number of streamlines when using the modified streamline method (1K = 1 000).

saturation errors in the the porosity-weighted L^1-norm,

$$\delta(S) = \|\phi(S - S^{\text{ref}})\|_1 / \|\phi S^{\text{ref}}\|_1, \tag{18}$$

averaged over all time steps of the simulation. Altogether, these results show that although scaling the time-of-flight values has limited effect on the accuracy of the saturation fields, the accuracy of the corresponding production curves is improved significantly. For instance, if one is primarily interested in the fractional-flow curves and allows an error of about 5%, it is sufficient to use only 5 000 streamlines for the modified method, whereas 25–50 000 streamlines would be required in the original method. This yields a significant speedup for the transport part of the simulation, since the computation time associated with transport in theory scales linearly with the number of streamlines. The timing results in **Table 1** show that the actual

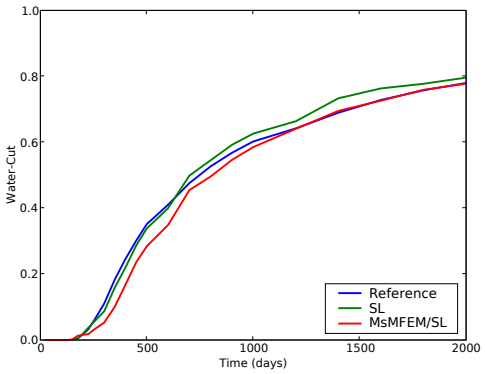

FIGURE 6. Fractional flow in Producer 1 for the modified streamline with 5 000 streamlines, using a standard two-point and the MsMFEM pressure solver.

scaling is not truly linear as the number of streamlines becomes very small. However, this is to be expected since our simulator is optimized for relatively large numbers of streamlines and otherwise negligible overhead associated with streamline distribution, flux computations, and saturation mappings may become significant when using a small number of streamlines. Still, we see that going from 50 000 to 5 000 streamlines gives at least five times speedup for the transport step.

As the number of streamlines is reduced, the total simulation time in **Table 1** is dominated by the solution of the pressure equation, **Eq. 1**. To obtain a more substantial speedup for the overall simulation, we use the multiscale pressure solver introduced in Section 2.1 on a $5 \times 11 \times 17$ coarse grid. The fractional-flow curves shown in **Fig. 6** demonstrate that utilizing MsMFEM for the pressure equation does not yield a significantly reduced accuracy in the production curves for the case with 5 000 streamlines, but the overall simulation time is reduced from 8 minutes and 36 seconds to an impressive 2 minutes and 22 seconds.

Finally, we emphasize that scaling the time-of-flight is primarily aimed at improving the *global mass balance* by increasing the accuracy of measuring reservoir production (i.e., global, low-resolution flow responses). In the next section we will look at another technique more aimed at improving local, high-resolution flow responses (pointwise saturation distributions).

3.3. Improving Local Mass Balance – Adaptive Streamline Coverage. The correction strategy introduced above is no guarantee for producing accurate saturation curves or fractional-flow curves. Indeed, insufficient streamline coverage may still induce large errors (for piston-like displacements) if we do not ensure that all grid cells are traversed by streamlines. This leads to errors in the computed pressure and velocity fields, thus shifting the predicted time of breakthrough. For scenarios with high mobility ratios, the pressure/velocity solutions are less sensitive to errors in the underlying saturation field, because the saturation variation is generally much smoother. On the other hand, our correction strategy never performs significantly worse than the original method, and can therefore always be applied safely.

To alleviate the accuracy problems for favorable displacement conditions, we could trace streamlines through every cell, using, e.g., the approach of *Batycky* (1997). However, many

TABLE 2. Errors in fractional flows ($\delta(w)$) and average number of streamlines (NSL) on the homogeneous model for the original and the adaptive streamline tracing for end-point mobility ratio $M_{\text{end}} = 0.1$.

β	NSL	P1	P2	P3	P4
—	2000	4.43e-02	9.30e-02	8.97e-02	9.47e-02
—	1500	5.27e-02	1.13e-01	8.96e-02	1.04e-01
—	1000	1.39e-01	1.62e-01	1.76e-01	1.67e-01
—	500	4.25e-01	4.34e-01	4.64e-01	4.61e-01
1.0	873	1.17e-02	7.52e-03	2.44e-02	1.37e-02
0.9	701	3.28e-02	2.95e-02	4.82e-02	2.17e-02
0.8	560	2.40e-01	2.31e-01	2.72e-01	2.43e-01
0.7	500	3.34e-01	3.85e-01	3.99e-01	3.90e-01
0.6	500	3.60e-01	3.78e-01	3.98e-01	3.86e-01

TABLE 3. Errors in fractional flow ($\delta(w)$) and average number of streamlines (NSL) on the homogeneous model for the original and the adaptive streamline tracing for end-point mobility ratio $M_{\text{end}} = 10$.

β	NSL	P1	P2	P3	P4
—	2000	2.58e-02	2.45e-02	2.33e-02	8.44e-03
—	1500	3.14e-02	1.00e-02	3.88e-02	9.23e-03
—	1000	6.68e-02	2.29e-02	5.79e-02	4.14e-02
—	500	7.42e-02	9.58e-02	1.20e-01	8.96e-02
1.0	873	3.45e-02	2.21e-02	2.26e-02	2.04e-02
0.9	722	3.42e-02	2.39e-02	2.41e-02	2.79e-02
0.8	616	2.69e-02	2.44e-02	3.35e-02	2.77e-02
0.7	519	2.19e-02	2.50e-02	5.94e-02	2.43e-02
0.6	500	2.39e-02	3.60e-02	6.80e-02	3.49e-02

cells will typically be located in low-flow regions that do not significantly affect the solution. We therefore propose an adaptive approach to streamline coverage, where we only demand that a given fraction β of the pore volume should be traversed by streamlines. Before the tracing starts, the cells are sorted in descending order by absolute velocity $|\vec{u}|$, and we trace back from untouched blocks in sorted order until the given pore-volume target has been met. We also ensure that each well is properly covered by starting a specified number of streamlines from fluid sources/sinks, with the distribution of streamlines on the faces of grid cells containing fluid sources/sinks given according to the fluxes, as before.

To demonstrate the effect of the adaptive tracing, we consider a homogeneous $32 \times 32 \times 8$ model of aspect ratio $1 : 1 : 0.1$, with wells placed in a five-spot pattern, where the four producers operate at equal bottom-hole pressures. We assume quadratic relative permeability curves with zero residual oil and water saturations, and perform simulations for two different values of the end-point mobility ratio $M_{\text{end}} = \mu_o/\mu_w$; favorable displacement ($M_{\text{end}} = 0.1$) and unfavorable displacement ($M_{\text{end}} = 10$). The dimensionless simulation time is 2.0 PVI, and for both displacement scenarios we verified that the chosen number of time-steps was sufficient for stability of the sequential time-stepping scheme.

Tables 2 and **3** show the average number of streamlines and errors in the fractional-flow curves when applying the adaptive approach in combination with the modified streamline

method. Initially we trace 100 streamlines from each well, which is why the minimum number of streamlines is 500. Compared with the non-adaptive version, the adaptive method gives significantly more accurate production curves using fewer streamlines. As expected, the optimal value of β depends on the displacement conditions, with favorable piston-like displacement requiring a larger fraction of the pore volume to be covered. In the unfavorable case, the production curves are good even without the adaptivity. In fact, we could actually have used even fewer streamlines. This helps explain why we obtained accurate results using *very* few streamlines for the SPE 10 model above.

4. Integration of Dynamic Data

In this section we present the inversion method in more detail and discuss its efficiency and robustness using three numerical test cases. In the following we assume that the subsurface model has been conditioned to static data and available geological information, such that the model already gives a reasonable description of the reservoir geology. Dynamic production data generally have low resolution and cannot be used to infer small-scale variations in reservoir properties. It is therefore important that changes to the subsurface model inferred from the dynamic data are kept as minimal as possible to preserve geological realism.

4.1. Generalized Travel-Time Inversion. Our method for integrating fractional-flow data utilizes approximate sensitivities calculated analytically along streamlines to update the heterogeneous subsurface model based on observed dynamic data (*Vasco et al.*, 1999; *He et al.*, 2002). The sensitivities quantify the influence of reservoir parameters on dynamical responses of the reservoir. As such, these sensitivities provide the fundamental relationships that allow us to integrate the dynamic reservoir responses. The major steps in our method are:

(1) Multiscale-streamline simulation to compute production responses at the observation points (wells) as discussed in Section 2.
(2) Quantification of the mismatch between observed and computed dynamic responses via a generalized travel-time formulation. An optimal travel-time shift is computed for each observation point (e.g., production well) by systematically shifting the computed production responses towards the observed data until the cross-correlation between the two is maximized (*He et al.*, 2002).
(3) Computation of streamline-based analytic sensitivities of the production responses (fractional-flow curves) to reservoir parameters, specifically permeability.
(4) Updating of reservoir properties to match the dynamical reservoir responses (production data) via inverse modeling. To this end, we will use an iterative least-square minimization algorithm (LSQR) (*Vasco et al.*, 1999; *He et al.*, 2002) to simultaneously minimize the travel-time misfit for all observation points, thereby matching all dynamic data within a specified tolerance.

This four-step process is repeated until a satisfactory match is obtained. Next, we describe the three last steps in more detail, starting with the formulation of a generalized travel-time misfit to quantify mismatch in dynamic data.

Misfit in dynamic data is commonly represented by a least-squares functional of the form:

$$E = \sum_k \sum_j \left[w_k^{\mathrm{obs}}(t_j^k) - w_k^{\mathrm{calc}}(t_j^k) \right]^2, \tag{19}$$

where $w_k^{\text{obs}}(t_j^k)$ and $w_k^{\text{calc}}(t_j^k)$ are the observed and calculated data, respectively, in well k at time t_j^k. Direct minimization of **Eq. 19** is called amplitude inversion, in which the observation times are fixed and one seeks to match the amplitudes. Travel-time inversion, on the other hand, chooses a specific point on the dynamic data curve (e.g., the breakthrough time or a distinct peak) and adjusts the model parameters so that a similar point is obtained in the computed reservoir response. Although crude, this approach has an important advantage: whereas amplitude inversion is highly nonlinear, travel-time inversion has quasilinear properties (*Cheng et al.*, 2005) and is thus more robust and less likely to be stuck in local minima. However, the resulting overall data match of dynamic data may not be satisfactory since only a single data point is matched (per well).

The generalized travel-time inversion combines the desirable properties of travel-time and amplitude inversion into one step (*He et al.*, 2002) by seeking a set of optimal time-shifts $\boldsymbol{\Delta t} = \{\Delta t_k\}$ that minimize the following misfit at each well:

$$E_k(\Delta t_k) = \sum_j \left[w_k^{\text{obs}}(t_j^k + \Delta t_k) - w_k^{\text{calc}}(t_j^k) \right]^2 . \tag{20}$$

Hence we can match multiple data points as in the amplitude inversion, while retaining the attractive quasilinear properties of the travel-time inversion. Computing time-shifts does not require any new flow simulation, but can be done using data from the single forward simulation used to evaluate the data mismatch.

Having determined the optimal time-shifts, the next step is to propagate them into changes in the reservoir parameters. Mathematically, the inversion of the time-shifts $\boldsymbol{\Delta t}$ leads to the minimization of a penalized misfit function (*Vasco et al.*, 1999; *He et al.*, 2002):

$$\|\boldsymbol{\Delta t} - \mathbf{G}\delta\mathbf{m}\| + \beta_1\|\delta\mathbf{m}\| + \beta_2\|\mathbf{L}\,\delta\mathbf{m}\|. \tag{21}$$

Here $\delta\mathbf{m}$ denotes the changes in the reservoir properties $\mathbf{m}$, $\mathbf{G}$ contains the sensitivities of the time shifts with respect to the reservoir parameters $\mathbf{m}$, and $\mathbf{L}$ is a second-order (Laplace) difference operator. The first term ensures that the difference between the observed and calculated dynamic responses is minimized. The second term is a norm constraint that penalizes deviations from the initial (prior) subsurface model and as such helps to preserve the geological realism of the inversion. The third term is a roughness constraint that measures the regularity of the changes and is introduced to stabilize the inversion by only allowing large-scale changes that are consistent with the low resolution of the production data. The weights β_1 and β_2 determine the relative strengths of the two regularization terms. The minimum in **Eq. 21** can be obtained by the iterative least-square minimization algorithm, LSQR (*Paige and Saunders*, 1982), for which the computational cost scales linearly with respect to the number of degrees-of-freedom (*Vega et al.*, 2004).

4.2. Time-Shift Sensitivities. For the sake of completeness, we briefly describe the analytical calculation of streamline-based sensitivities, which can be computed using a single flow simulation, leading to very fast algorithms for data integration or inverse modeling. Because the sensitivities are simple integrals along streamlines, the computation time scales very favorable with respect to the number of grid cells, thus making streamlines the preferred approach for integrating dynamic data into highly-detailed subsurface models.

The sensitivity of the shift in travel time Δt_k with respect to reservoir parameter m is given by (*Vasco et al.*, 1999; *He et al.*, 2002)

$$\frac{\partial \Delta t_k}{\partial m} = -\frac{1}{N_d}\sum_{j=1}^{N_d}\frac{\partial t_j^a}{\partial m}, \tag{22}$$

where N_d represents the number of observed data for the associated well and t_j^a is the common (or average) arrival time at the well for the connected streamlines. The sensitivity of the common arrival time with respect to a reservoir parameter m, is calculated by a flux-weighted average of the arrival-time sensitivities of the connected streamlines. The arrival-time in each streamline is related to the streamline time-of-flight by assuming a Buckley–Leverett profile

$$\tau_\ell = t_{j,\ell}^a \cdot \tilde{f}_w'(S). \tag{23}$$

Here $\tilde{f}$ denotes the convex hull of the fractional flow curve, and the derivative $\tilde{f}_w'$ is evaluated using the saturation at the outlet of streamline ℓ for streamlines with breakthrough, and using the front saturation for streamlines without breakthrough. In other words, $\partial t_{j,\ell}^a/\partial m$ is proportional to the sensitivity of the time-of-flight, which can be computed analytically from a single streamline simulation under the assumption that the streamlines do not shift because of small perturbations in reservoir properties. For example, the sensitivity with respect to permeability k_i in cell K_i is given by

$$\frac{\partial \tau}{\partial k_i} = \int_{\Sigma_i}\frac{\partial s(\zeta)}{\partial k_i}\,d\zeta = -\int_{\Sigma_i}\frac{s(\zeta)}{k_i}\,d\zeta = -\frac{\Delta\tau_i}{k_i}, \tag{24}$$

where the integral is along the streamline trajectory Σ_i through K_i and $\Delta\tau_i$ is the associated incremental time-of-flight. Similarly, sensitivities can be calculated with respect to mobility or to the product of mobility and permeability. Worth mentioning here is an important practical aspect. Our experience indicates that the selective work-reduction strategy and the data-integration process are more robust if the sensitivities are made dimensionless as described by *He et al.* (2002).

We are now fully equipped to integrate dynamic data into high-resolution subsurface models. In (*Stenerud et al.*, to appear), the accuracy and robustness of our inversion method were investigated for a small 2-D case with isotropic lognormal permeability and flow with end-point mobility ratios ($M_{\text{end}} = 0.2, 0.5, 10$). In the next two subsections, we investigate the accuracy and robustness of the proposed selective updating of basis functions more thoroughly using two 2-D test cases that involve dynamic well configuration and multiple realizations, respectively. *To pose a further challenge for our multiscale simulator, both cases involve anisotropic permeability structures with long streaks of high permeability aligned* exactly *with the diagonal direction of the grid.* As noted by *Kippe et al.* (to appear), this particular permeability structure is a worst-case scenario for MsMFEM, where the solver may exhibit loss of accuracy. For all other cases, the solver is generally very robust and accurate (*Kippe et al.*, to appear).

To measure the quality of the data integration, we use the *amplitude residual* $\sqrt{E}$ (see **Eq. 19**) and the *time-shift residual* $\|\mathbf{\Delta t}\|_2$. We also report the average discrepancy between the reference and matched permeability field measured by

$$\overline{\Delta \ln k} = \frac{1}{N}\sum_{i=1}^{N}\left|\ln k_i^{\text{ref}} - \ln k_i^{\text{match}}\right|. \tag{25}$$

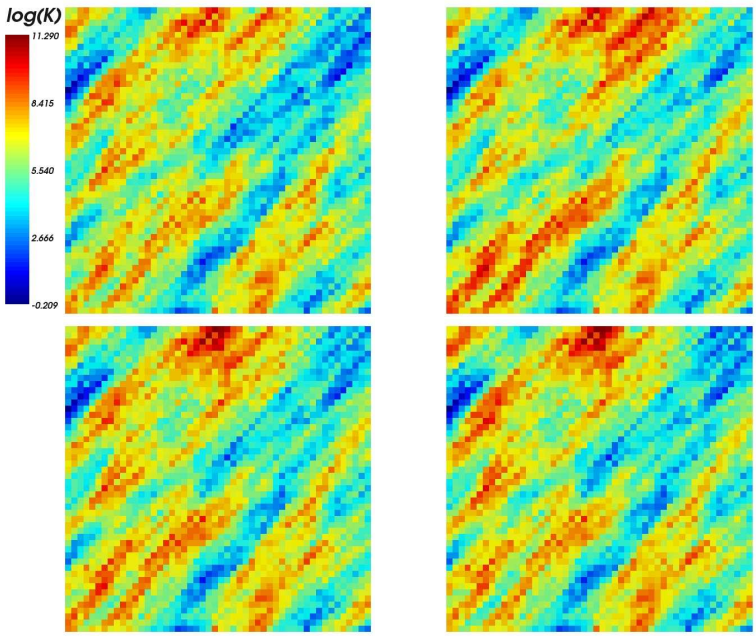

FIGURE 7. The plots show, from upper left to lower right, $\ln(k)$ for the reference permeability field, the initial permeability field, and the match obtained after eight iterations with and without updating basis functions.

4.3. Changing Well Conditions. We first consider a 2-D reservoir model with diagonal permeability streaks and a dynamic well configuration. The lognormal permeability field is given in terms of 50×50 uniform cells and has a diagonal structure with long correlation length, see **Fig. 7**. As above, we assume quadratic relative permeability curves with zero residual oil and water saturations and end-point mobility ratio $M_{\text{end}} = \mu_o/\mu_w = 0.5$. The forward simulator is run with pressure steps of 80 days, and for the MsMFEM pressure solver we construct a uniform 10×10 coarse where each block contains 5×5 fine cells.

Synthetic dynamic data were generated by adding 5% white noise to the fractional-flow curves computed from the reference permeability using a streamline simulator with a two-point pressure solver. Initially, the well configuration is a five-spot configuration, where the four producers operate with equal constant rate. The producer in the south-west corner has early breakthrough and is therefore converted to an injector after 640 days. Simultaneously, two new producers are introduced in the middle of each opposite boundary (north and east). After conversion and infill drilling, the south-west well is injecting 75% of the total injection rate and all producers are producing at equal constant rate. The motivation for the updated well configuration is to introduce an additional sweep from the south-west corner towards the opposite boundaries. The updated well configuration is kept throughout the rest of the production period. Hence, we wish to integrate 2000 days of production data from six producers in total.

To match observed data, we start from the prior permeability field shown in **Fig. 7** and treat the permeability in each cell as an adjustable parameter, giving a total of 2500 unknown parameters to be estimated. The time-shift sensitivities for each well are plotted in **Fig. 8**. The sensitivities are quite distinct and localized in channels due to the diagonal permeability

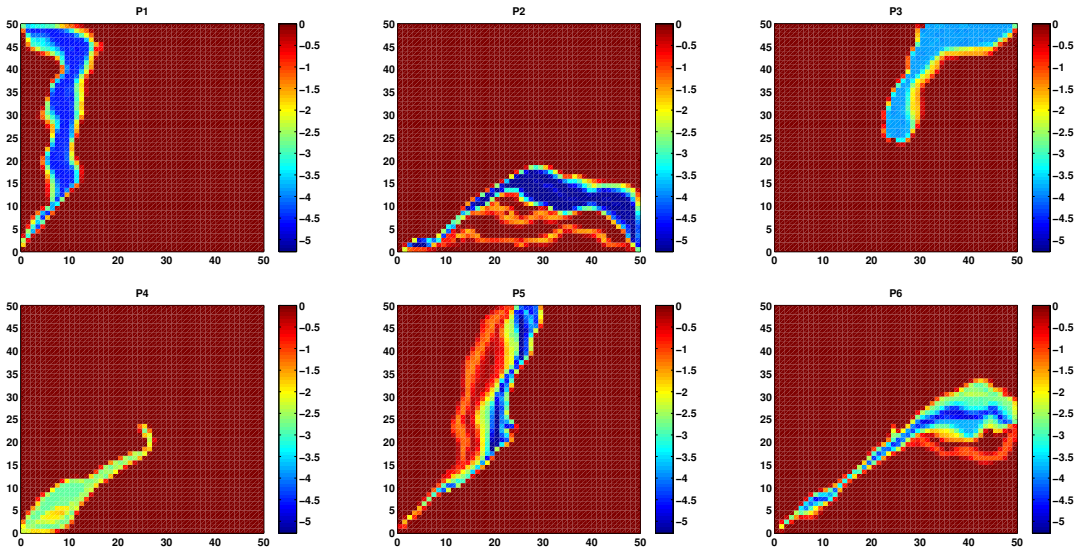

FIGURE 8. Streamline-based travel-time shift sensitivities for the six producers.

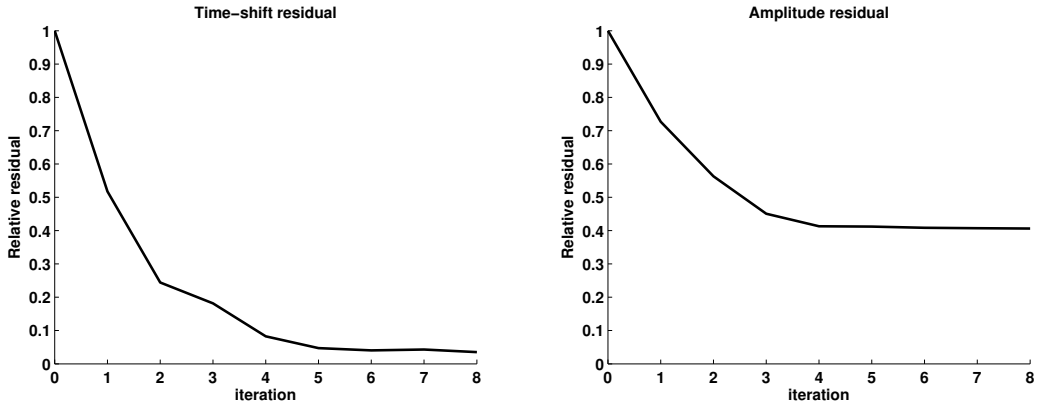

FIGURE 9. Reduction of residuals for all producers.

streaks. Plots of the residuals with respect to time-shift and amplitude in **Fig. 9** show that the iteration converges very fast (after 4–5 iterations). Results after eight iterations, updating all basis functions, are shown in **Fig. 7**. The updated permeability field is in general closer to the reference, and the realism of the permeability field is not degraded by the data integration process. **Figure 10** shows a comparison of the initial and final match of the fractional-flow curves for the wells with lowest initial, highest initial, and highest final mismatch (wells P3, P6, and P6, respectively). Overall, the match to the production data is quite satisfactory.

To test the robustness of our work reduction strategy we use a 5×5 test matrix with $x\%$ dynamical and $y\%$ initial update for $x, y = 0, 25, \ldots, 100$. **Figure 11** shows the reduction in residuals and permeability discrepancy after eight iterations. Judging from the amplitude residual and the permeability discrepancy, the data are well matched for all parameters $x, y >$

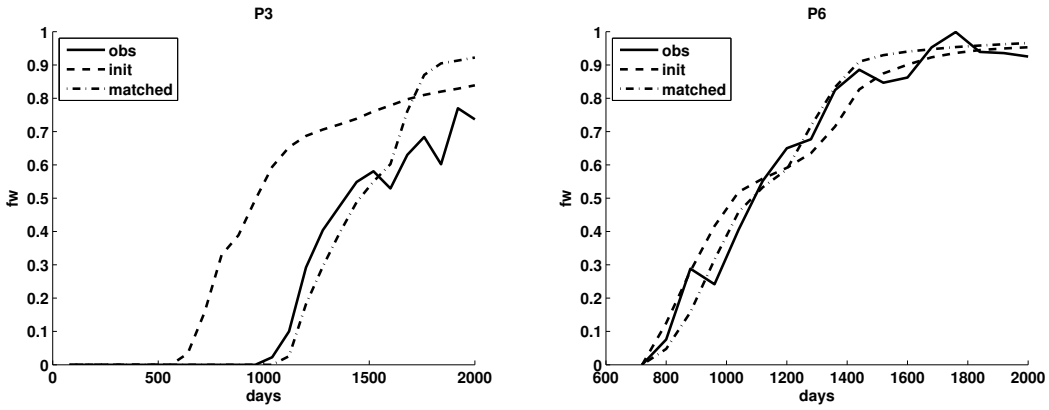

FIGURE 10. Fractional-flow curves for water for producers P3 (north-east), and P6 (east).

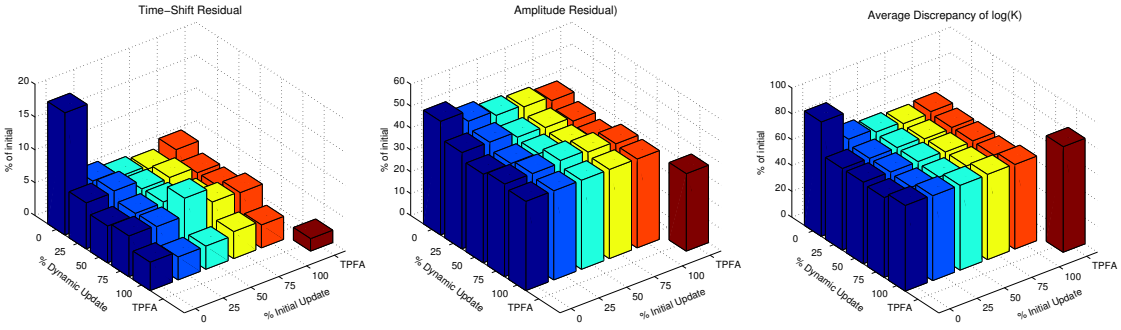

FIGURE 11. Robustness of selective work reduction.

0, and the quality of the match does not seem to decline dramatically compared with the TPFA solver. The time-shift residuals for MsMFEM are somewhat higher than for TPFA. The exception is $(x, y) = (0, 0)$, for which there is a significant decay in the quality of the match, in particular for the time-shift residual. **Figure 7** shows the resulting permeability field for $(x, y) = (0, 0)$ and $(100, 100)$. Even though the reduction in the residuals is significantly lower with no updating, the realism of the resulting permeability field seems as good as for full updating.

To explain the variations with respect to x and y, we consider the sensitivities. As seen in **Fig. 12**, the sensitivities are quite distinct and localized in channels (see also **Fig. 8**). The permeability field will typically change significantly from one iteration to the next in these channels, and failing to update the corresponding basis functions will lead to inaccurate results. However, for $x, y > 0$, our method seems to be able to select and update the basis functions contributing most to the production curves, see **Fig. 12**. The localized nature of the sensitivities makes it easier to cover the high-sensitivity areas with updated basis functions for quite low percentage values for x and y. In addition, the smoothing of permeability changes induced by the regularization in **Eq. 21** will also counteract the effect of sharp changes.

Finally, we emphasize that the reduction in runtime mainly will result from reducing the percentage of dynamically updated basis functions. It is therefore row $(x, 100)$ in the matrix

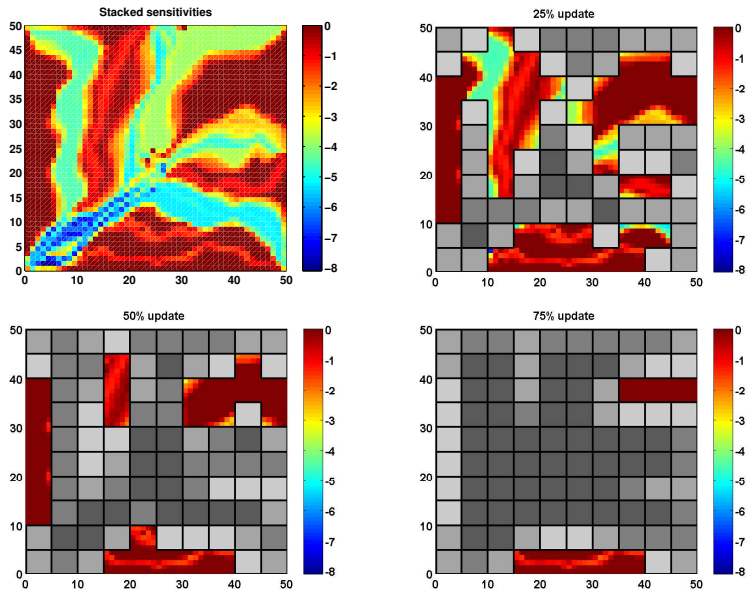

FIGURE 12. Stacked time-shift sensitivities (upper left). The three last figures show the coverage of updated basis functions for 25%, 50% and 75% updating. The four different levels of gray indicate the number of updated basis functions that cover each coarse grid block (brightest = 1, darkest = 4).

in **Fig. 11** that is of main interest when considering efficiency. In other words, we can avoid strategies in the matrix that give less stable results, and still get the intended speedup of the inversion process.

4.4. Multiple Equiprobable Realizations. We assume a multivariate Gaussian prior distribution for a 2-D reservoir model given on a 50×50 grid. As in the previous example, the prior distribution has long diagonal correlation length. The reference permeability field for this case is drawn from a slightly different multi-Gaussian distribution, see **Fig. 13**. The reservoir is produced from a five-spot pattern with an injector in the center and producers in the corners. As above, we assume quadratic relative permeability curves with zero residual oil and water saturations and end-point mobility ratio $M_{\text{end}} = 0.5$. For the MsMFEM pressure solver we construct a uniform 10×10 coarse grid such that each coarse block contains 5×5 fine cells.

Synthetic dynamic data were given by the fractional-flow curves obtained from the reference permeability field using the streamline method with a standard two-point pressure solver. To demonstrate the robustness of the generalized travel-time inversion, we match the observed data starting from a set of 25 permeability realizations of the assumed prior distribution. Here the permeability in each cell is treated as an adjustable parameter, giving a total of 2500 unknown parameters to be estimated for each realization.

Figure 13 shows three of the initial realizations and the corresponding matches after six iterations. The three matched permeability realizations are in closer agreement with the reference permeability field; a unique solution is not obtained since the data integration is ill-posed. **Figure 14** shows a comparison of the initial and final match of the fractional-flow

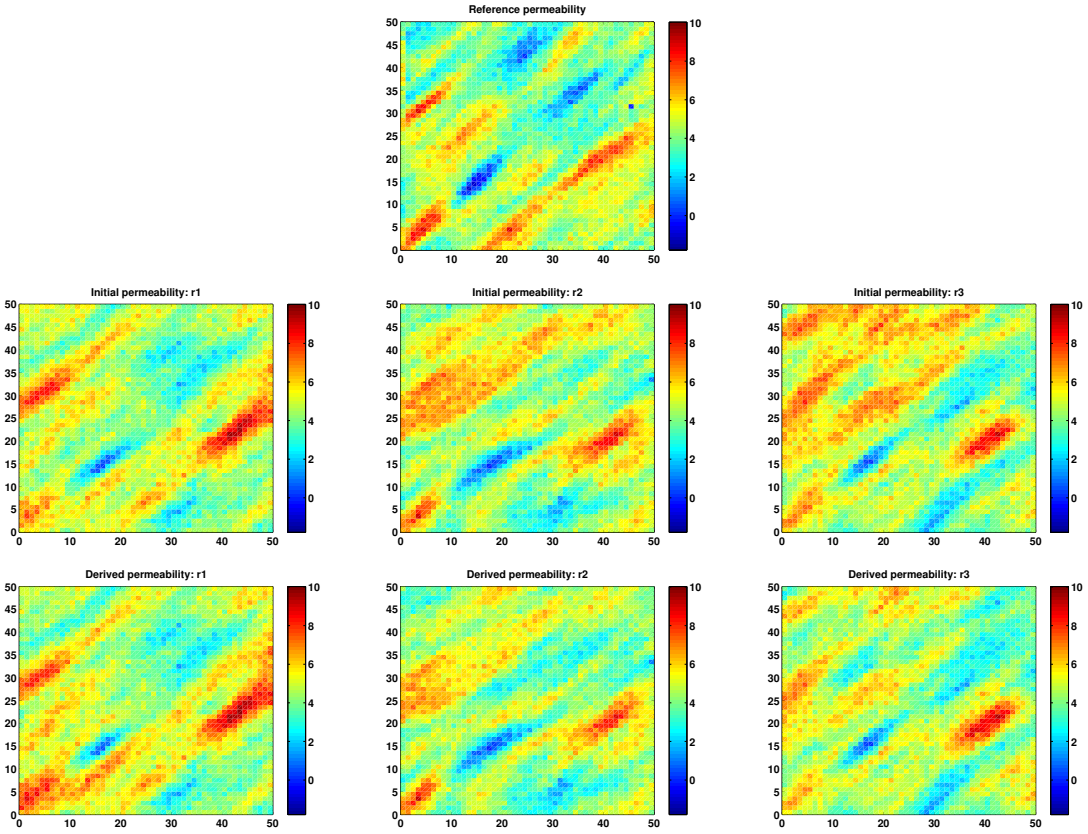

FIGURE 13. The plots show $\ln(k)$ for the reference permeability field (top) and initial (second row) and matched (third row) permeability fields for three different realizations.

TABLE 4. Mean and standard deviation of percentage reduction in misfit for time-shift residual (T) and amplitude residual (A).

	Misfit mean %		Std.dev. %	
Solver	T	A	T	A
Initial	100.0	100.0	100.0	100.0
TPFA	8.5	39.9	5.0	16.5
MsMFEM	7.8	38.9	4.6	17.6

curves for the set of permeability realizations for the four production wells. The time-shifts are obviously reduced considerably, and the amplitude is to some extent improved; also indicated in **Table 4**. Overall, the match to the production data is quite satisfactory.

Next we apply the same 5×5 test matrix for the set of realizations described above and measure the mean and standard deviations in the permeability discrepancy (**Eq. 25**) and the reduction in time-shift and amplitude residuals. **Figure 15** shows the result of the test matrix compared with results obtained with the TPFA solver. The data are well matched for all parameters x and y, and the quality of the history match does not seem to decline

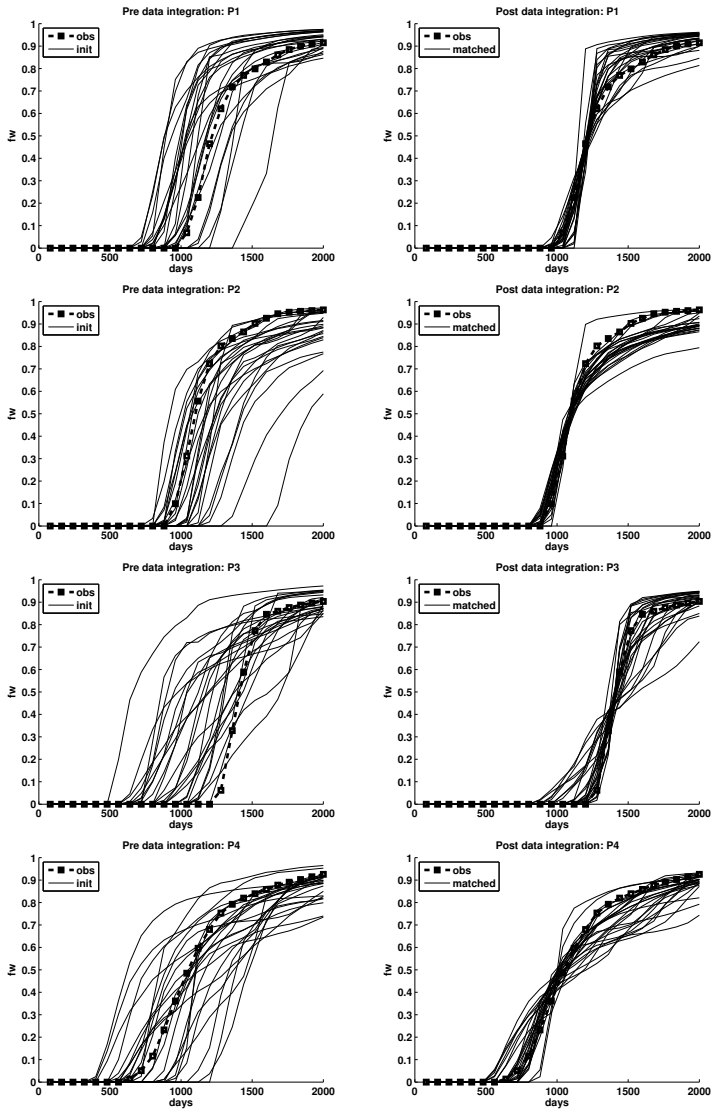

FIGURE 14. Fractional-flow curves prior and post data integration.

significantly compared with the TPFA solver even though a slight increase is observed by updating fewer basis functions.

4.5. History Matching a Full 3-D Geomodel. In (*Stenerud et al.*, to appear) we demonstrated the integration of dynamic fractional-flow data into a high-resolution 3-D geomodel with more than one million cells. We will now revisit this example and discuss the accuracy, robustness, and efficiency of our data-integration strategy in some more detail. In particular, we show that by combining generalized travel-time inversion with our modified streamline formulation and the selective work reduction, the computational challenging task of integrating data into a million-cell model can be surmounted in remarkable short time using a standard desktop or laptop computer.

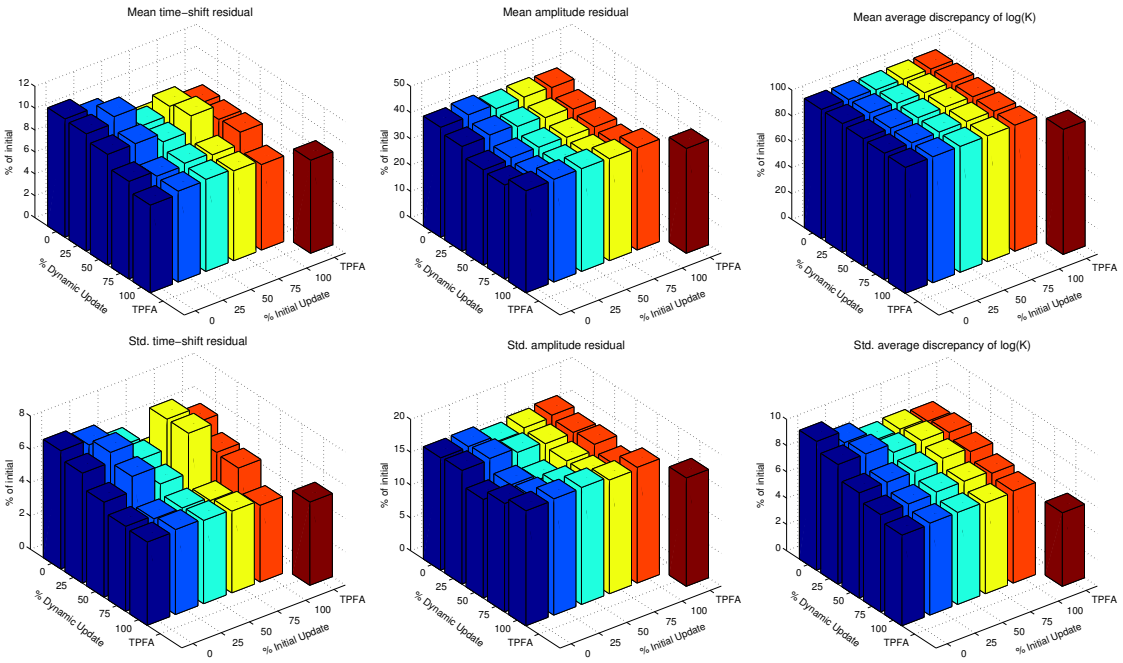

FIGURE 15. Mean (upper row) and standard deviation (lower row) of the reduction in time residuals, amplitude residuals and permeability discrepancies for a set of 25 permeability realizations.

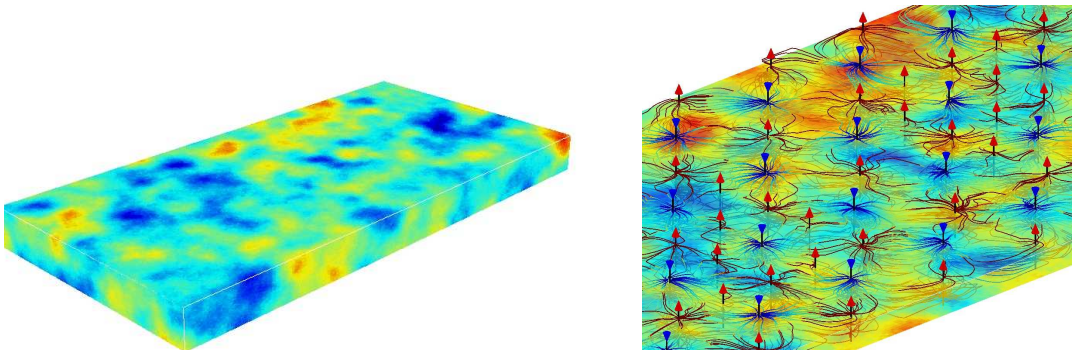

FIGURE 16. Permeability field and streamlines for the million-cell 3-D model.

The geomodel consists of a Cartesian fine grid with $256 \times 128 \times 32$ cells, which gives a total of 1 048 576 active cells, each of size $10 \times 10 \times 2$ m. We form a uniform $32 \times 16 \times 8$ coarse grid in which each block consists of $8 \times 8 \times 4$ fine cells. The permeability is log-normally distributed with a mean of 2.2 mD, a minimum of 0.017 mD and a maximum of 79.5 mD (see **Fig. 16**). The correlation length in the x- and y-directions is about 270 meters, and about 90 meters in the z-direction. The flow is described by the standard two-phase model with quadratic relative permeability curves and an end-point mobility ratio of $M_{\text{end}} = 5$.

The production history consists of 2475 days of fractional-flow data from the 69 producers, each operating with a constant rate fulfilling the total voidage rate induced by 32

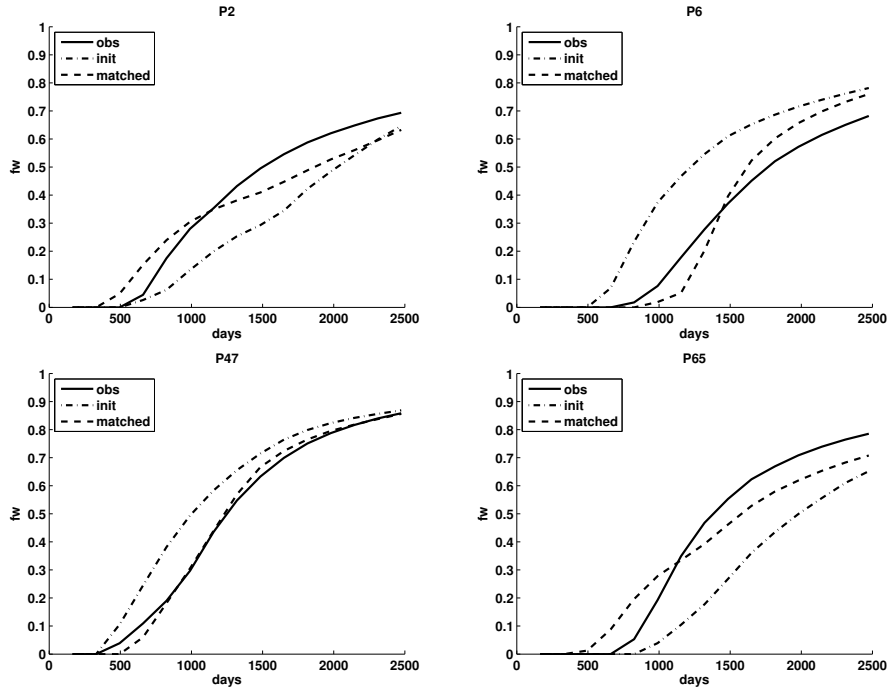

FIGURE 17. Match of fractional-flow curves for four of the 69 production wells included in the history match of the geologic model using the MsMFEM pressure solver.

water injectors operating with constant total reservoir-volume rate of 1609 bbl/day. For all simulations we used 15 pressure steps of 165 days. Good accuracy of the production curves required about 500 000 in the original streamlines method and about 50 000 streamlines for the modified formulation. Compared with the million-cell SPE 10 model in Section 3.2 this is a modest reduction. However, the current model has twenty times as many wells and is less dominated by heterogeneity structures compared with the SPE 10 model, in particular the bottom fifty fluvial layers.

An initial permeability model was generated using sequential Gaussian simulation (*Deutsch and Journel*, 1998) and conditioning on the permeability values in the well-blocks of the reference model. As reported in (*Stenerud et al.*, to appear), the misfit in time shift and amplitude had dropped appreciably after 5–6 iterations and the two pressure solvers gave almost identical derived permeability fields that both reserve the geologic continuity and the initial geologic features to the maximum possible extent. **Figure 17** shows initial and matched production curves for four producers.

First, we investigate to what extent the use of the modified streamline formulation and the multiscale pressure solver improves the computational efficiency of the data integration. As an example of a personal workstation, we use a recent commodity PC with a 2.4 GHz Intel Core 2 Duo processor with 4 Mb cache and 3 Gb memory. The TPFA pressure solver was compiled with full optimization and with multicore support for the underlying AMG linear solver. For MsMFEM, we were not able to optimize the underlying direct solver used to compute basis functions, nor did we exploit the parallelism of the Core 2 Duo processor.

TABLE 5. Reduction in percent in time-shift (T) and amplitude (A) residuals, and reduction in average discrepancy in log permeability ($\overline{\Delta \ln k}$). Runtimes are measured on a workstation PC with a 2.4 GHz Intel Core 2 Duo processor with 4 Mb cache and 3 Gb memory.

		Misfit			CPU-time (wall clock)		
Solver	O/M	T	A	$\overline{\Delta \ln k}$	Total	Pressure	Transport
Initial	—	100.0	100.0	0.821	—	—	—
TPFA	O	8.9	53.5	0.806	64 min	33 min	28 min
TPFA	M	9.6	50.4	0.806	39 min	30 min	5 min
MsMFEM	O	11.2	47.3	0.812	43 min	7 min	32 min
MsMFEM	M	10.4	45.4	0.828	17 min	7 min	6 min

Table 5 reports computational times (and reduction in misfit) using the TPFA and the MsMFEM pressure solvers in combination with the original and the modified streamline method. Here the total simulation time includes time for inversion, input/output, and seven forward simulations, each with fifteen pressure steps. Similarly, we report the total time for the pressure solves and the transport solves (including mappings and tracing of streamlines). Using the modified streamline method to reduce the number of streamlines from 500 000 to 50 000 reduced the time for the transport solves by 80% with negligible loss in accuracy. In (*Stenerud et al.*, to appear), we showed that reducing (or eliminating) the dynamical updates has almost no effect on the quality of the derived match for unfavorable mobility ratios. For MsMFEM, we used no initial and no dynamical updates and were thereby able to reduce time for pressure solves by about 80%, giving a significant reduction in the total runtime. Altogether, this meant that the full data integration could be performed in an impressive runtime of 17 minutes on a workstation PC!

To test the robustness of our selective work reduction, we apply the same 5×5 test matrix as in the two previous examples. For the strategies involving $x = 0\%$ dynamical update, no sensitivities are required to determine which basis functions to update. We therefore present results for both full dynamic update and no update during the first flow simulation for $x = 0\%$. **Figure 18** shows the reduction in residuals and permeability discrepancy after six iterations. Judging from the residuals and the permeability discrepancy, the data are well matched for all parameters, and the quality of the match is similar as for the TPFA solver. Altogether, the results indicate that the history-matching procedure is stable with respect to the selective work-reduction strategies.

Finally, we have tested how the speed-up for pressure solves for MsMFEM versus TPFA scales for the different work reduction strategies. To compare both solvers on more equal terms, we apply a somewhat older laptop PC with a 1.7 GHz Intel Pentium M processor so that both TPFA and the MsMFEM pressure solvers can be run with full optimization. Further, we are running all strategies with full dynamical update for the first flow simulation (because no sensitivities are available yet), except the strategies involving 0% dynamical update. Those strategies are run both with no and full dynamic updating during the first flow simulation. **Figure 19** shows the speed-up for the different combinations of updating strategies. The corresponding reduction in residuals and permeability discrepancy are shown in **Fig. 18**. As expected, the reduction in dynamic updates gives the greatest contribution

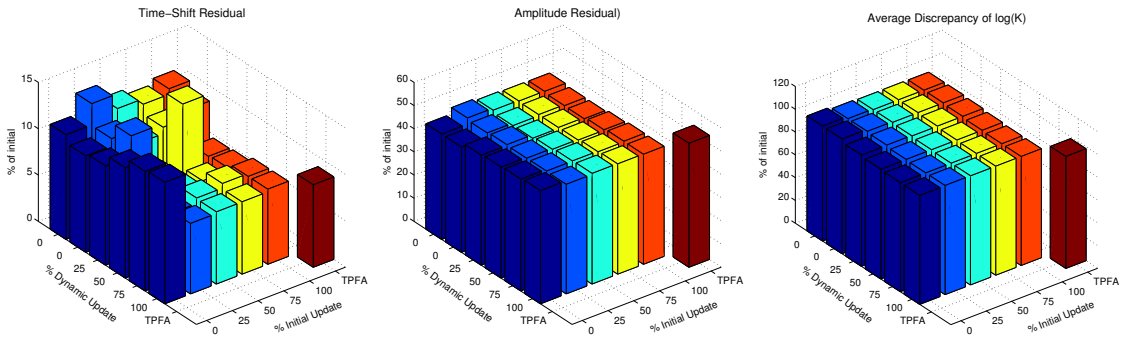

FIGURE 18. Robustness of selective work reduction. For 0% dynamical update, the first row corresponds no dynamic update during the first forward simulation and the second row to full update during the first simulation.

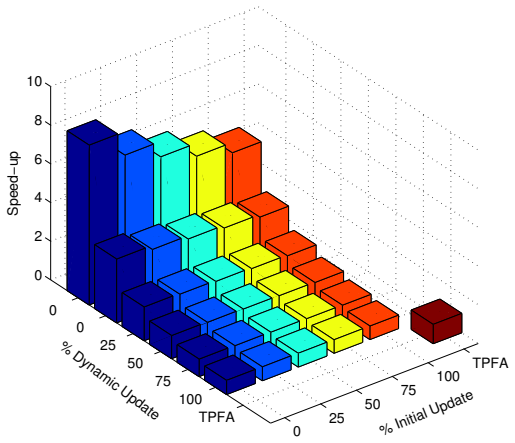

FIGURE 19. Speed-up matrix for time spent on pressure solves during the data integration. For 0% dynamical update, the first row corresponds no dynamic update during the first forward simulation and the second row to full update during the first simulation. Runtimes are measured on a 1.7 GHz Intel Dothan Pentium M processor with 2 Mb cache and 1.5 Gb memory

to the speed-up. With no updates, what so ever, the total data integration took 36 minutes on the laptop PC.

Finally, we notice that the memory requirements for the MsMFEM pressure solver are quite low and this solver could easily have been run on far larger models, as opposed to TPFA, for which the memory requirements of the AMG linear solver will rapidly limit the model sizes that can be run on a workstation or laptop PC.

5. Summary and Conclusions

A novel approach to data integration using multiscale-streamline simulation and analytic sensitivities is presented. There are four key components in our proposed approach:

(1) Inverse modeling by generalized travel-time inversion with quasilinear properties.
(2) Production-response sensitivities calculated analytically along streamlines.
(3) A modified streamline method that greatly reduces the mass-balance errors when simulating large and complex reservoir models using few streamlines.
(4) An efficient multiscale mixed finite-element method is applied as pressure solver, where the multiscale basis functions are recomputed selectively based on sensitivities.

The power and utility of our proposed approach was demonstrated using two 2-D models and a full field-scale geomodel consisting of more than a million grid cells. Starting with a prior subsurface model, production data were integrated using a generalized travel time inversion. The resulting permeability changes were found to be reasonable and geologically realistic (i.e., consistent with the initial geological model). For the one-million 3-D problem, the entire inversion process took about seventeen minutes using a commodity workstation PC. The very efficient forward simulation and sensitivity computations may generally enable history-matching of models with a large number of cells and/or a large number of (plausible) model realizations.

Altogether, we have presented very versatile method for integrating dynamic data into high-resolution subsurface models. The inversion method is applicable, with small modifications, to more general grid formats, as will be reported in (*Stenerud et al.*, submitted). We believe that using a MsMFEM pressure solver will prove particularly useful on complex grids, since the multiscale formulation gives a natural and automatic way of upscaling the grid in the pressure solver to speed up the forward simulation. Moreover, on highly skewed grids (e.g., corner-point grids), MsMFEM uses an accurate multipoint flux-approximation scheme to compute basis functions and therefore gives better spatial accuracy and more accurate predictions of flow than for a standard two-point method, see (*Aarnes et al.*, to appear).

Finally, we remark that the generalized travel-time inversion method has been extended to compressible three-phase flow, so that fractional-flow curves and gas-oil ratios are jointly incorporated (*Cheng et al.*, 2006). Moreover, data integration using streamline sensitivities has also been addressed for cases including gravity, changing field conditions, and fractured reservoirs (*He et al.*, 2002; *Al-Harbi et al.*, 2005).

Acknowledgments

The research of Stenerud was funded by the Uncertainty in Reservoir Evaluation (URE) program at the Norwegian University of Science and Technology. The research of Kippe and Lie was funded by the Research Council of Norway under grant number 152731/S30, 152732/S30 and 158908/I30.

References

Aarnes, J. E. (2004), On the use of a mixed multiscale finite element method for greater flexibility and increased speed or improved accuracy in reservoir simulation, *Multiscale Model. Simul.*, *2*(3), 421–439.

Aarnes, J. E., V. Kippe, and K.-A. Lie (2005), Mixed multiscale finite elements and streamline methods for reservoir simulation of large geomodels, *Adv. Water Resour.*, *28*(3), 257–271.

Aarnes, J. E., S. Krogstad, and K.-A. Lie (2006), A hierarchical multiscale method for two-phase flow based upon mixed finite elements and nonuniform coarse grids, *Multiscale Model. Simul.*, *5*(2), 337–363.

Aarnes, J. E., S. Krogstad, and K.-A. Lie (to appear), Multiscale mixed/mimetic methods on corner-point grids, *Comput. Geosci.*

Al-Harbi, M., H. Cheng, Z. He, and A. Datta-Gupta (2005), Streamline-based production data integration in naturally fractured reservoirs, *SPE J.*, *10*(4), 426–439.

Batycky, R. (1997), A three-dimensional two-phase field-scale streamline simulator, Ph.D. thesis, Stanford University, Dept. of Petroleum Engineering.

Bear, J. (1972), *Dynamics of Fluids in Porous Media*, American Elsevier, New York.

Chen, A., and T. Hou (2002), A mixed multiscale finite element method for elliptic problems with oscillating coefficients, *Math. Comp.*, *72*(242), 541–576.

Cheng, H., A. Datta-Gupta, and Z. He (2005), A comparison of travel-time and amplitude matching for field-scale production-data integration: Sensitivity, nonlinearity, and practical implications, *SPE J.*, *10*(1), 75–90.

Cheng, H., D. Oyerinde, and A. Datta-Gupta (2006), Compressible streamlines and three-phase history matching, in *SPE/DOE Symposium on Improved Oil Recovery*, Tulsa, Oklahoma, USA, SPE 99465.

Christie, M., and M. Blunt (2001), Tenth SPE comparative solution project: A comparison of upscaling techniques, *SPE Reservoir Eval. Eng.*, *4*(4), 308–317, url: www.spe.org/csp.

Deutsch, C., and A. Journel (1998), *GSLIB Geostatistical Software Library and User's Guide*, Oxford University.

He, Z., S. Yoon, and A. Datta-Gupta (2002), Streamline-based production data integration with gravity and changing field conditions, *SPE J.*, *7*(4), 423–436.

Hohl, D., E. Jimenez, and A. Datta-Gupta (2006), Field experiences with history matching an offshore turbiditic reservoir using inverse modeling, in *SPE Annual Technical Conference and Exhibition*, San Antonio, Texas, USA, SPE 101983.

Holden, H., and N. Risebro (2002), *Front Tracking for Hyperbolic Conservation Laws*, *Applied Mathematical Sciences*, vol. 152, Springer, New York.

Kippe, V., H. Hægland, and K.-A. Lie (2007), A method to improve the mass balance in streamline methods, in *SPE Reservoir Simulation Symposium*, Houston, Texas, USA, SPE 106250.

Kippe, V., J. E. Aarnes, and K.-A. Lie (to appear), A comparison of multiscale methods for elliptic problems in porous media flow, *Comput. Geosci.*

Matringe, S., and M. Gerritsen (2004), On accurate tracing of streamlines, in *SPE Annual Technical Conference and Exhibition*, Houston, Texas, USA, SPE 89920.

Paige, C., and M. Saunders (1982), LSQR: An algorithm for sparse linear equations and sparse least squares, *ACM Transactions on Mathematical Software*, *8*(1), 43.

Pallister, I., and D. Ponting (2000), Asset optimization using multiple realizations and streamline simulation, in *SPE Asia Pacific Conference on Integrated Modelling for Asset Management*, Yokohama, Japan, SPE 59460.

Pollock, D. (1988), Semi-analytical computation of path lines for finite-difference models, *Ground Water*, *26*(6), 743–750.

Ponting, D. (1998), Hybrid streamline methods, in *SPE Asia Pacific Conference on Integrated Modelling for Asset Management*, Kuala Lumpur, Malaysia, SPE 39756.

Qassab, H., M. K. R, Pavlas, N. Afaleg, H. Ali, A. Kharghoria, Z. He, S. Lee, and A. Datta-Gupta (2003), Streamline-based production data integration under realistic field conditions: Experience in a giant Middle-Eastern reservoir, in *SPE Annual Technical Conference and Exhibition*, Denver, Colorado, USA, SPE 84079.

Stenerud, V., V. Kippe, and K.-A. Lie (submitted), Generalized travel-time inversion on unstructured grids.

Stenerud, V., V. Kippe, K.-A. Lie, and A. Datta-Gupta (to appear), Adaptive multiscale streamline simulation and inversion for high-resolution geomodels, *SPE J.*

Stüben, K. (2000), *Algebraic Multigrid (AMG): An Introduction with Applications*, Academic Press, guest appendix in the book *Multigrid* by U. Trottenberg and C.W. Oosterlee and A. Schüller.

Vasco, D., S. Yoon, and A. Datta-Gupta (1999), Integrating dynamic data into high-resolution models using streamline-based analytic sensitivity coefficients, *SPE J.*, *4*(4), 389–399.

Vega, L., D. Rojas, and A. Datta-Gupta (2004), Scalability of the deterministic and bayesian approaches to production data integration, *SPE J.*, *9*(3), 330–338.

Yoon, S., A. Malallah, A. Datta-Gupta, D. Vasco, and R. Behrens (2001), A multiscale approach to production-data integration using streamline models, *SPE J.*, *6*(2), 182–192.

Paper IV

Generalized Travel-Time Inversion on Unstructured Grids

Vegard Røine Stenerud, Knut-Andreas Lie, and Vegard Kippe.

Submitted to *Journal of Petroleum Science and Engineering*.

Generalized Travel-Time Inversion on Unstructured Grids

Vegard R. Stenerud *,1

Department of Mathematical Sciences, NTNU, NO–7491 Trondheim, Norway

Knut–Andreas Lie [2]

Department of Applied Mathematics, SINTEF, P.O. Box 124 Blindern, NO–0314 Oslo, Norway

Vegard Kippe [2]

Department of Applied Mathematics, SINTEF, Oslo, Norway (Currently at StatoilHydro, Bergen, Norway)

Abstract

We propose an extension to fully unstructured grids for the so-called generalized travel-time inversion method for inversion of production data. The framework of the inversion method applies directly to fully unstructured grids, but there are aspects regarding sensitivities and regularization that have to be addressed. First, we propose a generalized smoothing operator for the regularization to impose smooth modification on reservoir parameters. Second, to handle reservoir models with great heterogeneity in cell sizes, we investigate the use of rescaled sensitivities (average cell volume multiplied by local sensitivity density) in the inversion.

We demonstrate the utility of our extensions by three numerical examples. First, we validate the inversion method by applying it to a reservoir model represented both on a Cartesian and on a refined triangular grid. Second, we apply the method for a highly unstructured grid with large differences in cell sizes. Finally, we consider an example with faults and non-neighboring connections. All examples show that our method is able to match the data with the same quality as has been obtained earlier on structured grids and without degrading the realism of the reservoir parameters.

Key words: History matching, Streamlines, Unstructured grids, Permeability

1 Introduction

The *generalized travel-time* (GTT) inversion method was introduced by Vasco et al. (1999) and He et al. (2002) and has been successfully applied to several field cases; see e.g., Qassab et al. (2003) and Hohl et al. (2006). Although the inversion method itself does not require a streamline simulator (Cheng et al., 2005b), it is most efficient if the required production-response sensitivities are approximated by analytical integrals streamlines and a streamline simulator is used for the forward simulation. However, the inversion method can be implemented on top of any simulator on a Cartesian grid that outputs velocity fields during the forward simulation (Cheng et al., 2005b). In this paper we discuss how to extend the GTT inversion method to fully unstructured grids.

Although the framework of the inversion method in principle can be generalized to unstructured grids, the method has not yet been applied to fully unstructured grids in practice, and there are issues to address regarding regularization and the use of sensitivities. First, the smoothing operator involved in the regularization has to be generalized to unstructured grids. For moderately skewed, logically Cartesian grids, finite-difference approximations for the Laplacian is used to measure the smoothness. The key question is therefore whether this stencil is directly generalizable or if one has to introduce some sort of spatial weighting. Second, the computation of production-response sensitivities on unstructured grids has to be investigated and verified. In addition, non-neighboring connections that can occur in connection with faults and fully unstructured grids have to be addressed.

In two recent papers (Stenerud et al., to appear,s) we proposed to combine GTT inversion with a highly efficient multiscale-streamline solver on Cartesian grids. In particular, we demonstrated how the sensitivities from the inversion method can be used to make certain simplifications in the multiscale flow solver in regions of low sensitivity, thereby reducing the total simulation time considerably with negligible loss in accuracy compared with a standard finite-difference simulator. The underlying multiscale mixed finite-element formulation (Chen and Hou, 2002; Aarnes, 2004) has later been extended as a very efficient flow solver for highly heterogeneous reservoirs on unstructured grids (Aarnes et al., to appear). We are confident that the combination of a

* Corresponding author. Fax: +47 73593524
Email addresses: vegarste@math.ntnu.no (Vegard R. Stenerud), Knut-Andreas.Lie@sintef.no (Knut–Andreas Lie).
URLs: http://www.math.ntnu.no/∼vegarste (Vegard R. Stenerud), http://folk.uio.no/kalie (Knut–Andreas Lie).
[1] Funded by the Uncertainty in Reservoir Evaluation (URE) program at the Norwegian University of Science and Technology.
[2] Funded by the Research Council of Norway through grant no. 152732/S30.

multiscale-streamline simulator and sensitivity-based work-reduction strategy of (Stenerud et al., to appear) can easily be extended to unstructured grids, thereby giving significant speedup of the forward simulations. Herein, however, we only use a standard mixed finite-element method (MFEM) as our flow solver. Moreover, we implicitly assume that the grid has adequate mesh quality to provide forward simulations of sufficient accuracy. Mesh quality is often determined by the smallest angles in the grid and a grid with quite equilateral cells therefore indicates good mesh quality. Hence, grids with high mesh quality can still have large differences in cell sizes, used to refine important regions of the reservoir, for instance in the near-well regions or near channels, flow barriers, etc.

The outline of the paper is as follows: First, we present the forward model and the inversion method and describe how to compute analytical approximations to the sensitivities. Then, we propose smoothing operators which are intended to be robust and avoid grid effects for fully unstructured 3-D grids with large differences in cell sizes. Finally, the applicability of our method is discussed in terms of a few numerical examples. In particular, we compare the new smoothing operator(s) with the standard finite-difference approximations for the Laplacian. In addition, we address aspects related to grid heterogeneity, sensitivities, robustness, and non-neighboring connections. For simplicity, we only consider two-dimensional triangular and quadrilateral grids.

2 Flow Model

We consider incompressible two-phase flow of oil and water in a non-deformable and permeable medium. For simplicity, we neglect the effects of gravity, compressibility, and capillary forces and assume no-flow boundary conditions. Our flow model then consists of an elliptic pressure equation

$$\nabla \cdot \vec{u} = q_t, \quad \vec{u} = -\lambda_t(S) K \nabla p, \tag{1}$$

and a quasilinear hyperbolic transport equation

$$\phi \frac{\partial S}{\partial t} + \nabla \cdot (f_w(S)\vec{u}) = q_w. \tag{2}$$

The primary unknowns in the coupled system (1)–(2) are the pressure p, the total Darcy velocity $\vec{u}$, and the water saturation S. The underlying porous rock formation is modeled in terms of the absolute permeability K and the porosity ϕ, which henceforth are assumed to depend on the spatial variable only. Further, q_t and q_w represent fluid sources and sinks (e.g., injection and

production wells). Finally, $\lambda_t = \lambda_w + \lambda_o$ denotes the total mobility, where the mobility λ_j of each phase ($j = o, w$) is given as the relative permeability k_{rj} divided by the phase viscosity μ_j, and $f_w = \lambda_w/\lambda_t$ is the fractional-flow function of water.

By making a coordinate transformation, the three-dimensional transport equation can be decoupled into a family of one-dimensional transport equations. Rather than using the arc length along the streamline as a spatial coordinate, we use the time-of-flight defined by,

$$\tau = \int_{\Sigma} \frac{\phi(\xi)}{|\vec{u}(\xi)|}\, d\xi =: \int_{\Sigma} s(\xi)\, d\xi,$$

where Σ denotes the streamline trajectory and s denotes the so-called slowness function $\phi/|\vec{u}|$. The operator identity $\vec{u} \cdot \nabla = \phi \frac{\partial}{\partial \tau}$ together with the incompressibility condition $\nabla \cdot \vec{u} = 0$ can be used to rewrite (2) as a family of one-dimensional transport equations along streamlines

$$\frac{\partial S}{\partial t} + \frac{\partial f_w}{\partial \tau} = 0. \tag{3}$$

The solution of (2) is obtained by tracing a set of streamlines, mapping the initial saturations from the 3-D pressure grid to 1-D streamlines, and then solving (3) along each streamline forward in time. Afterwards, the new streamline saturations are mapped (or averaged) back to the underlying 3-D grid to update mobilities before the pressure equation (1) is solved to recompute the pressure and velocity field. This solution process continues forward in time, alternating between a pressure step and a transport step for fluid saturation.

3 The Inversion Method

The heart of the inversion method is to determine perturbations $\delta\mathbf{m}$ that minimize the following function on a given simulation grid

$$\arg\min_{\delta\mathbf{m}} \; \|\delta\mathbf{d} - \mathbf{G}\delta\mathbf{m}\| + \underbrace{\beta_1 \|\delta\mathbf{m}\|}_{\text{norm}} + \underbrace{\beta_2 \|\mathbf{L}\,\delta\mathbf{m}\|}_{\text{smoothing}}. \tag{4}$$

The first term of (4) is the data-misfit term, where $\mathbf{d}$ denotes the observed data points, $\mathbf{m}$ the reservoir parameters, and $\mathbf{G} = \{\frac{\partial d_j}{\partial m_i}\}$ is the sensitivity matrix. The other two terms are regularization terms used to stabilize the under-determined inversion problem and β_1 and β_2 are scalars used to weight

the importance of each regularization term. The norm constraint $\|\delta\mathbf{m}\|$ measures the magnitude of $\delta\mathbf{m}$ and seeks to minimize the modifications made to the reservoir parameter $\mathbf{m}$. In the last term, $\mathbf{L}$ is a smoothing operator that measures the local roughness of $\delta\mathbf{m}$. This term therefore tends to keep the modifications made to the reservoir parameter $\mathbf{m}$ as smooth as possible. In other words, changes in the reservoir parameters are induced by size and sign of the data shifts $\delta\mathbf{d}$ and the magnitude and distribution of sensitivities $\mathbf{G}$, diminished by the norm regularization, and smeared out by the smoothing term.

A minimum for (4) can be obtained by a least-square solution of the augmented linear system

$$\begin{bmatrix} \mathbf{G} \\ \beta_1\mathbf{I} \\ \beta_2\mathbf{L} \end{bmatrix} \delta\mathbf{m} = \begin{bmatrix} \delta\mathbf{d} \\ \mathbf{0} \\ \mathbf{0} \end{bmatrix}. \tag{5}$$

This system is typically solved with the iterative least-square minimization algorithm, LSQR (Paige and Saunders, 1982). This minimization method has proven to be robust and applicable for permeability fields on non-deformable logically Cartesian grids; see e.g., Qassab et al. (2003) and Hohl et al. (2006). Even though each grid cell in a logically Cartesian grid is identified by an ijk-triple, it is often convenient to give the grid cells a natural numbering $\mathcal{G} = \{1, 2, \ldots, N\}$. Hence, the framework can be applied directly to fully unstructured grids (e.g., triangular or tetrahedral grids). However, as mentioned above there are issues to rule out to verify the applicability for fully unstructured grids.

3.1 Quantification of Data Misfit

Misfit in dynamic data is commonly represented by a least-squares functional of the form:

$$E = \sum_{k=1}^{N_w} \sum_{j=1}^{N_d^k} w_{kj} \left[y_k^{\text{obs}}(t_j^k) - y_k^{\text{calc}}(t_j^k) \right]^2. \tag{6}$$

Here y_k^{obs} and y_k^{calc} are the observed and calculated production responses in well k at time t_j^k; N_w and N_d^k denote the number of wells and the number of observed data per well, respectively; and w_{kj} represent data weights. The production responses can for instance be dynamic pressure, water cut, and/or gas-oil ratio. Henceforth we only consider water cut data.

Rather than minimizing (6) directly, we will use a one-step generalized travel-time (GTT) inversion (He et al., 2002), for which we seek a set of time-shifts $\mathbf{\Delta t} = \{\Delta t_k\}$ for the calculated production responses. A time-shift simply expresses how much a calculated production curve should be shifted in time to maximize the cross-correlation with the observed curve. To determine the optimal time-shifts, we minimize the following misfit at each well:

$$E_k(\Delta t_k) = \sum_{j=1}^{N_d^k} \left[y_k^{\text{obs}}(t_j^k + \Delta t_k) - y_k^{\text{calc}}(t_j^k) \right]^2 . \tag{7}$$

Using the GTT inversion, we can match multiple data points as in amplitude inversion, while retaining the attractive quasilinear properties of travel-time inversion (Cheng et al., 2005a). We emphasize that computing time-shifts does not require new flow simulations, but can be done using data from the single forward simulation used to evaluate the data mismatch.

In practice, we do not use (7) directly. Instead we maximize the coefficient of determination:

$$R_k^2(\Delta t_k) = 1 - \frac{\sum_{j=1}^{N_d^k} \left[y_k^{\text{obs}}(t_j^k + \Delta t_k) - y_k^{\text{calc}}(t_j^k) \right]^2}{\sum_{j=1}^{N_d^k} \left[y_k^{\text{obs}}(t_j^k) - \overline{y_k^{\text{obs}}} \right]^2}, \tag{8}$$

where $\overline{y_k^{\text{obs}}}$ is the average over all N_d^k data points at well k. Having determined the optimal time-shifts $\mathbf{\Delta t}$, the next step is to propagate them into changes in the reservoir parameters. For this we apply (5) with $\delta \mathbf{d} = \mathbf{\Delta t}$.

Finally, to measure the misfit in water cut during the inversion process we will use the amplitude and time-shift residuals ($w_{kj} = 1$ in (6))

$$E_{\text{amplitude}} = \sqrt{E}, \qquad E_{\text{time-shift}} = \Big(\sum_{k=1}^{N} (\Delta t_k)^2 \Big)^{1/2}.$$

3.2 Sensitivities on Unstructured Grids

For the sake of completeness, we briefly describe the analytical calculation of streamline-based approximate sensitivities. To this end, we consider a perturbation $\delta \mathbf{m}$ in the reservoir parameters, which will result in a time-shift δt in the calculated production curve for a given well. Thus, for each observation we have that (Vasco et al., 1999; He et al., 2002)

$$\delta t = \delta t_j = \Big[\frac{\partial t_j}{\partial \mathbf{m}} \Big] \cdot \delta \mathbf{m}. \tag{9}$$

Summing this equation over all data points N_d, we obtain an expression for the overall time-shift δt of the calculated production curve. By convention, $\Delta t = -\delta t$ (see (7)) and the sensitivity of the shift in the generalized travel time Δt with respect to reservoir parameter m_i is given by

$$\frac{\partial \Delta t}{\partial m_i} = -\frac{1}{N_d} \sum_{j=1}^{N_d} \frac{\partial t_j}{\partial m_i}. \tag{10}$$

Production data are calculated by averaging the flow rates of each connected streamline. Now we fix the water cut y_k^{calc} and the fractional flow contributions from each streamline. Then, by assuming a Buckley–Leverett profile along each streamline, the fractional flow at the outlet can be related to the streamline time-of-flight using the expression $\tilde{f}'_w(S_{o,\ell}) = \tau_\ell / t_j$, where $\tilde{f}_w$ is the convex hull of f_w and $S_{o,\ell}$ is the saturation at the outlet of streamline ℓ. Since $\tilde{f}'_w(S_{o,\ell})$ is fixed, it follows that $\partial t_j / \partial m_i$ is proportional to the sensitivity of the time-of-flight, which can be computed analytically from a single streamline simulation under the assumption that the streamlines do not shift because of small perturbations in reservoir properties. For example, the sensitivity of τ_ℓ with respect to permeability K_i in cell i is given by

$$\frac{\partial \tau_\ell}{\partial K_i} = \frac{\partial \Delta \tau_{\ell,i}}{\partial K_i} = \int_{\Sigma_{\ell,i}} \frac{\partial s(\xi)}{\partial K_i}\, d\xi = -\int_{\Sigma_{\ell,i}} \frac{s(\xi)}{K_i}\, d\xi = -\frac{\Delta \tau_{\ell,i}}{K_i}, \tag{11}$$

where the integral is along the streamline trajectory $\Sigma_{\ell,i}$ through cell i and $\Delta \tau_{\ell,i}$ is the associated incremental time-of-flight. Because the sensitivities are simple integrals along streamlines, the computation time scales very favorably with respect to the number of grid cells, thus making streamline-based sensitivities the preferred approach for integrating dynamic data into highly-detailed subsurface models.

As seen above, the parameter sensitivities in $\mathbf{G}$ can be computed as analytical integrals along streamlines and be obtained by post-processing output from a single flow simulation As such, the sensitivities are independent of the underlying grid geometry, which is accounted for in the tracing process. In the current paper, the tracing is performed by subdividing general polyhedral cells into triangles in 2-D and tetrahedra in 3-D and then computing the incremental streamline path analytically on each subcell. The sensitivity for an aggregated cell consisting of a collection of subcells can be obtained by summing the sensitivities of the subcells (Yoon et al., 2001). This follows from specifying a differential for the production response based on an equal perturbation of each subcell parameter. Further, from (11) it is observed that the time-of-flight sensitivities can be computed for any convex grid cell as long as one is able to trace the streamline to obtain the time-of-flight over the cell. Hence, the

volume of the cell is implicitly accounted for through the time-of-flight over the cell, which is in agreement with the additivity.

A problem with defining sensitivities this way is that small cells will in general have smaller sensitivities, and contrary large cells will in general have larger sensitivities. Thus, smaller modifications will in general be imposed on small cells, and grid effects may therefore occur if there are (large) variations in cell sizes in the underlying unstructured grid. This effect will, to a certain extent, be counteracted by the smoothing regularization if there are other cells with potential for greater modifications in the vicinity of a small cell. One way to remedy these grid effects is to apply rescaled sensitivities defined as the local sensitivity density (sensitivity per area/volume) multiplied by the average cell volume. Since the sensitivities are spatially additive, applying these rescaled sensitivities should therefore give a distribution more equal to the sensitivity distribution obtained on a equisized grid. Another way to remedy the problem is to lump together small cells to larger cells, to get a more uniform grid for the history matching. However, this will in general require some kind of upscaling/downscaling of the reservoir parameters $\mathbf{m}$ and will not be considered herein. We will return to a discussion of grid effects due to variations in cell sizes in the numerical examples below.

4 Generalized Smoothing Stencil

The smoothing operator $\mathbf{L}$ has to be generalized for fully unstructured grids. For Cartesian grids the smoothing operator $\mathbf{L}$ was constructed by applying a finite-difference approximation for the Laplacian. More precisely, the well-known five-point and seven-point stencils were used for 2-D and 3-D grids, respectively. Four-point and five-point finite-difference approximations for the Laplacian can also be derived on uniform triangular and tetrahedral grids (Iserles, 1996) (possibly also for non-uniform grids). Equivalent stencils for the Laplacian can also be derived as finite-volume stencils using two-point approximations. These stencils only involve the nearest neighbors and may be less robust because the triangles and tetrahedra have fewer nearest neighbors than the quadrilaterals and hexahedra, respectively. In 3-D, it is sometimes appropriate to use a separate stencil in the z-direction (vertical), because parameters in different layers are usually less correlated. In that way it is possible to match each layer more independently.

All the stencils discussed above can be written on the following general form

$$L_i \, \mathbf{m} \propto \left(\sum_{j \in \mathcal{N}(i)} w_j m_j \right) - w_i m_i, \qquad w_i = \sum_{j \in \mathcal{N}(i)} w_j. \tag{12}$$

Here the neighborhood $\mathcal{N}(i)$ contains other cells sufficiently spatially close that will contribute to the smoothing stencil of a given cell i. Notice that cell i is not included in $\mathcal{N}(i)$.

A naive direct generalization of the finite-difference stencils applied for logically Cartesian grids (using the nearest neighbors) may work fine for grids with quite equisized and equilateral grid cells. However, the generalized stencil will lack robustness and result in grid effects for the smoothing of fully unstructured grid that possibly has large variations in cell sizes. On the other hand, the smoothing operator does not necessarily have to accurately approximate the Laplacian; it is most important is that the operator results in a proper smoothing. Indeed, a good smoothing operator for unstructured grids should try to fulfill the following criteria:

(1) The operator should coincide with the five-point (or seven-point) stencil for uniform 2-D (or 3-D) Cartesian grids.
(2) The operator should give the same smoothing effect independently of the local grid density (unless some spatially varying smoothing parameter is incorporated).
(3) The smoothing of each grid cell i should be influenced by an appropriate neighborhood $\mathcal{N}(i)$.
(4) The influence of each neighbor should decay (or stay constant) by the distance $\zeta(i, j)$, and be zero outside some range.
(5) The influence of a neighbor should be bounded as the distance $\zeta(i, j)$ goes to zero.

To meet these criteria, we propose a generalized smoothing stencil on the form

$$w_j = w_{\text{norm}} \cdot \rho(\zeta(i, j); R, \ldots), \quad \text{for } j \in \mathcal{N}(i), \tag{13}$$

where $\mathcal{N}$ is either the radius or k-ring neighborhood, $\rho(\zeta; R, \ldots)$ is a standard correlation function from geostatistics, and w_{norm} is a normalization weight used to ensure that the influence of each neighborhood is approximately the same. The generalized correlation length R is used to control the range of influence for ρ.

4.1 Neighborhood

The k-ring neighborhood $\mathcal{N}_k(i)$ includes all cells that can be reached by k edges or less in the connectivity graph in which the centroids of each cell is a vertex; see Figure 1. The centroids can be precomputed efficiently by decomposing polyhedral cells into triangles/tetrahedra and using area/volume-weighted average of the centroids of the resulting subcells. The 1-ring neighborhood of cell

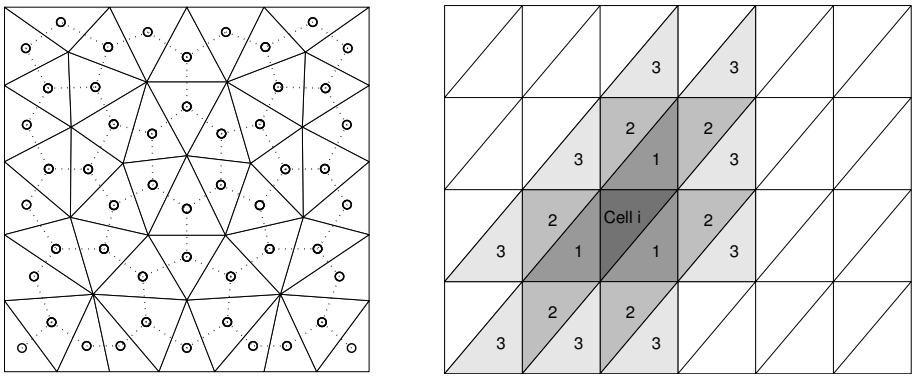

Fig. 1. (Left) An example of the connectivity graph, where the centroids of the triangles represent the vertices of the graph. (Right) An example of a k-ring neighborhood $\mathcal{N}_k(i)$ for $k = 1, 2, 3$.

i will be the collection of all cells adjacent to cell i. Figure 1 illustrates the 1-ring, 2-ring, and 3-ring neighborhood for grid cell i in a regular triangular grid. Note that in general $\mathcal{N}_1(i) \subseteq \mathcal{N}_2(i) \subseteq \mathcal{N}_3(i) \subseteq \ldots$. The k-ring neighborhood is sometimes referred to as a kth order neighborhood.

Second, the radius neighborhood, with a radius of x length units, is denoted by $\mathcal{N}_{r=x}(i)$. The radius neighborhood include all (i, j) that are reachable by a search in the connectivity graph without violating $\zeta(i, j) \leq x$. As our distance function, we will use the standard Euclidean distance between the cell centroids. To account for anisotropy, one may alternatively use a non-Euclidean distance measure

$$\zeta_{\mathbf{K}}(i, j) = \|\vec{\zeta}\|_{\mathbf{K}} = \sqrt{\vec{\zeta}^t \mathbf{K} \vec{\zeta}},$$

where $\vec{\zeta}(i, j) = [\zeta_x, \zeta_y, \zeta_z]$ is the vector containing the Euclidean distance in each coordinate direction and $\mathbf{K}$ is positive semi-definite.

Both the k-ring neighborhood and the radius neighborhood give symmetric neighborhood configurations in the sense that if $i \in \mathcal{N}(j)$ then $j \in \mathcal{N}(i)$. For the k-ring neighborhood, the number of cells are bounded so that

$$|\mathcal{N}_k(i)| \leq k \times (\#\text{edges/faces per cell}).$$

The more equisized and equilateral the grid cells are, the closer to the upper bound will in general the number of cells in the k-ring neighborhood be. In general the number of cells in the different k-ring neighborhoods will not vary much over the grid (for a fixed k). On the other hand, for a radius neighborhood the number of cells in a neighborhood can have great variations over the grid. By a proper weighting, we expect the radius neighborhood to give a more robust and less grid-dependent smoothing since the area of

influence does not vary much over the grid. Nevertheless, when defining the neighborhood radius one should take some considerations. The radius should be chosen so that the neighborhood of all cells at least includes the nearest neighboring cells, i.e., $\mathcal{N}_1(i) \subseteq \mathcal{N}_{r=x}(i)$. The radius neighborhood will therefore in general have a greater extent, so a smoothing stencil where the weights decay by distance may therefore be reasonable.

For a grid with non-neighboring connections it is not obvious how to define the neighborhood. For instance, close to a fault the grid cells on each side do not necessarily have faces that overlap completely, and consequently a grid cell can have several neighbors with partial overlap of faces. A simple solution is to define the "partial" neighbors as ordinary neighbors. Consequently, the connectivity graph can be defined, and thereby the neighborhood. A more thorough approach would be to in some sense weigh the partial neighbor connections in the stencil. However, in the numerical examples in this paper we will apply the simple approach without weighting.

4.2 Correlation Function

Correlation functions (Abrahamsen, 1997) are used to model the covariance structure of a random spatial quantity and are usually designed to be positive definite by satisfying the following criteria:

$$\rho(0) = 1, \quad |\rho(\zeta)| \leq 1 \; \forall \zeta, \quad \rho(\zeta) \in \mathrm{C}_0 \text{ for } \zeta > 0, \quad \lim_{\zeta \to \infty} \rho(\zeta) = 0. \tag{14}$$

Positive definiteness is not an issue for our smoothing stencil, and we are therefore free in general to choose from a broader range of functions. However, even though there are higher-order finite-difference stencils for the Laplacian with weights alternating sign based on distance (Iserles, 1996), we will henceforth stick to positive correlation functions. Hence, the first relation in (14) fulfills Requirement 5 above.

A correlation function usually has a parameter R called correlation length or range, which is often considered as the distance ζ for which $\rho \approx 0.05$, i.e., $|\rho(\zeta)| \lesssim 0.05$ for $\zeta > R$. Moreover, some readers may be more familiar with the variogram function $\gamma(\zeta; R)$ than the correlation function, which for stationary Gaussian random fields are given by $\gamma(\zeta; R) = \sigma^2(1 - \rho(\zeta; R))$, where σ^2 is the variance.

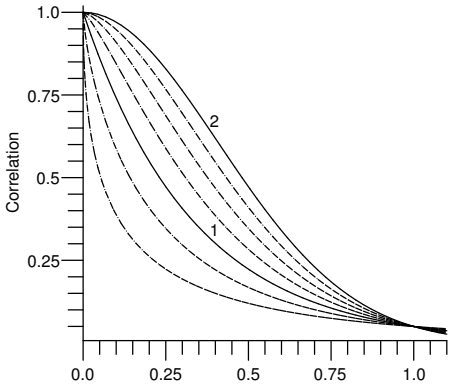

Fig. 2. Exponential correlation functions for $R = 1$ plotted as solid curves for $\nu = 1.0, 2.0$ (indicated on plot) and as dashed curves for ν =0.50, 0.75, 1.25, 1.50, and 1.75.

In the following we consider either the constant correlation function,

$$\rho_{\text{const}}(\zeta; R) = \begin{cases} 1\ , & \text{for } 0 \leq \zeta \leq R, \\ 0\ , & \text{else,} \end{cases}$$

which is discontinuous and thus violates (14), and the exponential correlation function

$$\rho_{\text{exp},\nu}(\zeta; R, \nu) = e^{-3(\zeta/R)^\nu}, \qquad 0 < \nu \leq 2,$$

which decays with increasing distance. For $\nu = 2$ the corresponding correlation function is sometimes referred to as the Gaussian correlation function. Figure 2 depicts some exponential correlation functions for different values of the parameter ν. To fulfill Requirement 4 and because positive definiteness is not an issue for our purpose, we set $\rho(\zeta)$ to zero for $\zeta > R$.

In spatial statistics it is common to replace $(\frac{\zeta}{R})$ with $\|[\frac{\zeta_x}{R_x}, \frac{\zeta_y}{R_y}, \frac{\zeta_z}{R_z}]\|_2$ in the correlation functions ρ to account for anisotropy in the principal coordinate directions. For $R_x = R_y = R_z = R$ the two representations will coincide. If the anisotropy directions are not aligned with the principal directions, a coordinate transformation may be required. This can be performed by measuring ζ through $\|\cdot\|_{\mathbf{K}}$ as described above. Another possibility to account for anisotropy, which is applied in geostatistics, is to construct the correlation function as a product of correlation functions related to different spatial directions, e.g., $\rho(\zeta) = \rho_{xy}(\zeta) \cdot \rho_z(\zeta)$.

4.3 Normalization Weights

For w_{norm} we seek a normalization weight such that the influence of each neighborhood is approximately the same. Inspired by Taubin (1995) we therefore propose the following choices:

$$w_{\text{norm}} = \Big(\sum_{j \in \mathcal{N}(i)} \rho(\zeta(i,j)) \Big)^{-1}, \tag{15}$$

$$w_{\text{norm}} = \Big(\bar{\rho} \cdot |\mathcal{N}(i)| \Big)^{-1}. \tag{16}$$

Here $\bar{\rho}$ is the average correlation over all neighborhoods of the grid:

$$\bar{\rho} = \frac{1}{|\mathcal{G}|\,|\mathcal{N}(i)|} \sum_{i \in \mathcal{G}} \sum_{j \in \mathcal{N}(i)} \rho(\zeta(i,j)).$$

The $\bar{\rho}$ function can be preprocessed or computed when the neighborhoods are traversed. The evaluation of $\bar{\rho}$ only involves arithmetic operations and is thus very fast. Further, since $\bar{\rho}$ can be accumulated, it does not increase the memory requirements.

The weight(15) multiplied by ρ sums to unity for all $j \in \mathcal{N}(i)$ and therefore gives the same weight to all neighborhoods. Further, (16) will also give a normalization on average over all neighborhoods, but (16) adaptively gives more weight to a neighborhood based on the average generalized correlation for the neighborhood. Further, both (16) and (15) will ensure that the total weight given to the smoothing in (4) does not vary much by changing the particular form of the ρ function. We will stick to (16), because it gives an adaptive weighting. Hence, in our weighting operator we have not taken any specific actions to account for boundary effects.

A natural question is if there should be a correspondence between the correlation length in the different directions of the permeability field and the correlation length used in the generalized stencil. In general it should not. The reason is that we assume the basic structure of the permeability field is incorporated into the prior/initial permeability field. The main task of the smoothing stencil is therefore just to preserve the structure by enforcing smooth changes in the inversion process, so the correlation length for the smoothing stencil is therefore more dependent on the grid density. However, it can for instance be advantageous to let the permeabilities change more independently in the different layers, and possibly also on each side of faults. This can partially be incorporated by the approach for anisotropic correlation functions described in Section 4.2. However, the layers and faults are not necessarily aligned with specific coordinate axes. A more advanced generalized correlation function that

incorporates not only the distance function, but also layer information may therefore be required. In other words, spatially varying stencil/neighborhood parameters are required.

For a uniform Cartesian grid, the standard five-point stencil can be represented by our definition by letting the neighborhood be $\mathcal{N}_1$ or $\mathcal{N}_{r=h}$, and w_{norm} be given by either (16) or (15). Further, $\rho(\zeta)$ will have the same value for the different adjacent grid cells for any positive bounded real function. Hence, Requirement 1 can be fulfilled for the generalized smoothing stencil.

In the next section we apply the proposed generalized smoothing stencil to a few numerical examples and discuss its utility.

5 Numerical Examples

For simplicity, we will in the following only focus on 2-D test cases using the simplified flow model for an incompressible, immiscible oil-water system as described in Section 2. First, we compare the performance of the generalized travel-time inversion on uniform Cartesian and uniform triangular grids (Case 1). Second, we investigate the applicability of the generalized travel-time inversion on a non-uniform, highly unstructured triangular grid (Case 2). Finally, we try to apply the generalized stencil to a corner-point grid with faults and non-neighboring connections at the faults (Case 3).

For all cases the flow is described using quadratic relative permeability curves with individually specified end-point mobility ratios. Further, for the forward simulations are performed with a streamline simulator where the pressure solver is a standard two-point flux-approximation (TPFA) scheme for Cartesian grids and a mixed finite-element method (MFEM) for triangular grids. For MFEM we apply the lowest-order Raviart–Thomas basis functions (Raviart and Thomas, 1977). Moreover, for all cases we match synthetic water-cut data obtained from a flow simulation on a reference permeability field. The permeability for each grid cell is treated as an adjustable parameter. Next, starting from an initial (prior) permeability field, we match the water-cut data via the generalized travel-time inversion method.

5.1 Case 1: Cartesian versus Triangular Grid

This synthetic case involves reconstruction of a reference permeability field given on a uniform 21×21 Cartesian grid (see Figure 3) based on the observed water-cut production history from a 9-spot pattern on the Cartesian grid (see

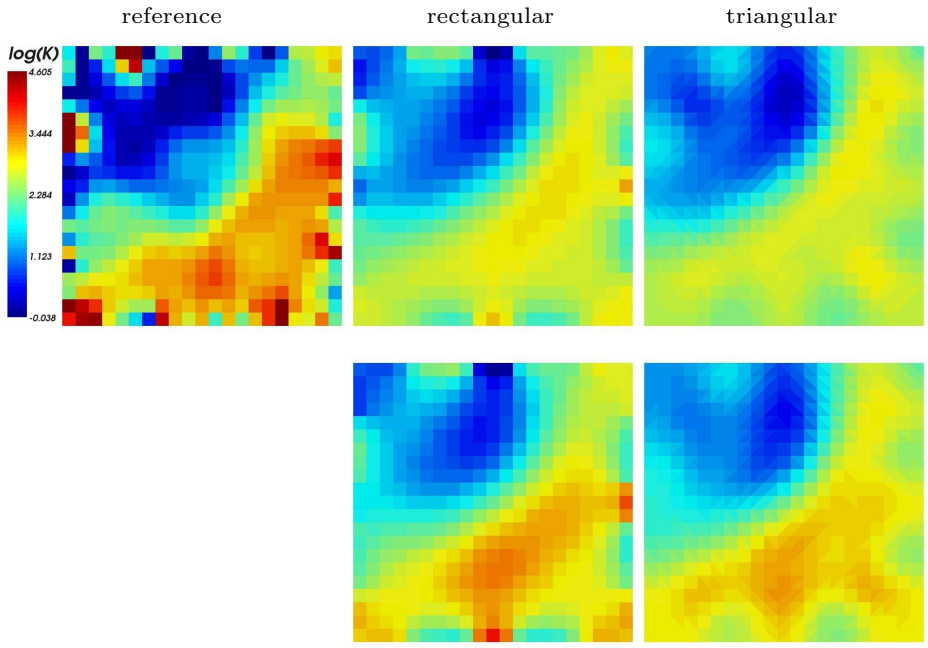

Fig. 3. Case 1: Reference and derived permeability fields on the rectangular grid with Laplacian smoothing and on the triangular grid with smoothing Stencil 3. In the top row $M_{\text{end}} = 0.2$, and in the bottom row$M_{\text{end}} = 10$.

Figure 4) with 5% white noise added. The permeability is reconstructed both on the rectangular grid and on a triangular grid obtained by subdividing each cell in the rectangular grid into two triangles. Hence, the history-matching problem will be more under-determined for the triangular grid, because twice as many parameters have to be matched by the same number of data points (a total of 441 and 882 parameters, respectively).

The dimension of the reservoir is 420×420 meters, and the flow is described by two different end-point mobility ratios, $M_{\text{end}} = 0.2$ and $M_{\text{end}} = 10$. We use a homogeneous permeability as the initial model and apply a standard five-point Laplacian regularization on the rectangular grid. For the triangular grid we apply four different generalized stencils described in Table 1, of which Stencil 1 corresponds with the five-point stencil on the rectangular grid.

The derived permeability fields are shown in Figure 3. Further, Table 1 reports the average discrepancy between the reference and derived permeability field measured by

$$\overline{\Delta \ln K} = \frac{1}{\bar{A}} \sum_{i=1}^{N} A_i |\ln K_i^{\text{ref}} - \ln K_i^{\text{match}}|. \tag{17}$$

Here A_i is the area of cell i and $\bar{A} = \sum_i A_i$ is the total area for all cells. Clearly, the final permeability models capture the large-scale trends of the reference

Table 1
Case 1: Reduction in percent in residual for time-shift (T) and amplitude (A), and reduction in permeability discrepancy ($\overline{\Delta \ln K}$) on the Cartesian grid with Laplacian smoothing and on the triangular grid with four different stencils.

			$M_{\text{end}} = 0.2$			$M_{\text{end}} = 10$		
Strategy	Nbh	ρ	T	A	$\overline{\Delta \ln K}$	T	A	$\overline{\Delta \ln K}$
Initial	-	-	100.0	100.0	1.045	100.0	100.0	1.045
Cartesian	-	-	6.8	12.7	0.570	7.5	21.7	0.548
Stencil 1	$\mathcal{N}_1$	ρ_{const}	5.5	13.7	0.614	7.5	23.0	0.599
Stencil 2	$\mathcal{N}_2$	$\rho_{\text{exp},2}$ $(R = 30)$	6.0	13.7	0.601	8.8	23.2	0.590
Stencil 3	$\mathcal{N}_{r=30}$	$\rho_{\text{exp},2}$ $(R = 30)$	6.2	13.6	0.595	9.5	22.9	0.575
Stencil 4	$\mathcal{N}_{r=30}$	$\rho_{\text{exp},2}$ $(R = 50)$	6.5	13.4	0.572	12.0	23.1	0.558

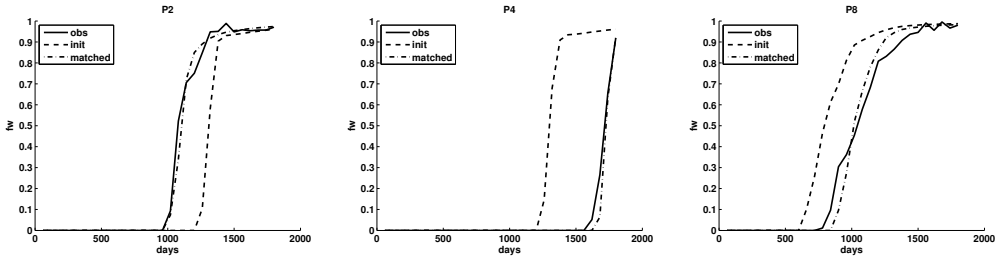

Fig. 4. Case 1: Water-cut curves for Stencil 3 on the triangular grid for producers P2 (North West), P4 (South East), and P8 (East). Mobility ratio $M_{\text{end}} = 0.2$.

permeability field on both grids. Figure 4 shows a comparison of the initial and final match of the water-cut curves for $M_{\text{end}} = 0.2$ for three wells with lowest initial (P2), highest initial (P4), and highest final mismatch (P8) for Stencil 3. Figure 5 shows the reduction in time-shift and amplitude residuals for each iteration using Stencil 3. Further, the reduction in water-cut residuals is also reported in Table 1 for the different stencils. Overall, the match to the production data is quite satisfactory.

The quality of the derived match is similar for all stencils reported in Table 1. The permeability discrepancy is slightly smaller for stencils with radius neighborhood. Conversely, using k-ring neighborhood gives a somewhat lower time-shift residual. A plausible explanation is that the radius neighborhoods usually involve couplings with more distant grid cells, causing the permeability modifications to be more spatially distributed. In other words, more of the modifications occur away from the high sensitivity regions where they would have the greatest impact. This tendency can be controlled by varying the neighborhood radius, the ρ function, and the R parameter.

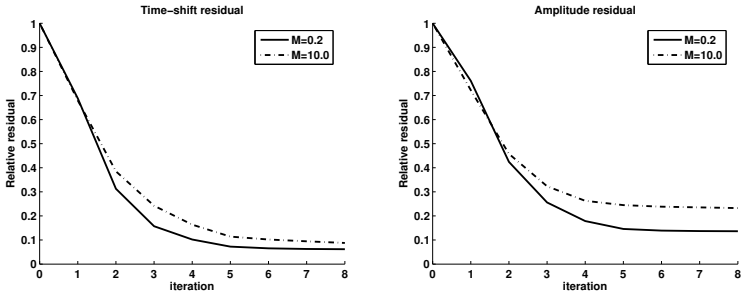

Fig. 5. Case 1: Reduction of residuals for all producers using Stencil 3 for mobility ratios $M_{\text{end}} = 0.2$ and $M_{\text{end}} = 10$.

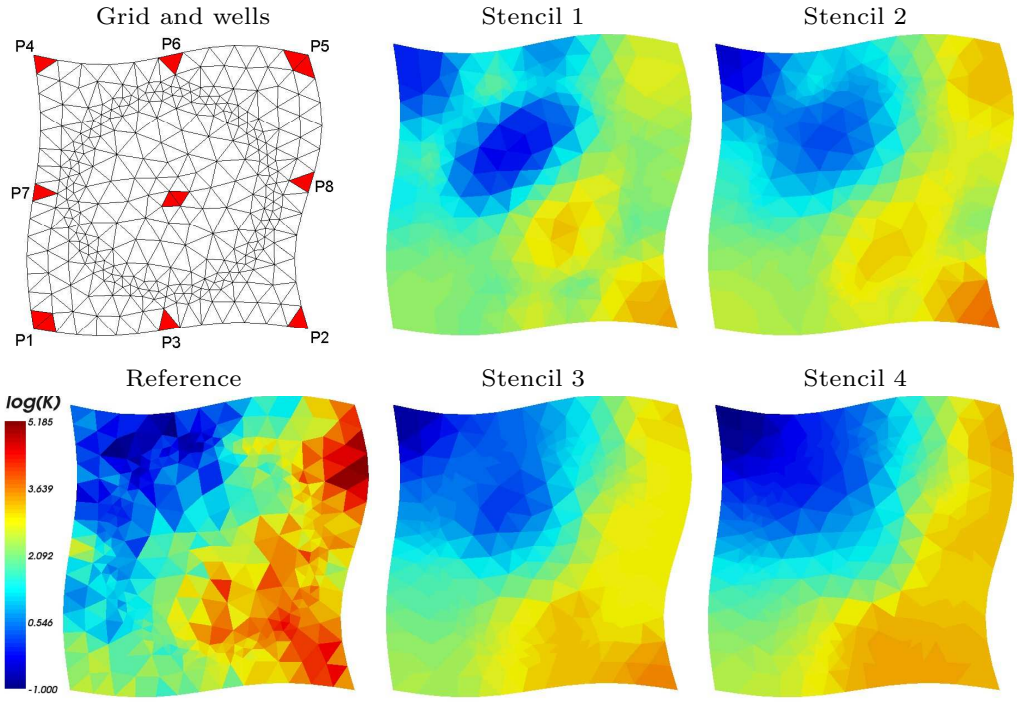

Fig. 6. Case 2: Grid and well-configuration, reference permeability field, and derived permeability fields for Stencils 1 to 4 using sensitivity.

5.2 Case 2: Nine-Spot with a Highly Unstructured Grid

Next we consider the reconstruction of a reference permeability field on an unstructured triangular grid with 581 grid cells. The dimensions of the bounding box for the reservoir is 322×318 meters. Further, the grid is highly unstructured with a ring of high grid density; see Figure 6. This grid is not very realistic for a real reservoir, but was chosen to investigate the effect of varying cell sizes. The initial permeability field for this case is homogeneous with a permeability mean of 7.0 mD. Moreover, the end-point mobility ratio is $M_{\text{end}} = 0.5$.

Table 2
Case 2: Reduction in percent in residual for time-shift (T) and amplitude (A), and reduction in permeability discrepancy ($\overline{\Delta \ln K}$) with four different stencils using sensitivity (Rows 3–6) and rescaled sensitivity (Rows 7–10).

Strategy	Nbh	ρ	T	A	$\overline{\Delta \ln K}$
Initial	-	-	100.0	100.0	1.165
Stencil 1	$\mathcal{N}_1$	ρ_{const}	6.0	14.2	0.771
Stencil 2	$\mathcal{N}_2$	ρ_{const}	8.2	18.9	0.612
Stencil 3	$\mathcal{N}_{r=30}$	ρ_{exp2} $(R = 50)$	9.5	18.6	0.585
Stencil 4	$\mathcal{N}_{r=40}$	ρ_{exp2} $(R = 50)$	12.0	20.9	0.555
Stencil 1	$\mathcal{N}_1$	ρ_{const}	7.0	16.1	0.631
Stencil 2	$\mathcal{N}_2$	ρ_{const}	12.6	22.5	0.525
Stencil 3	$\mathcal{N}_{r=30}$	ρ_{exp2} $(R = 50)$	12.1	20.8	0.546
Stencil 4	$\mathcal{N}_{r=40}$	ρ_{exp2} $(R = 50)$	12.4	21.7	0.568

Synthetic production data are obtained by simulating 1200 days of production from a 9-spot pattern (see Figure 7) with 5% white noise added. In the inversion we only use data from the first 800 days. Data from the remaining 400 days are used to assess the predictive ability of our inversion methods.

Table 2 reports the reduction in time-shift and amplitude residuals for four different stencils and Figure 6 shows the derived permeability fields. All four stencils capture the large-scale trends of the reference permeability, even though the derived permeability fields, especially for the radius neighborhood, are a bit too smooth. This is to be expected since there is no heterogeneity to preserve from the initial (prior) permeability field. As in the previous example, the time-shift residuals are lowest for the k-ring neighborhoods. On the other hand, Stencils 1 and 2 give undesired grid effects inside the ring with small cells, in which the initial homogeneous permeability field is still visible, in particular for Stencil 1 in the quadrant bounded by the injector and wells P6, P4 and P4. Stencils 3 and 4 are more able to capture the large-scale permeability structures, as seen in Figure 6 and from the permeability discrepancy. However, small artifact are also visible for these stencils, especially for Stencil 3. Without smoothing, small cells with small sensitivity will in general get smaller modifications than larger cells. However, the smoothing will tend to distribute the modifications. For the 1- and 2-ring neighborhoods, the stencils were not able to span over the ring with small cells and therefore resulted in too small modifications in this high-density band. For the radius neighborhood, on the other hand, the region of influence crosses over the high-density band and therefore distributed the modifications more properly.

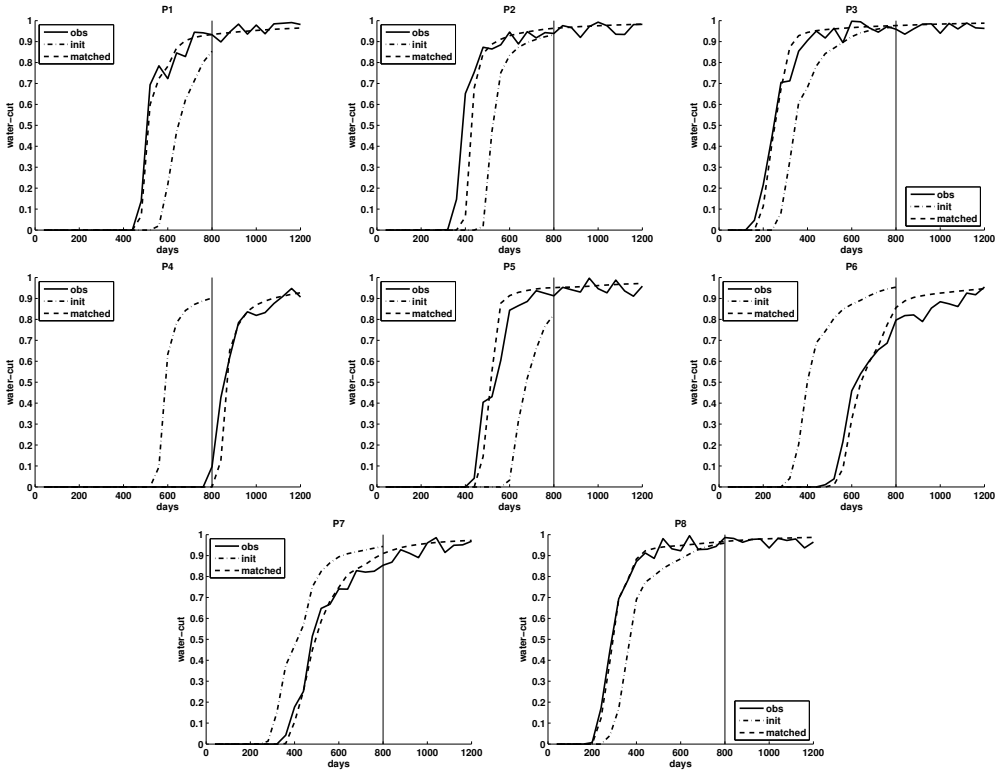

Fig. 7. Case 2: Water-cut match for Stencil 4 for the wells P1–P8. The time span 0–800 days is the matching period, while the time span 800–1200 days is prediction.

Figure 7 shows a comparison of the initial and final match of the water-cuts for Stencil 4. The overall match to the production data is satisfactory, and the prediction in the period from 800 to 1200 days shows good agreement. In particular, the prediction for well P4 is good, given that this well had almost no significant water responses during the matching period.

In Section 3.2 we proposed to use rescaled sensitivities rather than sensitivities in the inversion process to counteract effects from heterogeneous cell sizes. The rescaled sensitivity of a cell i is computed by $G_i\bar{V}/V_i$, where G_i is the sensitivity and V_i is the volume for cell i and $\bar{V}$ is the average volume of all cells. Figure 8 shows sensitivities G_i and sensitivity densities G_i/V_i for wells P4 and P6. As expected, the sensitivities for small cells are in general smaller than for large cells. The sensitivity densities, on the other hand, do not show any grid effects and are similar to those computed on an (almost) equisized grid. However, as seen in Figure 8, the sensitivities and sensitivity densities are of different magnitude. We therefore suggest to multiply the sensitivity densities by the average volume of all cells $\bar{V}$ to obtain what we will refer to as rescaled sensitivities. Hence, the sensitivities and the rescaled sensitivities will be more of the same magnitude and will coincide on uniform grids. The drawback with using rescaled sensitivities is that it might be harder to match the data, because rescaled sensitivities will enforce greater modifications in

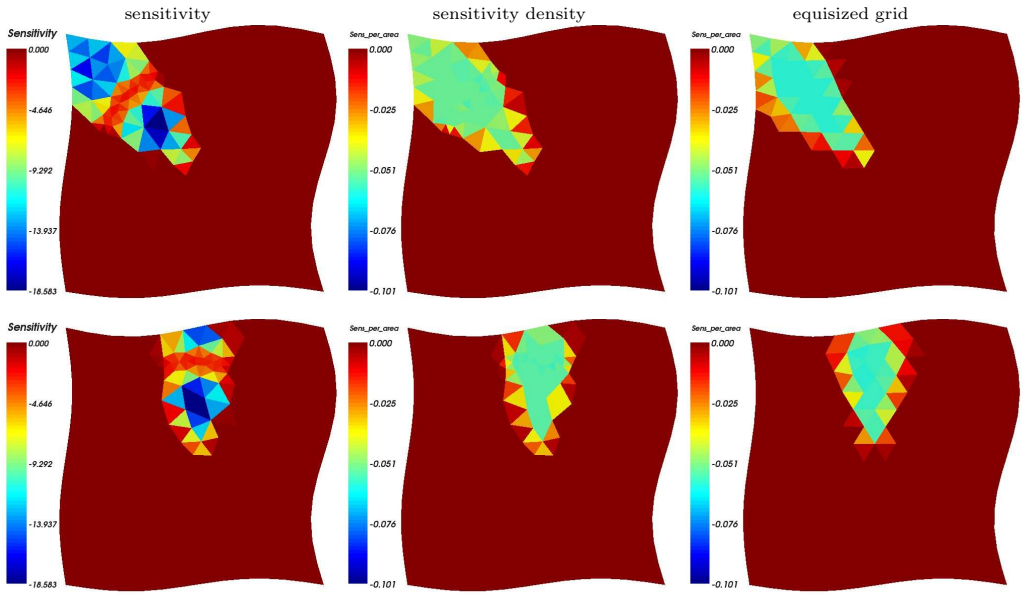

Fig. 8. Case 2: Time-shift sensitivity and sensitivity density (not rescaled) computed for a homogeneous permeability field for wells P4 (top) and P6 (bottom).

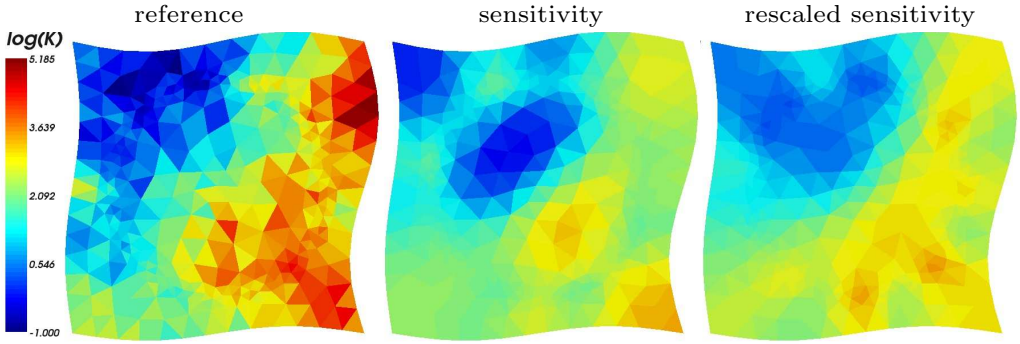

Fig. 9. Case 2: Permeability field derived using Stencil 1 with sensitivity and rescaled sensitivity.

cells that are less important with respect to shifting the production curves (less sensitivity).

Figure 9 shows a comparison of the derived permeabilities for Stencil 1 using sensitivities and rescaled sensitivities, respectively. The resulting permeability field applying the rescaled sensitivities does not show indications of grid effects from the high-density band. Further, Table 2 shows the reduction in residuals and average permeability discrepancies for both applying the sensitivities and the rescaled sensitivities for different stencils. The permeability discrepancies seems to improve by applying rescaled sensitivities. Especially the k-ring stencils seem to improve the quality of the derived permeability fields. Even so, the reduction in the residuals is in general slightly degraded, as expected.

To test the robustness of the generalized stencil, the neighborhood, and the

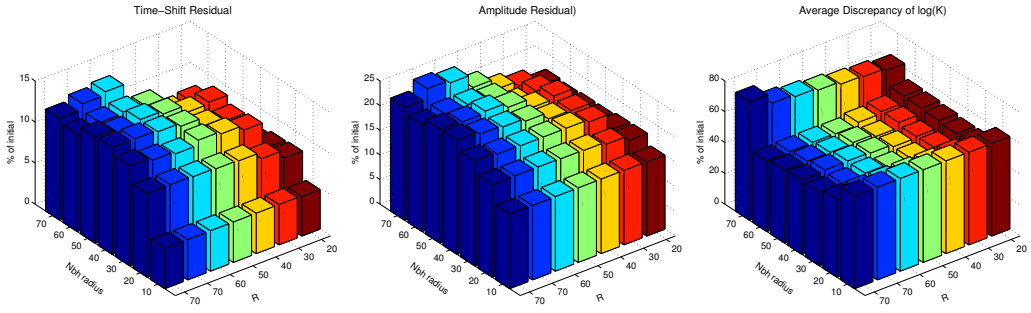

Fig. 10. Case 2: Robustness of stencil parameter R and neighborhood radius r.

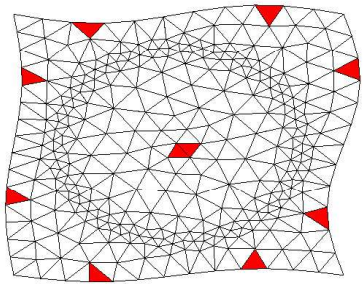

Fig. 11. Case 2: Altered well-configuration.

application of rescaled sensitivities, we have systematically performed the inversion for different stencil parameters for the stencil $(\rho_{\exp 2}, \mathcal{N}_{r=x})$. The results are presented in three 7×7 test matrices with the correlation length R and the neighborhood radius r as parameters. The correlation length takes the values $R \in \{20, 30, 40, 50, 60, 70, \infty\}$, while the the neighborhood radius takes the values $r \in \{10, 20, 30, 40, 50, 60, 70\}$; both measured in meters. Hence, by letting R go to infinity the exponential correlation function will approach the constant correlation function. Figure 10 shows the reduction of time-shift and amplitude residuals after eight iterations, as well as the average discrepancy between matched and reference permeability fields. Judging from the residual plots, it seems like the more weight is given to the smoothing stencil away from the center cell, the harder it is to match the data. In other words, more of the modifications are made away from where they would have the greatest impact on the simulated production responses. Even so, the quality of the match is not degraded considerably. The permeability discrepancy is very robust with respect to the smoothing parameters. There seems to be a lower and upper limit for the stability region with respect to the neighborhood extent, but the radius of the stable region is quite large given the dimension of the reservoir.

Finally, we test the predictive abilities of the derived permeability fields for the altered well-configuration shown in Figure 11. Table 3 reports the reduction in amplitude and time-shift residuals compared with a simulation using the prior homogeneous model. Here the best results, by far, are obtained using the radius neighborhood.

Table 3
Case 2: Reduction in percent for misfit in time-shift (T) and amplitude (A) by applying the derived permeability fields for the altered well-configuration.

Strategy	Nbh	ρ	T	A
Initial	-	-	100.0	100.0
Stencil 1	$\mathcal{N}_1$	ρ_{const}	47.1	50.4
Stencil 2	$\mathcal{N}_2$	ρ_{const}	33.4	38.3
Stencil 3	$\mathcal{N}_{r=30}$	ρ_{exp2} $(R = 50)$	27.8	33.0
Stencil 4	$\mathcal{N}_{r=40}$	ρ_{exp2} $(R = 50)$	27.0	32.0

5.3 Case 3: Faulted Corner-Point Grid

We consider a 2-D corner-point reservoir model with diagonal permeability streaks, dynamic well configuration and non-sealing faults that induce non-neighboring connections; see Figure 12. The lognormal permeability field has a 50×50 logical structure, but because of the faults, the grid has three shifted sections. Further, the dimensions of bounding box for the reservoir is 646×605 meters, and the end-point mobility ratio is $M_{\text{end}} = 0.5$.

The history-matching will be performed on the corner-point grid, but to be able to trace streamlines over the non-neighboring connections, we simulate the flow on a triangular grid where we have subdivided each corner-point cell into two triangles and in addition refined the grid by triangles close to the faults to obtain a matching grid. Hence, no upscaling/downscaling is required between the simulation grid and the history-matching grid because the permeability field originally is given on the coarsest grid. For each forward simulation we use a pressure steps of 100 days. In Section 4.1 we discussed how to handle the non-matching cell faces at the faults when defining the neighborhood.

Synthetic production data were generated by adding 15% white noise to the water-cut curves computed from the reference permeability. Initially, the well-configuration is a kind of five-spot configuration, with an injector in the center and four producers in the corners; see Figure 12. Further, the producers operate at equal constant rate. Producer P4 in the south-west corner has an early breakthrough and is therefore converted to an injector after 900 days. Simultaneously, a new producer (P5) is introduced in the lower-left corner of the section in the middle (south). This part of the reservoir has not been depleted at all yet. The new injector is injecting 3/5 of the total injection rate. The motivation for the updated well-configuration is also to introduce an additional sweep from the south-west corner. After the well conversion, all producers operate at constant equal rate. The updated well-configuration is kept throughout the rest of the production period. Thus, we wish to integrate

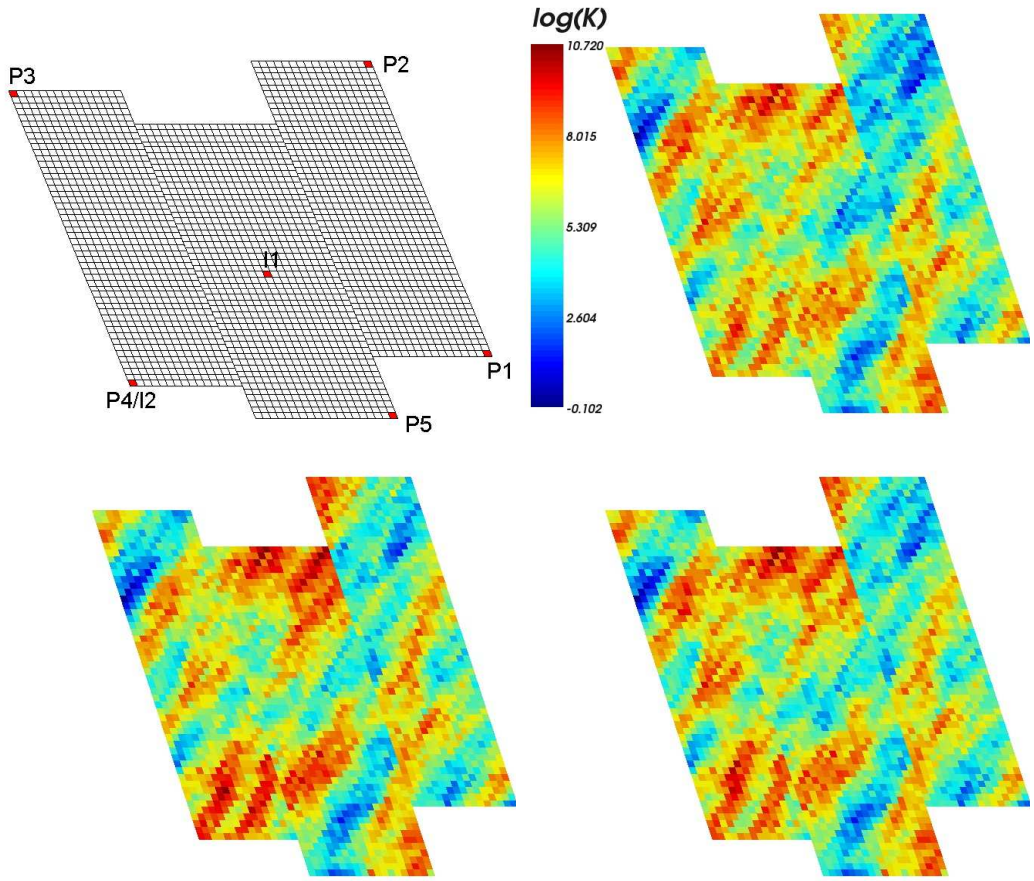

Fig. 12. Case 3: Grid and well-configuration (upper left), reference permeability field (upper right), initial (prior) permeability field (lower left) and derived permeability field by Stencil 3 (lower right).

2500 days of production data from five producers in total.

To match observed data, we start from the prior permeability field shown in Figure 12 and treat the permeability in each corner-point cell as an adjustable parameter, giving a total of 2500 unknown parameters to be estimated. The corner-point sensitivities are obtained by summing the sub-cell sensitivities; see Figure 13. Table 4 reports the reduction in residuals with respect to time-shift and amplitude. The resulting permeability field for Stencil 3 after eight iterations is shown in Figure 12. The updated permeability field is in general closer to the reference, and the realism of the permeability field is not degraded by the history matching. This is also confirmed by the average permeability discrepancies in Table 4. In the derived permeability fields there was no indications of smearing across the faults. This is caused by the regularization that keeps the modifications small and smooth, and the localization of the sensitivities; see Figure 13. Figure 14 shows a comparison of the initial and the final match of the water-cut curves for the production wells obtained with Stencil 3. Overall, the match to the production data and the quality of the

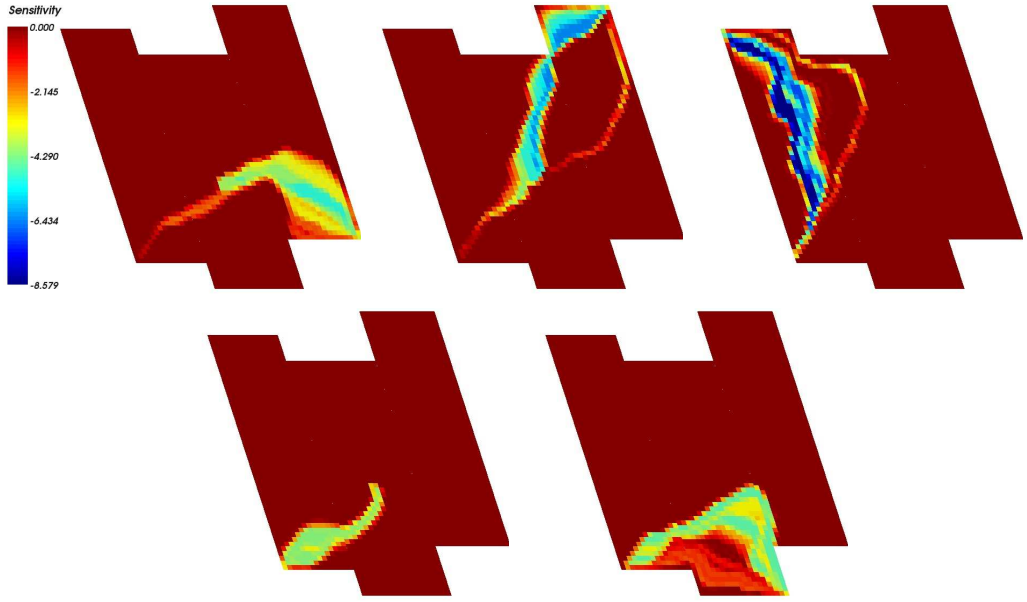

Fig. 13. Case 3: Time-shift sensitivities for the five producers.

Table 4
Case 3: Reduction in percent for misfit in time-shift (T) and amplitude (A), and reduction in average discrepancy in log permeability $\overline{\Delta \ln K}$).

Strategy	Nbh	ρ	T	A	$\overline{\Delta \ln K}$
Initial	-	-	100.0	100.0	0.421
Stencil 1	$\mathcal{N}_1$	ρ_{const}	5.5	35.0	0.334
Stencil 2	$\mathcal{N}_2$	ρ_{const}	4.9	35.0	0.332
Stencil 3	$\mathcal{N}_{r=30}$	ρ_{exp2} $(R = 50)$	5.8	35.2	0.334
Stencil 4	$\mathcal{N}_{r=40}$	ρ_{exp2} $(R = 50)$	5.7	35.8	0.332

derived permeability fields are satisfactory.

Concluding Remarks

The generalized travel-time method for inversion of production data has been successfully applied to unstructured grids. For equisized grids, the original framework developed previously by Vasco et al. (1999) and He et al. (2002) can be applied almost directly, as has previously been done for grids that are logically Cartesian and quite uniform. For fully unstructured grids that may have (large) differences in cell sizes and in the number of connections, our investigations revealed that a generalized smoothing operator should be introduced to obtain a good match. Our new smoothing stencils introduce

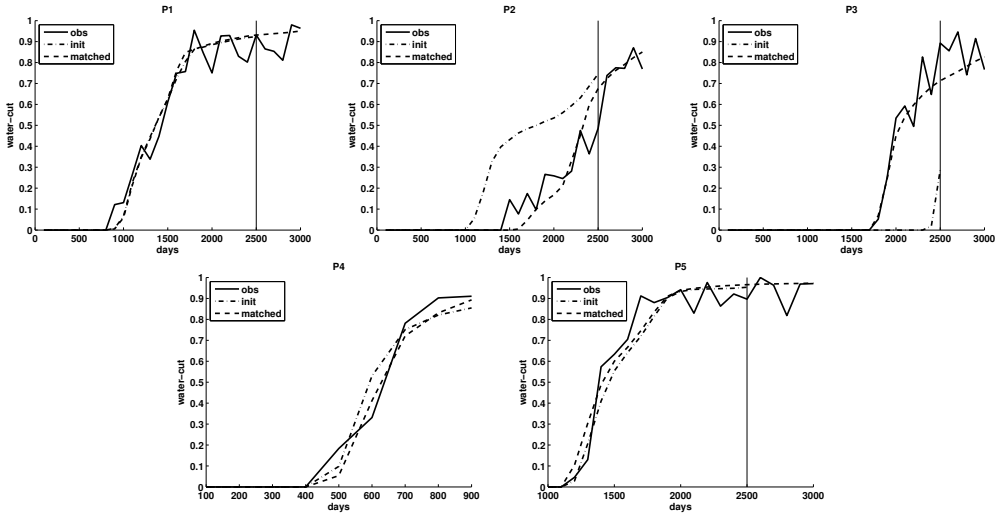

Fig. 14. Case 3: Water-cut match for the Stencil 3 for wells P1–P5. The time span 0–2500 days is the matching period, while the time span 2500–3000 days is prediction.

a few extra regularization parameters, but the inversion is robust to these parameter values and it is easy to make a good choice by considering the cell sizes of the grid.

Similarly, we found that rescaled sensitivities should be incorporated to give permeability fields without undesired heterogeneities induced by grid effects. The magnitude of potential modifications of the reservoir parameters are determined by the sensitivities and data misfits. Since small grid cells generally have smaller sensitivities than larger cells, the magnitude of the induced parameter modifications will depend on heterogeneity of the grid. Because the production-response sensitivities are spatially additive, it will often be better to use rescaled sensitivities instead of sensitivities in the inversion to obtain realistic modifications, even though this can make it slightly harder to match the observed data. For uniform grids the sensitivities and the rescaled sensitivities will coincide.

In the current paper we have only investigated two-dimensional numerical examples, including non-neighboring connections. This is partly because 2-D examples are well suited for visualization and for detecting the principal effects. Real 3-D reservoir models are, of course, much more challenging. Although the framework we have proposed for applying the generalized travel-time inversion on fully unstructured grids is general and should apply to 3-D grids as well, additional effects like layering and various grid-degeneracies may prove important in 3-D. Extensions to real-life 3-D models is therefore a topic of future research.

Acknowledgments

The research of Stenerud was funded by the Uncertainty in Reservoir Evaluation (URE) program at the Norwegian University of Science and Technology. Lie and Kippe were founded by the Research Council of Norway under grant number 152731/S30, 152732/S30 and 158908/I30.

References

Aarnes, J. E., 2004. On the use of a mixed multiscale finite element method for greater flexibility and increased speed or improved accuracy in reservoir simulation. Multiscale Model. Simul. 2 (3), 421–439.

Aarnes, J. E., Krogstad, S., Lie, K.-A., to appear. Multiscale mixed/mimetic methods on corner-point grids. Comput. Geosci.

Abrahamsen, P., 1997. A review of Gaussian random fields and correlation functions, second edition. Tech. Rep. 917, Norwegian Computing Center, Oslo, Norway.

Chen, A., Hou, T., 2002. A mixed multiscale finite element method for elliptic problems with oscillating coefficients. Math. Comp. 72 (242), 541–576.

Cheng, H., Datta-Gupta, A., He, Z., 2005a. A comparison of travel-time and amplitude matching for field-scale production-data integration: Sensitivity, nonlinearity, and practical implications. SPE J. 10 (1), 75–90.

Cheng, H., Kharghoria, A., He, Z., Datta-Gupta, A., 2005b. Fast history matching of finite-difference models using streamline-derived sensitivities. SPE Reserv. Eval. Eng. 8 (5), 426–436.

He, Z., Yoon, S., Datta-Gupta, A., 2002. Streamline-based productoin data integration with gravity and changing field conditions. SPE J. 7 (4), 423–436.

Hohl, D., Jimenez, E., Datta-Gupta, A., 24–27 September 2006. Field experiences with history matching an offshore turbiditic reservoir using inverse modeling. In: SPE Annual Technical Conference and Exhibition. San Antonio, TX, USA, SPE 101983.

Iserles, A., 1996. A First Course in the Numerical Analysis of Differential Equations. Cambridge University Press.

Paige, C., Saunders, M., 1982. LSQR: An algorithm for sparse linear equations and sparse least squares. ACM Transactions on Mathematical Software 8 (1), 43.

Qassab, H., R, M. K., Pavlas, Afaleg, N., Ali, H., Kharghoria, A., He, Z., Lee, S., Datta-Gupta, A., 5–8 October 2003. Streamline-based production data integration under realistic field conditions: Experience in a giant Middle-Eastern reservoir. In: SPE Annual Technical Conference and Exhibition. Denver, Colorado, USA, SPE 84079.

Raviart, P.-A., Thomas, J., 1977. A mixed finite element method for 2nd order elliptic problems. Mathematical Aspects of Finite Element Methods (Proc. Conf., Consiglio Naz. Delle Ricerche (C.N.R), Rome, 1975), Lecture Notes in Mathematics, Springer, Berlin 606, 292–315.

Stenerud, V., Kippe, V., Lie, K.-A., Datta-Gupta, A., submitted. Multiscale-streamline simulation and dynamic data integration for high-resolution subsurface models. Water Resources Research.

Stenerud, V., Kippe, V., Lie, K.-A., Datta-Gupta, A., to appear. Adaptive multiscale streamline simulation and inversion for high-resolution geomodels. SPE J.

Taubin, G., 6–11 August 1995. A signal processing approach to fair surface design. In: SIGGRAPH 95 Conference Proceedings. Los Angeles, California, USA, pp. 351–358.

Vasco, D., Yoon, S., Datta-Gupta, A., 1999. Integrating dynamic data into high-resolution models using streamline-based analytic sensitivity coefficients. SPE J. 4 (4), 389–399.

Yoon, S., Malallah, A., Datta-Gupta, A., Vasco, D., Behrens, R., 2001. A multiscale approach to production-data integration using streamline models. SPE J. 6 (2), 182–192.